Thermofluid design and performance analysis of an air-cooled heat rejection system for a 50 MWe sCO_2 concentrated solar power plant

Prepared by:

Liam M. Abrahams (ABRLIA001)

Supervised by

Colin F. du Sart

November 2023

Submitted to the Department of Mechanical Engineering at the University of Cape Town in partial fulfilment of the academic requirements for a Masters of Science degree in Mechanical Engineering

Key Words: Air-cooled heat rejection, concentrated solar power, supercritical carbon dioxide

Abstract

There is increasing interest in renewable energy technologies, both globally and within South Africa. An emerging renewable energy technology is concentrated solar power (CSP) plants utilising supercritical carbon dioxide (sCO_2) as a working fluid. This technology promises a more compact and efficient alternative to the current Rankine cycle based CSP plants. However, no such plant currently exists at the utility scale, and little is known about the heat rejection systems of such plants. If these plants are to be realised at a utility-scale, further research is required with regards to the process design, physical layouts, and operational philosophy of these heat rejection systems.

The present work includes the development of the conceptual layout and steady-state one-dimensional (1D) thermofluid network models of forced draft direct air-cooled heat rejection systems for a proposed 50 MWe sCO2 CSP plant. The models were developed using opensource software libraries in Python 3.8.5. The heat rejection systems consist of cooling cells, each with horizontal multi-pass staggered finned tube banks employing axial forced draft fans. In contrast to existing studies, the designs consider the mechanical integrity of the components e.g., tube wall thickness and the availability of standard components e.g., commercial fans. The number of cooling cells, fan selection, and tube geometry is determined by coupling the heat rejection system model to a sCO_2 power cycle model developed by others, and then developing precooler (PC) and intercooler (IC) designs which maximise cycle efficiency. The findings indicate that cycle efficiency increases with increased heat transfer area in the air-cooled heat rejection systems. However, any optimisation of the PC and IC needs to be performed together, and with the cycle model for the best results. Furthermore, an increase in the thermal efficiency of the power cycle was observed when including the detailed cooler models, as opposed to the simplified cooler models used in the original cycle model, demonstrating the value of including more detailed models in cycle-level studies. The methodology applied in this study may be used in future works to size heat rejection systems for sCO_2-CSP plants.

The PC and IC designs were then modelled in the Flownex ® SE software to perform quasi-steady state studies, and to assist with the development of complete dynamic plant models by others. The Python and Flownex models agree well, with the heat rejection rates within 3%. The Flownex ® SE model features improved (additional) discretisation of the heat exchangers on the sCO_2-side and includes distribution headers which consider mechanical integrity and simulate realistic flow distribution. Since air-cooled heat exchangers are known to be sensitive to ambient conditions, the performance of the systems under varying ambient air temperatures were investigated. This was done using data for a typical year for the Upington area in South Africa. Additionally, the performance of the systems under cycle part load conditions were also investigated. The results indicate that the performance of the systems is especially sensitive to air temperatures and cycle part-load operation. For temperatures lower than the nominal design temperature, and at cycle part-load operation, over-cooling of the working fluid occurs. This can be controlled by bypassing areas of the heat rejection system and by switching off fans. However, to ensure sufficient cooling at higher temperatures, the heat-rejection systems need to be oversized.

Plagiarism Declaration

I declare that the work contained in this dissertation is my own. Each contribution to, and quotation in, this thesis from the work(s) of other people has been attributed and has been cited and referenced using the Harvard convention. I have not allowed and will not allow anyone to copy my work with the intention of passing it off as their own work or part thereof.

Signed by candidate

Liam M. Abrahams

07 November 2023

Acknowledgements

First and foremost, I would like to thank my supervisor, Mr Colin F. du Sart for his consistent support, insight, and patience over the past three years. Without his guidance and encouragement, I would never have ended up where I am today. His commitment to helping me achieve this will always be appreciated as will the feedback and financial support provided throughout the process. I would also like to thank him for the opportunity to attend the HEFAT conference and the assistance when co-authoring a paper that was published in the proceedings. Finally, I would like to thank him for all the knowledge he has imparted over these last three years.

I would also like to thank Dr Ryno Laubscher for his input and feedback on the project, his knowledge of the subject matter and willingness to share were essential in completing both this report and when co-authoring the HEFAT conference paper. I will always be grateful for the time he spent helping me learn and grow my understanding of engineering and problem solving.

Additionally, I would like to thank all my friends and colleagues at the ATProM office and UCT for their support and kindness throughout the project. I could never have completed this journey without them. Special thanks to Kai Feng and Rashid Haffejee for their insight and willingness to discuss various topics with me.

Importantly, I would like to thank my partner, Talia Bernhardt for her unwavering support, especially in the final year of the project. Her counsel and encouragement have kept me going during times when balancing work and life became difficult.

Finally, I want to thank my parents. Their support, both financial and personal has seen me through to this point. I would not have succeeded without the encouragement and guidance they have provided. I would like to thank them for everything they have done to help me achieve my goals.

Contents

List of Figures

List of Tables

Nomenclature

Acronyms and Abbreviations

ACC	Air-cooled condenser
CSP	Concentrated solar power
DALR	Dry adiabatic lapse rate
DNI	Direct normal irradiation
e-NTU	Effectiveness-Number of transfer units
HPC	High pressure compressor
HPT	High pressure turbine
HTR	High temperature recuperator
IC	Intercooler
LMTD	Logarithmic mean temperature difference
LPC	Low pressure compressor
LPT	Low pressure turbine
LTR	Low temperature recuperator
MALR	Moist adiabatic lapse rate
MH	Main heater
MLR	Multivariate-linear regression
NDDCT	Natural draft dry-cooling tower
RCC	Recompression compressor
RH	Reheater
sCO_2	Supercritical carbon dioxide

General symbols

a	Dimensionless fin adjustment factor, regression coefficient	
A	Area, sum of fin and root areas	[m^2]
A_c	Area of fan casing	[m^2]
A_e	Effective fan area	[m^2]
A_F	Fan area	[m^2]
A_f	Fin area	[m^2]
A_{fr}	Frontal area of heat exchanger tubes	[m^2]
A_2	Inlet area between the tower supports	[m^2]
b	Dimensionless fin adjustment factor	
C	Specific heat capacity ratio, dimensionless fin adjustment factor	
C_D	Drag coefficient	

c	Dimensionless fin adjustment factor	
c_p	Isobaric specific heat capacity	[J/kg.K]
d	Diameter	[m], [mm]
d_e	Hydraulic diameter	[m]
d_{ea}	Hydraulic diameter of air	[m]
d_i	Tube inner diameter	[mm]
d_F	Fan diameter	[m]
d_f	Fin diameter	[mm]
d_o	Tube outer diameter	[mm]
d_r	Root diameter	[mm]
F_T	LMTD correction factor	
f	Dimensionless tube drag coefficient factor	
f_A	Arrangement factor	
f_D	Darcy-Weisbach friction factor	
$f_{n_{turb}}$	Row correction factor	
f_0	Base correction factor	
H_{ex}	Height of the air-cooled system exit	[m]
$H_{he,ex}$	Height of the heat exchanger exit	[m]
H_F	Fan platform height	[m]
H_f	Height of the fin	[mm]
H_{HX}	Heat exchanger height	[m]
H_{plenum}	Plenum height	[m]
H_V	Latent heat of vaporisation of water	[J/kg]
H_{ww}	Windwall height	[m]
h	Convective heat transfer coefficient, specific enthalpy	[W/m^2.K], [J/kg]
K	Loss coefficient	
k	Thermal conductivity	[W/m.K]
k_f	Fin thermal conductivity	[W/m.K]
L	Length	[m]
M_a	Molar mass of air	[kg/mol]
m_a	Mass flow rate of air	[kg/s]
N	Rotational speed of the fan	[rpm]
N_F	Number of fan rows in cooling system	
N_L	Number of longitudinal tubes	
N_{MR}	Number of main resistances in a flow network	
N_{passes}	Number of passes in the heat exchanger	
N_{paths}	Number of flow paths in the heat exchanger	

N_r	Number of tube rows in heat exchanger	
N_T	Number of transverse tubes	
N_{tubes}	Number of transverse tubes in a heat exchanger pass	
NTU	Number of transfer units	
Nu	Nusselt number	
$p_{a,sea}$	Ambient air pressure at sea-level	[kPa]
p_{a1}	Ambient air pressure at ground level	[kPa]
p_{max}	Maximum sCO_2 cycle pressure	[MPa]
PR	Pressure ratio	
Pr	Prandtl number	
Δp	Pressure drop	[Pa], [kPa]
Δp_{amb}	Ambient pressure change	[Pa]
Δp_{form}	Pressure drop due to duct geometry	[Pa]
Δp_{fric}	Frictional pressure drop through a tube	[Pa]
Δp_{he}	Pressure drop across the heat exchanger tubes	[Pa]
Q	Heat transferred	[W]
R	Thermal resistance	[W/K]
R_0	Universal gas constant	[J/mol.K]
R_d	Specific gas constant for dry air	[J/kg.K]
R_{hub}	Hub to tip ratio	
R_v	Specific gas constant for water vapor	[J/kg.K]
Re	Reynolds number	
Re_ψ	Void Reynolds number	
Re_d	Reynolds number in a duct	
r	Radial distance	[m]
r_{mix}	Mixing ratio of moist air	
S_x	Standard deviation of a variable	
S_d	Diagonal finned tube pitch	[m]
S_f	Fin pitch	[mm]
S_L	Longitudinal finned tube pitch	[m]
S_T	Transverse finned tube pitch	[m]
SF	Safety factor	
SOP	Send-out-power	[kW]
s_{clear}	Fan tip clearance percentage	[%]
s_F	Actual fan tip clearance	[m]
T	Temperature	[K/°C]
T_a	Air temperature	[K/°C]

$T_{a,sea}$	Ambient air temperature at sea-level	[K/°C]
T_{a1}	Air temperature at ground level	[K/°C]
T_{a6}	Air temperature at the heat exchanger exit	[K/°C]
T_m	Bulk mean fluid temperature	[K/°C]
T_w	Mean tube wall temperature	[K/°C]
ΔT	Change in temperature	[K/°C]
ΔT_{lm}	LMTD	[K/°C]
t_f	Fin thickness	[mm]
UA	Conductance	[W/K]
$\dot{V}$	Volumetric flow rate	[m^3/s]
$\dot{V}_{ideal}$	Ideal volumetric flow rate	[m^3/s]
v	Fluid velocity	[m/s]
v_{eff}	Effective fluid velocity	[m/s]
v_{ff}	Free flow fluid velocity	[m/s]
W_{HX}	Heat exchanger width	[m]
W_w	Walkway width	[m]
X	Dimensionless fan height factor	
x	Normalised input variable	
$\bar{x}$	Thermodynamic quality	
x_{F-he}	Distance between the fan and the heat exchanger	[m]
Y_s	Yield strength	[MPa]
y	Predicted output variable	
z	Altitude, elevation	[m]

Greek symbols

α	Ratio of heat exchanger area to total core volume	
β	Standardised regression coefficient	
ϵ	Surface roughness	
η	Efficiency	
η_f	Fin efficiency	
η_0	Overall surface efficiency	
θ	A-frame half apex angle	[°]
μ	Fluid dynamic viscosity	[kg/m.s]
μ_{a56}	Harmonic dynamic viscosity of air in the heat exchanger	[kg/m.s]
ρ	Density	[kg/m^3]
ρ_{a56}	Harmonic density of air in the heat exchanger	[kg/m^3]

σ	Area ratio
ϕ	Dimensionless correction factor for heat exchanger efficiency
ψ	Void factor

Subscripts

a	Air
c	Cold stream
ex	Exit
h	Hot stream
$header$	Manifold header
in	Inlet
L	Liquid
lam	Laminar
tbs	Tube(s)
ts	Tower supports
$turb$	Turbulent
V	Vapor
w	Wall

1. Introduction

1.1 Background and motivation

There is a growing focus on generating electricity from renewable energy technologies, particularly concentrated solar thermal power (CSP) plants (Manzano-Agugliaro et al., 2013; IRENA, 2019; Mehos et al., 2020; World Bank, 2021). A high-level schematic of a CSP tower plant is provided in Figure 1-1. Currently, the majority of these plants employ mature steam Rankine cycles in their power block, leaving little room for improvement. However, literature suggests that supercritical carbon dioxide (sCO_2) power cycles may be applicable for use in such plants (Ahn et al., 2015; Neises & Turchi, 2019). These cycles have the potential to achieve higher cycle thermal efficiencies in comparison to conventional Rankine power cycles (approximately 45% versus 40% (Brun, Friedman & Dennis, 2017; Wang, He & Zhu, 2017; Neises & Turchi, 2019)). Furthermore, this may be achieved with more compact turbomachinery and at lower operating temperatures and pressures (Sathish, Kumar & Nassar, 2021). This may lead to lower capital costs and a reduced plant footprint, possibly 4 times smaller than those using Rankine cycles (Ahn et al., 2015; Liu et al., 2018). Another benefit of sCO_2 cycles relative to conventional Rankine cycles is that the fluid remains in one phase throughout the process. According to Kruizenga et al. (2011), this greatly reduces the complexity involved in plant design.

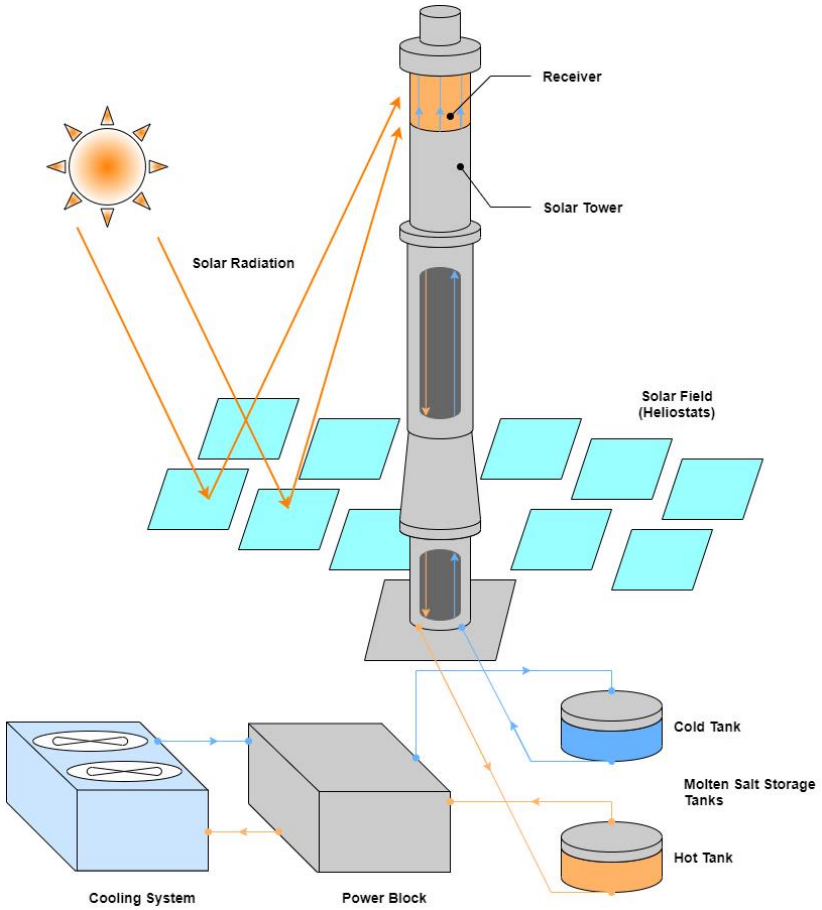

Figure 1-1: High-level schematic of a CSP tower plant, adapted from Binotti et al. (2017)

The sCO_2 cycle is a derivative of the closed gas Brayton cycle. In a simple Brayton cycle the working fluid is compressed, then heated and passed through turbines to extract energy, then cooled before being compressed again. Modifications can be made to this layout to improve the cycle efficiency. For example including intercooling with multiple compression stages, reheating with multiple work extraction stages and recuperation (Cengel & Boles, 2015a). Different process fluids also affect the efficiency. With the aim being to raise cycle efficiencies, one of the more innovative and promising options is sCO_2 (Brun et al., 2017). Many sCO_2 Brayton cycle layouts have been investigated. Of these, the modified simple cycle (with intercooling, reheating and recuperation), the precooling configuration and the recompression cycle show potential for improved cycle efficiencies (Binotti et al., 2017; Wang et al., 2017; Neises & Turchi, 2019). In collaboration with others, the present work will adopt the recompression with intercooling and reheating (RCICRH) cycle investigated by Du Sart, Laubscher & Rousseau (2021), shown in Figure 1-2.

The RCICRH starts with the sCO_2 being compressed by the low-pressure compressor (LPC). The fluid is then cooled by the intercooler (IC), before being compressed again by the high-pressure compressor (HPC). After this it passes through the low temperature recuperator (LTR) on the cold side before merging with a second fluid stream from the recompression compressor (RCC). The flow is originally divided into two streams after the recuperators. The combined stream then travels through the high temperature recuperator (HTR) on the cold side and on to the main heater (MH). The sCO_2 is heated by the MH then passed through the high-pressure turbine (HPT). It is then reheated by the reheater (RH) before passing through the low-pressure turbine (LPT). The turbines extract energy from the sCO_2 to generate electricity. From the turbines it travels through HTR and LTR on the hot side. The flow of the process fluid now splits before the precooler (PC) and the cycle begins again. (Cengel & Boles, 2015b; Wang et al., 2017).

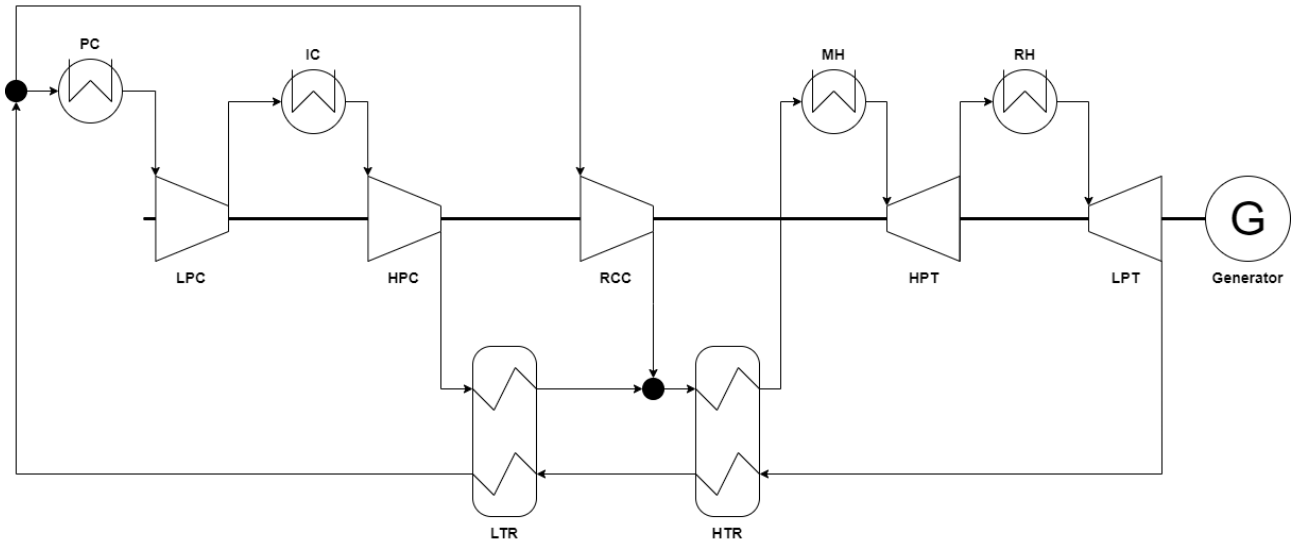

Figure 1-2: Schematic of the RCICRH cycle

Currently, South Africa is on the brink of both an electricity and water security crisis. However, South Africa is ideally situated for the use of CSP technologies, receiving (by country) some of the highest levels of direct normal irradiation (DNI). For perspective, DNI levels in South Africa range from 2700 kWh/m^2 to 3100 kWh/m^2 per year (Solargis, 2017). This is well above a recommended minimum of 1 800 kWh/m^2 for the use of CSP technologies, suggested by Weinstein, et al. (2015). Given this, the use of sCO_2 CSP plants in South Africa is an idea which holds great potential, especially if dry cooling systems are be used. However,

no sCO_2 CSP plant generating over 10 MWe exists (Ahn et al., 2015). If utility scale plants are to be realised in future, there is a need to determine the layout, specifications and operating philosophy of these plants and their respective systems. While research in this area is ongoing, little is known about the cooling system of these proposed plants. The present work will focus on the development of a such a system.

1.2 Project scope and objectives

The aim of the project is to develop conceptual layout and process designs for air-cooled heat rejection systems which will serve as the pre-cooler and intercooler of a proposed 50 MWe sCO_2 CSP plant in South Africa. This will be achieved by completing the following objectives:

- Conduct a literature review on the design and operation of air-cooled heat rejection systems applicable to sCO_2 CSP plants.
- Develop conceptual layout designs for air-cooled heat rejection systems which will serve as the precooler and intercooler of a proposed 50 MWe sCO2 CSP plant.
- Develop a steady state one-dimensional (1D) thermofluid network model of an air-cooled heat rejection system, and using this model, determine near-optimal process and geometrical designs and select key components.
- Further develop the near-optimal heat rejection system models using the Flownex ® SE software which will provide the platform for future dynamic simulation studies to be performed.
- Using the Flownex ® SE models, investigate the behaviour of the systems under off-design conditions such as varying ambient air temperatures (using real-world weather data) and part-load operation.
- Based on the results of the off-design studies, recommend control strategies and comment on the designs of the heat rejection systems.

This project forms part of a larger project which includes the development of a dynamic model of a proposed 50 MWe sCO_2 CSP plant in South Africa. Consequently, the design criteria (e.g., boundary values and constraints) are adopted from the larger project. The scope of this project is limited to the design of air-cooled heat rejection systems for the proposed plant at the system-level. This includes the development of realistic physical layouts, and the selection of key components. Furthermore, tube wall thickness requirements are considered. However, the scope excludes detailed component design, drafting of detailed drawings and costing. Given the complexity of the models developed in this work, the scope further excludes the use of formal optimisation techniques but employs parametric techniques to determine near-optimal solutions. Lastly, this project is limited to the use of proven technologies rather than the state-of-the-art.

2. Literature review

2.1 Air-cooled and ACC systems

Proper selection of heat rejection systems is important for industrial applications where water has historically been used as a heat sink, often to the detriment of the environment. Air-cooled systems can provide a more environmentally friendly method of rejecting heat in these cases. Air-cooled heat rejection systems (or air-cooled systems for short) are widely used in closed loop power cycles to reject residual heat to the environment. A typical air-cooled system is comprised of finned tubes carrying the process fluid. Heat is transferred from the process fluid to a cooling airstream via finned tubes or extended surfaces. This heat rejection is essential in closed loop cycles (Kröger, 2004; Held, Miller & Buckmaster, 2016).

Bustamante, Rattner & Garimella (2016) note that power plants using air-cooled heat rejection systems such as air-cooled condensers (ACCs) suffer a 5 – 10% drop in efficiency when compared to once through cooling systems and wet cooling towers. Air-cooled heat rejection systems (or air-cooled systems) are also more sensitive to varying ambient conditions than wet cooling systems, causing cycle performance to decrease when ambient temperatures exceed the air-cooled system's design conditions (Moisseytsev & Sienicki, 2016). On the other hand, air-cooled systems are flexible and can operate in almost any location, like the dry Upington area in South Africa for example.

Gavic (2012) investigated different air-cooled systems for an sCO_2 application. The work done shows that a direct method (no water) performs better from an auxiliary power and size perspective than an indirect method which employs water (see Figure 2-1). This is because direct systems eliminate the pump and sCO_2-to-water heat exchanger required in indirect systems. Furthermore, indirect cooling will require heat transfer across another boundary, subsequently additional temperature difference is required. This section presents literature on direct air-cooled systems.

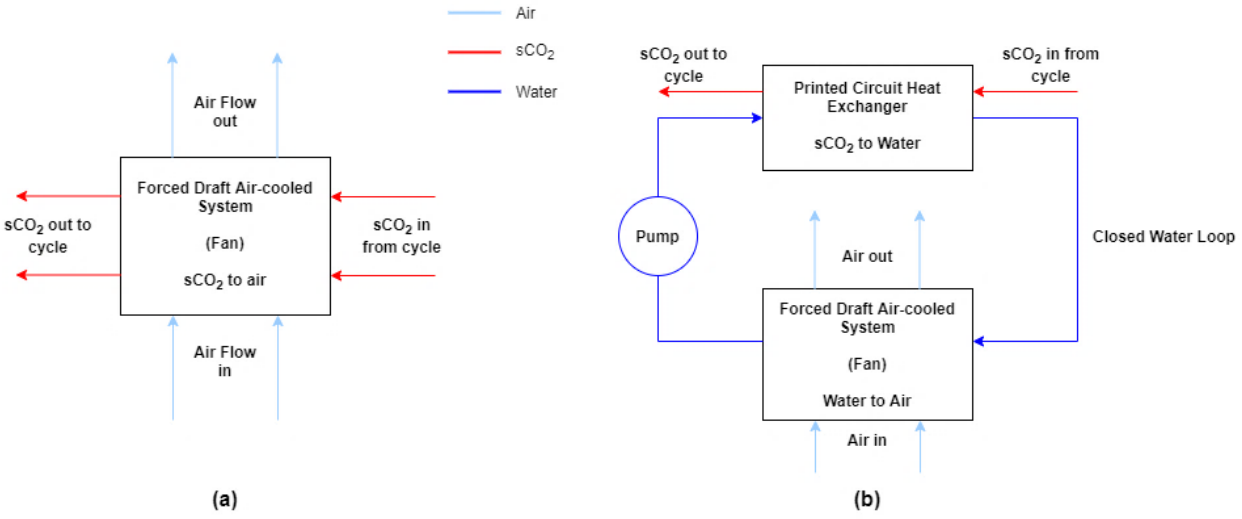

Figure 2-1: Process flow diagrams for (a) direct air-cooled and (b) indirect air-cooled systems

2.1.1 Overall configurations

Two major types of air-cooled systems exist, namely, natural draft systems and mechanical draft systems. Natural draft systems rely on buoyancy forces to draw air up and through towers. These towers have many different configurations and are often enhanced by using water in the cooling process. However, in dry regions where water is not readily available in the quantities required, natural draft dry-cooling towers (NDDCTs) are used. In contrast, mechanical draft systems use either forced or induced draft coolers which use fans to achieve the airflow desired in the heat exchanger banks. ACCs are a specific type of air-cooled system used to condense steam in Rankine cycles. Conventional air-cooled systems usually utilise horizontal finned tube bundles (Kröger, 2004). Figure 2-2 shows a conventional forced draft air-cooled system. Features and conditions include: (1) ambient conditions; (2) the tower supports; (3) and (4) are the fan inlet and outlet respectively, while (5) and (6) are the heat exchanger inlets and outlets respectively; (7) cooler exit conditions; and (8) the windwall.

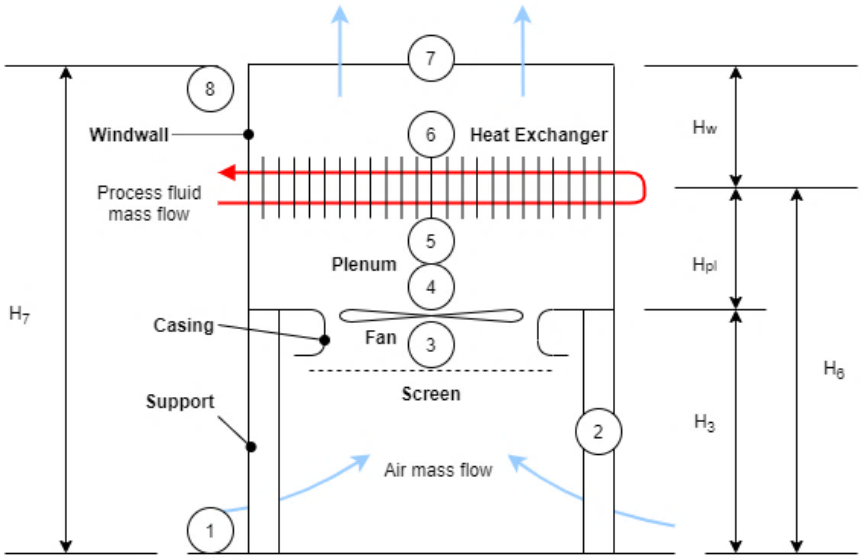

Figure 2-2: Conventional forced draft air-cooled system configuration

Doodman, Fesanghary & Hosseini (2009) found that the type of draft (forced or induced) has an insignificant impact on the optimization of the cooler and the findings of Carvalho et al. (2019) support this. Both studies optimised direct air-cooled system from a capital cost perspective. Forced draft systems make use of a fan below the heat exchanger bundles which forces air through them, whereas induced draft systems have the fan placed above the heat exchanger bundles which pulls air up through them. Kröger (2004) presents the benefits associated with both types of cooler. Relative to one another, forced draft systems consume less power, the fans are easier to maintain, and the fans are not exposed to high air temperatures at the exit of the tube bundles. On the other hand, induced draft systems are less susceptible to hot plume recirculation.

Kröger (2004) has developed a thermal-hydraulic modelling methodology for both ACCs and conventional mechanical draft air-cooled systems. In the mechanical draft air-cooled system model, tube-side pressure drops include header losses, inlet losses from tube headers to the bundles, as well as frictional losses and exit losses. The heat transfer coefficients for both the air-side and tube-side are determined using empirical correlations, and the air-side pressure drop is solved using a draft equation. The draft equation balances the

pressure drops through the cooling system, as well as the pressure rise caused by the fan with the ambient pressure change across the heat exchanger. Airflow through the heat exchanger is assumed to have a uniform flow distribution and the mass flow rate of air is iteratively solved for an associated control volume (a single tube row, double pass heat exchanger). One issue with the model, in the context of cooling sCO_2, is the lack of discretization. This means that the model may not account for the sudden changes in sCO_2 properties as it cools (further discussed in Section 2.2.1.) The specific correlations from Kröger (2004) used in the present work are presented in Section 4.

Shabanian et al. (2011) investigated heat transfer enhancement in horizontal tube air-cooled systems. The work done was validated with a CFD model and enhancement techniques focused on tube inserts. This method of enhancement is not entirely relevant to the present work. However, some useful findings were presented from an air-cooled system modelling perspective. Internal convection was modelled using the Gnielinski (1976) equation with the Blasius equation for friction factor. It was found that at high Reynolds numbers the Gnielinski equation overpredicts heat transfer while the Blasius equation becomes increasingly accurate as Reynolds number rises.

In practice, forced draft direct air-cooled systems for sCO_2 power cycles do not exist at the utility scale. As a result, there is little literature on them. In sCO_2 cycle research, coolers are often modelled as simple heat sinks as in van der Westhuizen (2020) or with assumed boundary conditions as in Sathish et al. (2021). Other studies are limited to simplified models or small scale applications such as those by Guo et al. (2019), McEligot & Jackson (2004), Gavic (2012), and Zhang et al. (2019). There may be a shortage of research on these specific air-cooled systems, but these systems may be modelled similarly to existing Rankine cycle dry-cooling systems. Rankine cycle power plants in dry regions use ACCs for heat rejection. Air, moved by fans over tubes, condenses the steam within the tubes. A typical ACC and its key components are shown in Figure 2-3 and Figure 2-4. These are: (1) support structures for the fans and tube bundles; (2) walkways for maintenance access; (3) the pump house which distribute steam from the turbine exhausts; (4) cooling cell layout; (5) fans; (6) fan inlet shrouds; and the tube bundles which are difficult to see but are contained above the fans and underneath the exterior walls in Figure 2-3. The design of some of these components directly affects the performance of the ACC. Direct air-cooled systems share most of these features with ACCs and a large portion of the literature discussed can be applied to sCO_2 air-cooled systems. Of these several components, those most studied in literature and discussed in the sections below are the tube configurations, heat exchanger configurations, walkways, fans, and cooling cell layouts.

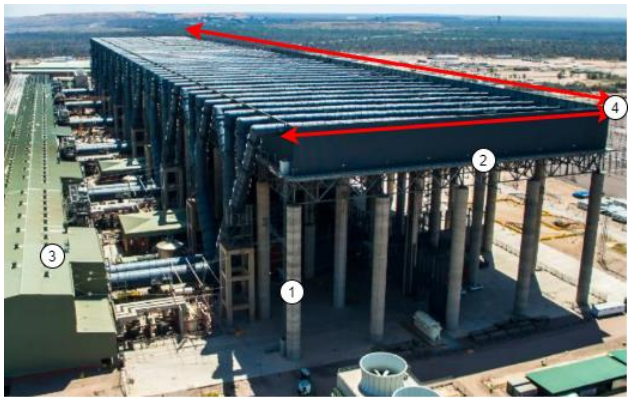

Figure 2-3: ACC at Medupi power station, South Africa (Augustyn, 2017)

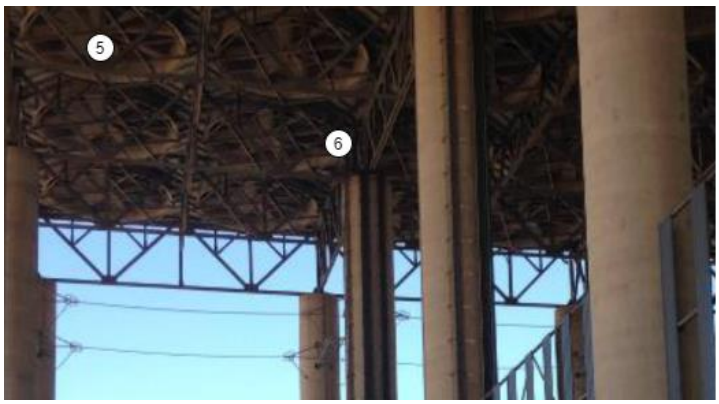

Figure 2-4: Fans for the ACC at Medupi power station, South Africa (Augustyn, 2017)

2.1.2 Tube configurations

The tube bundles are the most important components of an ACC or air-cooled heat rejection system, affecting both the heat transfer and process fluid pressure drop characteristics of the heat exchanger. Tubes are usually finned because heat transfer increases as the surface area available to reject heat does. For these finned tube bundles, the major parameters identified in literature include those listed below, most of which can be seen in Figure 2-5:

- Tube outer diameter (d_o)
- Root diameter (d_r)
- Transverse pitch between tubes (S_T)
- Longitudinal pitch between tubes (S_L)
- Number of longitudinal tube rows (N_L)
- Number of transverse tube rows (N_T)
- Number of tube passes (N_{passes})
- Length of one tube pass (L_{pass})
- Type of tube cross-section
- Fin diameter (d_f)
- Fin pitch (P_f)
- Fin thickness (t_f)
- Fin height (H_f)
- Type of fin used
- Arrangement pattern of tubes (staggered or in-line)

Zhang et al. (2019) investigated the heating and cooling characteristics of sCO_2 in tubes of different cross-sections. The study used CFD simulations to analyse the performance of each cross-section and constrained the problem by setting a constant heat flux. It was concluded that circular tubes could provide the best overall heat transfer performance while square cross-sections experience the smallest fluid friction effect on heat transfer. Furthermore, it was noted that there is no heat transfer deterioration for all cross-sections under cooling conditions.

A study by Lin et al. (2020) investigated improving airside heat transfer performance in ACCs by varying the height, spacing (pitch) and type of fins (wavy, plain, and louvered). It was found that smooth, plain fins performed best when optimized. The optimization process included reducing the fin spacing and increasing the fin height slightly from the baseline. The optimized plain fins increased the cycle efficiency by just over 1%, outperforming the wavy and louvered configurations. In the context of utility scale plants this can mean an additional 1 MW of send out power. Plain fins also have the benefit of being less complex to manufacture. Sayed Ahmed et al. (2015) compared the flow and thermal performance of several different finned tube configurations (plain, louvered, slit, wavy, longitudinal, and annular finned tubes). The study recommended that louvered fins be used for a fixed air pumping power as they have the best heat transfer coefficient. However, plain and wavy configurations also performed adequately. It was noted that for plain fins, discrete fins are better than continuous ones. Furthermore an increase in tube diameter and fin pitch decreased airside pressure drop at the cost of heat transfer performance. Additionally, heat transfer deteriorates when the fin pitch increases relative to the fin thickness and vice-versa. The later work of Lin et al. (2020), mentioned above, shows that optimising plain fins is the best approach to improving performance while maintaining a simple design.

The work of Lin et al. (2020) and Sayed Ahmed et al. (2015) show that plain, discrete fins perform adequately and can be optimised to perform well in air-cooling applications. Both studies utilise circular plain fins in their comparisons and analyses. More complex fins can achieve marginal thermal-hydraulic gains but at the cost of complexity. Plain, discrete fins are also easier to manufacture and maintain. This is a definite benefit in the context of operating a utility-scale power plant. As discussed above, it can be said that finned tubes are preferred. Additionally, staggered tubes are preferred because the heat transfer performance is better as a result of a reduced thermal wake effect (Sayed Ahmed et al., 2015). A finned tube configuration with annular, plain fins is shown in Figure 2-5.

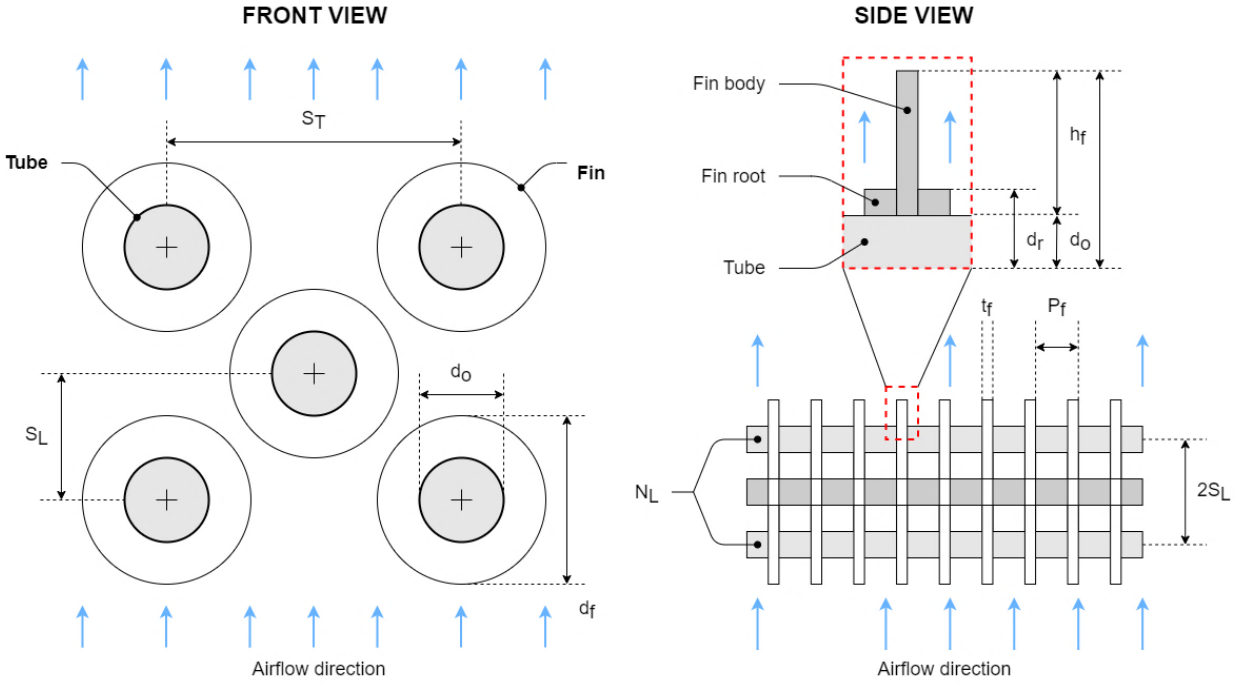

Figure 2-5: Staggered tube configuration

2.1.3 Heat exchanger orientations

There are various ways that the tube configuration discussed in the previous section can be arranged or housed to form a heat exchanger configuration. Common arrangements for ACCs and air-cooled systems include the A-frame shown in Figure 2-6 and the horizontal configuration in Figure 2-7 (Kröger, 2004). Both configurations have their respective advantages and disadvantages, the specific geometry of the configurations can also enhance heat transfer.

The A-frame is useful for ACCs because the sloped banks of tubes take advantage of gravity to help remove condensate from the tubes. The slope is determined by the apex angle (θ) which is a defining feature of these configurations. For this arrangement, the flow of the process fluid may split across many rows of tubes to enhance heat transfer and save space (Kröger, 2004).

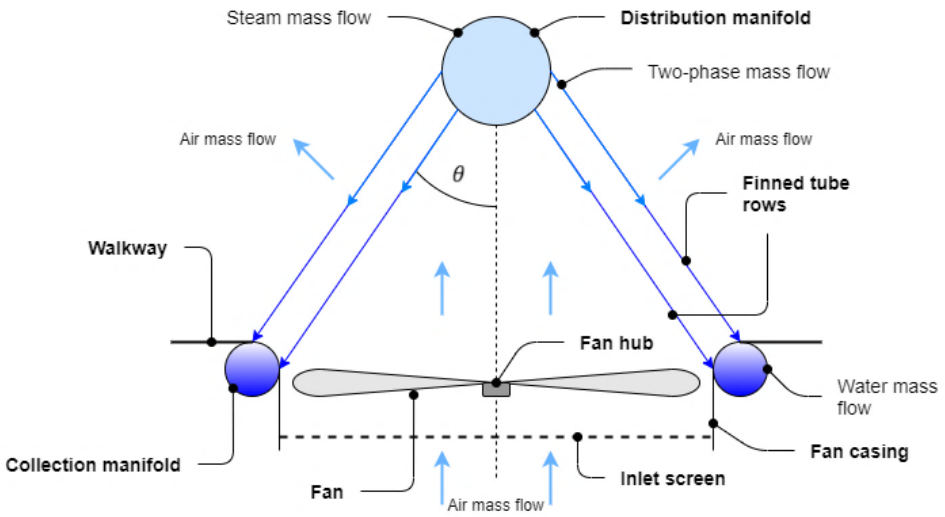

Figure 2-6: Typical A-frame heat exchanger configuration

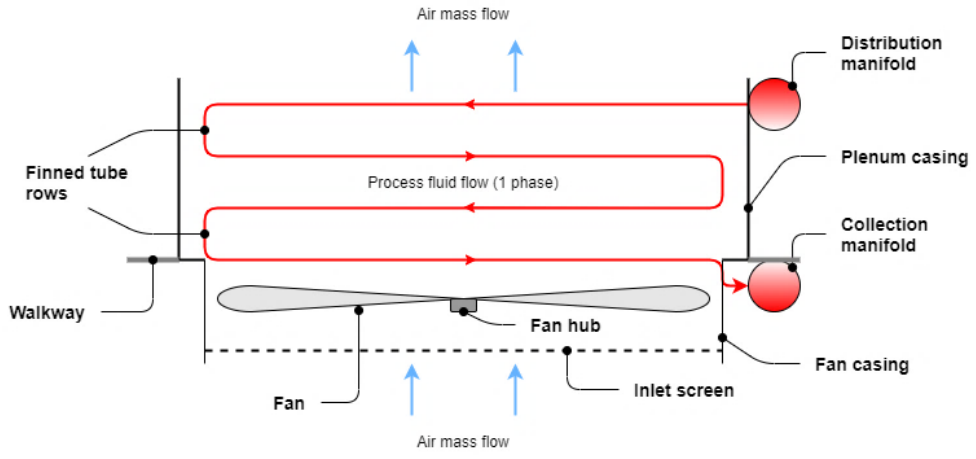

Figure 2-7: Typical horizontal heat exchanger configuration

Horizontal bundle air-cooled systems are commonly used to cool gases, which remain in one phase. An example of one of these coolers is shown in Figure 2-7. Key parameters of these systems include the heat exchanger height (H_{HX}), width (W_{HX}), and length (L_{HX}). L_{HX} and W_{HX} describe the frontal area and are usually very close or the same value. These values can also be defined (or dictated) by the fan diameter (d_F)

in the system. Please refer to Figure 4-2 and the equations in Section 4.2 – Section 4.5 for further information on how these values influence the layout of potential heat rejection systems.

In horizontal tube heat exchangers, tubes are arranged in a matrix above the fan. The layout and geometry of this matrix is important when it comes to heat exchanger performance. Performance in heat exchangers can be enhanced by varying the geometric parameters, this is known as passive enhancement. Passive enhancement does not require external power. It can, however, influence the performance of the active enhancement methods which do, such as the use of a fan (Sayed Ahmed et al., 2015). Changing the geometry and configuration of an air-cooled heat exchanger can alter the air-side pressure drop which will increase the static pressure rise required by the fan in the system. This will affect the amount of power drawn by the fan, either increasing or decreasing it depending on the change in air-side pressure drop. Importantly, both passive and active enhancement are requirements for an optimal heat exchanger design.

Kong et al. (2019) investigated the use of A-frame and conventional heat exchanger bundles in NDDCTs. A-frames, as shown in Figure 2-6, were placed around the base of a NDDCT at a certain platform height above the ground to observe their effect on heat rejection under various ambient conditions. The results indicated that vertically placed A-frames (with the point facing upwards) around the perimeter of the tower helped to increase heat transfer rates at crosswinds greater than or equal to 9 m/s. However, the A-frame configuration was found to be sensitive to a combination of wind speed and platform height. It also performed worse than a conventional heat exchanger configuration, as seen in Figure 2-7, under uniform air flow conditions.

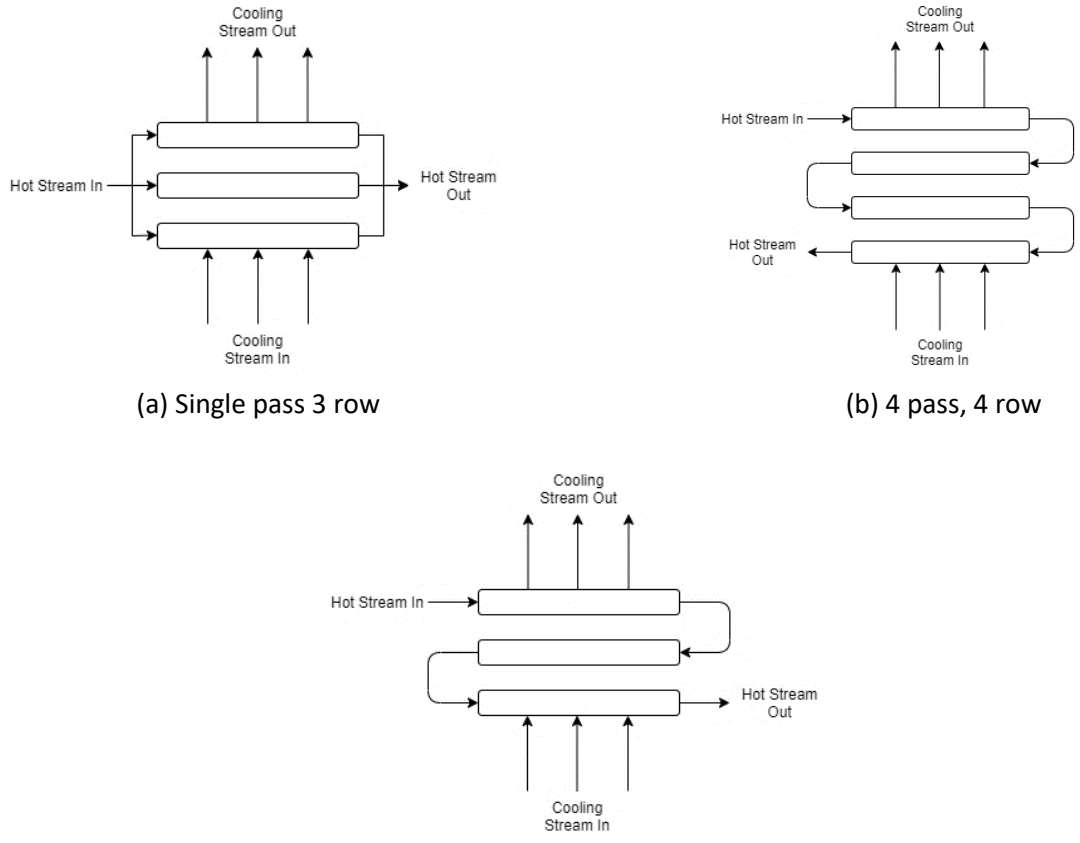

(a) Single pass 3 row

(b) 4 pass, 4 row

(c) 3 pass 3 row

Figure 2-8: Cooling heat exchanger tube configurations adapted from Holger (2018)

Different configurations for the heat exchanger tubes can be seen in Figure 2-8. The flow of the hot stream will usually have an inlet above the outlet because this is a requirement for a heat exchanger to achieve counterflow, it also results in a lower final temperature difference which is beneficial. Additionally, it can reduce the effect of gravity on pressure drops. All of these are crossflow heat exchangers as is common in air-cooled systems. Figure 2-8 (a) shows a single pass 3 row crossflow heat exchanger having the fluid cross the cooling stream only once, and potentially along multiple flow paths. This is true for all single pass heat exchangers. On the other hand, multi-pass heat exchangers have the fluid cross more than once, exiting on the same side as the inlet for an even number of passes or on the opposite side for an odd number of passes. These respective configurations are shown in (b), which is a 4 pass 4 row counter directed counter current crossflow heat exchanger and (c), which is a 3 pass 3 row counter directed counter current crossflow heat exchanger.

An investigation by Gavic (2012) included the development of an air-cooled heat exchanger for sCO_2 applications. A horizontal heat exchanger configuration was used with the tubes following a path as in Figure 2-8, (c). The study found this to be an appropriate layout for cooling sCO_2 and suggested that space and air-side pressure drops can be minimised by selecting an optimal finned tube configuration.

Reza & Zabihollah (2011) performed an analysis and optimization of a conventional, 6 row air-cooled heat exchanger from an entropy generation perspective. The study utilises the Nusselt correlations from Gnielinski (1976) for internal convection, and from Briggs & Young (1963) for external convection. They concluded that increasing the internal Reynolds number increased the irreversibility in the heat exchanger. Also, that an increase in the external Reynolds number enhances heat transfer but increases external irreversibilities. The calculations performed in their study were not validated but the trends presented are expected. It is important to note that when designing an air-cooled heat exchanger both external air mass flow rate and internal fluid mass flow rate should be appropriately controlled. Internal flow rate can be controlled by splitting the process fluid across multiple rows while the external flow rate will depend on the axial fan and ambient conditions.

Where gravity is not required to assist the movement of the process fluid, as in ACCs, it may be better to use conventional bundles which are horizontal. This is because process fluids remaining in one phase at high pressures can easily move through the heat exchanger tube networks of horizontal bundles. Furthermore, modelling is simpler if the flow generated by an axial fan is assumed to be uniform (Kröger, 2004; Deshmukh & Kapat, 2020). Lastly, space may be saved by selecting optimal design parameters for the finned tubes.

2.1.4 Fans

Fans form an essential part of air-cooling systems by providing the required airflow for heat transfer. Several studies have been conducted to optimize and improve the prediction of fan performance in air-cooling systems (Van Der Spuy, Von Backström & Kröger, 2009; Van Der Spuy, 2011; Augustyn, 2013; Louw, Von Backström & Van Der Spuy, 2015; Engelbrecht, 2018; Rohwer, 2019).

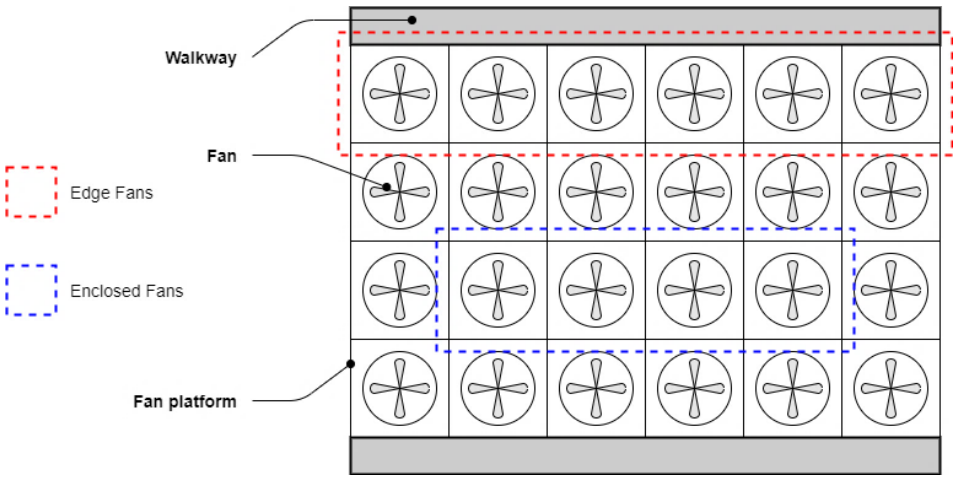

Figure 2-9: Air-cooled heat rejection system fan array extracted from Van der Spuy et al. (2009)

Fan performance may be characterized by a volumetric effectiveness, defined by Salta & Kröger (1995) as the ratio of actual flow through an installed fan to the same free-standing fan unit operating with no inlet flow distortions. This ratio is provided in equation (2-1).

Fan performance also varies based on the location of each fan in the air-cooling system. Fans can either be located on the periphery of the system, these are known as edge fans, or be enclosed by other fans. Figure 2-9 shows these fans within a potential air-cooling system. Edge fans are affected negatively by crosswinds and other factors, while enclosed fans tend to only experience off-axis inflow according to Van der Spuy et al. (2009).

The volumetric effectiveness of a fan is linked to the platform height, this has been shown in several studies. The platform height is the distance from the ground at which the fan inlet sits. A study by Salta & Kröger (1995) presents an empirical correlation for fan volumetric effectiveness as a function of this height. The relation was validated by Van Der Spuy et al. (2009). The empirical relation is shown below:

$$\frac{\dot{V}}{\dot{V}_{ideal}} = 0.985 - e^{-X} \qquad (2\text{-}1)$$

In this equation, X is a dimensionless factor associated with the height of the platform above the ground in metres, H_F, the number of fan rows, N_F, and the diameter of the fan in metres, d_F. The equation for this dimensionless value is provided in Equation (2-2).

$$X = \left(1 + \frac{45}{N_F}\right)\frac{H_F}{6.35 d_F} \qquad (2\text{-}2)$$

The findings indicate that raising the platform height will improve the performance of the cooling system up to a certain point. This is for a set fan diameter and amount of fan rows.

Aside from this, the study by Van der Spuy et al. (2009) makes two key recommendations and observations regarding the design of the fan and platform. To avoid negatively affecting the volumetric effectiveness in edge fans they recommend that buildings are placed further than one platform height from the cooling cells and that low-noise fans should be used to resist flow distortions. Buildings close to the cooling cells increase

the crossflow velocity through the system which leads to worse flow separation in edge fans. Low-noise fans tend to have steeper fan static performance curves and a higher solidity according to Van der Spuy et al. (2009). Fan solidity is a measure of free flow to fan blade and hub area within a fan casing. The number of blades and blade thickness will affect the solidity. These attributes allow them to better resist flow distortions and reduce separation in edge fans, enhancing the air-cooled system's performance. Typically, such a detailed blade and fan design also result in increased costs.

An example of a low-noise fan is the B2a-fan, investigated by Engelbrecht (2018). The study compared two fans, an A-fan and the B2a-fan. The A-fan in their study is the same as the B-fan in the works of Augustyn (2013) and Van der Spuy (2011). It is a commercially available fan in South Africa (Augustyn, 2017) and will be referred to as a B2-fan henceforth. The B2-fan and the details of its design can be found in the work of Bruneau (1994). The primary difference between a B2-fan and a B2a-fan is the blade angle, the B2a-fan has a higher blade angle. The work of Engelbrecht (2018) demonstrated that the B2a-fan achieves a superior overall performance. The findings were validated using a CFD model. Rohwer (2019) also investigated the B2a-fan alongside an M-fan which is similar but with a smaller hub diameter. Another study by Louw et al. (2015) analysed the lift and drag characteristics of a B2a-fan using CFD simulations. It was found that maximum static efficiencies of over 60% are obtainable while still maintaining a high volumetric effectiveness.

The work of Van der Spuy (2011) looks at perimeter fan performance in forced draft ACCs. Several different axial flow fans are investigated, including the B2-fan as well as a V-fan, several H-fan configurations, and an N-fan. The different H-fan configurations are defined by the number of blades, for example, the H-7 fan has 7 blades. The study includes analysis of H-5, H-7, H-10, and H-14 fans. The diameters of the B2-fan and V-fan are the same, while the H-fans and N-fan share a smaller diameter relative to the other two. Refer to Table 2-1 for a full geometric comparison of all the fans discussed in this section.

The results of Van der Spuy (2011) were validated using three different CFD methods; volumetric effectiveness and static efficiency were used as metrics to compare performance. It was found that the H-14 fan experiences the highest volumetric effectiveness, followed by the H-10 and B2-fans. The worst performing fans, in terms of volumetric effectiveness, are the H-5 and N-fans. The findings indicate that fans having higher solidity values achieve higher volumetric effectiveness, which agrees with the results of Van der Spuy et al. (2009). However, from an efficiency perspective, the H-14 fan performed the worst. The B2-fan and N-fan had the highest static efficiencies because of their significantly lower shaft power requirements. The results point towards the B2-fan having superior overall performance with adequate volumetric effectiveness and the best efficiency.

An experimental and numerical analysis of different axial flow fans was also conducted by Augustyn (2013). The fans examined included the B2-fan, N-fan, L1-fan, and L2-fan. However, the L1-fan was excluded from the numerical validation. In other words, validated numerical data was only available for the other three fan types. The B2-fan and N-fan have already been described above and the L2-fan is very similar to the N-fan, differing only in blade angle and thickness. The results of their work provide power and static pressure curves for these specific fans. It is also noted that when scaling, the fans efficiency may vary significantly in practice, it is therefore important to select a fan with a high base efficiency. The N-fan and L2-fan were shown to have

maximum efficiencies in the range of 52 – 55%, while the B2-fan is noted as having maximum efficiencies close to 60% by Van der Spuy (2011). An additional study by Bredell, Kröger & Thiart (2006) also demonstrated the superior performance of B2-fans having a 0.4 hub-tip ratio over those with a 0.153 ratio such as the N-, M-, and V-fans.

Table 2-1: Test fan parameters for different fans studied in literature

Fan	Diameter (m)	Hub-tip ratio	Number of blades
B2a-fan	1.542	0.4	8
B2-fan	1.542	0.4	8
M-fan	1.542	0.15	8
V-fan	1.542	0.15	8 / 9
H-fans	0.630	0.24 / 0.39	5, 7, 10, 14
N-fan	0.630	0.15	8
L2-fan	1.240	0.135	8

From the results for the fans discussed above, the B2a-fan and B2-fan are the superior options in terms of volumetric effectiveness and efficiency which characterise fan performance. It is important to note, however, that B2-fans are commercially available and currently widely used in South Africa. On the other hand, the B2a-fan is not commercially available despite the significant research and benefits it has from a performance perspective. This makes it a slightly less attractive option for implementation in a South African based utility-scale air-cooled system. It is likely that simulations run with currently installed fans will produce more useful results.

2.1.5 Walkways

Flow separation and distortion at fan inlets tend to dominate performance deterioration in air-cooled systems. This is due to decreased flow losses resulting from flow separation, non-uniform inlet flow profiles to the fans, and off-axis inflow conditions decreasing the static pressure rise across the fan (Bredell et al., 2006). The selection of the fan type is not the only way to decrease this effect. Additional methods of mitigating the negative effects of crosswinds is through the appropriate selection of a fan inlet, shown in Figure 2-10 and the installation of a walkway along the edges of the cooling cell at the fan platform height. Several studies have shown that this leads to flow separation taking place beneath the walkways instead of at the fan inlets (Salta & Kröger, 1995; Meyer, 2005; Bredell et al., 2006). The use of a bellmouth inlet, which provides good resistance to flow distortions already and reduces pressure loss on the air-side is also known to improve the performance of the air-cooled system (Kröger, 2004).

Salta & Kröger (1995) showed that the installation of walkways reduces flow separation at the fan inlets for single and multiple fan systems for a range of different walkway widths (W_w) between $0.159d_F$ and $0.476d_F$. The study involved experimentally determining the effect of the walkway installation and the results were later confirmed by Van der Spuy et al. (2009) and Meyer (2005). The same study by Meyer (2005) found that walkway installation decreases flow separations across all types of fan inlets. Types of fan inlets include cylindrical, conical and bellmouth configurations, visible in Figure 2-10. The study experimentally shows a 96% volumetric effectiveness for a rectangular ACC layout having 2 banks of 2 x 5 cooling cells when a

walkway is implemented and a bellmouth inlet is used. This effectiveness is reached when the dimensionless height (X) is between 4 and 5 and the walkway width is $W_w = 0.33d_F$.

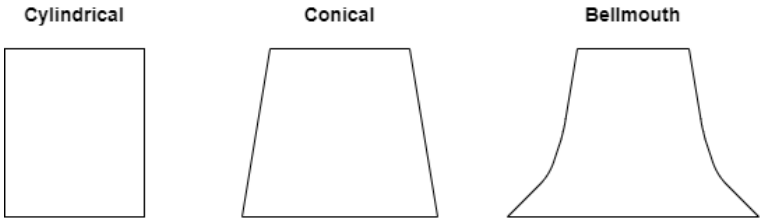

Figure 2-10: Cross-sections of various fan inlets

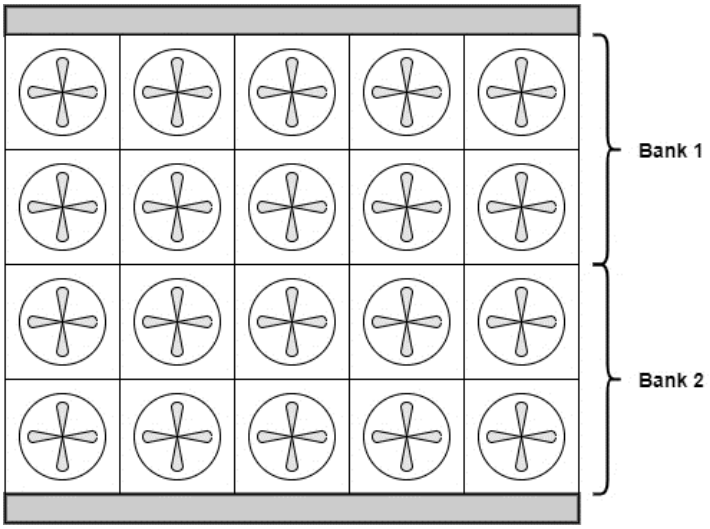

Figure 2-11: A 2 bank, 2 x 5 ACC layout adapted from Meyer (2005)

Bredell et al. (2006) investigated the impact of walkways with the same width as Meyer (2005) of $0.33d_F$ for two different fans. The results of the study are validated using a CFD code for three fans, one of them being an edge fan with a walkway. It was found that performance increases up to a certain platform height of $2.4d_F$ with this specific walkway geometry. Past this point, diminishing returns were observed. This is likely because the model is confined to three fans. In larger air-cooling systems, greater platform heights still have a significant effect on fan performance (Meyer, 2005).

From the discussion of the literature above, the installation of a walkway will have an impact on fan performance. Walkways will increase volumetric effectiveness in air-cooled systems and an optimal value for walkway width is demonstrated to be $0.33d_F$. A raised platform height and use of a bellmouth fan inlet will also increase fan performance.

2.1.6 Air-cooled system cell layouts

The negative effect of wind on the performance of air-cooled systems has been discussed and is significant. Crossflow at the inlet to the fans lowers fan performance and decreases the efficiency of the cycle by decreasing the volume flow rate of air and subsequently the heat transfer rate in the cooling system. It is important to mitigate this effect. This can be achieved by adding walkways and increasing the platform height

as previously discussed. However, an additional approach used to decrease the effect of wind is to place the individual cooling cells in a layout which reduces the number of edge fans and flow distortion. A single cooling cell is comprised of a fan and a complete bank of heat exchanger bundles. Cooling cell layouts and their ability to mitigate wind effects have been researched for A-frame ACCs and the same concepts will apply to conventional air-cooled systems (Yang et al., 2012; Kong et al., 2017; Engelbrecht, Laubscher & van der Spuy, 2020). Figure 2-12 to Figure 2-14 depict the different layouts found in literature.

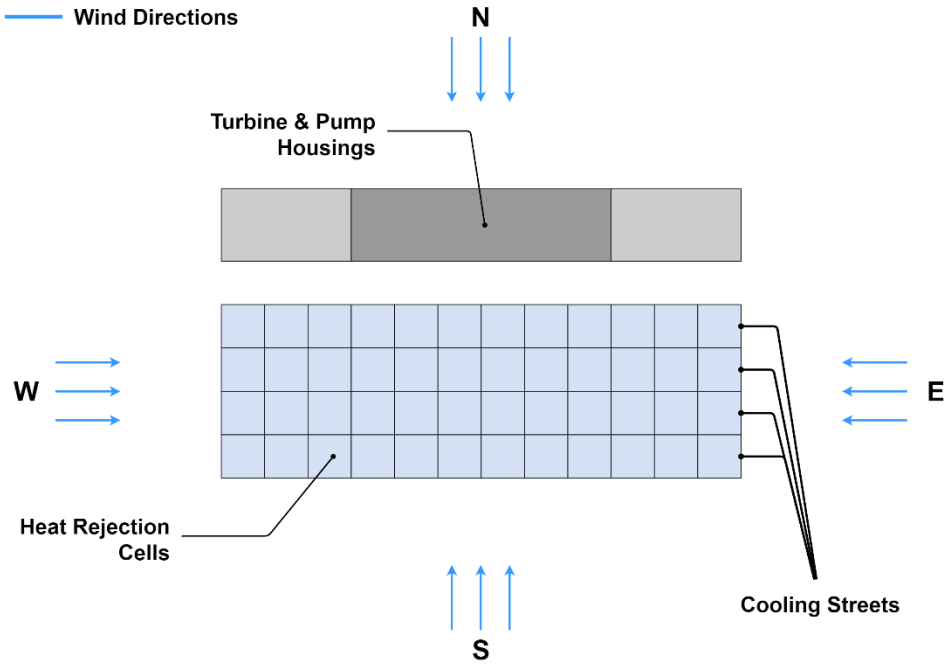

Figure 2-12: Conventional ACC cooling unit layout (with 4 streets and 12 cells per street)

The work of Engelbrecht, Laubscher & Van der Spuy (2020) in particular focuses on a conventional (rectangular) 4 x 3 cell layout. Or, in other words, a 3 street heat rejection system with 4 cells per street. The significant effect of the wind on volumetric flow rate, fan power, heat transfer and steam quality are all determined using a co-simulation approach, with the air-side validated using a CFD model. The trend is for heat rejection to decrease with increasing crosswinds and for volumetric flow rates to decline. This means that the fan power required to maintain design point conditions will increase. Because these conventional layouts are susceptible to crosswinds, further study comparing them to novel layouts has been conducted.

Kong et al. (2017) investigated a circular arrangement of ACCs, seen in Figure 2-13 and compared the results for various wind speeds from different wind directions against the conventional layout. 112 industrial scale ACC cells were modelled and the results were validated using CFD model simulating a crosswind of 8 m/s. It was shown that for flow from the open-side, direction ‘S’ in the diagrams, the conventional ACC layout performs worse than the circular arrangement. This is because the wind hits the long edge of the rectangular arrangement and there are therefore more edge fans which have are known to perform worse than enclosed fans. There was also found to be increased reversed flow in cells upwind of each other within the body of the layout. When wind flows over the turbine housing, direction ‘N’ in the diagrams, no reverse flow occurred but low pressure zones are found in the conventional layout. This may lead to hot plume recircualtion of the air. Importantly, under pure crossflow conditions (when wind strikes from direction ‘W’ or ‘E’ in the diagrams)

both layouts performed at a very similar level. This is because the advantages of the circular arrangement are reduced by the fact that there are more edge fans than the conventional layout for this wind direction.

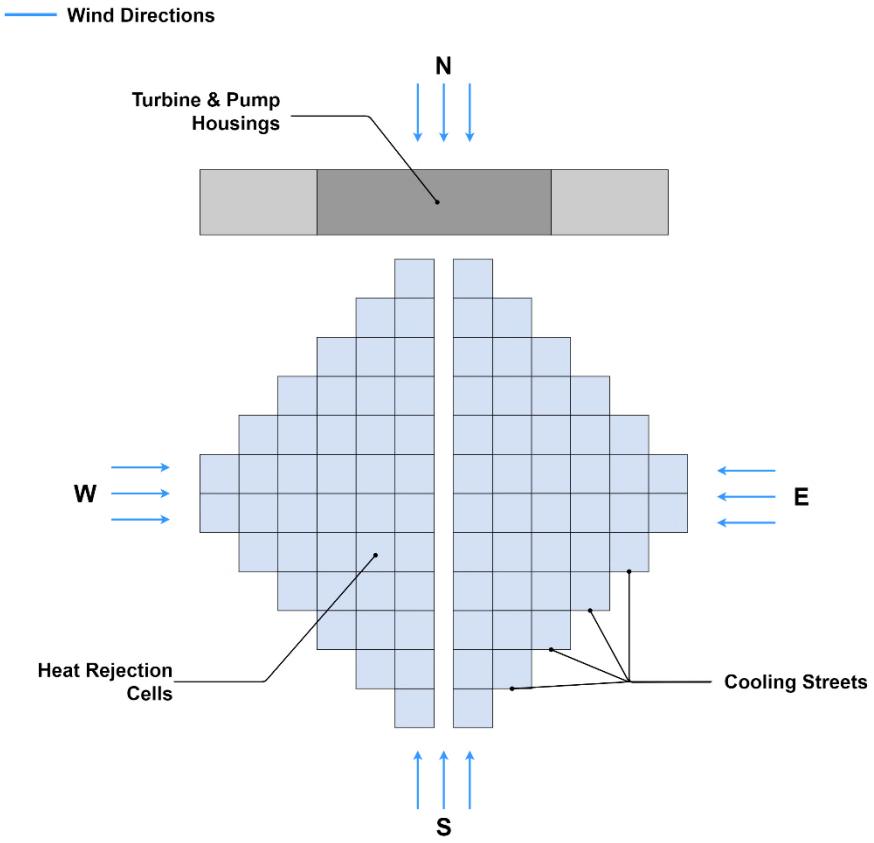

Figure 2-13: Circular ACC cooling unit layout

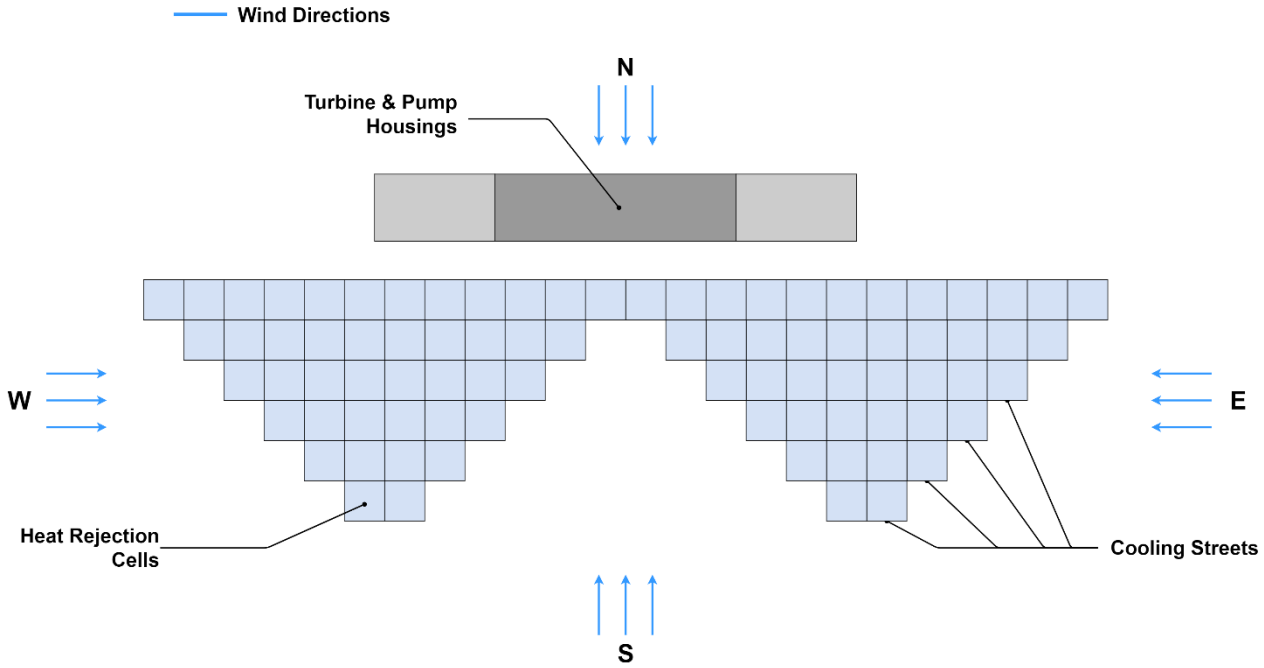

Figure 2-14: Trapezoidal ACC cooling unit layout

This result indicates that when using a conventional layout the shorter edge of the rectanglular block of cells should be aligned perpendicular to the prevailing wind direction. This is because the mass flow rate of air through the cells is higher and more consistent throughout the arrangement. Ofcourse, it is then necessary to know this prevailing wind direction. Fortunately, there is sufficient climate and weather data available for most sites where power plants are likely to be developed. This makes it possible to know the prevailing wind direction and arrange the cooling cells accordingly.

Yang et al. (2012) studied the mitigating effects of a trapezoidal arrangement on crosswind effects. This was done for a 2 x 600 MW dry-cooling power plant. The layout of the cells was inside a 7 row, 24 column grid. Across the 7 rows, the number of ACC cells varied from 1 to 7 as follows: 6, 6, 6, 6, 10, 10, 12. This layout is mirrored across the centreline of the grid for a total of 112 cooling cells. The performance of this ACC layout was compared to that of a conventional one and validated using CFD simulations with a wind speed of 9 m/s. The results of the investigation show that the trapezoidal layout performs better (with higher air mass flow rates) than the rectangular layout regardless of wind direction. Hot plume recirculation was reduced as was flow distortion at the fan inlets and reversed flow in upwind cells. Additionally, the work done further confirms that aligning the narrow side of any arrangement with the prevailing wind direction has a positive impact on ACC performance.

The aforementioned literature suggests that for large amounts of cooling cells the trapezoidal arrangement offers the best performance. It is less susceptible to crosswinds than the conventional and circular arrangements. However, it requires a significant number of cooling units to be properly implemented. This may not be required for a sCO_2 air-cooled system. Another key outcome is that there is no significant overall advantage to using a circular arrangement over a conventional one. Furthermore, the conventional layout can be optimally situated with respect to the prevailing wind direction to produce similar or potentially better performance results than the circular layout.

2.2 Direct air-cooling for sCO_2 applications

The following section is divided into two major sections, namely, sCO_2 fluid properties and direct air-cooling of sCO_2. The properties of sCO_2 are an important factor when cooling the fluid as they directly affect heat transfer. Direct air-cooling of sCO_2 is a relatively new field of research and there is limited literature available, where the majority of research has focused on sCO_2 cycles at a high level or modelling the properties and heat transfer of the fluid in specific scenarios.

2.2.1 sCO_2 fluid properties

The fluid properties of sCO_2, such as density (ρ), dynamic viscosity (μ), isobaric specific heat capacity (c_p) and thermal conductivity (κ), fluctuate significantly near the critical point of the fluid. The critical point can be defined by a temperature and pressure. In the case of sCO_2, these values are 31.0 ℃ and 7.38 MPa respectively (Wahl et al., 2021). Figure 2-15 and Figure 2-16 show the property fluctuations as the pressures and temperatures approach these values. Note that the pressure affects the temperature at which the properties peak or are changing the most. For any pressure, the temperature at this point is known as the pseudocritical temperature (T_{pc}). Oh & Son (2010) present a function for the pseudocritical temperature as

well as an investigation into the cooling of sCO_2 in horizontal macro tubes, this involved an analysis of the fluid properties. The pseudocritical point in the plots below is denoted in each case by the point at which the vertical line intersects the property curve. These trends and effects have been noted in multiple other studies (McEligot & Jackson, 2004; Zhang et al., 2019; Wahl et al., 2021).

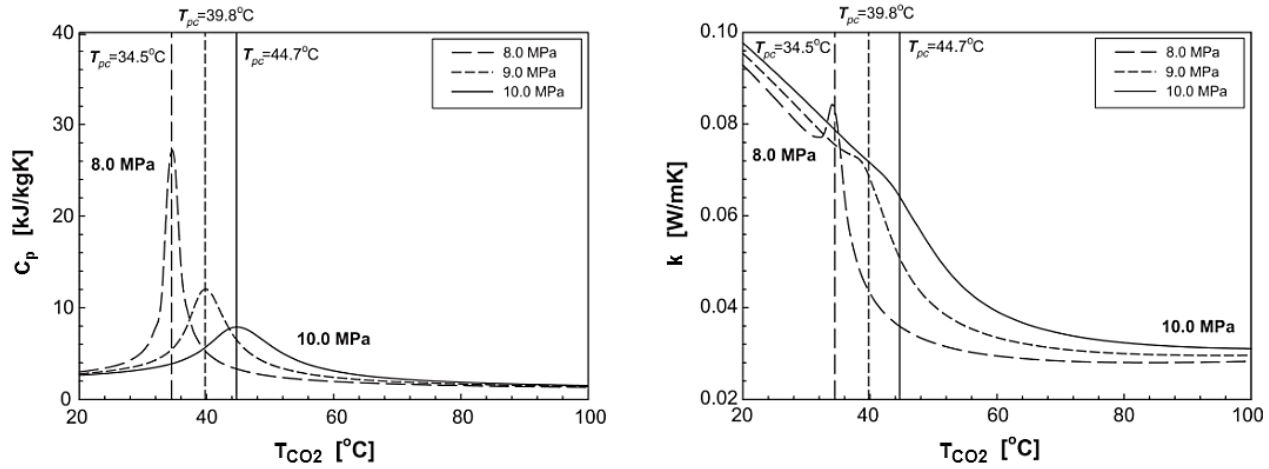

Figure 2-15: Thermal conductivity and isobaric specific heat of sCO_2 near the critical point, taken from Oh & Son (2010)

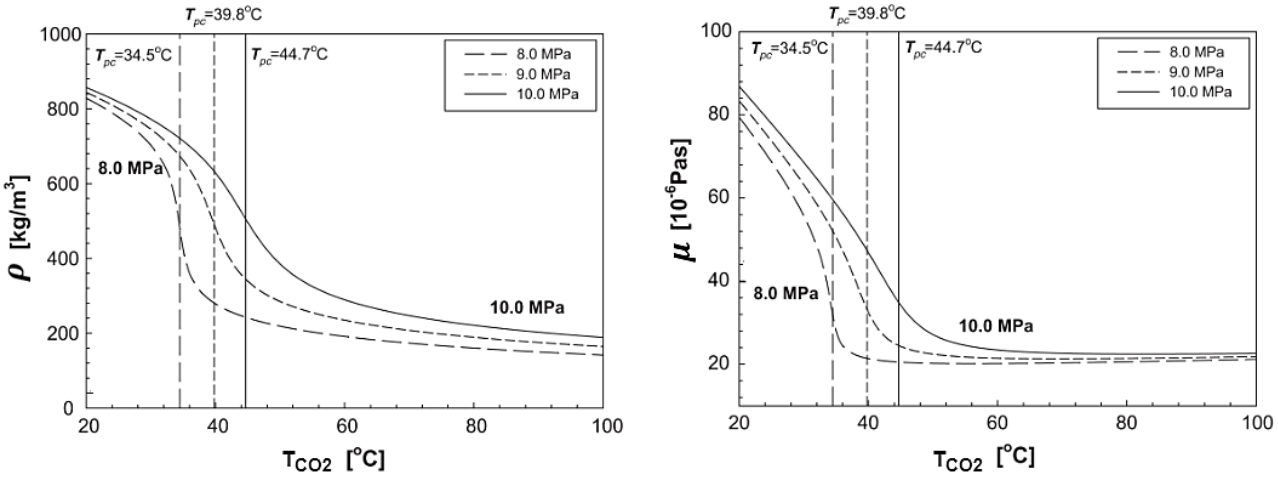

Figure 2-16: Density and dynamic viscosity of sCO2 near the critical point Oh & Son (2010)

When cooling the fluid, temperatures will tend towards T_{pc} for approximately constant pressure. The curves shown in the plots above demonstrate how properties affecting heat transfer can tend towards favourable values for heat rejection when sCO_2 is cooled. Wahl et al. (2021) studied the cooling of sCO_2 in 2 mm tubes with the aim of developing a new heat transfer correlation for the fluid. The work done produced experimental results which were used to develop an expanded Dittus-Boelter equation. Their correlation predicts the experimental heat transfer results with an accuracy of 20%, and so it is not presented here. Oh & Son (2010) also experimentally investigated the cooling of sCO_2 with the aim of developing a new heat transfer correlation, but in horizontal macro tubes. The study compared experimental results against existing correlations for the sCO_2 heat transfer coefficient and then developed a new correlation based on the Dittus-Boelter equation. It was found that most of the existing correlations do not properly account for the strong property variation of sCO_2. The most promising options noted were the Gnielinski (1976) correlation

for single-phase in-tube forced convection and that of Pitla, Groll & Ramadhyani (2002). The correlation proposed by Oh & Son (2010) also accurately predicts the experimental data to within a 13% error.

Based on the discussion of known information on sCO_2 fluid properties and the studies conducted, heat rejection improves because C_p increases as the temperature approaches T_{pc}. Density also rises rapidly which results in higher turbulence and improved heat transfer for a fixed tube diameter and flow velocity. However, the property behaviour is unfavourable for calculations because it is highly non-linear when most equations rely on bulk mean property values (Kröger, 2004). Of the correlations developed in literature, expanded Dittus-Boelter equations are preferred when predicting sCO_2 heat transfer coefficients. Aside from this, the correlations of Gnielinski (1976) and Pitla et al. (2002) perform well outside of regions very close to the pseudocritical point.

2.2.2 Direct air-cooling of sCO_2

In this work, both direct mechanical and direct natural draft dry-cooling methods have been researched for sCO_2 applications. The distinguishing feature of a direct air-cooled system is that the air extracts heat straight from the process fluid without an intermediate water or gas loop. Natural draft dry-cooling towers (NDDCTs) have recently been gathering interest while detailed research into mechanical dry-coolers has received relatively little attention.

The work of Gavic (2012) includes the modelling of a direct air-cooled system for sCO_2 power cycle applications in Engineering Equation Solver (EES). The power cycles investigated were the recompression, simple high efficiency, and simple low efficiency Brayton cycles (Gavic (2012) provides more information). The modelling of the air-cooled system was done by solving for the length and width of the heat exchanger which balanced the governing equations using set boundary conditions. The heat exchanger's length and width were also set to be equal in Gavic's (2012) model. The heat exchanger was discretized into several smaller control volumes to account for the sCO_2 property variation, and the effectiveness - number of transfer units (e-NTU) method was used to calculate heat transfer. For each of these 'sub-heat exchangers', the e-NTU heat transfer coefficient was equated to the thermal resistance network coefficient to find the length of each segment. The NTU values were found using heat exchanger functions in EES which implement e-NTU solutions based on whether the air temperatures are to be modelled as mixed or unmixed. The model also sets the fan power at 0.5 MW, as well as the boundary conditions such as heat transfer, the inlet and outlet sCO_2 temperatures, and the pressure ratio. The results found that utility-scale tubes in the range of 25 mm tend to produce the largest heat exchangers. Furthermore, a smaller longitudinal pitch lowers the air-side pressure drop for such tubes in an sCO_2 direct air-cooled system. Gavic's model only investigates a limited number of set staggered tube heat exchanger geometries which is a limiting factor when optimising a design. Furthermore, the tube wall thicknesses are set at 1 mm in the model and do not account for the high-pressure applications the heat exchangers are intended for. The cycle models developed by Neises & Turchi (2019) used the work of Gavic to model the direct air-cooled systems. Cycles designed include the simple, recompression, and partial-cooling Brayton cycles. The air-cooled system models were discretized and used to solve the length of one pass and the number of transverse tube rows in the heat exchanger. A

target sCO_2 pressure drop and fan power consumption constrained the models to allow for these values to be solved for.

Deshmukh & Kapat (2020) performed a detailed analysis of the pinch-point in an sCO_2 Brayton cycle direct air-cooled system. In the context of an sCO_2 Brayton cycle, the pinch-point problem occurs in the heat exchangers, typically the recuperators. The pinch-point is represented as the minimum temperature difference between the hot and cold fluid streams that needs to be maintained for efficient heat transfer to take place. Dostal, Hejzlar & Driscoll (2006) provide a more detailed analysis of the pinch-point problem in sCO_2 power cycles. The air-cooled system model developed in the study of Deshmukh & Kapat (2020) is part of a larger recuperated 100 MWe cycle model. Initially a steady-state air-cooled system model was developed to observe the effect of air-cooled system size on the cycle efficiency. A transient model was then generated to study the effect of varying ambient air temperature on the pinch-point. A constant mass flow rate of sCO_2 is maintained in the models, as were the cooler inlet temperature and pressure. The steady-state model also set the outlet pressure and solved the compressor inlet temperature and cycle efficiency at an ambient air temperature of 15 ℃ for 11 steadily increasing air mass flow rates. The model excluded fan power from the efficiency calculation and found that efficiency increases with air mass flow rate in the cooler. The outlet temperature of the sCO_2 also nears the critical point as mass flow rate of air decreases. The more complete transient model used a discretized lumped parameter approach to analyse the air-cooled system. The lumped parameter analysis is applied to each node sequentially to solve the system accurately. An 8 pass counter directed counter current crossflow heat exchanger with 7 nodes in each pass was developed and applied to three specific sizes from the steady-state model. Heat transfer coefficients for internal forced convection and external forced convection were found using the Gnielinski (1976) correlation and a constant value respectively. The transient analysis results found that while the largest air-cooled system is attractive from a power and efficiency perspective because the outlet temperature of the sCO_2 from the cooler is closer to the critical point. This increases the density of the sCO_2 entering the compressor. However, it is too sensitive to ambient air temperature variations and unrealistically large. The smaller sizes will not experience the same issues under these transient conditions while still achieving adequate outlet conditions.

NDDCTs have also recently been investigated for sCO_2 Brayton cycle applications. In comparison to mechanical systems, these NDDCTs eliminate fan parasitic power and reduce maintenance costs according to Wang et al. (2020). However, NDDCTs are extremely susceptible to ambient conditions, specifically crosswinds and air temperature (Kröger, 2004; de la Calle, Bayon & Soo Too, 2018). The study by Wang et al. (2020) found that the peak thermal efficiency of a recompression sCO_2 power block using NDDCTs dropped from around 30% at 15 ℃ ambient temperature to around 10% at 35 ℃. Another study by Al-Waked et al. (2007) found that crosswinds can decrease the thermal efficiencies of these systems by more than 30% at crosswind speeds greater than 10 m/s. To mitigate this, it was suggested that windbreak walls be installed. On the other hand, de la Calle (2018) notes that mitigating the effects of ambient temperature when dry-cooling is difficult and all dry-coolers will suffer as a result. This is supported by the study's findings which indicate that a power plant can experience a 50% reduction in electricity generation when the ambient air temperature rises higher than 3 ℃ above the designed compressor inlet temperature. To reduce the risk of this happening, the compressor inlet temperature is typically overdesigned. However, the cycle efficiency

can drop by more than 2% between 33 and 45 ℃. This is undesirable in a utility-scale plant but may have to be accepted when setting the air-cooled system design outlet temperature.

Despite their sensitivity to these specific upset conditions, further study has been conducted on the use of NDDCTs in sCO_2 power cycles. Monjurul Ehsan et al. (2020) developed a detailed thermal-hydraulic model for an NDDCT for both a recompression and a partial cooling cycle in a 25 MW power plant. The model uses the correlation developed by Yoon et al. (2003) for the sCO_2-side heat transfer coefficient. A draft equation from Kröger (2004) is used to balance pressure drops with the natural pressure rise across the tower. The design of the cooler itself was exhaustive. The fixed geometric parameters for the heat exchanger bundles and tower were extensive and the ambient conditions were maintained below upset conditions (a wind speed below 1 m/s and an ambient temperature of 20 ℃). A methodology for calculating finned tube bundle areas is also presented for circular fins. The findings of the study show that for an increase in cooler inlet temperature, cycle efficiency rapidly decreases because the turbine inlet temperature is maintained in the cycle model. Furthermore, the recompression cycle achieves higher cycle efficiencies. The effect of ambient air temperature on the recompression cycle is also shown; compressor inlet temperature rises sharply as air temperature does.

Duniam et al. (2018) compared direct and indirect NDDCTs used as the precoolers in an sCO_2 Brayton cycle for CSP power plants. The difference in modelling is that the direct model developed in the study does not contain the intermediate water loop from the indirect model. The direct model used the NDDCT method from Kröger (2004). To better account for sCO_2-to-air heat transfer it also adopted the sCO_2 heat transfer coefficient correlation from Yoon et al. (2003). The modelling approach taken was to discretize the tube rows into nodes and perform the logarithmic mean temperature difference (LMTD) method for each node, iteratively solving the outlet temperatures. In this way, the heat transfer for each node was found and subsequently the mass flow rate of air was solved based on the total heat transfer. The comparison found that direct NDDCTs require 40% less heat transfer area than indirect NDDCTs, making them smaller but at the cost of control (which comes by setting the water loop mass flow rate).

Discussion of the above sCO_2 direct air-cooled system models indicates that there are benefits to cooling relatively close to the critical point of sCO_2 but that it is risky. Deshmukh & Kapat (2020) note a reduction in compressor work with lower cooler outlet temperatures at the cost of cooler footprint. On the other hand, Sathish et al. (2021) observed higher cycle efficiencies when the cooler outlet temperature is in the range of 44 ℃ to 50 ℃. Other potential risks are that pinch-point issues can occur and the potential of condensing the sCO_2. Furthermore, a target outlet temperature further from the critical point will allow for air-cooled system sizes to decrease. This means reduced mass flow rates of air and fan power. There is also general agreement in the literature that models should be discretized to account for sCO_2 property variation. Additionally, the use of the correlations developed by Gnielinski (1976) and Yoon et al. (2003) for internal forced convection is prominent.

Review of literature regarding direct forced draft mechanical air-cooled systems for sCO_2 cycles points to several gaps in the research. The work of Gavic (2012) is done for a specific set of finned tube configurations, there is room for optimisation in this regard. Moreover, the models developed by Gavic (2012) do not consider tube wall thicknesses suited for high-pressure applications. The fan power and heat rejection rate

in the models are also set at constant values, this allows for no variation in the volume and mass flow rates of air. Because of this limited scope, a more detailed model is required to fully analyse these types of systems. Additionally, the work of Sathish et al. (2021) calls for the detailed design of components in sCO_2 Brayton cycles and the analysis of their off-design performance. The study by Deshmukh & Kapat (2020) is detailed but developed for a simple recuperative cycle with a single air-cooled system. The model also sets mass air flow rates instead of fundamentally solving for them based on system specifications and ambient conditions, this is possible using the correlations from Kröger (2004). There is a need to develop a model for a direct sCO_2 air-cooled system which is defined by a set, utility-scale axial fan which is commercially available, and which considers readily available tube sizes and wall thicknesses which are suitable for high-pressure applications. There is also a need to find optimal configurations for the finned tubes and heat exchanger which comprise the heat rejection system. Combining these aspects and fundamentally solving the air-cooled system for a utility-scale sCO_2 power plant operating with a cutting-edge cycle will contribute to filling the current gap in literature.

3. Plan of development

Following the literature presented, the conceptual layout and steady-state sizing methodology of the air-cooled heat rejection systems will be presented. The method and results of parametric studies completed to determine near-optimal designs are then presented. The development of the Flownex ® SE models are then presented. Thereafter, the off-design studies are presented, which includes a study using annual weather data and a proposed control scheme. Finally, conclusions and recommendations are made.

4. Steady-state heat rejection system model

This section presents the required duties and the conceptual layouts, as well as the method used to develop the model to size the two forced draft air-cooled heat rejection systems. The method employs a steady-state 1D thermofluid network modelling approach with established dry-cooler modelling methods and correlations (Kröger, 2004; *VDI Heat Atlas*, 2010). Models of fans used in industry have also been incorporated instead of assuming a set fan performance as in previous works (Gavic, 2012; Deshmukh & Kapat, 2020). Readily available tube sizes and wall thicknesses which are appropriate for high pressure applications were also considered.

4.1 Supercritical carbon dioxide cycle

PC	- Precooler	RCC	- Recompression compressor	HPT	- High-pressure turbine
LPC	- Low-pressure compressor	MH	- Main heater	G	- Generator
IC	- Intercooler	LPT	- Low-pressure turbine	HTR	- High-temperature recuperator
HPC	- High-pressure compressor	RH	- Reheater	LTR	- Low-temperature recuperator

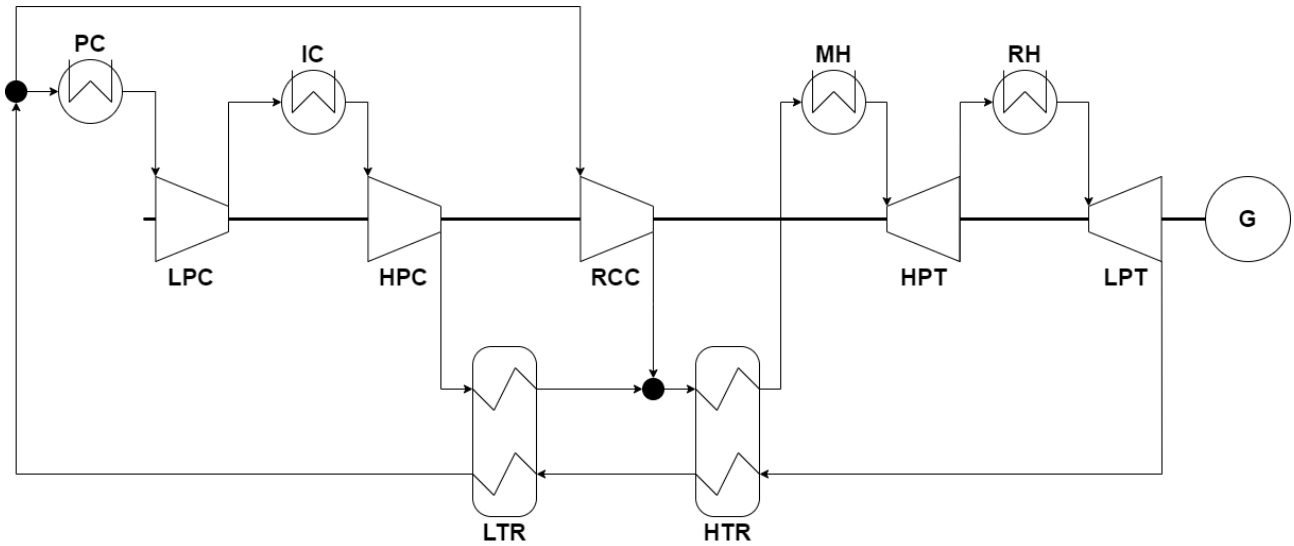

Figure 4-1: RCICRH cycle schematic

The present work incorporates design boundary values taken from a revised version of the work presented by Du Sart et al. (2021), who investigated optimal cycle layouts and boundary conditions for a 50 MWe sCO_2 CSP plant. They found that the recompression with reheating and intercooling (RCICRH) cycle is the most

promising in terms of cycle thermal efficiency. It is therefore used in this work. A schematic of the cycle can be seen in Figure 4-1.

The relevant boundary values for both the precooler and intercooler are shown in Table 4-1. It is important to note that several of these values are for the referenced pressure drops in the table, in reality any change upstream or downstream of the coolers will influence these conditions.

Table 4-1: Boundary and target conditions for the air-cooled system models

sCO_2 parameter	**Unit**	**Precooler**	**Intercooler**
*Mass flow rate	kg/s	392.1	392.1
*Inlet pressure	kPa	7503	10 515
Pressure drop	kPa	≤ 150	≤ 211
*Inlet temperature	℃	85.77	73.92
Outlet temperature	℃	45	45
*Cycle thermal efficiency	%	44.15	

*Values at referenced pressure drops

4.2 Heat rejection system description

The heat rejection system designed in the present work is for a potential plant located in the region of Upington, South Africa. The system takes the form of many multiple pass cross-flow heat exchangers, referred to as cooling cells. Each cell consists of a finned tube bundle located above a large axial forced draft fan. Both the fan and the bundle in each cell are supported by concrete columns called tower supports. The tube bundles are arranged such that sCO_2 flows into the cell from its header at the top to its collector at the bottom through multiple sheets of finned tubes stacked in the transverse (horizontal) direction. Each sheet consists of one or more vertically stacked tubes arranged in a serpentine pattern. The number of tubes stacked vertically in each sheet is referred to as the number of flow paths, N_{paths}, found using Eq. (4-1). The flow of sCO_2 is split between the number of transverse tubes, N_{tubes}, based on N_{paths} and the number of transverse rows, N_T, as it enters the heat exchanger.

$$N_{paths} = \frac{N_L}{N_{passes}} \tag{4-1}$$

$$N_T = \left(\frac{W_{HX}}{S_T} + 1\right) \tag{4-2}$$

$$N_{tubes} = N_{paths} \times N_T \tag{4-3}$$

Where $N_{paths}, N_{passes}, N_L, N_T$ and N_{tubes} are all whole numbers. In the equations above, N_L is the total number of tubes in the longitudinal (vertical) direction and N_{passes} is the desired number of passes for the sCO_2. It is noted that N_L needs to be a multiple of N_{passes}, and this is a constraint placed on the heat exchanger design. The width, W_{HX}, of each cell is determined by the fan size and approximately equal to the length of each pass, L_{pass}. Furthermore, the tubes between each vertical sheet are staggered to improve heat transfer in the cells and N_T is rounded up to avoid dead zones. The dead zones referred to here are not flow dead zones which can increase fouling and backflow (Gu et al., 2020) but rather heat transfer dead

zones. Heat transfer dead zones reduce the efficiency of a heat exchanger and result in reduced heat transfer primarily because the hot or cold stream fluid velocity is low. This effect is more common in shell and tube heat exchangers but worth accounting for if the heat rejection system developed is to be realised (He, Huang & Tan, 2017).

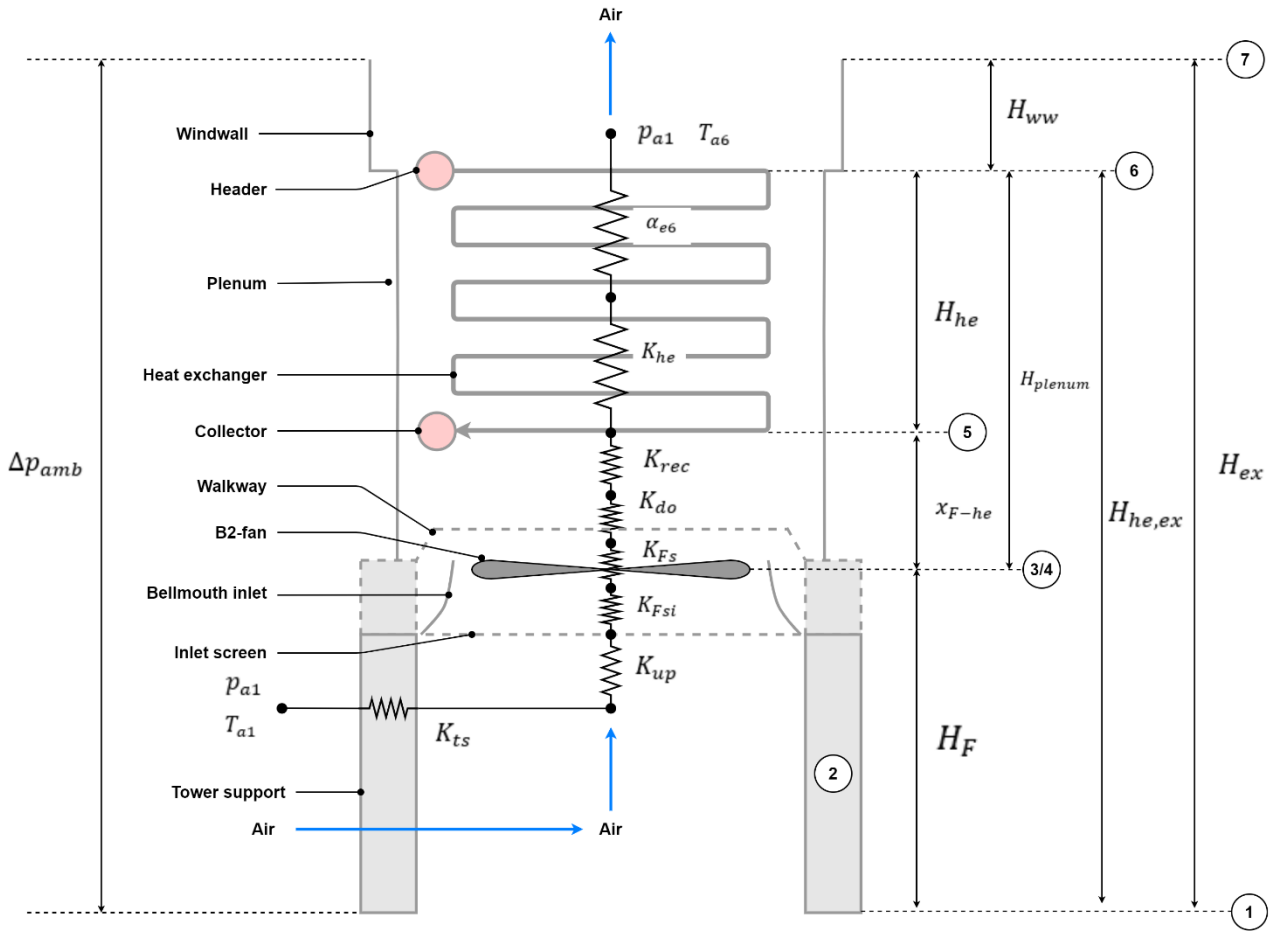

Figure 4-2: Air-side pressure resistance network and detailed schematic

Figure 4-2 shows both a detailed schematic of an entire cell in the air-cooled heat rejection system as well as the air-side pressure resistance network which is later referred to in section 4.9. The diagram shows the way in which the components of the system are located with respect to one another while also displaying the geometry that defines the overall cell. The tower supports, inlet screen, walkway, windwall and plenum can all be seen. It is important to note that the plenum which contains the heat exchanger will have an associated height, H_{plenum} in metres. This height is significant because it includes the distance from the fan to the heat exchanger, x_{Fhe}. If this distance drops below a critical value, it can lead to a rapid drop in system performance. For all industrial forced draft air-cooled systems, Kröger (2004) recommends that a ratio of $x_{Fhe}/d_c \geq 0.3$ be used to ensure performance is maintained. This methodology is adopted in the present work. Furthermore, certain key points within the pressure resistance network have been numbered and are used in Eq. (4-51).

Figure 4-3 shows a schematic of the heat exchanger and overall air-cooled system layout in further detail. In this specific schematic, the diagram displays a tube bundle arrangement where each sheet contains two vertically stacked tubes arranged in a four pass serpentine pattern, providing a total of eight longitudinal

rows. Figure 4-3 also shows some of the tube bundle geometry. S_L and S_T represent the longitudinal and transverse pitches between tubes respectively.

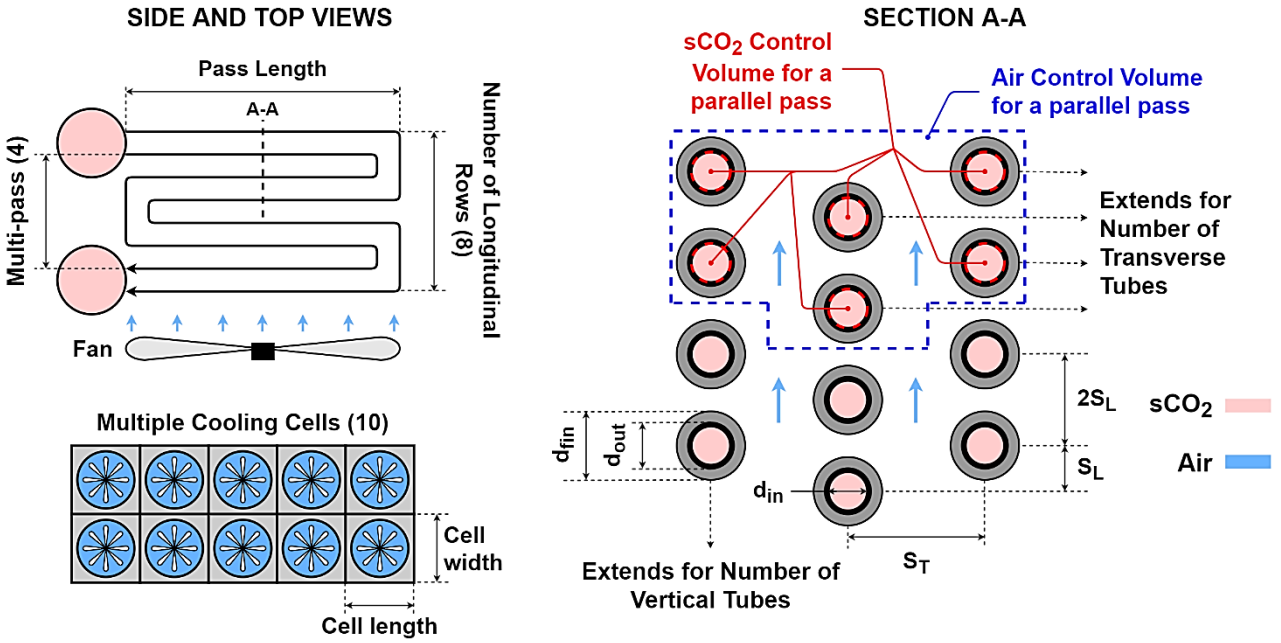

Figure 4-3: Heat rejection system with a four pass, eight longitudinal row heat exchanger

Mathematical models have been developed which simulate a single cell for both coolers, assuming equal distribution of sCO_2 between all cells within the specific heat rejection system and consistent ambient conditions across all cells. In other words, the results for a single cell model are representative of all cells within the precooler or intercooler. The next few sections outline the determination of the various geometric parameters required in the mathematical models. This includes the tube wall thickness, cell footprint and finned tube geometry.

4.3 Tube thickness calculation

The tubes have been designed as per standard sizes and wall thicknesses available in South Africa (Process Pipe, 2016). An external diameter of 25.4 mm was set considering the mass flow rate of sCO_2 and associated pressure drop across the heat exchanger, as well as a maximum potential pressure, p_{max}, of 16.2 MPa. This pressure has been selected as a reasonable value assuming that in the case of a system shutdown, the pressure will equalise at the average of the cycle minimum (7.4 MPa) and maximum (25 MPa) pressures. The wall thickness was then found by performing a yield calculation for thick cylinders, derived from expressions in Hearn (1997) and shown in Eq. (4-4).

$$t_w = r_o - \sqrt{\frac{{r_o}^2\left(\frac{Y_{tbs}}{SF} - p_{max}\right)}{p_{max} + \frac{Y_{tbs}}{SF}}} \qquad (4\text{-}4)$$

Where r_o is the outer radius of the tube in mm and Y_s is the yield strength of the tube material in MPa. A safety factor, SF, of 2 was applied to the design which corresponds with a maximum pressure of 32.4 MPa. This safety factor takes into consideration potential manufacturing defects, the difficulties associated with

repairing or replacing tubes, the handling and potential damage of thin-walled tubes, as well as the corrosion of such tubes. The tube material used was EN P235GH steel which is a commonly used carbon steel in heat exchanger design. Details of the tube material can be found in Table 4-2 below.

$$SF = \frac{Y_{tbs}\left[1 - \left(\frac{(r_o - t_w)^2}{{r_o}^2}\right)\right]}{p_{max}\left[1 + \left(\frac{(r_o - t_w)^2}{{r_o}^2}\right)\right]} \quad (4\text{-}5)$$

Table 4-2: EN P235 steel material properties from

Material property	Symbol	Unit	Value
Yield strength	Y_s	MPa	235.0
Ultimate tensile strength	U_s	MPa	360.0
Density	ρ_{tbs}	Kg/m^3	7850.0
Surface roughness	ϵ_{tbs}	mm	0.0015
Thermal conductivity	k_{tbs}	W/m.K	58.0
Operating temperature	T_{op}	℃	up to 300.0

The density, yield strength, and ultimate tensile strength were taken from SteelNumber (2022). The surface roughness and thermal conductivity were extracted from Kröger (2004) for drawn steel tubes. The final wall thickness was then set at the standard size of 3 mm, which is thicker than the calculated amount (2.92 mm) considering the risk of damage associated with handling thin-walled tubes and the potential corrosion of the tubes during their operation. This allows for the recalculation of the actual SF on the tube wall design using Eq. (4-5). This resulted in an actual value of $SF = 3.82$ which was deemed appropriate taking into account the considerations mentioned above. The standard tube wall thickness of 3 mm also determined the tube internal diameter, d_i, of 19.4 mm.

4.4 Cell footprint

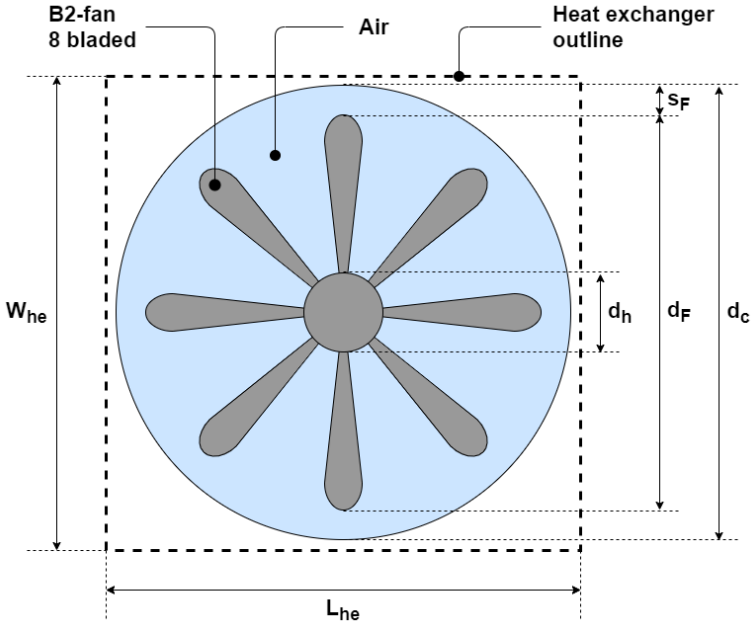

Figure 4-4: Detailed B2-fan geometry for setup of thermofluid model

Because the fan dimensions and geometry, seen in Figure 4-4, define the width and length of each cooling cell, they must be defined before the heat exchanger geometry can be set up. Naturally, the size of the fan will influence this, but the general process begins with the determination of the fan hub diameter (d_{hub}) using the hub-tip ratio, R_{hub}:

$$d_{hub} = d_F R_{hub} \tag{4-6}$$

The effective fan area, used in the draft Eq. (4-58), can now be found:

$$A_e = \frac{\pi}{4}\left({d_F}^2 - {d_{hub}}^2\right) \tag{4-7}$$

Following this, the tip clearance percentage (s_{clear}), must be used to find the actual tip clearance (s_F), the casing diameter (d_c) and subsequently the casing area (A_c) and distance from the fan to the heat exchanger, x_{F-he}. Note that s_{clear} has been set to a conservative value of 1% and x_{F-he} is assumed to be a fraction of d_c taken from Kröger (2004).

$$s_F = s_{clear} d_F \tag{4-8}$$

$$d_c = d_F + 2s_F \tag{4-9}$$

$$x_{F-he} = 0.3 d_c \tag{4-10}$$

The width (W_{he}) and length (L_{he}) of the heat exchanger can now be determined. It is important to note that the width and length are assumed to be equal to each other and to the length of one tube pass, L_{pass}. Both W_{he} and L_{he} have been marginally increased and rounded to one decimal place to ensure that no heat transfer 'dead zones' are present in the heat exchanger.

$$L_{HX} = W_{HX} = L_{pass} = (d_c + 0.2) \;\; rounded\ to\ 1\ decimal \tag{4-11}$$

Finally, the determination of the heights, all measured in metres, across the system needs to take place before the model can be simulated and the governing equations solved. The relevant heights are visible in Figure 4-2 and are calculated using Eq. (4-12) – Eq. (4-16) below.

$$H_{HX} = S_L N_L - 0.5 S_L$$
$$For\ a\ staggered\ configuration \tag{4-12}$$

$$H_{ww} = H_{HX} \tag{4-13}$$

$$H_{plenum} = H_{HX} + x_{F-he} \tag{4-14}$$

$$H_{he,ex} = H_F + H_{plenum} \tag{4-15}$$

$$H_{ex} = H_F + H_{plenum} + H_{ww} \quad (4\text{-}16)$$

Where H_{ww} is the windwall height; a simplifying assumption has been made that H_{ww} is nominally the height of the heat exchanger. H_{HX}, H_{plenum}, $H_{he,ex}$, and H_{ex} are the heat exchanger, plenum, heat exchanger exit, and overall exit heights respectively.

4.5 Geometry of finned tube bundles

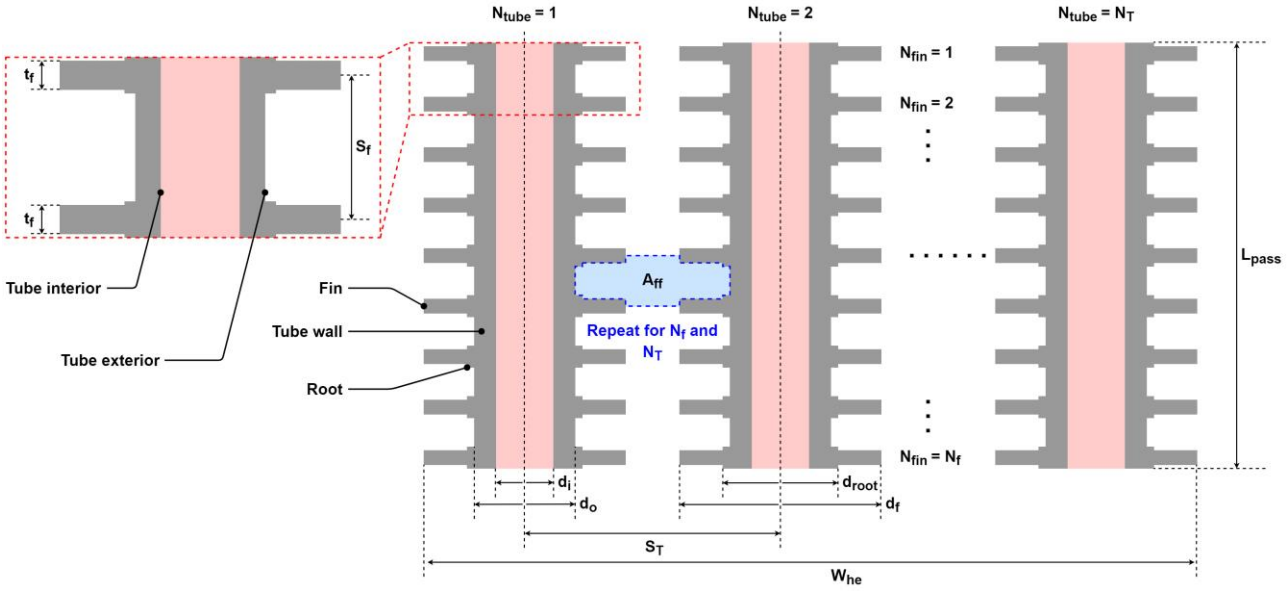

Figure 4-5: Detailed finned tube geometry

A geometric setup of the finned tube bundles is also required before the model can be solved. Figure 4-5 shows the detailed geometry of the finned tube bundles. The calculation of all relevant areas (in m^2), and other geometric factors are included below the diagram. It is important to note that all diameters, thicknesses and pitches are specified in millimetres before being converted to metres in the mathematical models.

The external and internal heat transfer areas, A_c and A_h respectively, are calculated using Eq. (4-17) and Eq. (4-18). These two areas are later used in Eq. (4-33) and Eq. (4-35) when determining the thermal resistances per pass in the heat transfer network.

$$A_c = A_{ext} + A_f \quad (4\text{-}17)$$

$$A_h = A_{int} = \pi d_i L_{pass} N_{tubes} \quad (4\text{-}18)$$

Where d_i, L_{pass}, and N_{tubes} all represent the internal tube diameter, pass length, and number of transverse tubes in a pass respectively. A_{ext} is the external tube surface area per pass found using Eq. (4-19), while A_f is the finned area per pass, calculated with Eq. (4-20).

$$A_{ext} = \pi d_o L_{pass} N_{tubes} \quad (4\text{-}19)$$

$$A_f = N_{tubes}\left(\frac{N_f}{N_{passes}}\right)\left(\pi\left(\frac{{d_f}^2 - {d_{root}}^2}{2} + d_f t_f\right)\right) \quad (4\text{-}20)$$

In the above expressions, d_o is the tube's outer diameter. d_f and d_{root} represent the fin and root diameters respectively as seen in Figure 4-5. The number of fins per single tube and number of passes are shown as N_f and N_{passes} respectively. N_f is calculated using the pass length, number of passes, and the pitch between fins, S_f, as in Eq. (4-21).

$$N_f = \frac{L_{pass} n_{passes}}{S_f} \quad rounded\ to\ a\ whole\ number \quad (4\text{-}21)$$

Several other areas and geometric factors which affect both the fluid mechanics and heat transfer on the air- and sCO_2-sides of the heat exchanger. The hydraulic diameter of air (d_{ea}) is used when finding the air-side Nusselt number, Nu_c. d_{ea} is calculated as per Eq. (4-22).

$$d_{ea} = \frac{4A_{ff}S_L}{A_f} \quad (4\text{-}22)$$

Where A_f is the finned area from Eq. (4-20) and A_{ff} is the air-side free flow area through a heat exchanger pass:

$$A_{ff} = (S_T - d_{root})(S_f - t_f)\left(\frac{N_f}{n_{passes}}\right)N_T \quad (4\text{-}23)$$

In the equations above, S_L and S_T represent the tube longitudinal and tube transverse pitches respectively. The air porosity, σ, is used when calculating the air-side pressure drops as it influences the velocity distribution factor of the heat exchanger shown in Eq. (4-56). σ depends on A_{ff} and the total frontal area of the heat exchanger, A_{fr}.

$$A_{fr} = W_{he}L_{he} \quad (4\text{-}24)$$

$$\sigma = \frac{A_{ff}}{A_{fr}} \quad (4\text{-}25)$$

Where the width (W_{he}) and length (L_{he}) of the heat exchanger are calculated as shown in section 4.4. In any finned tube heat exchanger, there is a surface efficiency, η_0, which affects the thermal resistance on the air-side. Surface efficiency is calculated using Eq. (C-17) and requires the total exposed surface area of the fins, A_{total}, shown in Eq. (4-26). A_{total} is the sum of A_f and the exposed fin root area, A_{root}, determined using Eq. (4-27) below.

$$A_{total} = A_f + A_{root} \quad (4\text{-}26)$$

$$A_{root} = \pi N_{tubes} L_{pass} d_{root} \left(\frac{S_f - t_f}{S_f} \right) \quad (4\text{-}27)$$

Finally, the inlet airflow area between the tower supports, A_2, is required when accounting for the air-side pressure drop characteristics in the draft Eq. (4-58) and when calculating the loss coefficient of the tower supports, K_{ts}, in Eq. (4-54). The location of A_2 is indicated in Figure 4-2 and it is calculated as follows:

$$A_2 = H_F W_{he} \quad (4\text{-}28)$$

Where H_F is the height of the fan above the ground in metres.

The various geometry, geometric factors and areas defined in section 4.3 - 4.5 are all used as inputs to the mathematical models. They are essential in determining the heat transfer and pressure drop characteristics of both fluid streams which provide the steady-state solution of the heat rejection system's governing equations.

4.6 Governing equations

The modelling methodology applied in this work uses interlinked 1D control volumes for the internal and external fluids, and solves their mass and energy balance equations for a steady-state scenario (Eq. (4-29) and (4-31), respectively). The momentum balance equation for sCO_2 is solved using Eq. (4-30) while the air-side momentum balance is found using the draft equation, Eq. (4-57) seen in section 4.9. The balance equations are solved iteratively in the model using a combination of a binary search and the *optimize.fsolve* function from the *SciPy* 1.6.2. library, which is a numerical Newton-Raphson based solver. A detailed solver methodology can be found in section 4.10. Each air-cooled cell consists of both air-side and sCO_2-side control volumes. As can be seen in Figure 4-3, the sCO_2-side control volumes include the flow through all the transverse and vertically stacked tubes for a pass, while the air-side consists of the flow over these tubes. To account for the variation in sCO_2 fluid properties (which change rapidly near the critical point), the heat exchanger tubes were discretised on a pass-by-pass basis. At this point, it is important to note that each pass (or control volume) may contain multiple longitudinal rows, as this effects the e-NTU correlation applied later. A simplifying assumption that the inlet and outlet air properties are the same for each parallel pass was also made. Each discrete element (or control volume) computes the fluid properties at the mean (m) enthalpies and pressures using the *CoolProp* 6.4.1. library (Bell et al., 2014), which is based on the NIST REFPROP database (National Institute of Standards and Technology, 2013). The inlet (in) and exit (ex) properties are found using the same method. It is important to note that the mass flow rate of sCO_2 is assumed to be evenly distributed between all the tubes and constant from inlet to exit in each control volume. Additionally, altitude (z) has been ignored in the models because the difference between z_{ex} and z_{in} is small and contributes a negligible amount to the momentum balance. The secondary losses ($\sum K$) are comprised of only the bend losses for all passes except the last, and the exit loss in the final pass.

$$\dot{m}_{in} = \rho_{in} v_{in} A_{in} = \rho_{ex} v_{ex} A_{ex} = \dot{m}_{ex} \quad (4\text{-}29)$$

$$p_{in} + \frac{1}{2}\rho_{in}{v_{in}}^2 + \rho_{in}gz_{in} = p_{ex} + \frac{1}{2}\rho_{ex}{v_{ex}}^2 + \rho_{ex}gz_{ex} + \left(f_D\frac{L}{D} + \sum K\right)\frac{\rho_m{v_m}^2}{2} \quad (4\text{-}30)$$

$$\dot{m}_{ex}h_{ex} - \dot{m}_{in}h_{in} = \dot{Q} = e_{he}C_{min}\left(T_{h,in} - T_{c,in}\right) \quad (4\text{-}31)$$

4.7 Heat transfer

The thermal resistance network for the air-cooled system model is shown in Figure 4-6. The model accounts for sCO_2-side internal forced convection, conduction in the tube walls of the heat exchanger and air-side external forced convection. Heat is transferred from the hot sCO_2 to the wall by convection, through the wall by conduction, and then to the cold air by convection again. The model does not account for fouling (a build-up of deposits on heat exchanger surfaces) and radiative effects. This is because, for most applications, radiation effects are minimal and accounted for in the convection heat transfer coefficients (Cengel, 2006). Fouling effects may need to be considered at a later stage, equivalent fouling resistances are widely available in literature (*VDI Heat Atlas*, 2010). In the present work a thermal resistance network is used and all fluid properties are evaluated at the mean temperature of the tube row. The overall conductance for one row in the heat exchanger was found using:

$$UA = (R_h + R_w + R_c)^{-1} \quad (4\text{-}32)$$

The heat transfer resistances used above are shown in Figure 4-6. These resistances are found using equations (4-33) to (4-35) and once the UA value for the row is known, the heat transfer per discrete element is found using the e-NTU method for crossflow with both fluid streams unmixed from Appendix C-4. This approach has been taken because it accurately captures heat transfer for passes with more than one vertically stacked tube rows. In the case of a single tube row per pass, a mixed-unmixed correlation would be better suited.

$$R_h = \frac{1}{h_h A_{h_h}} \quad (4\text{-}33)$$

$$R_w = \frac{\ln\left(\frac{d_o}{d_i}\right)}{2\pi L_{pass}N_{tubes}k_{tbs}} \quad (4\text{-}34)$$

$$R_c = \frac{1}{\eta_o h_c A_c} \quad (4\text{-}35)$$

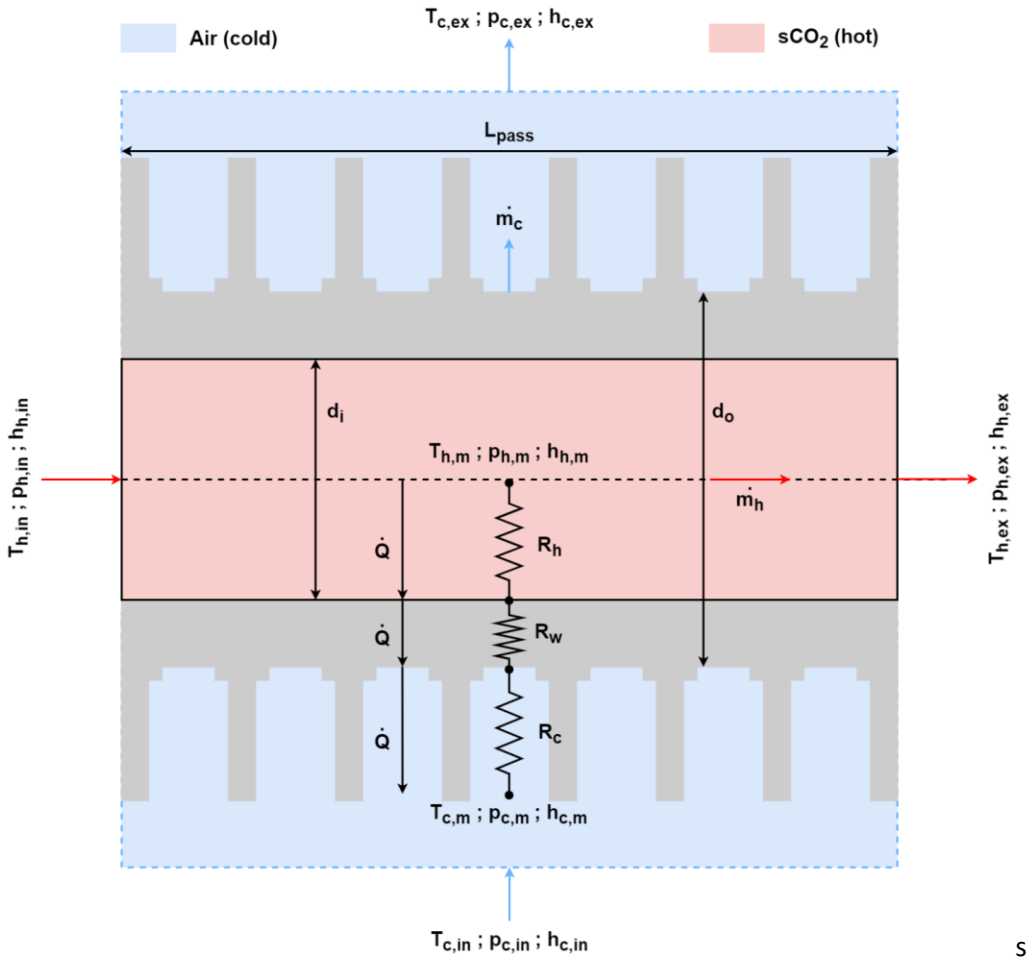

Figure 4-6: Cross-section of a typical thermofluid network for one tube row per pass

Heat transfer coefficients (h values) are found using equation (C-10) and the relevant Nu and thermal conductivity, k. The overall surface efficiency, η_o, is found using the methodology from Section C-3 and Eq. (C-17). Gnielinski (1976) has developed empirical correlations for Nu_h and Nu_c.

$$Nu_h = \frac{\left(\frac{f_D}{8}\right) Re_h Pr_h}{1 + 12.7\sqrt{\frac{f_D}{8}}\left(Pr_h^{\frac{2}{3}} - 1\right)}\left(1 + \left(\frac{d_i}{L_{pass}}\right)\right)^{2/3} \qquad (4\text{-}36)$$

$$for\ 10^4 \le Re_h \le 10^6;\ \ 0.1 \le Pr_h \le 1000;\ \ \frac{d_i}{L_{pass}} \le 1$$

$$Nu_c = 0.3 + \sqrt{Nu_{lam}{}^2 + Nu_{turb}{}^2} \qquad (4\text{-}37)$$

$$for\ 10 \le Re_\psi \le 10^6;\ \ 0.6 \le Pr_c \le 1000$$

Equation (4-36) requires f_D for turbulent flow, found using the equation developed by Konakov (1946), this specific equation is recommended for use in determining $Nu_{c,i}$ with this method (*VDI Heat Atlas*, 2010):

$$f_D = (1.8\log(Re_h) - 1.5)^{-2} \qquad (4\text{-}38)$$

$Nu_{lam,i}$ and $Nu_{turb,i}$ are both dependent on the heat exchanger tube arrangement, for staggered tube arrangements they can be found as shown below:

$$Nu_{lam} = 0.664\sqrt{Re_{\psi}}\sqrt[3]{Pr_c} \tag{4-39}$$

$$Nu_{turb} = \frac{0.037{Re_{\psi}}^{0.8}Pr_c}{1 + 2.443{Re_{\psi}}^{-0.1}\left(Pr_c^{\frac{2}{3}} - 1\right)} \tag{4-40}$$

Re_{ψ} is the void Re and it is found by dividing Re_c by a void factor, ψ, which is dependent on two dimensionless values, a and b. Equations (4-41) - (4-44) below show the method for calculating these values and ψ.

$$a = \frac{S_T}{d_o} \tag{4-41}$$

$$b = \frac{S_L}{d_o} \tag{4-42}$$

$$\psi = 1 - \frac{\pi}{4a} \quad for\ b \geq 1 \tag{4-43}$$

$$\psi = 1 - \frac{\pi}{4ab} \quad for\ b < 1 \tag{4-44}$$

When the heat exchanger bundle consists of multiple rows an adjustment must be made. Eq. (4-45) shows the adjusted Nu_c for the entire bundle.

$$Nu_{bundle} = \frac{1 + (N_L - 1)f_A}{N_L}Nu_c \tag{4-45}$$

The arrangement factor, f_A is also dependent on heat exchanger bundle geometry for staggered tubes. It is found using:

$$f_A = 1 + \frac{2}{3b} \tag{4-46}$$

4.8 sCO_2-side pressure drops

The sCO_2-side pressure characteristics were captured by incorporating several pressure drops from the inlet distribution headers to the outlet of the heat exchanger tube rows. Many of these pressure drop correlations have been derived by Kröger (2004). The header pressure drop (Δp_{header}), was found using a form loss factor, $K_{header} = 2.5$, the velocity in the header (v_{header}) is dependent on the mass flow rate of sCO_2 ($\dot{m}_h$) and the header diameter, $d_{header} = 1.25$ m. This header diameter is taken from an example system (Kröger, 2004) and represents a standard size for existing power plants. A more detailed header sizing is planned for the final designs. Frictional losses have been assumed negligible in the header ducting for this model. Upon

entering the heat exchanger tube rows, the sCO_2 experiences a contraction pressure loss. The secondary loss factor for this pressure drop is given below:

$$K_{in} = (1 - \sigma^2 + K_c) \tag{4-47}$$

Where σ is the ratio of free flow area (A_{ff}) to frontal area (A_{fr}) in a control volume for the heat exchanger. These two areas can be found using Eq. (4-23) and Eq. (4-24) from Section 4.5. The contraction loss factor, $K_c = 0.6$, is taken from Kröger (2004). The form loss factors mentioned above are incorporated in the model using Eq. (C-6) as seen in Appendix F-4.

The pressure drops Δp_{header} and Δp_{in} are both subtracted from the design point boundary conditions to provide the actual inlet pressure to the heat exchanger. The frictional pressure drops for each pass are then found across the entire length of the tubes is found using the correlation from Swamee & Jain (1976) and the Darcy-Weisbach equation:

$$f_D = \frac{0.25}{\left[\log\left(\frac{\epsilon_{tbs}}{3.7 d_i} + \frac{5.74}{Re_d{}^{0.9}}\right)\right]^2} \tag{4-48}$$

$$\Delta p_{fric} = f_D \left(\frac{L_{pass}}{d_i}\right)\left(\frac{\rho_m v_{tbs}{}^2}{2}\right) \tag{4-49}$$

The Reynolds number in the tubes, Re_d, velocity in the tubes, v_{tbs}, and the density, ρ, are evaluated at the mean pressure and enthalpy of each pass for tubes with a set cross-sectional area. A further pressure drop occurs because of the 180° bends between passes. This pressure drop, Δp_{bends}, is determined using a secondary loss factor, $K_{bends} = 0.18$ derived by Miller (1978), and Eq. (C-6). The outlet expansion pressure loss at the exit of the heat exchanger tube rows is accounted for using the same equation and a simple form loss factor, $K_{ex} = 1.0$. A sample of these two pressure drop calculations can be seen in Appendix F-4.

4.9 Air-side pressure drops

The ambient (boundary) conditions for the air-side are based on a typical summer's day for Upington in South Africa (Weather Spark, 2021). An operating ambient temperature, T_{a1}, of 28.9 ℃ was set and the ambient air pressure, p_{a1}, was calculated based on Upington's altitude, z, which is 808 m above sea level. This is done by adjusting the air pressure at sea-level, $p_{a,sea}$, taken as 101.325 kPa and used in Eq. (4-50) below.

$$p_{a1} = p_{a,sea} \times e^{\left(\frac{-gM_a z}{T_{a,sea} R_0}\right)} \tag{4-50}$$

Where g is the gravitational acceleration of 9.81 m/s^2, M_a is the molar mass for dry air, $T_{a,sea}$ is the ambient temperature at sea-level of 15 ℃ or 288.15 K, and R_0 is the universal gas constant. p_{a1} was found to be 92.064 kPa using Eq. (4-50).

An adiabatic lapse rate (ALR) is used to capture the natural temperature change with elevation. The ALR can be either a moist adiabatic lapse rate (MALR) or a dry adiabatic lapse rate (DALR). The present work uses a MALR to balance the pressure drops as the air flows past the heat rejection system's structures, fan assembly,

and finned tubes of the heat exchanger with the pressure rise through the axial fan. The MALR is used because it accounts for moisture in the air whereas the DALR works on a dry air assumption. Equations (4-52) and (4-53) provide the method for determining the MALR and equation (4-51) below specifies the pressure boundary condition imposed at the outlet of the heat exchanger bundles.

$$\Delta p_{amb} = p_{a1}\left[\left\{1 - MALR\frac{H_{ex} - H_{he,ex}}{T_{a6}}\right\}^{3.5} - \left\{1 - MALR\frac{H_{ex} - H_{he,ex}}{T_{a1}}\right\}^{3.5}\right] \quad (4\text{-}51)$$

Where the subscripts 1 and 6 denote the ambient and heat exchanger exit temperatures respectively.

$$MALR = g \times \frac{\left(1 + \frac{H_V r_{mix}}{R_d T_{a1}}\right)}{\left(1 + \frac{H_v^2 r_{mix}}{R_v T_{a1}^2}\right)} \quad (4\text{-}52)$$

Where H_v is the latent heat of vaporization for water in J/kg.K, r_{mix} is the mixing ratio of the moist air, found using Equation (4-53), R_d and R_v are the specific gas constants for dry air and water vapor respectively, measured in J/kg, and T_{a1} Is the ambient air temperature at ground level measured in K.

$$r_{mix} = \frac{\frac{R_d}{R_v} \times p_v}{p_{a1} - p_v} \quad (4\text{-}53)$$

In the equation above, p_{a1} is the ambient air pressure in Pa and p_v is the water vapor pressure in Pa. The MALR calculated for the model and set at that value for all simulations at design conditions, $T_{a1} = 28.9$°C, is equal to 0.004437 K/m. Refer to Appendix F-4 for more details on this calculation.

Like the sCO_2-side, the air-side was modelled using interlinked 1D control volumes. A series of flows through the volumes and secondary loss factors were used to model the pressure drops. The governing equations make use of these loss factors and the pressure rise across the fan to solve for an air mass flow rate which satisfies the pressure boundary condition from equation (4-51). Figure 4-2 in Section 4.2 shows a detailed cross section of the air-side resistance network along with the relevant heights used in the setup of the air-side.

The equations used to determine the loss factors as well as other coefficient values are shown in Table 4-3. The pressure drop as air travels between and around the tower supports is included using K_{ts}. This loss factor is a function of the number of columns, N_{ts}, the drag coefficient of the columns, $C_{D_{ts}}$, the length (L_{ts}) and diameter (d_{ts}) of the columns in meters and the free flow area between the columns, A_{inlet}, taken in m^2. Please note that $C_{D_{ts}}$ was taken as 2.01 in the present work which is representative of an upright structure with the fluid flow impinging on the long side of the body (Kröger, 2004). The heat exchanger pressure drops are accounted for by K_{he} and a velocity distribution factor α_{e6}. K_{he} is found using equations (4-60) and (4-61). K_{Fsi} is treated as negligible because the shroud used in the model is a bellmouth. K_{rec} is negligible because no pressure recovery occurs in the short space between the fan and a horizontal heat exchanger bundle. A-frame bundles will experience some pressure recovery (Kröger, 2004).

Table 4-3: Air-side pressure loss and rise coefficients

Coefficient	Equation	
Tower support loss coefficient	$K_{ts} = \frac{C_{D_{ts}} L_{ts} d_{ts} n_{ts}}{A_2}$	*(4-54)*
Fan inlet shroud coefficient	$K_{Fsi} = 0.0$	-
Fan pressure coefficient	$K_{Fs} = \frac{2\Delta p_{Fs} \rho_{a3}}{\left(\frac{m_a}{A_c}\right)^2}$	*(4-55)*
Plenum recovery coefficient	$K_{rec} = 0.0$	-
Velocity distribution factor	$\alpha_{e6} = 1.6 - 0.48\sigma - 0.012K_{he}$	*(4-56)*

The draft equation is presented in its simplest form in Eq. (4-57) and its fully expanded form in Eq. (4-58). The left-hand side of the equation represents the ambient air pressure change which is balanced by the pressure drops on the air-side and the pressure rise through the fan. Both K_{up} and K_{do} are modelled using polynomial curves extracted from the work of Kröger (2004), the polynomials are shown in Appendix F and the interpolation between these curves is achieved using the method shown in Appendix F-3. A step-by-step hand calculation of these interpolated values is also shown in Appendix F-4.

$$\Delta p_{amb} = \sum \frac{K}{2\rho_a}\left(\frac{m_a}{A}\right)^2 - \Delta p_{Fs} \qquad (4\text{-}57)$$

$$\Delta p_{amb} = \frac{K_{ts}}{2\rho_{a1}}\left(\frac{m_a}{A_2}\right)^2 + \frac{K_{Fsi}}{2\rho_{a3}}\left(\frac{m_a}{A_c}\right)^2 + \frac{K_{up} + K_{do}}{2\rho_{a3}}\left(\frac{m_a}{A_e}\right)^2 - \frac{(K_{Fs} + K_{rec})}{2\rho_{a3}}\left(\frac{m_a}{A_c}\right)^2 + \frac{K_{he}}{2\rho_{a56}}\left(\frac{m_a}{A_{fr}}\right)^2 + \frac{\alpha_{e6}}{2\rho_{a56}}\left(\frac{m_a}{A_{fr}}\right)^2 \qquad (4\text{-}58)$$

Where m_a refers to the mass flow rate of air through the unit in kg/s, areas, A, are measured in m^2 and densities, ρ, in kg/m^3. The air properties are found using a dry air assumption to simplify the calculation and the mean harmonic density, ρ_{a56}, is taken for the heat exchanger terms (K_{he} and α_{e6}). The subscript 3 denotes properties at the fan height. A_2 specifically refers to the frontal area along the side of the cooling unit where the tower supports are situated. A_c, A_e, and A_{fr} are the fan casing, effective fan, and heat exchanger bundle frontal areas respectively. K_{Fs} depends on the static pressure rise through the fans.

In this work an 8-bladed axial fan referred to as a B2-fan will be used. The details of this fan are included in Appendix F-2. This fan is widely used in South African industry because its design is tailored to match the typical duty points found in air-cooled heat exchangers (Augustyn, 2017). The fans were modelled using fan curves for power and static pressure as a function of volume flow rate. Polynomial curves were extracted from the work of Augustyn (2013), for the B2-fan, and scaled using the laws from Appendix C-5 for five

different fan speeds. Variable fan speeds (between developed polynomial curves) are accounted for using the same interpolation shown in Appendix F-3. Varying the fan speed allows for an outlet sCO_2 temperature to be targeted. This shown in the detailed solver architecture below.

There are two major fan sizes for which polynomials and interpolation schemes were developed. Both fan sizes are based on existing axial flow fans (Howden, 2021). The specific fan diameters are 10.98 m (36 ft) and a 7.9248 m (26 ft), referred to as the large and small fan henceforth. Two different sizes were used to (i) help when optimising the system; (ii) avoid overcooling the sCO_2 when using the large fan; and (iii) to avoid having too few cooling cells when using the large fan because this results in high pressure drops across the tubes.

For the crossflow heat exchanger, K_{he} is found by first determining the drag coefficient for the tubes ($C_{D_{tbs}}$), subsequent pressure drop (Δp_{he}), and finally K_{he}. The equations presented come from the work of Gaddis & Gnielinski (1983) and Bergelin, Colburn & Hull (1950). Calculating $C_{D_{tbs}}$ is the most complicated step in the process, a sample calculation can be seen in Appendix F-4.

$$C_{D_{tbs}} = f_{lam} + \left(f_{turb} + f_{n_{turb}}\right) \times F \tag{4-59}$$

$$\Delta p_{he} = N_{MR} C_{D_{tbs}} \rho_{a56} \frac{{v_{eff}}^2}{2} \tag{4-60}$$

$$K_{he} = \frac{2\Delta p_{he}}{\rho_{a56} {v_{eff}}^2} \tag{4-61}$$

Where f_{lam}, f_{turb}, $f_{n_{turb}}$, and F are all dimensionless factors for the heat exchanger based on the geometry and flow regime. N_{MR} is the number of main resistances in the flow direction is equal to N_L or one less than N_L, depending on the narrowest cross section through the tube bundles. The methodology used to find $C_{D_{tbs}}$ is shown in detail below. v_{eff} is the effective velocity through this section and is adjusted from the free flow velocity:

$$v_{ff} = \frac{A_{fr}}{\dot{V}_a} \tag{4-62}$$

Where $\dot{V}_a$ is the volumetric flow rate of air through the heat exchanger in m^3/s. v_{eff} is found using the dimensionless values calculated as below, and a and b from Eq. (4-41) and Eq. (4-42):

$$c = \sqrt{\left(\frac{a}{2}\right)^2 + b^2} \tag{4-63}$$

$$S_D = \sqrt{\left(\frac{S_T}{2}\right)^2 + {S_L}^2} \tag{4-64}$$

$$C = \frac{S_D}{d_{tbo}} \times c \tag{4-65}$$

Where S_D is the diagonal pitch of the tube bundle, and c and C are dimensionless numbers used in the determination of $C_{D_{tbs}}$ and K_{he}. The row correction factor, $f_{n_{turb}}$, for the tube bundle can now be found using a base correction factor, f_0, and adjusting for the number of longitudinal rows. Note that this factor accounts for turbulence between the rows and falls away for heat exchangers with 10 or more longitudinal rows.

$$f_0 = \left(\frac{2(c-1)}{a(a-1)}\right)^2 \quad (4\text{-}66)$$

$$f_{n_{turb}} = f_0\left(\frac{1}{N_L} - \frac{1}{10}\right) \quad (4\text{-}67)$$

With this initial setup complete, the methodology continues by comparing an adjusted a' value to the dimensionless b value and continuing the calculation based on which is larger.

$$a' = \frac{1}{2}\sqrt{2a+1} \quad (4\text{-}68)$$

If a' is less than the b value, then the methodology is as follows:

$$n_{MR} = N_L \quad (4\text{-}69)$$

$$v_{eff} = v_{ff} \times \frac{a}{a-1} \quad (4\text{-}70)$$

$$Re_{he} = \frac{v_{eff} d_{tbo} \rho_{a56}}{\mu_{a56}} \quad (4\text{-}71)$$

$$f'_{lam} = \frac{280\pi((b^{0.5} - 0.6)^2 + 0.75)}{(4ab - \pi)a^{1.6}} \quad (4\text{-}72)$$

$$f_{lam} = \frac{f'_{lam}}{Re_{he}} \quad (4\text{-}73)$$

$$F = 1 - \exp\left(-\frac{Re_{he} + 200}{1000}\right) \quad (4\text{-}74)$$

$$f'_{turb} = 2.5 + \frac{1.2}{(a-0.85)^{1.08}} + 0.4\left(\frac{b}{a} - 1\right)^3 - 0.01\left(\frac{a}{b} - 1\right)^3 \quad (4\text{-}75)$$

$$f_{turb} = \frac{f'_{turb}}{Re_{he}{}^{0.25}} \quad (4\text{-}76)$$

If, however, the a' value is greater than the b value, the following calculation steps change:

$$n_{MR} = N_L - 1 \quad (4\text{-}77)$$

$$v_{eff} = v_{ff} \times \frac{a}{2(C-1)} \quad (4\text{-}78)$$

$$f'_{lam} = \frac{280\pi((b^{0.5} - 0.6)^2 + 0.75)}{(4ab - \pi)c^{1.6}} \quad (4\text{-}79)$$

The remaining steps remain unaltered, although the heat exchanger Reynolds number, Re_{he}, will change because of v_{eff} being determined differently. This will affect all the subsequent dimensionless factors. With all the dimensionless factors known, Eq. (4-59) can be used to find $C_{D_{tbs}}$ and subsequently the heat exchanger loss coefficient.

4.10 Solver

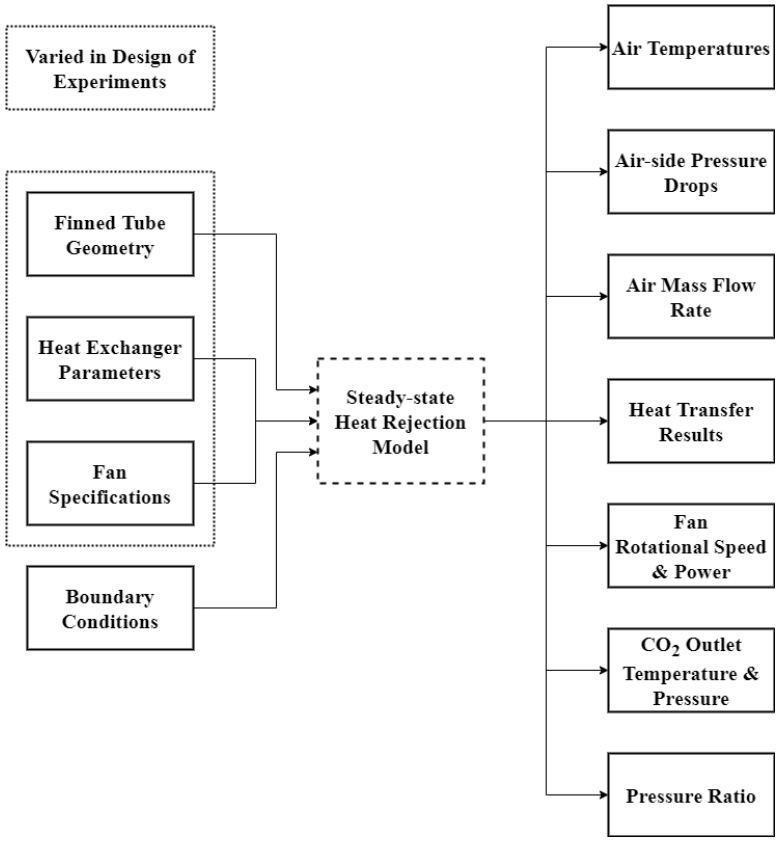

Figure 4-7: Steady-state air-cooled heat rejection system model inputs and key results

Steady-state 1D thermofluid network models were developed for both the PC and IC using the available opensource software libraries in Python 3.8.5. The single cell models developed balance the governing equations from Section 4.6 for both the hot and cold fluid streams. The models achieve mass, energy, and momentum balance using a solver comprising of two iterative loops. One for the energy and sCO_2-side momentum balance and another for the air-side momentum balance. An additional iterative loop is included which adjusts the fan's rotational speed (N) to achieve the targeted outlet sCO_2 temperature of 45 °C. Several inputs are given to the solver, as shown in Figure 4-7 and it returns several outputs for the steady-state solution. The detailed solver architecture can be seen in Figure 4-8 below.

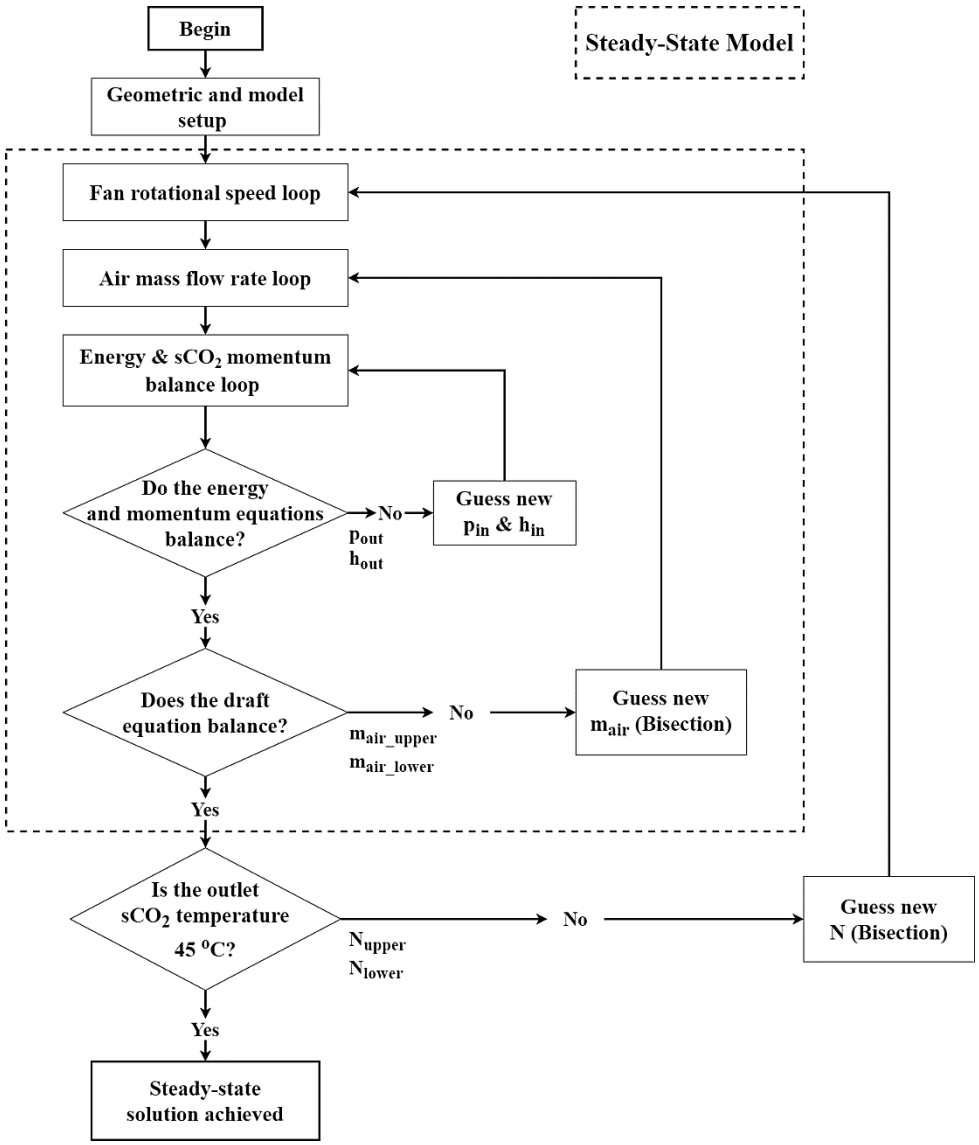

Figure 4-8: Detailed solver architecture for the modelled heat rejection system

The bisection method, or binary search, is used to iteratively solve for N and the mass flow rate of air. These values are solved for separately as shown in Figure 4-8. The bisection method works by converging on the solution of an equation using two initial limit values and their average as inputs to the function representing the equation. The method uses the calculated results at all three values and adjusts the upper and lower limits based on a comparison with the result from the case where their average is used as an input. This adjustment occurs iteratively until the difference between the upper, lower, and average values are all within a certain tolerance value of one another.

The iterative loop which adjusts the fan speed is included because the steady-state model is not constrained to provide a specific sCO_2 outlet temperature. This temperature is a result of the outlet enthalpies, pressures and mass flow rate of air which balance the governing equations at a set N. The difference between the targeted sCO_2 outlet temperature and the calculated temperature above can then be determined and this difference is a function of N. Placing the steady-state model within a loop which adjusts N using the bisection method described above allows for a 45 ℃ sCO_2 outlet temperature to be obtained. For the purposes of this bisection method, the limit values for N are based on the minimum (75 rpm) and maximum (150 rpm) fan

speed curves generated, which determine the static pressure rise across the fan depending on what the mass flow rate of air through the system is. The bisection method requires that the limit values for the input variable produce results that have opposite signs, otherwise a solution cannot be found. In this case, the one limit value for N should produce steady-state sCO_2 outlet temperature above 45 ℃ and the other should result in a temperature below 45 ℃. The value for N is then adjusted as per the methodology.

The limit values for the mass flow rate of air are set so that they produce draft differences of opposite signs across the air-side of the cooling cell. The draft difference is the variation between the ambient pressure change and the air-side pressure drops shown in Eq. (4-51) and Eq. (4-58). Because these two values need to be equal for the air-side momentum equation to balance, the draft difference is representative of how close the air-side momentum equation is to converging on a steady-state solution. Adjusting the mass flow rate of air based on the draft difference using the bisection method described above leads to the steady-state solution of the air-side momentum Eq. (4-58). The maximum (2300 kg/s) and minimum (100 kg/s) limit values for the mass flow rate of air were found by testing the model with only a set mass flow rate and excluding the iterative loop for N.

Within the iterative solver loop for the mass flow rate of air, the energy and sCO_2-side momentum balances, are solved simultaneously using the *optimize.fsolve* function from the *SciPy* 1.6.2. library which makes use of the Newton-Raphson method. The function takes in guess values for the outlet sCO_2 pressures for each pass and the outlet enthalpies for each air and sCO_2 pass and returns the solutions for these values such that the relevant energy and momentum equations balance. With the solutions known for the energy and sCO_2-side momentum governing equations, the solver then calculates the ambient pressure rise and change in pressure across the cooling cell's air-side and computes the draft difference. The initial guess for the mass flow rate of air is then adjusted according to the bisection method. At this stage, the initial guess values for the outlet pressures and enthalpies are also adjusted using relaxation parameters of $\beta_h = 0.8$ and $\beta_p = 0.75$ for enthalpies and pressures respectively. The process repeats until the mass flow rate of air converges to within a tolerance of 1×10^{-3} or 100 iterations have taken place.

With the mass flow rate of air now converged, the model then compares the outlet sCO_2 temperature to the target value of 45 ℃ and adjusts the fan speed according to the bisection method. The entire process then repeats until the fan speed converges to within a tolerance of 1×10^{-3} or 100 iterations have taken place. It is worth noting that in practice, the convergence criteria was always reached before a 100 iterations. This may be because an additional measure was coded which breaks out of the loop if the fan speeds fall outside the limits of 75 rpm and 150 rpm. At this point, there is energy balance across the heat exchanger, momentum balance on the sCO_2-side, a converged mass flow rate of air which provides momentum balance on the air-side and an outlet sCO_2 temperature of 45 ℃. It is important to note that a limited range of fan speeds was taken, which meant that there wasn't always a steady-state solution possible. For each steady-state solution, several important variables were recorded. As previously mentioned, for the total heat rejection system performance the individual cells were assumed to operate the same. Results recorded include those seen in Figure 4-7. Some of the important results are (i) the total and per cell heat transfer, as well as a pass-by-pass breakdown of the heat transfer, (ii) the sCO_2-side pressure ratio, (iii) the total and per cell auxiliary power drawn by fans, and (iv) the fan rotational speed. The code listings for the solver and the functions used are not presented in this report but can be made available on request.

5. Parametric studies

5.1 Model verification

The methodology for modelling air-cooled heat exchangers was partially verified using an example from Kröger (2004). A mathematical model was developed and solved for a single cell forced draft steam condenser. The steady-state results of the model and the results from the example were compared to verfiy the efficacy of the methodology for use in this work. It is important to note that the fan rotational speed in the example is set and its performance determined by two specific equations for power and static pressure rise. This means that only the bisection method for the mass flow rate of air was tested using the example. The code listing is not presented here but can be made available on request.

Comparison of the mathematical model results and those from Kröger (2004) show good agreement. The converged mass flow rate of air was 604.483 kg/s in the example and 604.534 kg/s in the model, these values are within 0.01% of each other. This demonstrates the bisection method to be a valid approach to solving the air-side momentum balance. Furthermore, the calculated outlet air temperatures in the model are within 0.025% of the values from the example. The heat transfer values also agree within 0.35% and 0.03% for the first and second rows in the A-frame heat exchanger respectively.

Table 5-1: PC sample calculations verification to the Python single cell model results

Parameter	**Unit**	**Python Model Result**	**Sample Calculation Result**	**Relative Error on Python Model (%)**
Heat transfer per cell	MW	3.446323	3.446272	0.0015
Pressure ratio	-	0.9972	0.9974	0.0201
Mass flow rate of air	kg/s	181.912	181.912	0.0
Total fan power consumption	kW	184.5	184.5	0.0
Outlet air temperature	°C	47.728	47.728	0.0
Outlet sCO_2 temperature	°C	45.0	45.0	0.0
Fan static pressure rise	Pa	63.003	63.003	0.0
Heat exchanger pressure drop	Pa	18.374	18.374	0.0

The actual mathematical models for the PC and IC were then verified by performing a sample calculation for a converged steady-state solution. In other words, the sample calculation uses a set mass flow rate of air and fan rotational speed. The sample calculation for the PC can be found in Appendix F-4. A calculation was also performed for the IC but is not included in this report. Comparisons of the important steady-state results for two of the designs generated are shown in Table 5-1 and Table 5-2 for the PC and IC respectively.

The results are very close to one another for both the PC and the IC. It is worth noting that the fluid properties used in the sample calculated were computed using the same *CoolProp* 6.4.1. library (Bell et al., 2014) from the Python model. Based on the acceptable levels of variation between the developed models and the sample calculations, the mathematical models were deemed to be solving the steady-state solution in accordance with the thermohydraulic modelling methodology defined in Section 4.

Table 5-2: IC sample calculations verification to the Python single cell model results

Parameter	Unit	Python Model Result	Sample Calculation Result	Relative Error on Python Model (%)
Heat transfer per cell	MW	4.592779	4.592653	0.0027
Pressure ratio	-	0.9945	0.9947	0.0201
Mass flow rate of air	kg/s	181.300	181.300	0.0
Total fan power consumption	kW	230.8	230.8	0.0
Outlet air temperature	°C	54.069	54.069	0.0
Outlet sCO_2 temperature	°C	45.0	45.0	0.0
Fan static pressure rise	Pa	63.087	63.087	0.0
Heat exchanger pressure drop	Pa	18.332	18.332	0.0

5.2 Objective function

In order to obtain near-optimal designs for the heat rejection systems, a suitable objective function is needed. In this work, the near-optimal designs are considered those which maximise the ratio of power generated by the cycle less the auxiliary power required to cool the working fluid, to the rate of heat put into the cycle. This ratio is presented in equations 4.80 and 4.81, and resembles the equation for cycle thermal efficiency:

$$SOP = \dot{W}_{cyc,gen} - \dot{W}_{aux} \quad (5\text{-}1)$$

$$\eta_{cyc} = \frac{SOP}{\dot{Q}_{heat}} \quad (5\text{-}2)$$

Where $\dot{W}_{cyc,gen}$ is the cycle's net power, $\dot{W}_{aux}$ is the auxiliary power required to cool the working fluid, $\dot{Q}_{heat}$ is the rate of heat input, SOP is the send-out-power (assuming there are no other auxiliary loads) and η_{cyc} is the adjusted cycle thermal efficiency (the objective function).

In order to calculate the objective function, the cooler models developed in this work were coupled to a revised version of the RCICRH cycle model presented by Du Sart et al. (2021).

With the 1D thermofluid model solving and producing steady-state results, the goal was to generate a large set of air-cooled system designs by varying nine key design parameters, indicated in Figure 4-7 and shown in detail in Table 5-3. The primary objective of this step was to establish feasible fan and heat exchanger geometry for the heat rejection systems. In other words, designs that achieved the desired sCO_2 outlet temperature. For each air-cooled system design, the results could be recorded and then filtered by the values which have an impact on cycle performance. The method of achieving this, was to couple the results of all the heat rejection system designs to the updated RCICRH cycle model developed by Du Sart, et al. (2021). By coupling the steady-state models to the cycle model, optimal designs which improved the thermal efficiency of the cycle ($\eta_{cyc,th}$) could be selected for further analysis. The pressure drops and fan powers for the simulated precooler and intercooler designs were used as inputs in the cycle model. The outputs calculated were the apparent send-out-power (SOP) and adjusted cycle thermal efficiency (η_{cyc}), found using Eq. (5-1) and Eq. (5-2) respectively.

5.3 Design of experiments

A design of experiments (DoE) study was completed to find feasible air-cooled system designs. To this end, a total of 3 000 design input datasets were generated, using Latin Hypercubic Sampling (LHS) via the *pyDOE* 0.3.8. library, for nine key design parameters. The input datasets are not included in this report but are available on request. The parameters and their ranges are shown in Table 5-3. Most of the heat exchanger geometric parameters have limits based on the literature reviewed and existing design practices (Kröger, 2004; Gavic, 2012; Deshmukh & Kapat, 2020). The limits for H_F come from the correlations of Salta & Kröger (1995) for fan volumetric effectiveness and represent the height at which the fan's volumetric effectiveness is no longer severely impacted by its proximity to the ground and the height at which there are diminishing returns on volumetric effectiveness. The two discrete fan sizes are for off-the-shelf 8-bladed B2-fans that provide an idea of how the heat rejection system may operate with both large and small fans.

Table 5-3: DoE input parameters

Parameter	Symbol	Unit	Min.	Max.	Rationale
Tube longitudinal pitch	S_L	mm	50.0	80.0	From existing design practices and literature (Kröger, 2004; Gavic, 2012; Deshmukh & Kapat, 2020)
Tube transverse pitch	S_T	mm	50.0	80.0	As above for longitudinal pitch
Fin pitch	S_f	mm	1.2	5.0	As above for longitudinal pitch
Fin thickness	t_f	mm	0.4	1.5	As above for longitudinal pitch
Fin diameter	d_f	mm	35.0	50.0	Ensures no interference between fins in different rows and sheets and existing design practices and literature (Kröger, 2004; Gavic, 2012; Deshmukh & Kapat, 2020)
*Mean pass length	L_{pass}	m	8.3	11.4	Based on fan geometry
*Transverse rows	N_T	-	105	167	Based on fan geometry
Longitudinal rows	N_L	-	2	10	Reasonable values from initial modelling calculations
Tube passes	n_{passes}	-	4	10	As above for longitudinal rows
Cooling cells (total)	N_{cells}	-	4	12	As above for longitudinal rows
Fan height	H_F	m	20.0	45.0	Based on fan volumetric effectiveness (Salta & Kröger, 1995)
**Fan diameter	d_F	m	7.925	10.980	Small and large B2-fans

*Values calculated using other design parameters

**Discrete values that required separate models to simulate

When generating designs, several restraints were also imposed: (i) H_F, N_L, N_{cells}, n_{passes} had to be discrete integer values; (ii) N_L had to be divisible by n_{passes} and not equal to zero; (iii) d_f had to be less than the smaller of the two tube pitches by a margin of 5.0 mm. With the input dataset defined, 3 000 potential air-cooled system designs were simulated for each of the four models (PC with a small or large fan, and IC with a small or large fan). The results were recorded and then assessed, leaving many valid design options with pressure drops equal to or lower than desired and outlet sCO_2 temperatures equal to 45 °C. At this point, it was observed that the large fans almost always over-cooled the sCO_2, even at their lowest fan rotational speed. Therefore, they were eliminated as a design option. Furthermore, because there were many valid designs remaining, a decision was made to filter the design options further by filtering them to exclude designs with high auxiliary power consumption and sCO_2-side pressure drops. The specific limits set in this filtering process can be seen below:

Table 5-4: Valid design result filtering conditions and criteria

Condition	**PC Criteria**	**IC Criteria**	**Rationale**
sCO_2-side pressure drop (kPa)	≤ 150	≤ 211	Impacts cycle thermal efficiency negatively below the target value
Fan auxiliary power (kW)	≤ 600	≤ 400	Impacts cycle thermal efficiency negatively above the target value
Number of cells	$Must\ be\ an\ even\ number$		An odd number of cells is detrimental in terms of wind effects when physically arranging the cells
Number of passes	$Must\ be\ an\ even\ number$		It is desirable to have the header and collector situated on the same side of the heat exchangers

The reason why the limiting fan power consumption is lower in the IC is because there were many valid designs from the DoE. This meant that the limit could be stricter without an unnecessary loss of potential designs. It is likely, that the IC had more valid designs from the DoE than the PC because its operating pressure and temperature are further from the critical point, reducing the risk of sudden changes in fluid properties affecting heat transfer.

Table 5-5: Best performing design RCICRH cycle inputs and results for a design ambient temperature of 28.3 °C

Design result	**Symbol**	**Unit**	**Precooler**	**Intercooler**
Pressure ratio	PR	-	0.9970	0.9944
Fan rotational speed	N	rpm	76.93	75.42
Auxiliary power consumption	$\dot{W}_{aux}$	kW	198.95	234.40
Heat rejection rate	$\dot{Q}$	MW	27.5587	45.9166
Mass flow rate of air	$\dot{m}_{air}$	kg/s	179.512	184.812
Cycle thermal efficiency	$\eta_{cyc,thermal}$	-	44.59%	
Adjusted cycle thermal efficiency	η_{cyc}	-	39.39%	
Send-out-power	SOP	kW	50 855	

The filtering process left 41 PC and 76 IC valid designs remaining, this equates to 3 192 combinations which were coupled to the updated RCICRH cycle model using their sCO_2-side pressure drops and fan power

consumptions as inputs. For each of these combinations the SOP and η_{cyc} were recorded and tabulated. The best performing designs (producing the highest η_{cyc}), shown in Table 5-6, were then selected. The results of these designs are shown in Table 5-5. The selected combination of PC and IC designs produced both the highest efficiency (39.39%) and SOP (50 855 kW). This efficiency is higher than the original cycle model's value of 39.33% where fan power is ignored and the pressure ratio across the PC and IC assumed to be 0.98. The value for SOP is important because one other combination of designs did produce the same η_{cyc} of 39.39% but with a lower SOP of 50 846 kW. The decision was made to use the designs producing the higher SOP (however marginal).

Table 5-6: Best performing design parameters per air-cooled system cell

Parameter	Symbol	Unit	Precooler	Intercooler
Tube longitudinal pitch	S_L	mm	76.5	62.7
Tube transverse pitch	S_T	mm	52.8	51.6
Fin pitch	S_f	mm	2.8	1.6
Fin thickness	t_f	mm	1.3	1.0
Fin diameter	d_f	mm	42.6	38.3
Mean pass length	L_{pass}	m	8.3	8.3
Transverse rows	N_T	-	159	162
*Longitudinal rows	N_L	-	8	10
*Tube passes	n_{passes}	-	4	10
*Cooling cells (total)	N_{cells}	-	8	10
Fan height	H_F	m	21.0	21.0
Fan diameter	d_F	m	7.925	7.925

*Discrete values that were excluded when developing the multi-linear regression model

The results of this process show the way in which the PRs and fan powers affect the cycle. Lower fan powers tend to increase cycle efficiency because the auxiliary load decreases. On the other hand, higher PRs increase cycle efficiency by reducing compressor work. Furthermore, to raise the cycle efficiency it is not good enough to just have a high PR. Almost exclusively, air-cooled system designs with combinations of low PC and IC fan powers raise the efficiency.

5.4 Multivariate-linear regression model and sensitivity analysis

Following the selection of the best performing designs from the DoE, an additional analysis was completed to determine the key variables, the effect they have on the performance of the cooling systems, and in doing so, improve the designs further. Table 5-5 shows that neither the PC nor the IC are running their fans at the lowest possible speed of 75 rpm. Theoretically this speed will provide the minimum limit for the designs' auxiliary power consumption. Another method of decreasing the auxiliary power drawn is to reduce the number of cells in each heat rejection system, however, this in turn increases the pressure drop across the heat exchangers. Designs with higher pressure drops will have lower pressure ratios and this has a negative effect on cycle performance in terms of efficiency. Given these intricacies, a multivariate-linear regression (MLR) model was developed to predict η_{cyc}, the adjusted cycle thermal efficiency.

The MLR model developed predicts η_{cyc} as a function of the non-discrete PC and IC design variables listed in Table 5-6. The discrete variables (N_L, N_{passes}, N_{cells}) were fixed at the values for the best performing designs

in Table 5-6 and 336 datapoints with matching discrete values were extracted from the DoE dataset. The data were normalized and used to train and test the MLR model using an 80% training and 20% testing split. The training method uses an ordinary least squares approach to fit regression coefficients to each normalized variable such that the normalized efficiency can be predicted as in Eq. (5-3):

$$y = a_1 x_1 + a_2 x_2 + \cdots + a_n x_n \qquad (5\text{-}3)$$

Where the a-values are the regression coefficients, the x-values are the design parameters, y is the predicted output, and n denotes the total number of input variables. The resulting regression model showed a mean absolute error of 0.12% when tested. Furthermore, comparison of the thermohydraulic models with the MLR model showed a maximum relative error 0.23% on η_{cyc} and a maximum absolute error of 0.08%. These errors were deemed acceptable for this level of study.

To gauge the influence each design variable has on η_{cyc}, a sensitivity analysis was performed by standardising the regression model coefficients using the method from Siegel (2016), seen in Eq. (5-4). The standardised regression coefficients are found by adjusting each regression coefficient by a ratio of standard deviations.

$$\beta_i = a_i \frac{S_{x,i}}{S_{\eta_{cyc}}} \qquad (5\text{-}4)$$

In the equation above, β_i and a_i represent the standardised and ordinary regression coefficients respectively while $S_{x,i}$ and S_y represent the standard deviation of the input variable and the standard deviation of the output respectively. The process of standardization is done to account for the fact that although the regression coefficients are normalized, they may all have different measurement units. This can make analysing the influence of the input variables by comparing their regression coefficients difficult. These standardised regression coefficients are measured in units of standard deviations of the predicted variable per standard deviation of the specific input variable (Siegel, 2016). Their absolute values can be compared, however, to provide a better representation the absolute values are shown as percentages of their summed total in Figure 5-1 for the MLR developed. This representation of the standardised coefficients indicates the influence that each design variable has on cycle efficiency.

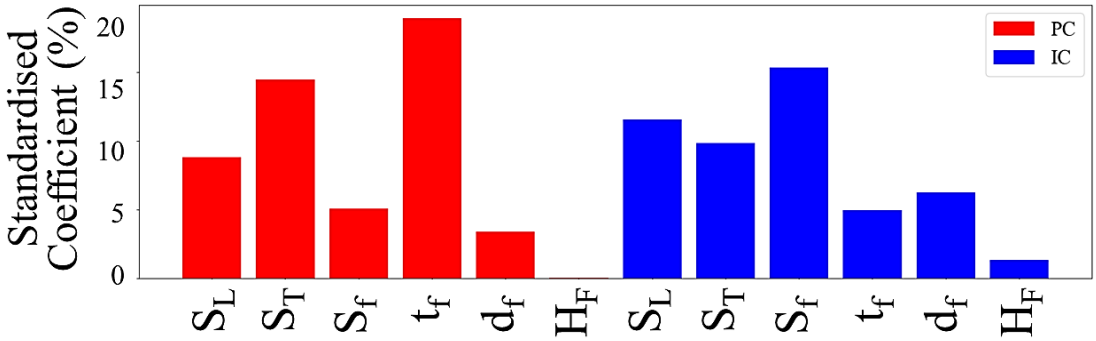

Figure 5-1: Standardised regression coefficients for the air-cooled system design parameters

The results show that the PC longitudinal and transverse tube pitches, and fin thickness influence efficiency the most. PC fin diameter and fin pitch also have an influence but to a lesser extent than the previously

mentioned inputs. On the other hand, the IC longitudinal and transverse tube pitches and fin pitch are shown to have the largest impact on cycle efficiency. The less influential parameters for the IC are the fin thickness and diameter. For both the PC and the IC, the fan height is shown to have very little impact on heat rejection system and cycle performance. However, in reality it will play a more important role in mitigating flow distortions due to crosswinds. Unfortunately this effect could not be accounted for using a 1D thermofluid network model. Similary, for both systems, fin diameter is not as influential despite it having a direct effect on the transfer area. This is likely due to the narrow range of fin diameters considered in the DoE. Collectively, the longitudinal and transverse tube pitches and fin pitches are the most influential and were selected for further investigation, noting that they have a large effect on heat transfer area in the designs. With this in mind, fin thickness was not selected as a key variable because it primarily affects the blockage area and airflow between the tubes.

5.5 Parametric study

Using the MLR model, but fixing the fin thickness, fin diameter, and fan height to that of the best performing design, the influence of transverse and longitudinal tube pitches, and the fin pitches on cycle efficiency was studied parametrically. The effect that these variables have on cycle efficiency is shown in Figure 5-2 for the PC when the design for the IC is fixed as the best performing design, and in Figure 5-3 for the IC when the PC is set to the best performing design. Each plot contains 2 500 input datapoints for each of the three variables. The input data were generated using the *pyDOE* library.

The trends in both the PC and IC indicate that the cycle efficiency increases with a collective increase in the longitudinal tube pitch, decrease in the transverse tube pitch, and decrease in fin pitch. The results show that the best performing designs generally lie within or close to the region of best efficiency. The PC design longitudinal and transverse tube pitches are seemingly within the highest efficiency region. The exception for the PC is the fin pitch of 2.8 mm, Figure 5-2 indicates that values below 2 mm result in the best cycle efficiency. On the other hand, the IC transverse tube pitch and fin pitch are within the region of best efficiency and the longitudinal pitch of 62.7 mm is seemingly too low according to Figure 5-3. Longitudinal pitches upwards of 70 mm are indicated to increase cycle efficiency. According to the plots, smaller fin pitches and larger longitudinal tube pitches may be beneficial in the PC and IC.

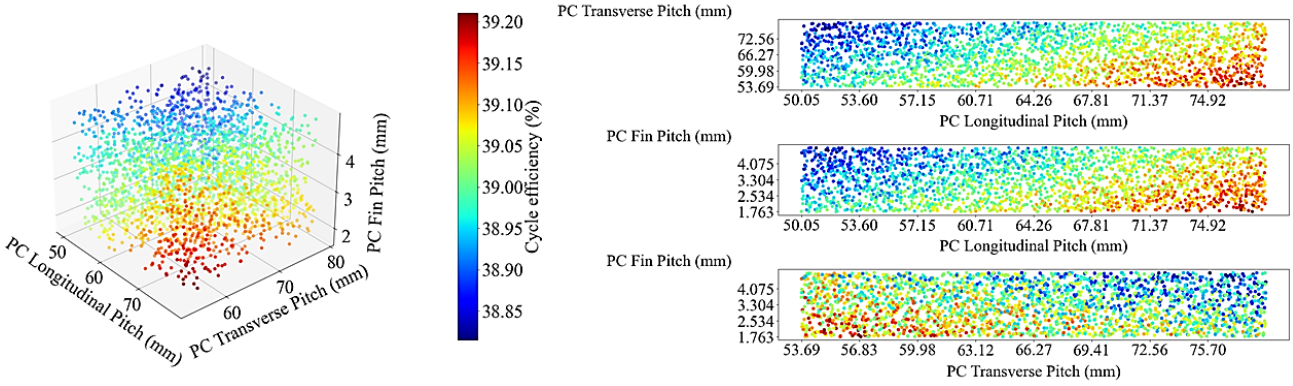

Figure 5-2: Effects of varying PC longitudinal and transverse tube pitches, and fin pitch on cycle efficiency

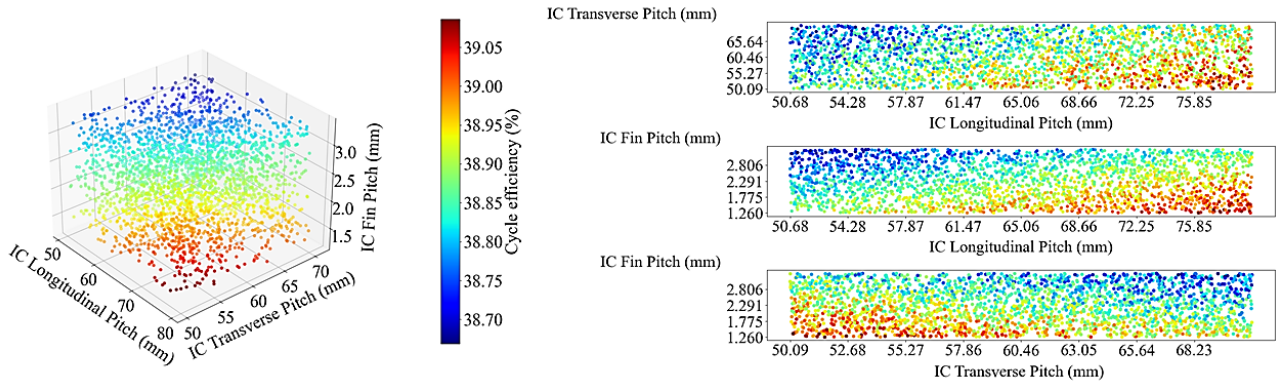

Figure 5-3: Effects of varying IC longitudinal and transverse tube pitches, and fin pitch on cycle efficiency

Another noteworthy trend visible in Figure 5-2 and Figure 5-3 is the decrease in the best performing cycle efficiency from 39.39% to 39.20% when the IC design is fixed and approximately 39.10% when the PC design is fixed.

The parametric studies indicate that the designs could be improved, however, in reality, any change in the PC or IC design will have an impact on the upstream and downstream performance of each cycle component. This, in turn, will impact the cycle performance as a whole. Therefore, any optimisation of the heat rejection system designs should be performed together and with the cycle model. Notwithstanding, perturbance tests were conducted for both cooler designs, where the design parameters investigated above were altered according to the trends visible in Figure 5-2 and Figure 5-3. These trends were selected for perturbing the design parameters because increasing longitudinal tube pitches and decreasing transverse tube pitches is common in both studies. For a PC with a longitudinal tube pitch of 77 mm, transverse tube pitch of 52 mm, and a fin pitch of 2.8 mm, and an IC with a longitudinal tube pitch of 64.5 mm, transverse tube pitch of 51.8 mm, and a fin pitch of 1.6 mm, cycle efficiency increased to 39.41%. These designs and some of the key outputs are shown in Table 5-8 and Table 5-7 respectively. The transverse tube pitch of the IC was increased marginally to account for the fact that it over-cooled the sCO_2 slightly with the increased longitudinal tube pitches, even at the lowest fan speed. Notably, the fin pitches had to remain the same. This is because the best performing design was already near the minimum limit for fan speed of 75 rpm and any decrease in fin pitch and subsequent increase in heat transfer area resulted in over-cooling.

Additionally, it is clear from Eq. (5-1) and Eq. (5-2) that a maximum theoretical efficiency would be achieved if the fan power were set to zero. Furthermore, if the pressure drop on the sCO_2-side of each cooler were zero, i.e., a pressure ratio of 1.0, a higher thermal efficiency and therefore cycle efficiency would be obtained due to a reduction in entropy generation. Setting these values above in the cycle model results in a cycle efficiency of 39.82% which is higher than the efficiency for the perturbed case designs. This highlights the potential for further optimisation of the designs. However, it is worth noting that the thermal efficiency of the cycle model went up from 44.15% in the original (without detailed cooler models) to 44.59% where the detailed cooler models were included. This is a significant improvement and demonstrates the value of including detailed heat rejection models in future works. It should be noted that heat transfer correlation uncertainties were not propagated through the model and therefore, slight deviations from the above conclusions can arise.

5.6 Final design results and analysis

To observe the way in which the PC and IC performance is affected as the design variables from the parametric study vary, several key results were recorded for the best performing designs, seen in Table 5-7. These results are for the final, best performing designs shown in Table 5-8. It is important to note that the heat exchanger mass was not considered when selecting the best performing designs, further discussion on this topic is included in Appendix B. A potential approach not taken in the present work would be to parametrically study the heat exchanger mass and cycle efficiency.

Table 5-7: Key results for the best performing PC and IC designs

Key result	Symbol	Unit	Precooler	Intercooler
Heat Extracted	$\dot{Q}_{cell}$	MW	3.446	4.593
Mass flow rate of air	m_a	kg/s	181.91	181.30
Pressure ratio	PR	-	0.9972	0.9945
sCO_2 tube velocity	v_{tbs}	m/s	3.638	3.188
Auxiliary fan power	$\dot{W}_{aux}$	kW	184.50	230.77
Fan rotational speed	N	rpm	75.03	75.04
Outlet air temperature	$T_{a,ex}$	℃	47.73	54.07
Outlet sCO_2 temperature	$T_{CO2,ex}$	℃	45.0	45.0
Heat exchanger effectiveness	e_{he}	-	0.318	0.174
Heat exchanger conductance	UA	W/K	135 090	256 513

The best performing designs for the PC and IC have many key results in common. m_a, $\dot{W}_{aux}$, and N are all low values. This is expected considering the objective in selecting a best performing design was to mitigate the auxiliary power drawn by the heat rejection systems and thereby increase the adjusted cycle thermal efficiency.

Table 5-8: Final design parameters and values for the PC and IC per cell

Parameter	Symbol	Unit	Precooler	Intercooler
Tube longitudinal pitch	S_L	mm	77.0	64.5
Tube transverse pitch	S_T	mm	52.0	51.8
Fin pitch	S_f	mm	2.8	1.6
Fin thickness	t_f	mm	1.3	1.0
Fin diameter	d_f	mm	42.6	38.3
Mean pass length	L_{pass}	m	8.3	8.3
Transverse rows	N_T	-	161	162
Longitudinal rows	N_L	-	8	10
Tube passes	n_{passes}	-	4	10
Cooling cells (total)	N_{cells}	-	8	10
Fan height	H_F	m	21.0	21.0
Fan diameter	d_F	m	7.925	7.925

The PC does consume less $\dot{W}_{aux}$ than the IC but this is primarily due to it having less cells. The number of cooling cells is a design parameter that will significantly alter the performance of the design and therefore reducing it in the IC is not an option. Changing the number of cells in either system would require redesigning the entire system itself. The pressure ratios are also very high in both coolers, which is line with the goal of

increasing cycle thermal efficiency. High pressure ratios across the coolers decreases the power required by the compressors and will reduce entropy generation.

The outlet air temperatures are also high although this can likely be attributed to the fact that the ambient air temperature is also high (28.9 ℃). However, relatively high values for $T_{a,ex}$ have been found to be beneficial in the designs because they raise the Δp_{amb} across the system and reduce the pressure recovery required by the fan. Higher $T_{a,ex}$ values are a result of increased heat transfer area and heat rejection which can be improved directly by changing the heat exchanger geometry as described in Section 5.5. It must be noted that high values for $T_{a,ex}$ may impact the lifespan and integrity of the fins and tubes in the passes of the heat exchanger. However, the tubes have been designed with a large safety factor of 3.82 and EN P235GH carbon steel can handle temperatures up to 300 ℃. Fortunately, because the systems are designed as forced draft air-cooled heat exchangers, these high temperatures will not impact the fan as much as if the designs used induced draft air-cooled systems.

In terms of heat exchanger effectives, e_{he}, the PC has a noticeably higher value than the IC. This is likely due to the higher C_{min} across the IC passes and the fact that it has more passes, the increased C_{min} is a result of the operating pressure of the IC which leads to higher c_p values for sCO_2. The properties for this pressure can be seen in Figure 6-4 for the *CoolProp* 6.4.1. library. Finally, the UA in the IC is noticeably higher than the PC, this is a result of a reduced LMTD and an increased heat rejection rate in the IC.

To summarise, a DoE was performed to generate potential PC and IC designs, these designs were then filtered to find those that achieved a required pressure drop and heat extraction. This left many valid designs which were further filtered according to their auxiliary power requirements. The remaining valid designs were then coupled to the RCICRH cycle model and the design with the highest cycle efficiency was selected. Based on the discrete design parameters for the best performing PC and IC design combination, a MLR model which predicts cycle efficiency based on the design parameters for the heat exchangers was trained and tested using DoE datapoints. The MLR model was then used to perform parametric studies with the aim of identifying key variables and finding trends which would assist in improving the designs. Based on the parametric plots produced, the original designs were perturbed, despite the fact that in reality this would affect the upstream and downstream cycle components and subsequently the cycle performance. The perturbed PC and IC designs were then analysed and compared, with regards to key performance indicators and mass, to other potential designs The final PC and IC designs were then selected using the perturbed geometry. These designs and some of their key performance indicators and the final design specifications are shown in Table 5-6 and Table 5-8 respectively. These performance indicators and several other steady-state outputs were later compared with the results of the advanced 1D thermofluid network models and sample calculations for verification purposes.

6. Flownex ® SE models

This section presents the development of the Flownex® SE models for the final PC and IC designs. These models allow for increased model discretisation, quicker and easier modelling of the entire heat rejection system (all cells) and will serve as the platform for future dynamic studies.

Because both the Python models encompass only a single cell with the entire system's performance extrapolated assuming each cell operates the same, it was first necessary to develop a single cell model for both coolers in Flownex® SE 2019. This allows for the verification of the Flownex model. It is important to note that these single cell models were developed using the same pass-by-pass discretisation present in the Python models.

6.1 Application of the Flownex ® SE software

The Flownex ® SE software is a 1D thermohydraulic network solver which allows for both steady-state and transient conditions to be easily modelled and visualised. While the software does provide a built-in component for a heat exchanger, the present work required the creation of a thermohydraulic network using the basic components adopted for use when modelling heat transfer and fluid flow problems in Flownex ® SE. These components are shown in Figure 6-1.

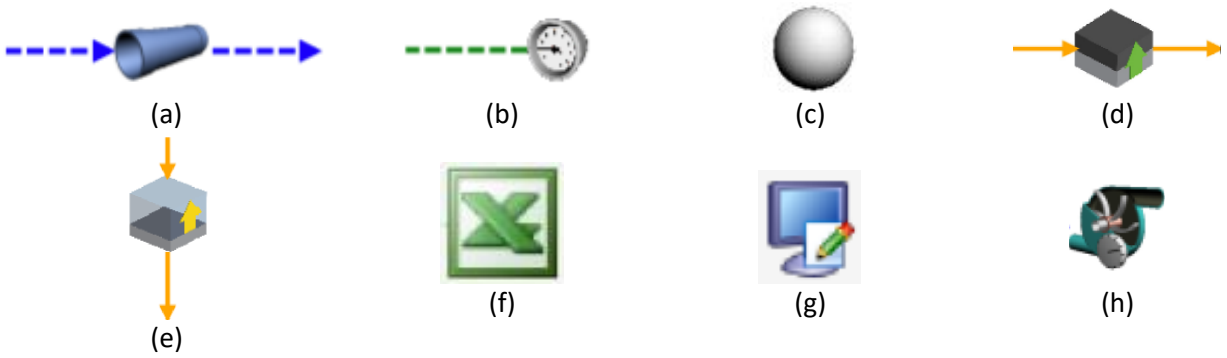

Figure 6-1: Flownex ® SE components (a) pipe, (b) boundary condition, (c) connecting node, (d), conduction heat transfer component, (e) convection heat transfer component, (f) Excel sheet, (g) calculation script, and (h) fan

The components from Flownex ® SE above have been represented as seen in Figure 6-2 for the sake of displaying the network model neatly and as simply as possible. These symbols are further used when visualising the Flownex ® SE models in Figure 6-5 and Figure 6-6 It is important to note that elements such as the upstream and downstream pressure losses on the air-side are incorporated using pipe control volumes with a set pressure loss factor. The fan has also been represented in Figure 6-6 as a control volume to simplify the diagram.

Pipe elements are used in the software to model fluid flow through pipes or ducting and, in the case of the air-side, through a bank of finned tubes. The component can have a constant or variable cross-sectional area and can have steady or transient flow in the form of gas, liquid, or a two-phase fluid. The boundary condition components must be attached to a node within the thermohydraulic network and will specify the boundary condition at that node. Conditions can be temperature, pressure, enthalpy, mass flow rate, and (in the case of two-phase flow) quality. Nodes are used to connect elements and components and can represent the inner

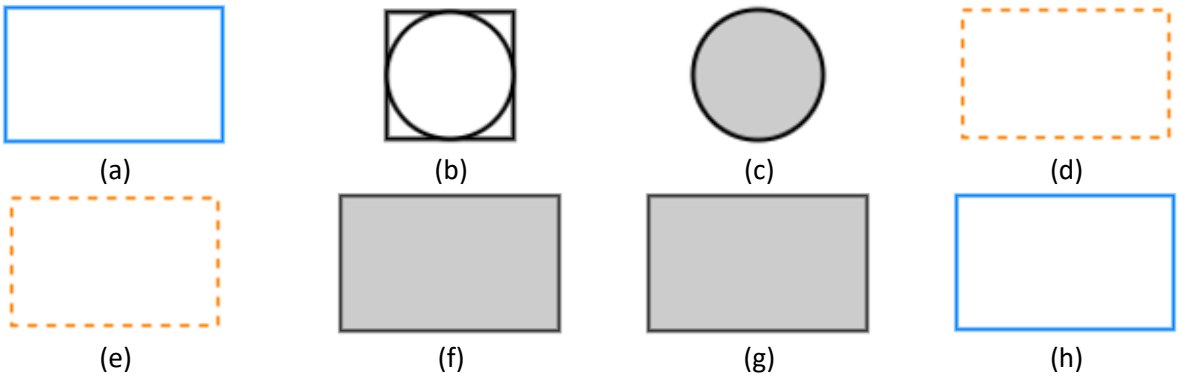

Figure 6-2: Representative components (a) pipe, (b) boundary condition, (c) connecting node, (d), conduction heat transfer component, (e) convection heat transfer component, (f) Excel sheet, (g) calculation script, and (h) fan

and outer tube wall in the case of a conduction heat transfer component. The two heat transfer components, (d) and (e) in Figure 6-1 are for conduction and convection respectively. These components can be connected to nodes or to control volumes (pipes) as is the case in the present work. Heat transfer, thermal inertia and thermal resistance are all incorporated with a linear temperature distribution assumed between elements in a solid (conduction component). The convective heat transfer components take a constant heat transfer coefficient and heat transfer area as inputs. These two values are calculated using script components, (g) in Figure 6-1, for the heat transfer coefficient and an Excel sheet, (f) in Figure 6-1. Script components allow for multiple fluid properties and variables to be used as inputs by transferring data from other components such as nodes, pipes, and Excel sheets. Scripting in Flownex ® SE is done using the C# programming language. Script components can return multiple outputs which are then transferred to other components in the network. Scripts have been used for the heat transfer and air-side pressure drop calculations in this project. The fan component is actually a variable speed pump in Flownex ® SE. It requires that a static pressure curve be defined across a range of mass flow rates. These components also require a rotational speed is set along with an electrical efficiency.

6.2 Governing equations

The modelling methodology in this work uses interconnected 1D control volumes for sCO_2 and air which are solved for the mass, momentum, and energy balance equations. The Flownex ® SE components from Section 6.1 are used to generate the network. For the single cell models, and subsequently any given cell throughout the entire PC or IC, the interconnected control volumes are pipe elements, (a) from Figure 6-1. Each air and sCO_2 control volume, or heat exchanger pass in the single cell model, are connected via heat transfer components and links as discussed further down below in Section 6.3.

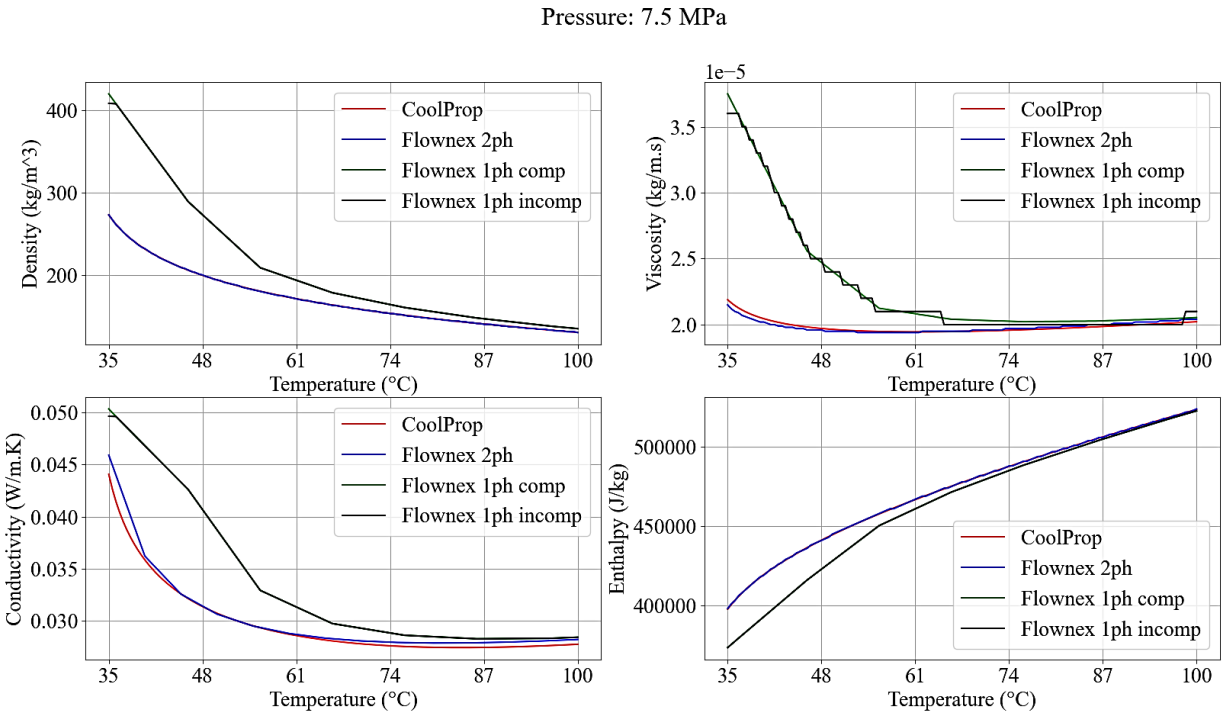

Figure 6-3: Fluid property comparison for sCO_2 at 7.5 MPa in Flownex® SE versus CoolProp

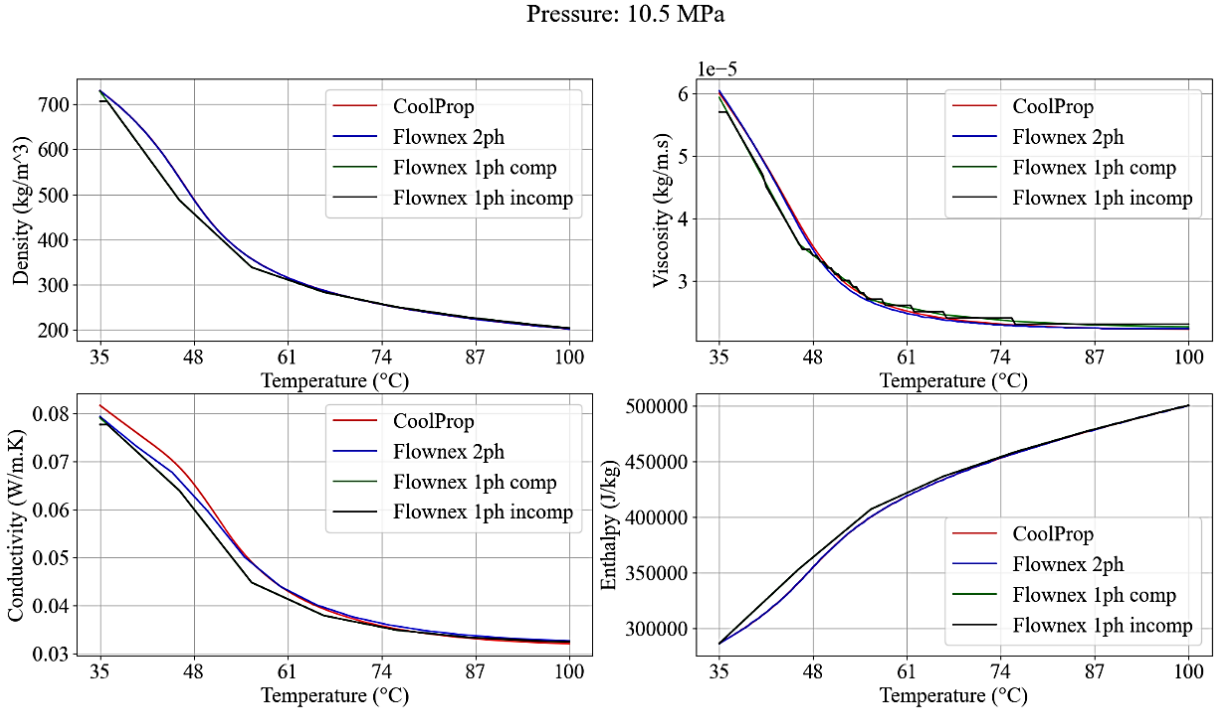

Figure 6-4 Fluid property comparison for sCO_2 at 10.5 MPa in Flownex® SE versus CoolProp

Flownex® SE 2019 has many built-in fluid property libraries and models. Given that CO_2 in the supercritical state is neither a liquid nor a gas, the appropriate CO_2 library and model combination needed to be determined. Therefore, a comparison of the most appropriate combinations (compressible pure gas, incompressible pure gas, and two-phase homogenous mixture) in the software was deemed necessary because fluid properties closely matching *CoolProp* were desired. The comparison is shown in Figure 6-3 and

Figure 6-4, which examines the changes in specific properties across a range of temperatures for the approximate operating pressures of both coolers. Based on the results, it was decided that the two-phase homogenous fluid would be used for sCO_2-side flow since the results best matches the properties from *CoolProp*. There is, however, still some discrepancy between the two for thermal conductivity. This is important to note as it may impact the heat rejection rate results in the single cell and entire cooler models. Note that a transient analysis has not been performed in this work. The steady-state governing equations, solved by Flownex® SE, are as follows below with fluid properties, velocities and flow rates calculated at control volume centres.

Mass conservation:

$$0 = \rho_{in} v_{in} A_{in} - \rho_{ex} v_{ex} A_{ex} = \dot{m}_{\mathrm{in}} - \dot{m}_{\mathrm{ex}} \tag{6-1}$$

Momentum conservation:

$$p_{0,in} - p_{0,ex} = \frac{\rho^2 v^2 A^2 (\rho_{in} - \rho_{ex})}{2\rho_{in}\rho_{ex}A_{in}A_{ex}} + \frac{\tau_w d_e L}{A} + \rho g (z_{ex} - z_{in}) \tag{6-2}$$

where p_o denotes the pseudo total pressure found using Eq. (6-3), which is a function of the static pressure, p. τ_w is the wall shear stress, which is a function of the Reynolds number and a two-phase friction multiplier. The Reynolds number is calculated as per Eq. (C-4), and d_e and L represent the wetted perimeter and distance in the flow direction which the working fluid travels. It is also important to note that elevations (z) have been ignored in the model.

$$p_0 = p + \frac{1}{2}\rho v^2 \tag{6-3}$$

Energy conservation:

$$\dot{m}_{ex}\left(H_{0,ex} + g z_{ex}\right) - \dot{m}_{in}\left(H_{0,in} + g z_{in}\right) = \dot{Q} \tag{6-4}$$

where H_0 is defined as the total enthalpy by Eq. (6-5):

$$H_0 = H + \frac{1}{2}v^2 \tag{6-5}$$

6.3 Heat Transfer

The advanced thermofluid model accounts for sCO_2-side forced convection within the tubes, conduction through the tube walls, and external forced convection on the external air-side. Fouling and radiative effects have been considered negligible. Figure 6-5 shows the discretisation and setup for one pass in the single cell models. The thermal resistance network of heat transfer components connects the sCO_2-side to the air-side using heat transfer links which lead from the internal sCO_2 control volume to a node representative of the internal tube wall. From there, the heat travels by means of a conduction heat transfer component from the internal wall to another node which is the external wall and then on to the external air control volume.

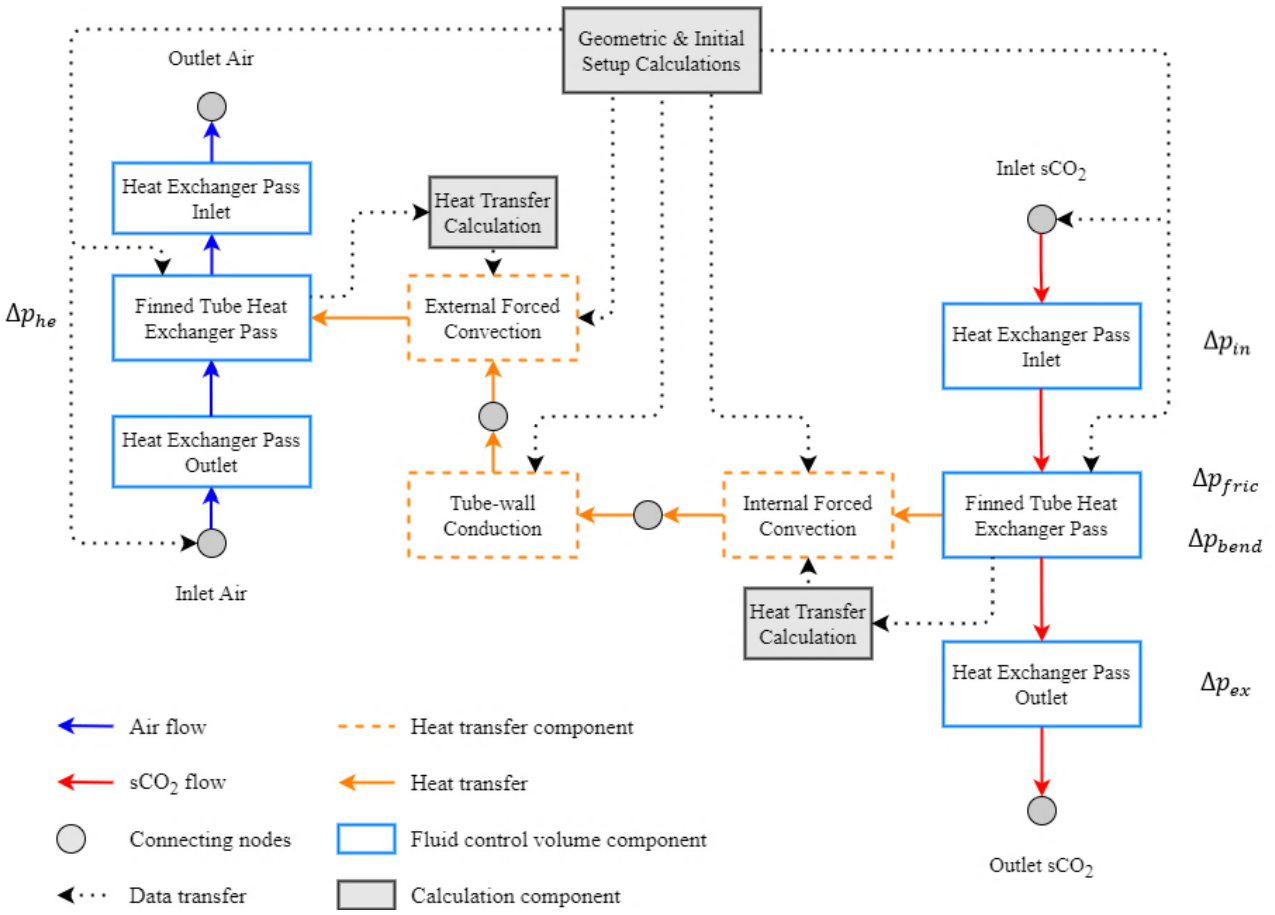

Figure 6-5: Advanced thermofluid model heat exchanger pass

The various heat transfer components are collectively used to calculate the overall heat transfer coefficient as per Eq. (4-32) with the heat transfer coefficients determined using the correlations seen in Section 4.7 and for the entire length of one pass. These calculations and correlations are included using Flownex ® SE scripts which take the mean fluid properties of the sCO_2 or air control volume as inputs and then transfer the calculated heat transfer coefficient to the relevant component. The convection and conduction heat transfer areas and lengths are set in the model using an embedded Excel workbook which transfers all the information to the relevant components prior to each steady-state simulation. These geometric values are found using the methodology from Section 4. Furthermore, the conductivity of the fins and tubes is set in this model to match the value of 58 W/m.K used in the Python model, the same process is followed for the various other tube material properties. The overall heat transfer coefficient, UA, for the heat exchanger pass is then used in conjunction with the mean sCO_2 and air temperatures to find the heat transfer rate.

$$\dot{Q} = UA\left(T_{CO2,m} - T_{a,m}\right) \tag{6-6}$$

The respective inner and outer wall temperatures $T_{w,int/ext}$ are solved for based on the heat transfer rate, mass flow rate, $\dot{m}$, isobaric specific heat, C_p, and the inlet static temperatures, T_i, of both sCO_2 and air respectively. This is shown in Eq. (6-7) – Eq. (6-9) which are specific forms of the e-NTU method utilised in Flownex ® SE.

$$\dot{Q} = \dot{m}C_p\left(1 - \exp\left(-\frac{UA}{\dot{m}C_p}\right)\right)\left(T_{w,\frac{int}{ext}} - T_i\right) \; for \; C = 0 \qquad (6\text{-}7)$$

$$\dot{Q} = \dot{m}C_p\left(1 - \exp\left[\frac{\left(\frac{UA}{\dot{m}C_p}\right)^{0.22}\left\{\exp\left(-C\left(\frac{UA}{\dot{m}C_p}\right)^{0.78}\right) - 1\right\}}{C}\right]\right)\left(T_{w,\frac{int}{ext}} - T_i\right) \qquad (6\text{-}8)$$

$$with \; both \; fluid \; streams \; unmixed$$

$$\dot{Q} = \dot{m}C_p\left(\frac{1}{1 - \exp\left(-\frac{UA}{\dot{m}C_p}\right)} + \frac{C}{1 - \exp\left(-\frac{UA}{\dot{m}C_p}C\right)} - \frac{1}{\frac{UA}{\dot{m}C_p}}\right)\left(T_{w,\frac{int}{ext}} - T_i\right) \qquad (6\text{-}9)$$

$$with \; both \; fluid \; streams \; mixed$$

6.4 sCO_2-side modelling

The sCO_2-side flow path is modelled and discretised for the single cell models as seen in Figure 6-5, using multiple interconnected 1D control volumes with several pressure drop characteristics incorporated from the distribution headers to the outlet of the heat exchanger tubes. The pressure drop in the sCO_2 distribution headers is included in the single cell models using a secondary loss factor and header diameter as detailed in Section 4.8. The advanced model also incorporates an inlet contraction pressure loss using K_{in} from Eq. (4-47). In the model, all discrete passes, excluding the last experience frictional pressure drops along the length of the pass and through the bends before the next pass. Note that a secondary loss factor of 0.18 has also been maintained for the bends. The last pass experiences only frictional pressure drops along its length and an expansion loss at the outlet, which was assumed to be a value of 1. Flownex® SE calculates pressure drops due to friction using the equations below (Flownex, 2020b):

$$\Delta p_{fric} = \left(\frac{f_D L}{d}\right) \times \frac{\rho|v|v}{2} \qquad (6\text{-}10)$$

$$f_D = \begin{cases} \dfrac{0.25}{\left(\log\left[\frac{\epsilon_{tbs}}{3.7d} + \frac{5.74}{Re^{0.9}}\right]\right)^2} & if \; 5000 \leq Re \leq 10^8 \\ \dfrac{64}{Re} & if \; Re < 2300 \end{cases} \qquad (6\text{-}11)$$

where the tube roughness, ϵ_{tbs}, was set in the models according to Table 4-2 and linear interpolation for f_D is carried out for transitional flow, $2300 < Re < 5000$.

6.5 Air-side modelling

The MALR of 0.004437 K/m was used to balance the change in air pressure with increased elevation with the pressure drops as air flowed over the heat exchanger tubes and obstacles throughout the air-cooled cell and

the pressure rise experienced across the fan. The outlet air pressure boundary condition was found by subtracting the ambient pressure drop calculated in Eq. (4-51) from the ambient pressure of 92 064.3448 Pa as shown in Eq. (6-12).

$$p_{a,ex} = p_{a1} - \Delta p_{amb} \tag{6-12}$$

The required heights of heat exchanger components were calculated prior to each steady-state simulation before being set in the model. The air-side was also modelled using interconnected 1D control volumes in series. These control volumes were comprised of flow conduits and secondary loss factors, which can be seen in Table 6-1. The pressure losses through the heat exchanger tubes and due to the velocity distribution at the outlet were incorporated using K_{he} and α_{e6}. These values were found using the method shown in Section 4.9, then summed and divided equally between the flow conduit control volumes in the model. The detailed draft equation, which balances the air-side momentum can be seen in Eq. (4-58). This equation calculates a mass flow rate of air which will balance the air-side pressure drops and the pressure rise across the axial fan with the ambient pressure rise on the left-hand side of the equation.

Table 6-1: Air-side secondary loss coefficients per cell

Secondary Loss Factor	**Precooler**	**Intercooler**
K_{ts}	1.92	2.88
K_{up}	3.62	3.62
K_{do}	1.69	1.69
K_{Fsi}	0.0	0.0
K_{rec}	0.0	0.0

K_{ts} is higher for the IC because it has more cells than the PC for the best performing designs. A heat rejection system with 8 cells can be supported by two large concrete support columns, however, systems with between 8 and 12 cells will require three. Because K_{ts} is directly proportional to and a function of the number of tower supports, it increases in the IC. Both K_{do} and K_{up} were calculated using the polynomial curves in the Python model and set in Flownex® SE. Additionally, because the fan geometry and height is consistent in the best performing PC and IC designs, these loss factors are unchanged between the systems' cells. The fans were modelled using variable speed pumps with the static pressure rise fan curves extracted and scaled from Augustyn (2013) specified. The rotational speed was set at the values for the best performing designs and an electrical efficiency of 90% was set. The fans in the model also incorporated density scaling based on the test density of 1.2 kg/m^3.

6.6 Heat rejection cell setup

The general layout for an air-cooled cell in either the PC or IC is shown in Figure 6-6. The complete heat transfer and sCO_2-side pressure drops are captured within each "pass" component shown in Figure 6-5 and these components connect directly to the air-side by linking the inlets and outlets of the air-side in each pass. The heat transfer components are set up and calculated as per Figure 6-5. The boundary conditions and inlet conditions can be seen in Figure 6-7 below. The single cell models assume an even distribution of sCO_2 between the cells (49.0125 kg/s for the PC and 39.21 kg/s for the IC), this is the boundary condition defined at the outlet of the sCO_2-side. The mass flow rate of air is solved for as described in the previous section, while the ambient air inlet conditions are as per Section 4.9 and the sCO_2 inlet conditions are taken from the RCICRH cycle model.

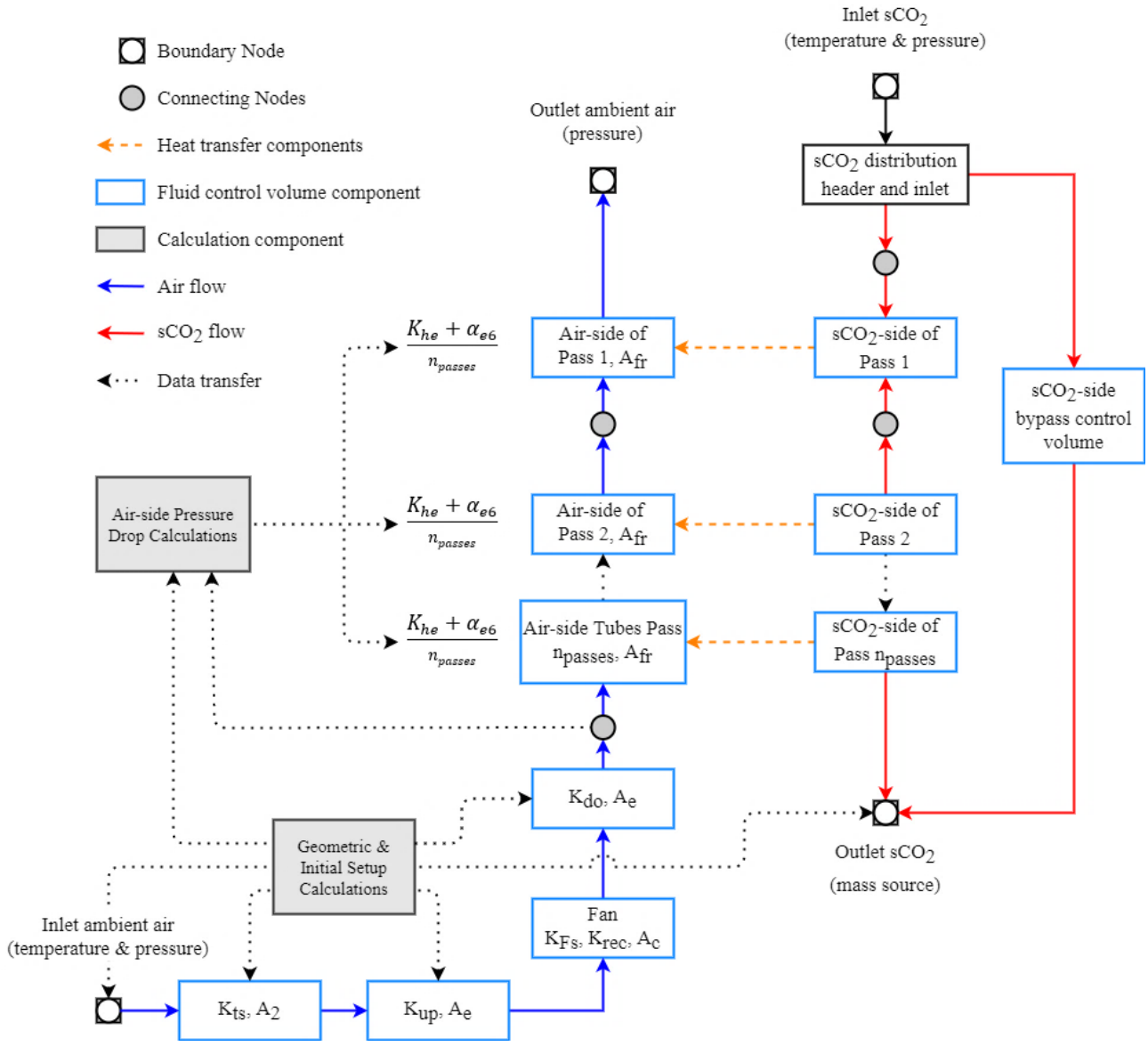

Figure 6-6: Air-cooled single cell layout

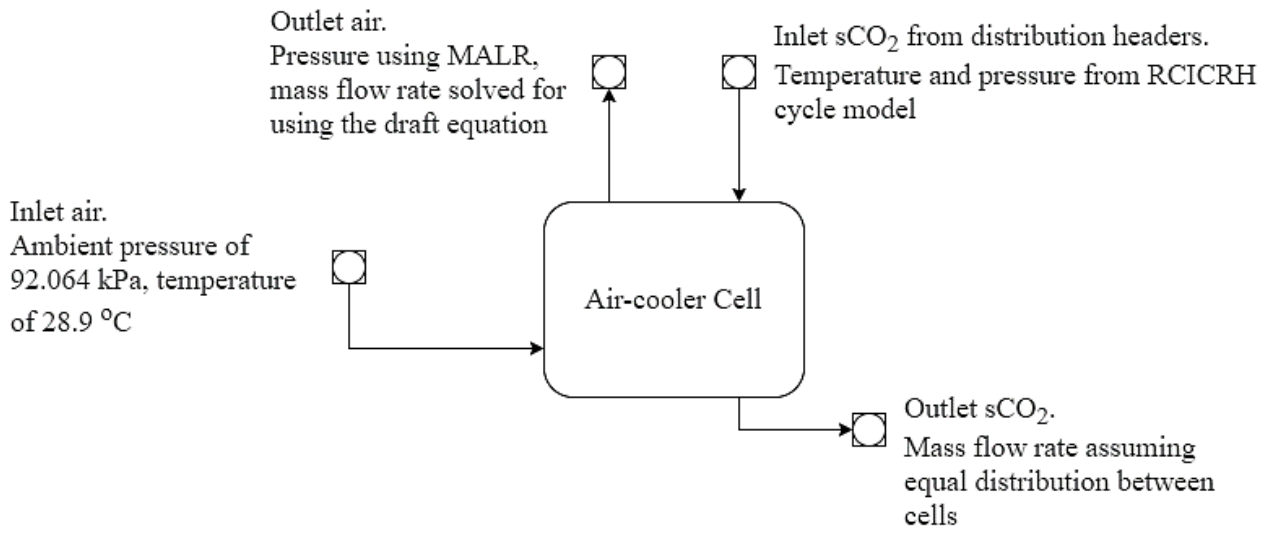

Figure 6-7: Air-cooled cell inputs, outputs, and boundary conditions

With control studies in mind, an additional control volume was included in the single cell models. This is the sCO_2 control volume labelled as a bypass in Figure 6-6. The pipe component in Flownex ® SE was configured to have a fixed mass flow rate. The sCO_2 control volume in the models acts as a 'bypass valve' to counteract the effects of overcooling and connects the inlet of each cell directly to the outlet. Under design conditions, i.e., no bypassing, the fixed mass flow rate for the control volume is 0 kg/s. The bypass valve was essential when controlling the outlet sCO_2 temperature at low ambient air temperatures. However, it was not sized as a pipe with a diameter, length, and wall thickness because only an observation of the basic effect of a bypass valve was desired in this work.

6.7 Solver setup and methodology

The Flownex® SE software uses an implicit pressure correction (IPC) solution algorithm which allows for rapid and accurate simulations. This IPC method was used to solve for the steady-state solutions of the single cell models in this work. The methodology is shown in Figure 6-8 and works by guessing initial node pressures, solving the mass flows using the relationship between pressure drop and flow rate. The node pressures are adjusted until there is convergence for continuity, following this, the energy equation is solved. If there is

Table 6-2: Flownex® SE solver relaxation parameters

Relaxation parameter	**Value**
Pressure	0.7
Density	1.0
Mass	1.0
Temperature solver	0.985
Two-phase density	0.985
Two-phase convection coefficient	0.3
Junction losses	0.1

convergence at this point, a solution has been reached, if there isn't convergence, the solver repeats the preceding steps until there is. Another noteworthy aspect of the software's solver are the values it uses for gravity (g) and the universal gas constant (R_0). These are set to 9.806 m/s^2 and 8.3145 J/mol.K respectively and cannot be changed. In this work, the relaxation parameters in Flownex® SE were set as shown in Table 6-2. The fractional convergence criteria for pressure, temperature, and continuity were set to 1×10^{-4}.

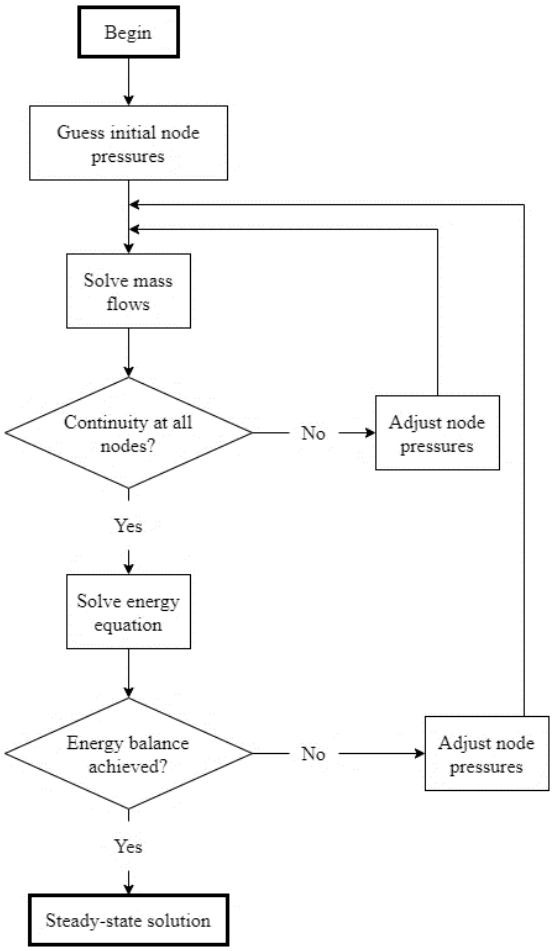

Figure 6-8: Flownex® SE solver architecture using the IPC method (Flownex, 2020c)

The single cell models for both coolers were set up and solved as described above, using the methodology detailed previously in this section. The single cell models were further used in two different ways: (i) to perform a second verification of the results of the Python model; and (ii) as a benchmark for increasingly discretised single cell models.

6.8 Model discretisation

To account for the variation in sCO2 fluid properties across the range of the PC and IC design temperatures and pressures it was decided to further discretise each heat exchanger pass. The increased number of control volumes within each pass would account for heat transfer and pressure drops more accurately. There are two methods to achieve finer discretisation within the single cell models. The first approach, seen in Figure 6-9, involved matching sCO_2 control volumes with their own respective air control volumes for however many discrete control volumes. For example, if there were four sCO_2 control volumes per pass then there would be four accompanying air control volumes. The second approach, shown in Figure 6-10, involved discretising

the sCO_2-side but having each sCO_2 control volume linked to a single air control volume for each pass. It is important to note that the model was simplified slightly by excluding the fans and ignoring the air-side modelling outside of the heat exchanger. This was done to streamline this process and means that each single cell model has a set mass flow rate of air equal to the value from the best performing designs in Python. For the PC this value is 181.912 kg/s and for the IC it is 180.300 kg/s.

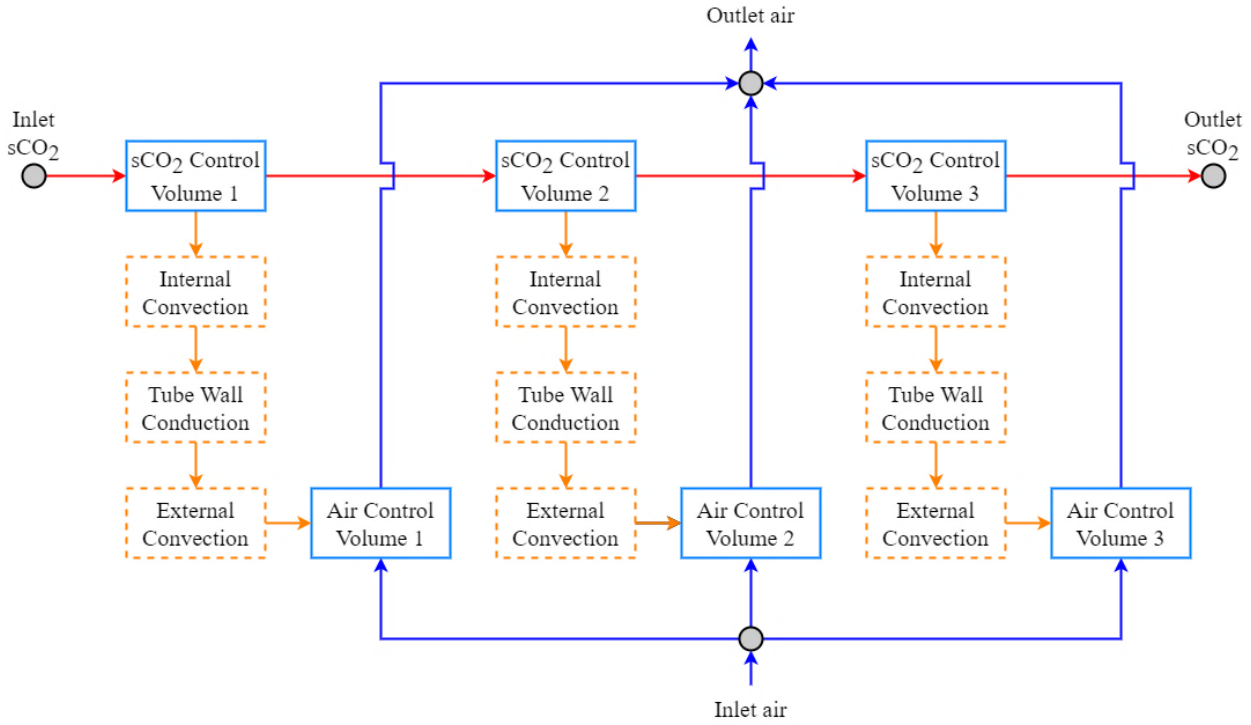

Figure 6-9: Discretisation setup for a single pass with 3 increments using the matching air-sCO_2 control volume approach

The objective of this process was to decide on which approach to use and what level of discretisation was adequate for the models. With this in mind, several discretisation schemes of varying fineness were implemented in the models using both the approaches above. The different schemes tested were as follows: (i) coarse (3 increments); (ii) medium-coarse (4 increments); medium (5 increments); and fine (10 increments). The overall heat rejection rates per cell were recorded along with the steady-state solution time for each case, Plots of these results are shown in Appendix A for both the PC and the IC modelled using the discretisation approaches outlined here. The grid independence study was conducted for the heat rejection rates and control volume length. Linear trendlines were fitted for each approach and cooler to determine the effective 'zero spacing' heat rejection rate. This allowed for the absolute errors on these 'zero spacing' values to be calculated and compared. Furthermore, the ease of implementation was strongly considered when comparing the two discretisation approaches and the fineness of the scheme.

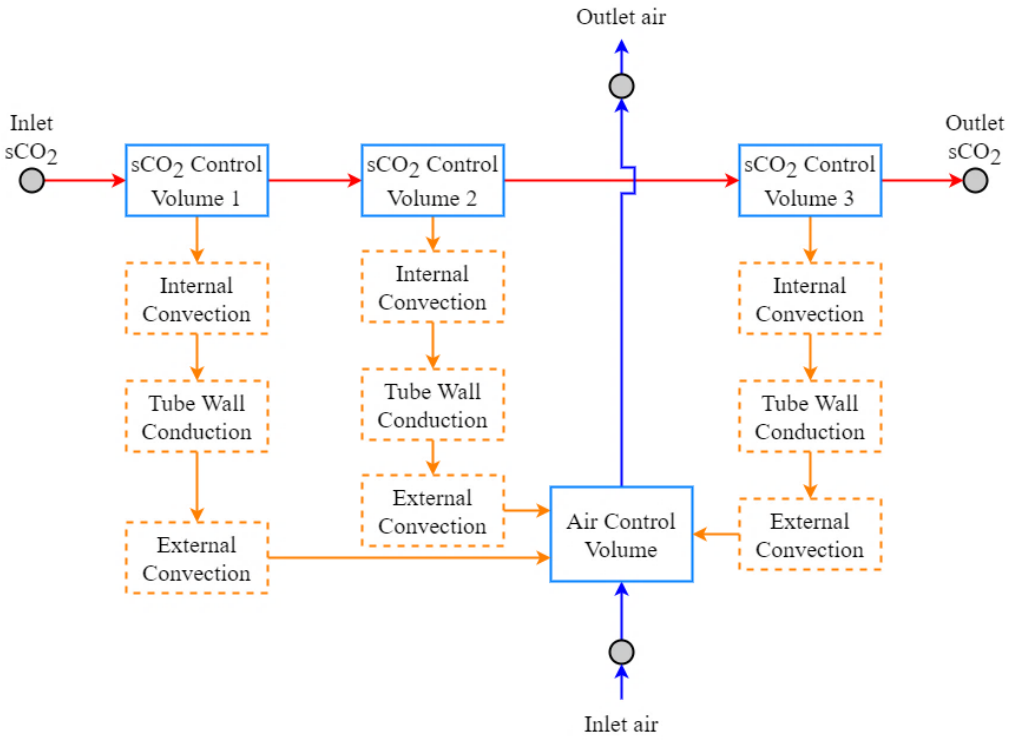

Figure 6-10: Discretisation setup for a single pass with 3 increments using the single air control volume approach

Following the grid independence study, the appropriate control volume length was 2.075 m (4 control volumes per pass) which limits the error to less than 0.4% on the 'zero spacing' heat rejection rate for both the PC and IC. The discretisation scheme adopted was the single air control volume approach. This is because it is easier to implement and there are no notable differences between the approaches from a solution time and heat rejection perspective. This is evident in the difference between single air and matching 2.075 m control volumes' heat rejection rates are 1.466% and 1.174% for the PC and IC respectively. These errors were deemed acceptable. Therefore, all single cell models used to develop the entire heat rejection system models for the PC and IC are discretised to have four sCO_2 control volumes and one air control volume per pass.

6.9 Multiple cell system models

Based on the findings of the studies performed on cooling cell layouts (Yang et al., 2012; Kong et al., 2017; Engelbrecht et al., 2020), this work will use a conventional configuration shown in Figure 6-11, where the cooling cells are indexed first by their street and then number within that street. This indexing convention has been used to display the results seen in the sections below. The PC with 8 cells, has 2 streets with 4 cells per street and the IC has 2 streets with 5 cells per street. Note that this was the reasoning behind having even numbers of cells for designs from the DoE. Furthermore, cell configurations with 12 or more cells can be arranged to mitigate the number of edge cells, for example, 3 streets with 4 cells per street.

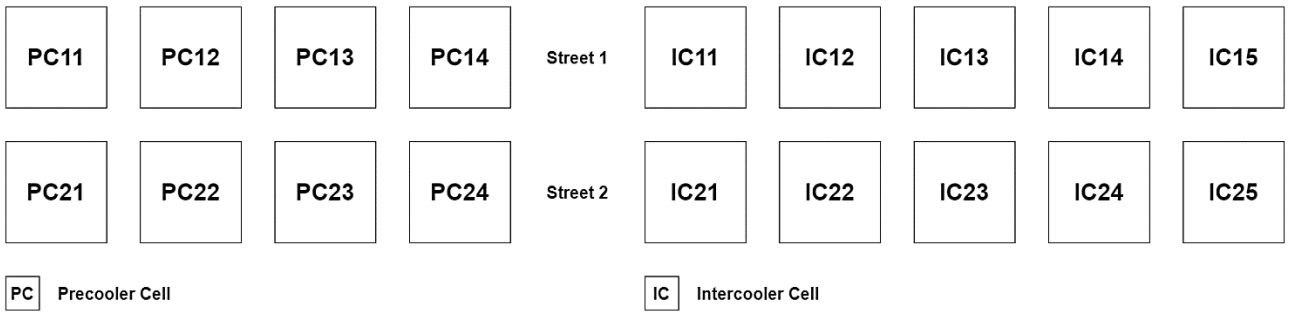

Figure 6-11: Heat rejection cell layouts for the PC and IC system models

Ideally, this type of cell layout would be aligned such that the prevailing wind is incident on the narrow side of the rectangle. This strategy would serve to mitigate the effects of wind on the inlet flow to the fans. Recirculation effects cannot be counteracted by rearranging the cells, this is because significantly less coolers are required in sCO_2 power plants than in Rankine power plants. As a result, all the cells in both heat rejection systems are edge cells. This also makes the trapezoidal array an unlikely candidate for implementation. Additionally, the circular arrangement performs worse than the conventional when the flow is aligned as stated above and it too requires more cooling cells than would be available in a sCO_2 plant to function properly.

The cell configurations as shown in Figure 6-11 were created in the Flownex® SE software, sCO_2 is distributed to each cell in each street via headers constructed from EN P235GH carbon steel. The total mass flow rate of sCO_2 is divided between the two streets by two 20 m long entry headers and each entry header is followed by a series of 8.3 m long headers which supply the cells. All the headers were included in the models as sCO_2-side control volumes with specified lengths, diameters, and tube material properties. Note that the header sCO_2 side pressure drop characteristics, previously included using a secondary loss factor are now found according to the frictional pressure drop along these fully-defined control volumes. The final geometric parameters of the headers in the PC & IC are shown Appendix D in Table D-6 and Table D-11 respectively.

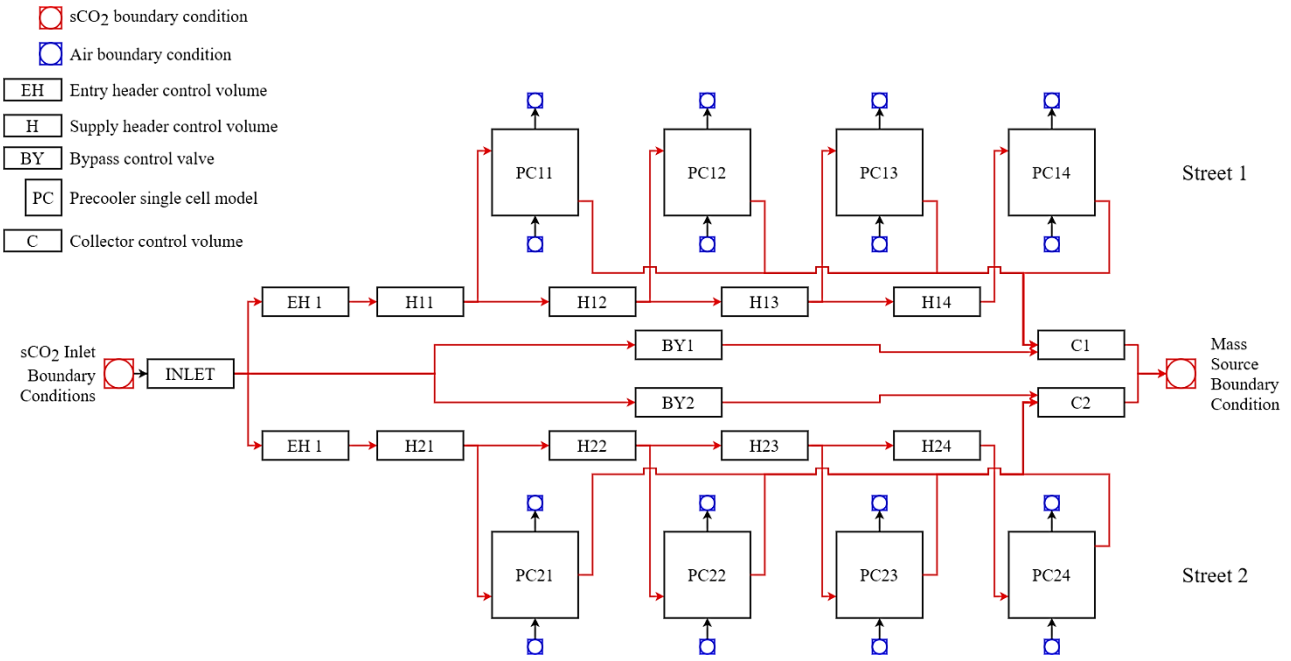

Figure 6-12: Entire system model schematic for the PC

Prior to the inclusion of headers, a secondary loss was incorporated to approximately account for any pressure drops that may occur as the sCO_2 travels from the upstream cycle component to either the PC or the IC. Multiple single cell models have been used in the entire system models, each supplied by a header, and the exiting sCO_2 flow is merged by connecting each cell's outlet to collector control volumes assuming that no further pressure drops occur. A basic schematic of the network for the PC is shown in Figure 6-12, the IC has the same setup with one additional cell per street.

Note that each single cell model within the entire system model is setup according to the methodology and discretisation scheme as in Section 6.1 – Section 6.8. The only exceptions are the bypass control volumes which are per street and not per cell in this model. Each cell does include a bypass valve which may be used for even finer and more flexible control of the system but for the relevant studies in Section 7 a bypass per street approach was used. This is because it reduces the number of mass flow rates which need to be controlled and subsequently solved for to achieve the target sCO_2 oulet temperature. The other major difference is that the sCO_2 is being distributed to multiple of these single cell models by actual headers with the boundary conditions set at the system inlet and outlet and not each individual cell's inlet and outlet. The detailed sizing of these headers is shown in Appendix D.

7. Off-design studies

This chapter was split into five distinct sections, the first outlines the verification of the models with the sample calculations and Python models. The second, third, and fourth sections detail the varying ambient air temperature studies, where a sensitivity analysis on multiple air-cooled system performance parameters was carried out across a range of ambient temperatures. These studies also involve the introduction of controls used to achieve the correct outlet sCO_2 temperature for both the PC and IC when overcooling occurs. The control methods involve bypassing cells on the sCO_2-side, turning off fans, and a combination of these two. Finally, an annual analysis of each heat rejection system's key performance indicators was carried out using real-life weather data spanning the last 28 years.

7.1 Model verification

The Python single cell models were verified using sample calculations and the results shown in Section 5.1. The Flownex ® SE single cell models are now verified using the Python models as a benchmark. The aim of this process was to check for agreement between the models and verify the precision of the thermofluid modelling methodology used. Comparison of several key design results showed relatively good agreement between the calculation methods, note that fan static pressure rise, and heat exchanger pressure loss have been included because they were found to be important results in the initial Python model analysis. The Flownex® SE model results differ from the Python models, as can be seen in Table 7-1 and Table 7-2 below which show the relative errors between the calculation methods. However, these errors were deemed acceptable for this level of study. A detailed discussion of the variations between the results of both models is included below as well.

Table 7-1: PC Flownex ® SE model verification to the Python single cell model results

Parameter	Unit	Python Model Result	Flownex® SE Model Result	Relative Error on Python Model
Heat transfer per cell	MW	3.446323	3.344963	2.941%
Pressure ratio	-	0.9972	0.9971	0.010%
Mass flow rate of air	kg/s	181.912	176.027	3.235%
Total fan power consumption	kW	184.5	168.472	8.687%
Outlet air temperature	℃	47.728	47.870	0.298%
Outlet sCO_2 temperature	℃	45.0	45.815	1.811%
Fan static pressure rise	Pa	63.003	63.203	0.317%
Heat exchanger pressure drop*	Pa	18.374	15.168	17.449%

*Includes pressure loss due to velocity distribution in the heat exchanger

Some of the variations in results are because some the properties of sCO_2 were shown to be different in the software when compared to the *CoolProp* library used in Python. The differences may also be a result of the IPC solution algorithm employed by Flownex® SE to solve the thermofluid network. This solver method differs from the Python models' solver architecture as it first solves the pressures at the nodes and mass flow rates then balances the energy equations.

Table 7-2: IC Flownex ® SE model verification to the Python single cell model results

Parameter	Unit	Python Model Result	Flownex® SE Model Result	Relative Error on Python Model
Heat transfer per cell	MW	4.592779	4.486490	2.314%
Pressure ratio	-	0.9945	0.9944	0.010%
Mass flow rate of air	kg/s	181.300	175.844	3.009%
Total fan power consumption	kW	230.8	210.5	8.795%
Outlet air temperature	℃	54.069	54.330	0.483%
Outlet sCO_2 temperature	℃	45.0	45.059	0.131%
Fan static pressure rise	Pa	63.087	63.244	0.249%
Heat exchanger pressure drop*	Pa	18.332	15.374	16.136%

*Includes pressure loss due to velocity distribution in the heat exchanger

On the other hand, the solver in Python balances the sCO_2-side momentum equation and the energy equations simultaneously and then the air-side momentum equation. Furthermore, the assumption in the Python model that air pressure is constant across the heat exchanger pass control volumes contributes to the discrepancies in the Flownex® SE results. Because the more advanced model (in Flownex) computes the

air properties of each control volume separately as well as the individual pressure drop across each pass, the overall performance will differ on the air-side. Specifically, the performance will differ more significantly when it comes to air mass flow rate and subsequently fan power consumption. The mass flow rate of air specifically has a large influence on the air-side pressure drop values in the heat exchanger. A small change in the mass flow rate of air can have a significant impact on these pressure drop values, this is shown in the relative error on these values in Table 7-1 and Table 7-2. Nonetheless, the small relative errors on the calculated heat transfer and sCO_2-side pressure drop values demonstrates that the Flownex ® SE model is solving for the steady-state solution properly.

To summarise, the Flownex ® SE single cell models were verified using the Python models as a benchmark. There are some high relative errors due to differences in solver architecture, fluid properties, and simplifying assumptions made in the Python model. However, in general, the level of error was deemed acceptable and the Flownex ® SE models were further used in the off-design studies below.

7.2 Single cell ambient air temperature studies

Following the verification of the single cell model, simulations were performed at design conditions across a range of operating ambient air temperatures from 5.0 ℃ to 40.0 ℃ in 5.0 ℃ increments. This means that there are no crosswinds or recirculation and only the ambient air temperature changes. The objective of these studies was to assess the effect of the ambient air temperature on heat rejection system performance. Air-cooled systems are noted to be sensitive to ambient air temperature (Kröger, 2004; Moisseytsev, Jian & Sienicki, 2016) and the effects on the potential air-cooled system need to be investigated if the system is to be realised. The temperature range used comfortably covers the potential ambient air conditions which the heat rejection systems will experienced at the proposed location in the region of Upington in South Africa. It is important to note that a simplifying assumption that the MALR remains constant was made for this and all subsequent ambient air temperature studies, in reality, it will shift as the air temperature goes up and down.

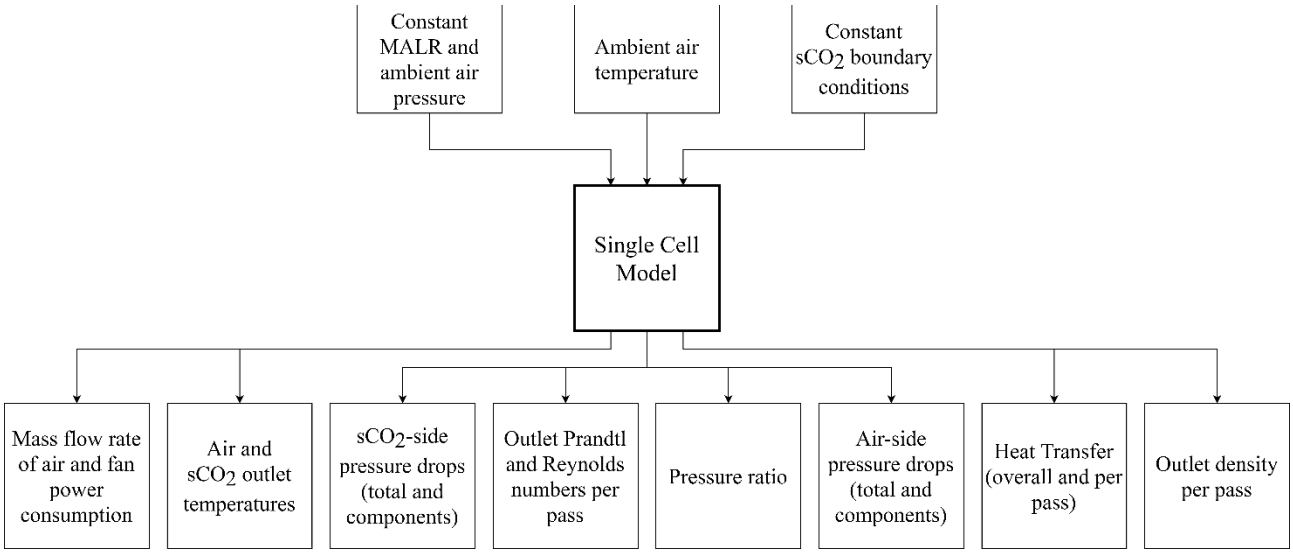

Figure 7-1: Flownex single cell model inputs and outputs for the ambient air temperature studies

The aim of the single cell studies was to observe the trends for several key design results, shown in Figure 7-1, as the operating ambient air temperature deviated from the design point. In general, any trends

identified will be useful indicators as to how the entire PC and IC systems will operate at off-design ambient temperatures. In summary, the results measured were as follows: the overall heat rejection rate as well as the heat rejection rate per pass and the sCO_2 outlet temperature were measured; the total and individual sCO_2-side pressure drops were measured along with the pressure ratio across the cell; additionally, the air-side performance was captured and included the mass flow rate of air, fan power consumption, air outlet temperature, and air-side pressure drops; finally, to further enable the analysis of the results mentioned previously, the outlet sCO_2 density, Prandtl number, and Reynolds number were measured for each pass. These results and their trends will provide an idea of whether changing ambient temperatures cause over- or under-cooling and the way in which ambient air temperature may influence cycle performance through the PR and $\dot{W}_{aux}$ of each cell. A control study was also performed on the single cell models in cases of overcooling where sCO_2 was bypassed to achieve the desired 45.0 ℃ sCO_2 outlet temperature. This study informed on future decisions regarding the control of the entire heat rejection systems and provided insight into the advantages and disadvantages of bypassing sCO_2 on a cell-by-cell basis. The results for the PC and the IC can be seen further below in this section.

PRECOOLER

The PC single cell model is set up and discretised as per Section 6, it also operates at a lower sCO_2 pressure and a larger sCO_2 temperature range than the IC, this affects the properties of the fluid as it is cooled.

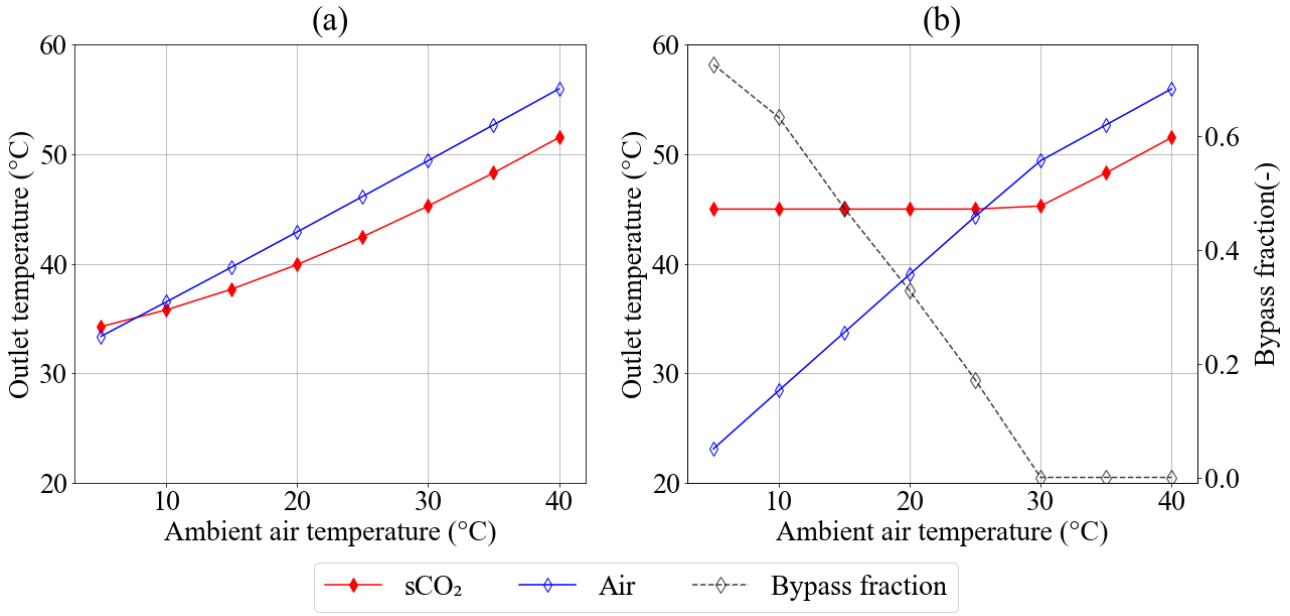

Figure 7-2: PC single cell sCO_2 and air outlet temperatures (a) without bypassing and (b) with bypassing

Furthermore, the PC has fewer passes (4) and cells (8) than the IC. This means that the sCO_2 is flowing at a higher rate in the PC cells and that the heat rejection per pass must be higher than in the IC. The plots in this section compare the operation of the PC without bypassing and with bypassing. Bypassing only becomes necessary and useful when the ambient temperature results in over-cooling of the sCO_2, in the cases where the sCO_2 is under-cooled there is no method available in the model which allows for an outlet temperature of 45.0 ℃ to be reached and bypassing sCO_2 would only result in higher outlet temperatures. Bypassing in the model is achieved by iteratively solving for the fixed mass flow rate through the bypass control volume using the *Designer* in Flownex® SE such that the sCO_2 exits the heat exchanger at the target temperature. It

is also important to revisit some of the important boundary conditions for the PC. The inlet sCO2 temperature and pressure are 85.77 ℃ and 7 503 kPa respectively and the mass flow rate of sCO2 entering the system is 392.1 kg/s. Finally, the ambient design air temperature is 28.3 ℃.

Figure 7-2 and Figure 7-3 show that with the inclusion of a controlled bypass 'valve' over-cooling can be corrected for. It can also be seen in Figure 7-2 that the outlet air temperature drops by around 10 ℃ at each temperature increment when sCO_2 is bypassed. This is because less heat is being transferred to the cold air. The total heat transfer results for a single cell in the PC can be seen in Figure 7-3 and the per pass heat transfer results can be seen in Figure 7-4. The results indicate that heat rejection rate increases almost linearly with reducing ambient air temperatures (T_{amb}). This was expected because lower T_{amb} values raise the temperature difference between the hot and cold fluid streams in the heat exchanger. Notably, at the lowest T_{amb} the third and fourth passes have very similar heat rejection rates. This is a result of the sudden variations in sCO_2 fluid properties as it cools well below the design case. The Prandtl number (Pr) increases in the third and fourth passes as the sCO_2 reaches lower outlet temperatures with decreasing T_{amb}.

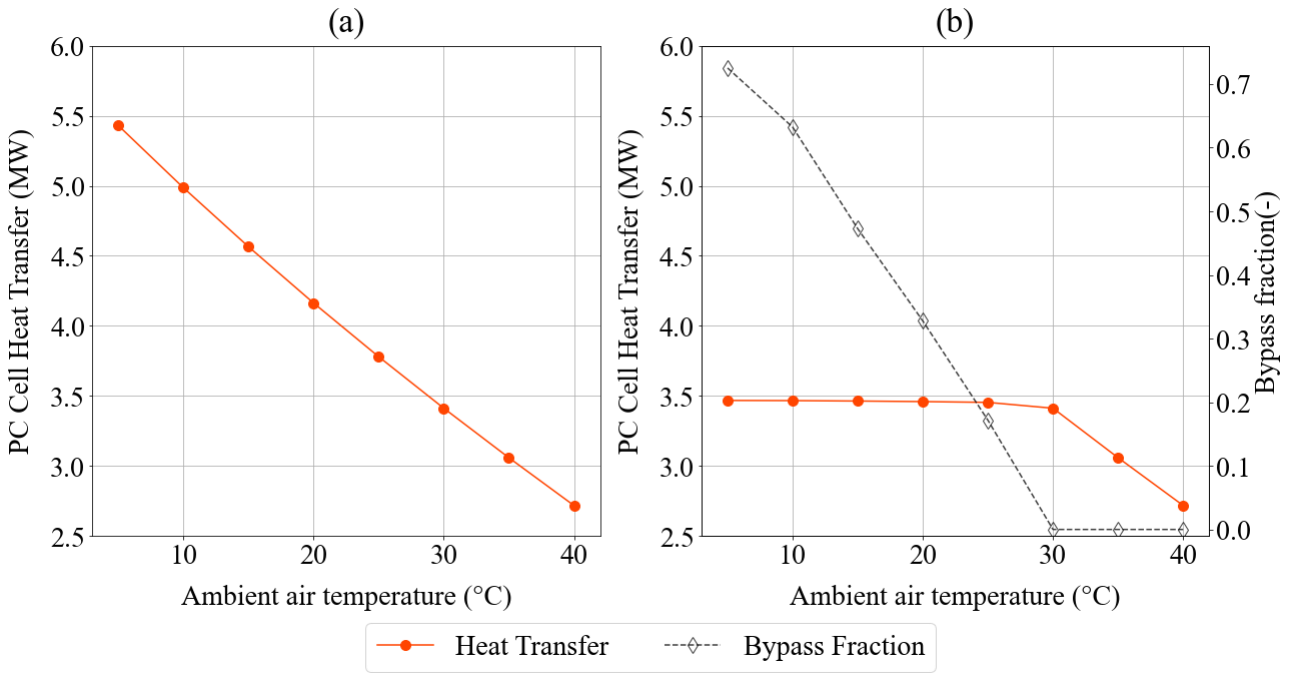

Figure 7-3: PC single cell total heat transfer (a) without bypassing and (b) with bypassing

The Reynolds numbers (Re) for these last two passes were also found to be lower at these T_{amb}. These plots can be found in Appendix E-1. The trends observed were due to increased viscosity and thermal conductivity as the sCO_2 temperature drops below 50 ℃ at the operating pressure of the PC. Because the heat transfer coefficient for sCO_2 is directly proportional to its thermal conductivity and the Nusselt number (Nu) which is in turn directly proportional to the Re and Pr, the last two passes achieve similar heat rejection rates in the absence of bypassing. This demonstrates the influence of the sCO_2 properties in these systems and reinforces the concept of discretising the heat exchanger passes in air-cooled systems for sCO_2 applications.

The effect of the sCO_2 properties on heat transfer is also evident when bypassing is included to achieve the target outlet temperature, as seen in Figure 7-4 (b) where all passes excluding the first exhibit irregular trends for heat transfer at low T_{amb}. It must be noted that bypassing sCO_2 reduces the mass flow rate through the

heat exchanger. For temperatures of 15 °C and below at least half of the mass flow rate needs to be bypassed as seen in the bypass fraction values of Figure 7-3 (b) and Figure 7-4 (b). This affects the sCO_2-side pressure drop, which is discussed further below, but it also decreases the maximum and actual heat rejection rates with the overall effect being a near constant heat rejection rate which resembles that of the performance under design conditions. Figure 7-4 shows the decreased heat rejection rates on a per pass basis and the general trend outside the region where the sCO_2 properties are significantly altering heat transfer is an increase in heat rejection up to a certain T_{amb} after which it decreases steadily. This was attributed to the trade-off between decreasing heat transfer as T_{amb} rises and the increased heat transfer as more sCO_2 is channelled through the heat exchanger. Initially, the increased heat transfers due to increased heat exchanger sCO_2 mass flow rate dominates at lower T_{amb} before it plateaus and declines in all the passes. Granted that this is the general trend, the second, third, and fourth passes experience significant fluctuations in heat transfer at ambient temperatures below 15 °C.

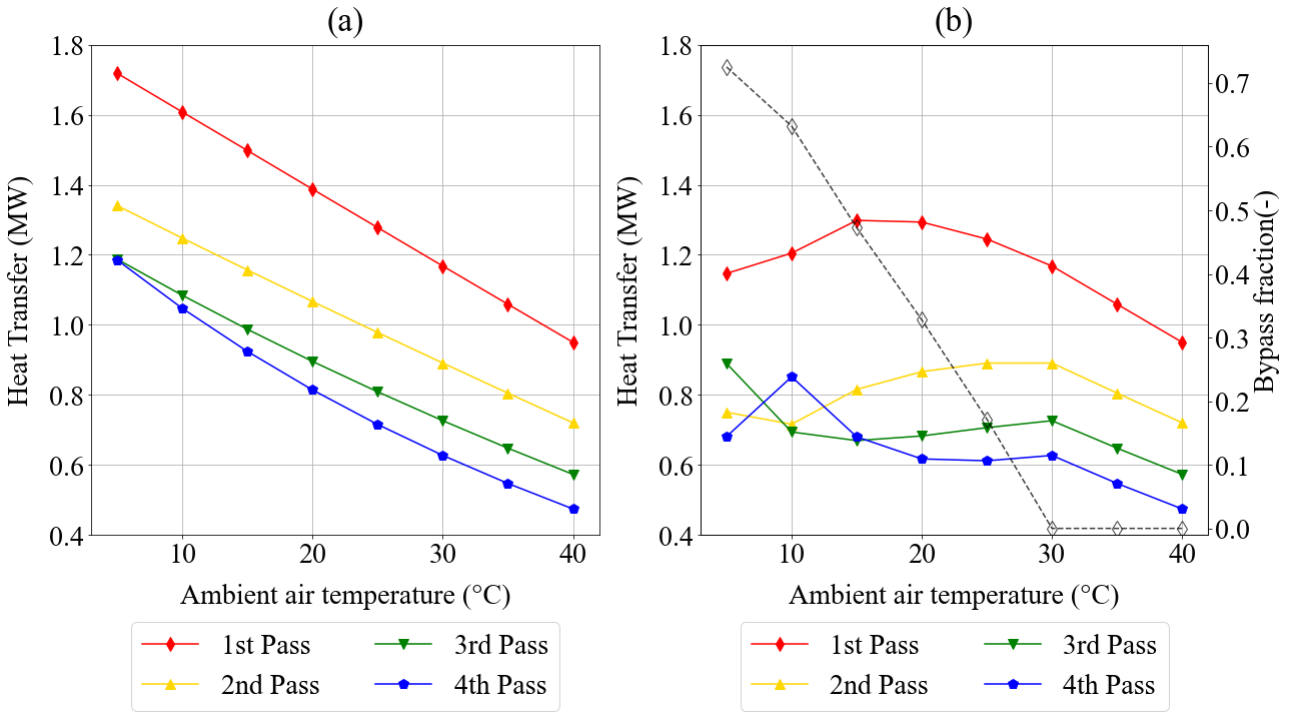

Figure 7-4: PC single cell per pass heat transfer (a) without bypassing and (b) with bypassing across a range of operating ambient air temperatures

Importantly, the target sCO_2 outlet temperature of 45 °C is achieved when the high temperature and pressure sCO_2 that was bypassed mixes with the cooled sCO_2 at the heat exchanger outlet. The sCO_2 in the heat exchanger has been over-cooled because the heat rejection rate is near design conditions (≈ 3.5 MW) but the sCO_2 mass flow rate is a fraction of what it was under the original design conditions. This means that at lower T_{amb}, the sCO_2 has likely come close to the pseudocritical temperature and pressure as it was cooled. The actual sCO_2 behaviour in these cases is shown on the temperature-entropy plots in Figure 7-5. The trends confirm that when bypassing is employed, the sCO_2 in the heat exchanger passes near the critical point at lower T_{amb}. This behaviour indicates that bypassing should not be the only strategy used to counteract over-cooling in the system. It is likely that for the entire PC a combination of bypassing and an alternative control strategy such as turning fans off in certain cells will provide a method of control which avoids potential phase changes and large fluctuations in sCO_2 properties. In any case, an important observation

made is that the quality within each pass of the model indicated that the fluid remained supercritical. Any drop below a supercritical quality would have a negative impact on the downstream compressor in the cycle. Even if adequate mixing of the bypass flow is achieved, the heat exchanger may still experience pinch-point issues. The sCO_2 temperature, quality, and pressure within the heat exchanger would have to be monitored closely to avoid complications when exclusively bypassing sCO_2 at colder air temperatures.

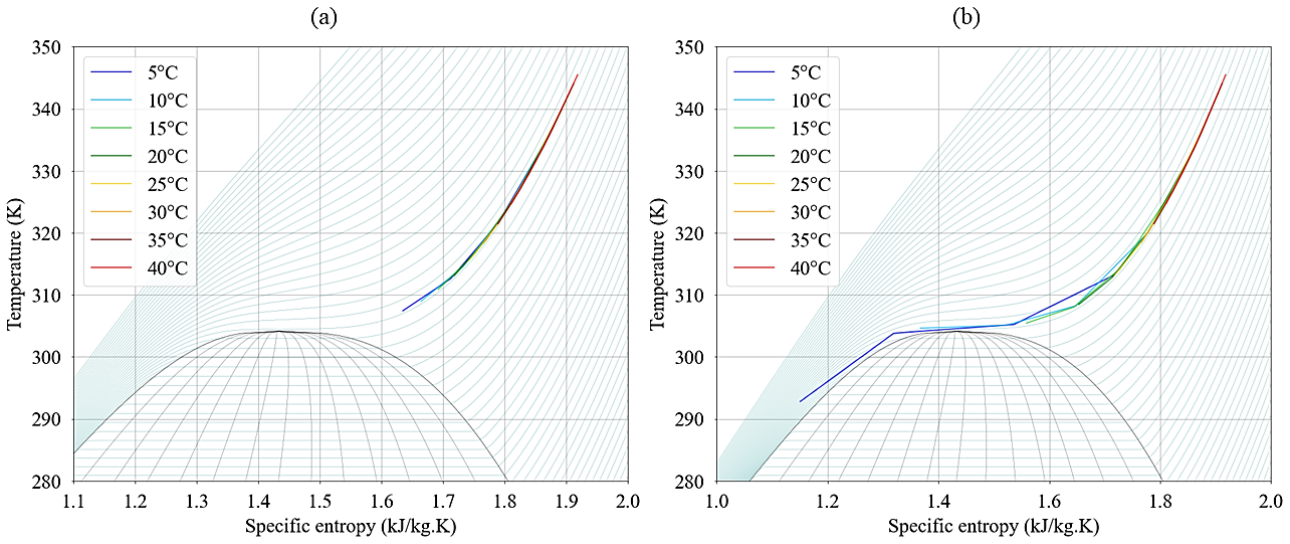

Figure 7-5: sCO_2 temperature-entropy plots for the PC (a) without bypassing and (b) with bypassing at various ambient air temperatures

Figure 7-6 below displays the lower sCO_2 mass flow rates through the heat exchanger when bypassing. The trends shown indicate that bypassing does not influence the mass flow rate of air significantly and that the mass flow rate of sCO_2 vary almost linearly. Any minor deviations can be attributed to the rapid fluctuations in sCO_2 density as the fluid is over-cooled.

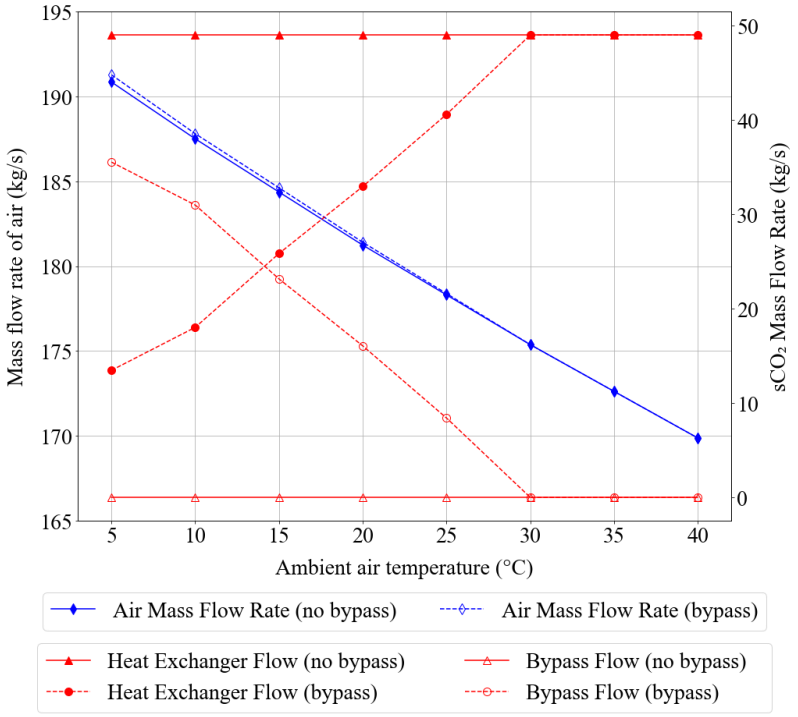

Figure 7-6: PC single cell air and sCO_2 mass flow rates with and without bypassing

These flow rates also affect the sCO_2-side pressure drops as seen in Figure 7-8, decreasing them. This correlation was expected, as the flow rate drops in the heat exchanger tubes so does the frictional pressure drop. This is because the frictional pressure drop is primarily affected by the fluid's velocity in a tube as per Eq. (4-49). In other words, the more sCO_2 that is bypassed, the lower the sCO_2-side velocity becomes which leads to lower the frictional and total sCO_2 pressure losses across the heat exchanger. Subsequently, the PR also increases. Figure 7-7 shows that for the case with the highest bypass fraction and the lowest T_{amb}, the pressure ratio is close to 1.0. While this is desirable from a cycle performance perspective, it comes with the complications discussed above that could potentially hinder plant operation. Additionally, in practice, the highest bypass cases will require the valve to have a low pressure drop, which in turn may require throttling of the main flow to the air-cooled heat exchangers.

Further analysis of the sCO_2-side pressure drops in Figure 7-8 indicates that both the inlet and exit pressure losses remain relatively constant and low without bypassing and decrease even further when sCO_2 is bypassed. This may be a result of the scale of the graph, in reality, these will increase and decrease proportionally with the velocity of the sCO_2 in the tubes This was also expected because the frictional pressure drop is the primary sCO_2-side pressure loss, hence the total and frictional pressure loss values follow the same trends with and without bypassing.

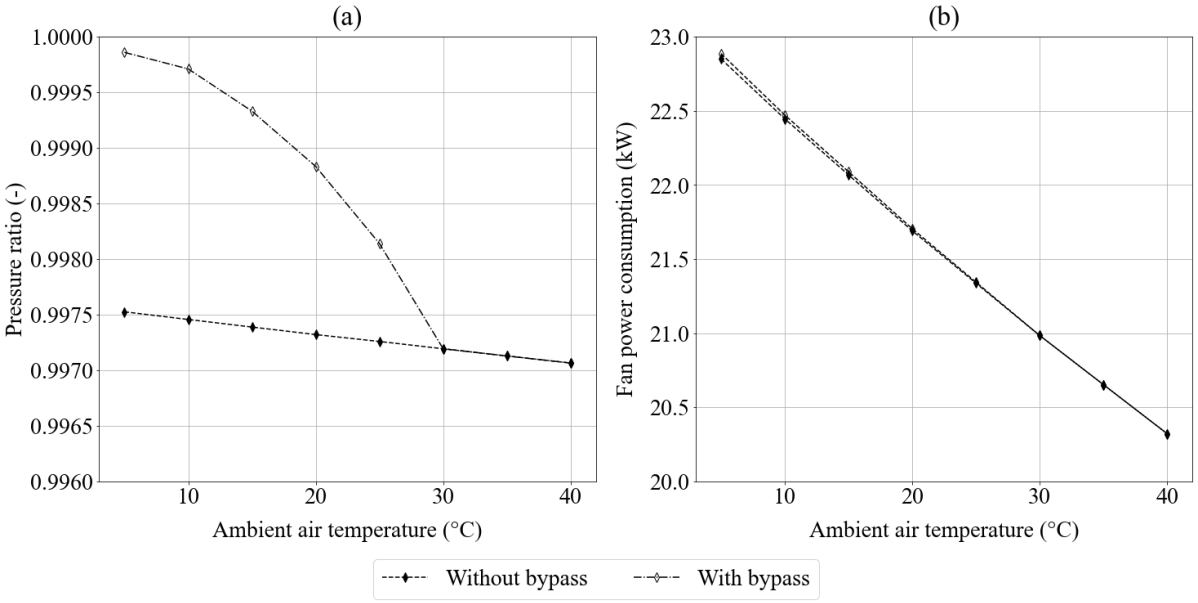

Figure 7-7: PC single cell (a) sCO_2-side pressure ratio and (b) fan power consumption with and without bypassing

As previously mentioned, the frictional pressure loss increases in Figure 7-7 (b) as the amount of sCO_2 bypassed decreases. Interestingly, it also increases steadily with T_{amb} in the absence of bypass conditions. This was attributed to the lower sCO_2 outlet temperatures in these ambient conditions which result in higher sCO_2 densities across the heat exchanger passes. An increase in the average density per pass as T_{amb} drops is shown in Figure E-3 (a) from Appendix E-1. This effect is exacerbated when sCO_2 is bypassed, refer to the densities in Figure E-3 (b). This indicates again that the sCO_2 is being over-cooled under bypass conditions and that the frictional pressure loss reduction is also strongly linked to the sCO_2 density in the heat exchanger.

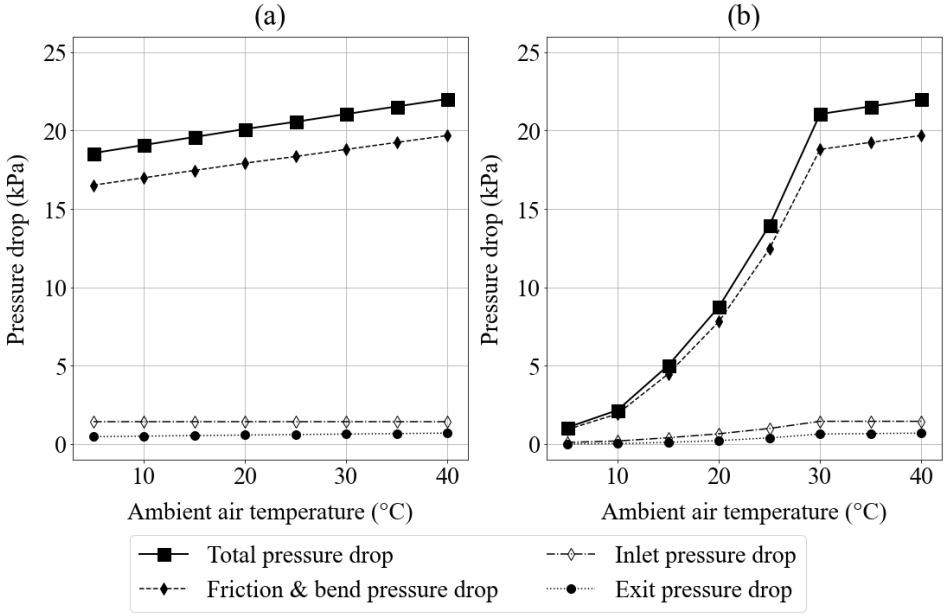

Figure 7-8: PC single sCO_2-side pressure drops (a) without bypassing and (b) with bypassing

Figure 7-6 and Figure 7-7 (b) show the air mass flow rates and auxilliary fan power consumption with and without bypassing respectively. In general, both the mass flow rate of air and fan auxilliary power ($\dot{W}_{aux}$) show decreasing trends with increasing T_{amb}. This is because, when T_{amb} rises, the mean air temperature in the system increases. This results in a lower density of air and reduced mass flow rate, subsequently the fan power reduces as well. This is also the reason why the air-side pressure drops decrease with increasing T_{amb}. Furthermore, as with the mass flow rate of air, $\dot{W}_{aux}$ was almost unaffected by the bypass fraction across the range of T_{amb}. The most noticeable differences in mass flow rate of air and $\dot{W}_{aux}$ were at T_{amb} values lower than 15 ℃ where, under bypass conditions, both the were slightly higher than the cases without bypassing. This is a result of the set fan rotational speed and reduced ambient pressure rises observed at lower T_{amb}. Lower ambient pressure rise values, coupled with the near constant air-side pressure drops regardless of bypassing, mean that the fan needs to recover slightly more static pressure when sCO_2 bypasses the cell. Because the fan rotational speed is set, the only way to achieve this is for the volumetric flow rate to increase slightly so that the air-side momentum equation balances.

In any case, the effect of bypassing on the air-side of the cell can be considered negligible and while it has a positive influence on PR, the region of T_{amb} where this positive effect is most significant is also the region where $\dot{W}_{aux}$ is highest. This must be considered when performing the ambient air temperature studies for the entire PC. Limiting the bypass fraction per cell is also an advisable strategy considering the trends seen above which indicated that the sCO_2 was heavily over-cooled under bypass conditions. Perhaps an alternative method of control which involves turning off fans to raise the sCO_2 outlet temperature may be utilised in combination with bypassing to achieve the 45 ℃ target. This would save auxiliary power while also retaining some of the sCO_2-side pressure drop benefits of bypassing.

To summarise, overall heat rejection rate decreases almost linearly from 5.4 MW at an ambient air temperature of 5 ℃ to around 2.75 MW at 40 ℃. This was expected as colder air will be able to extract more heat from the sCO_2. Furthermore, outlet sCO_2 temperature increases with increasing T_{amb} and is always over-cooled at ambient temperatures below that of the design condition (28.9 ℃). However, both heat

rejection and sCO_2 outlet temperature can be controlled by bypassing some of the sCO_2 from the inlet of the heat exchanger to the outlet. This affects heat transfer in the passes after the first, resulting in over-cooling and rapid sCO_2 property fluctuations at low T_{amb}. These fluctuations must be carefully considered because drastic changes in the temperature and entropy of the sCO_2 may result in a phase change which would impact the downstream compressor in the cycle. Furthermore, sudden, and large changes could also affect heat exchanger performance. Overall, it was deemed worthwhile to combine bypassing with another form of control when expanding the analysis to the entire PC. Bypassing the cell also decreases the sCO_2-side pressure drop, increasing the PR, but it has little to no effect on the air-side performance of the cell. The air-side performs best at higher ambient air temperatures because of the reduced heat rejection and lower static pressure recovery required by the fan in the system.

INTERCOOLER

The IC single cell model was also set up and discretised as per Section 6. It operates at a higher sCO_2 pressure than the PC which will result in more gradual property fluctuations under bypassing conditions. Additionally, the IC has more cells (10) and more passes (10) than the PC which means that there is a lower mass flow rate of sCO_2 per cell and a lower heat rejection rate required per pass. The plots in this section of the report compare the performance of a single IC cell with and without bypassing. The IC single cell bypass 'valve' is incorporated into the model using the same method as the PC and was also used to counteract the effects of over-cooling. At this stage it is important to recall the boundary conditions present in the IC. The inlet sCO2 temperature and pressure are 73.92 ℃ and 10 515 kPa respectively and the mass flow rate of sCO2 entering the system is 392.1 kg/s. Finally, the ambient design air temperature is 28.3 ℃.

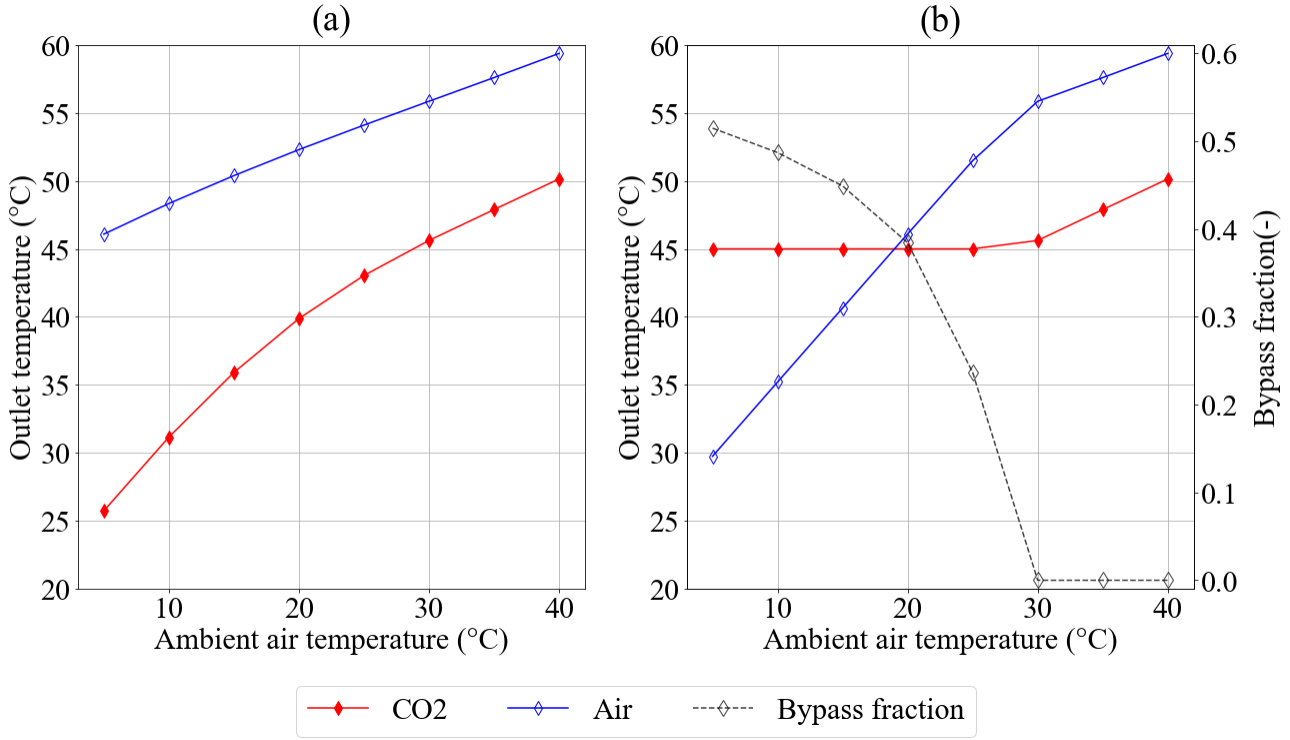

Figure 7-9: IC single cell sCO_2 and air outlet temperatures (a) without bypassing and (b) with bypassing

The effectiveness of including bypassing is shown in Figure 7-9 (b) and Figure 7-10 (b) where the targeted results for outlet temperature (45 ℃) and heat rejection (≈ 4.6 MW) have been achieved consistently below

the design T_{amb}. As previously mentioned, there is no control, besides increasing the fan speed, which can counteract the effects of under-cooling which occurs at higher T_{amb}. A variable speed drive for each of the fan motors would be required to achieve this which may prove costly in practice. Note that the amount of bypassing required is also generally less than in the PC which required that almost 70% of the sCO_2 be bypassed at the lowest T_{amb}. The IC, on the other hand, only required around 50% to be bypassed. Interestingly, the bypass fraction is more parabolic in the IC than in the PC where it was almost linear. This could be a result of the different fluctuations in sCO_2 properties that occur at the operating temperatures and pressures in the IC. Appendix E-1 can be referred to for some of these fluid properties.

The outlet temperatures of the air are higher in the IC, ranging from 45 ℃ to 60 ℃ in the absence of control. This is because the heat rejection rates are also higher due to the number of passes in the IC. The greater heat transfer area present with ten heat exchanger passes increases the amount of heat transferred from the sCO_2 to the air. This is an important consideration as higher air temperatures at the exit and throughout the system may affect the thermal lifespan of the finned tubes. However, EN P235 has an operating temperature limit of 300 ℃ which negates this potential disadvantage. If the system was designed using a different material for either the tubes or the fins, the elevated air temperatures might be detrimental. It is important to carefully consider the materials used when designing the heat exchanger. Also note that the outlet air temperature drops when sCO_2 is bypassed to control the heat transfer in the system. This is a result of reduced sCO_2 mass flow through the heat exchanger which causes lower heat rejection rates per pass, this is shown further down in Figure 7-11 and Figure 7-12.

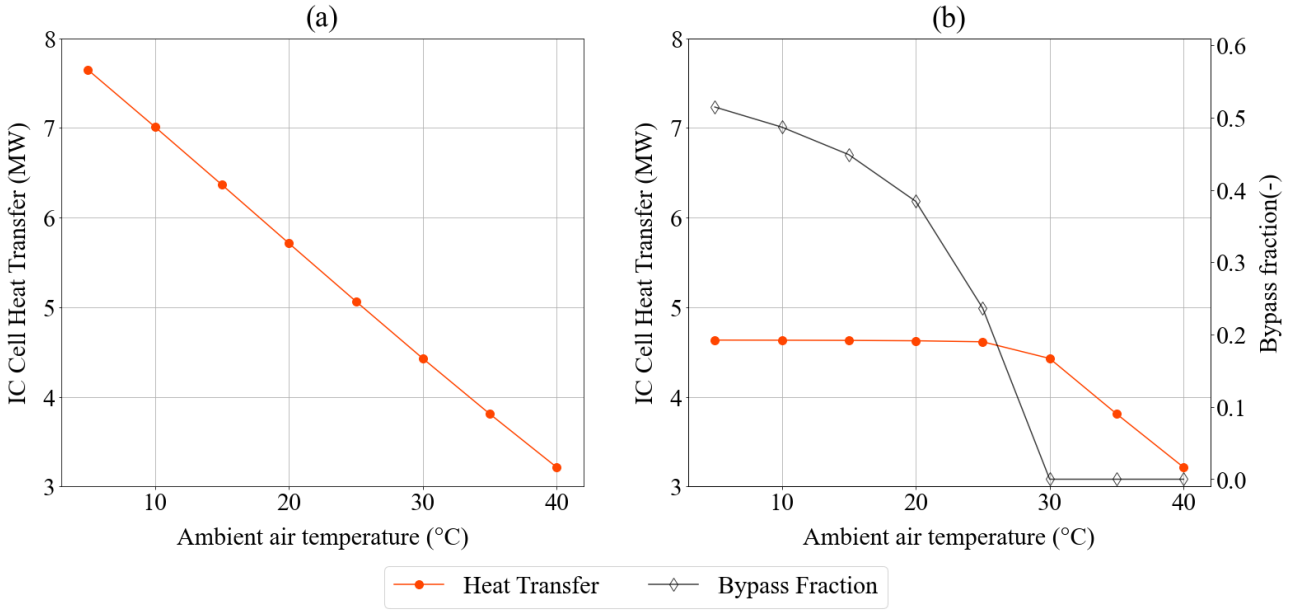

Figure 7-10: IC single cell total heat transfer (a) without bypassing and (b) with bypassing

Without bypassing the heat rejection rate per pass in the IC follows a linear trend across the range of T_{amb}, only deviating in the final two passes at the lowest T_{amb}. This was clarified by observing that at these T_{amb} values the outlet temperatures of sCO_2 have come close to the pseudocritical temperature at the IC's operating pressure. This causes sudden changes in the sCO_2 properties which govern heat transfer. However, the effect is far more gradual than in the PC which operates at pressures near the critical point of sCO_2.

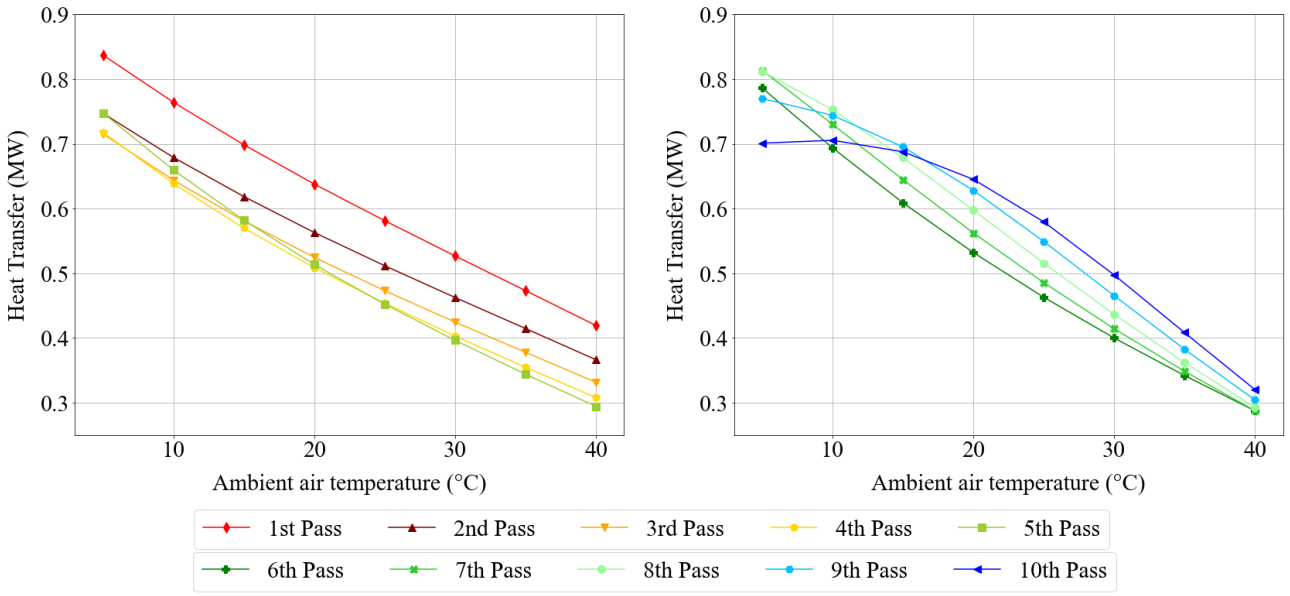

Figure 7-11: IC single cell heat transfer per pass without bypassing

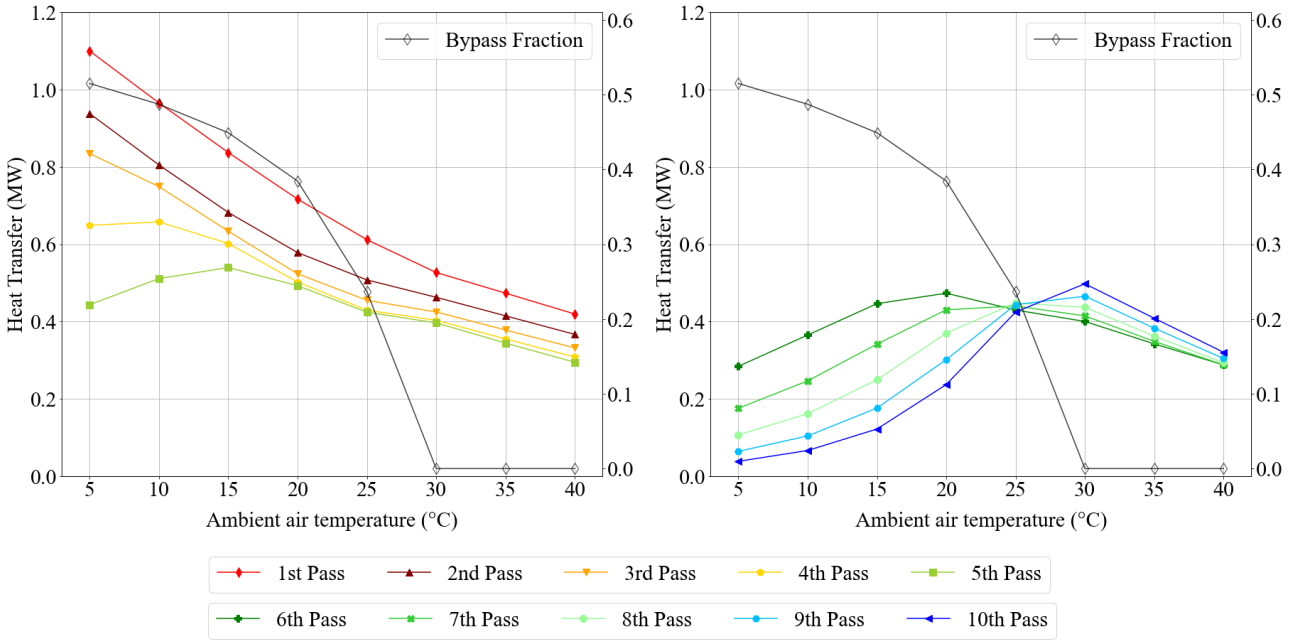

Figure 7-12: IC single cell heat transfer per pass with bypassing

The pressure lines for the IC have smoother changes in temperature and entropy, this is shown below in Figure 7-13, subsequently the heat rejection rates in the IC follow gentler non-linear trends instead of the sudden spikes observed in the PC. Additionally, bypassing has the same effect as in the PC where the sCO_2 is over-cooled and then mixes with the bypassed sCO_2 to achieve the desired outlet temperature. This is evident in Figure 7-12 where the heat rejection rate becomes non-linear from the fourth pass. This trend indicates that the properties of sCO_2 are fluctuating early in the cooling process, especially at low T_{amb}. As in the PC, the risk is that the sCO_2 may change phase in the heat exchanger tubes before it mixes with the bypassed supercritical gas at the outlet of the system. This could adversely affect the performance and operation of the downstream components in the cycle. These trends indicate that bypassing should be kept below a certain amount and combined with another form of control across the entire system.

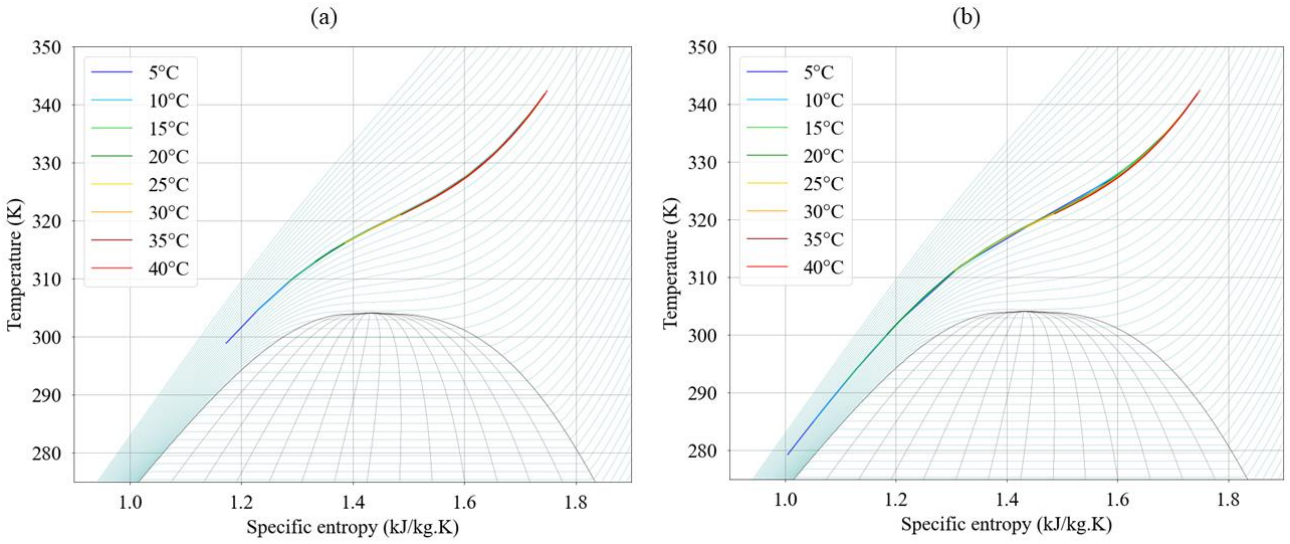

Figure 7-13: sCO2 temperature-entropy plots for the IC (a) without bypassing and (b) with bypassing at various ambient air temperatures

Although, even at the lowest bypass fractions of about 20% the final five passes in the IC have all experienced significant change in sCO_2 properties and heat rejection rate. This means that the changes in performance observed may be unavoidable. Fortunately, the sCO_2 was shown to remain in a supercritical condition in all the cases. This does not diminish the fact that the control and monitoring of these systems will be complex and needs to be performed diligently. Accurate monitoring of the sCO_2 in both air-cooled systems and stringent controls in the case of low T_{amb} operating conditions will be necessary.

The trends in Figure 7-13 (b) indicate that the sCO_2 within the heat exchanger has been over-cooled to a large extent with the inclusion of bypassing. At the lowest T_{amb} of 5 °C the outlet sCO_2 temperature of the final pass is almost equal to the inlet T_{amb}. This introduces the potential issue of a pinch-point problem occurring in the heat exchanger at low T_{amb} when sCO_2 is bypassed. It is ideal to avoid this and keep the outlet temperature of the hot stream sufficiently above the inlet temperature of the cold stream. As in the PC, an alternative control strategy may need to be utilised in combination with bypassing to achieve the desired system performance. Additionally, the low temperatures of sCO_2 in Figure 7-13 (b) explain the non-linear rise and fall of the heat rejection rate across the passes when bypassing is incorporated. These fluctuations are because the fluid has come close to the pseudocritical temperature for the IC's operating pressure of approximately 10.5 MPa. Subsequently, the fluid properties of sCO_2 which govern heat transfer have gone through sudden increases. This is further evident in the trends throughout the passes for the Prandtl number, which is determined by the viscosity, thermal conductivity, and isobaric specific heat capacity of sCO_2. These are provided in Appendix E-1 and very closely mirror the heat rejection results per pass seen in Figure 7-11 and Figure 7-12. The behaviour of the Prandtl numbers for each pass also give some explanation for the pass-by-pass heat rejection behaviour in the IC.

The mass flow rate of sCO_2 also influences the Reynolds number (see Appendix E-1) in each pass. When sCO_2 is bypassed the Reynolds numbers are much lower because the fluid velocity is also much lower. Additionally, these values were observed to decrease from the inlet to the outlet of the heat exchanger both with and without bypassing. This is a direct result of the viscosity increasing the colder the sCO_2 gets which is why the reduction in Reynolds number was found to be more significant in the later passes of the IC.

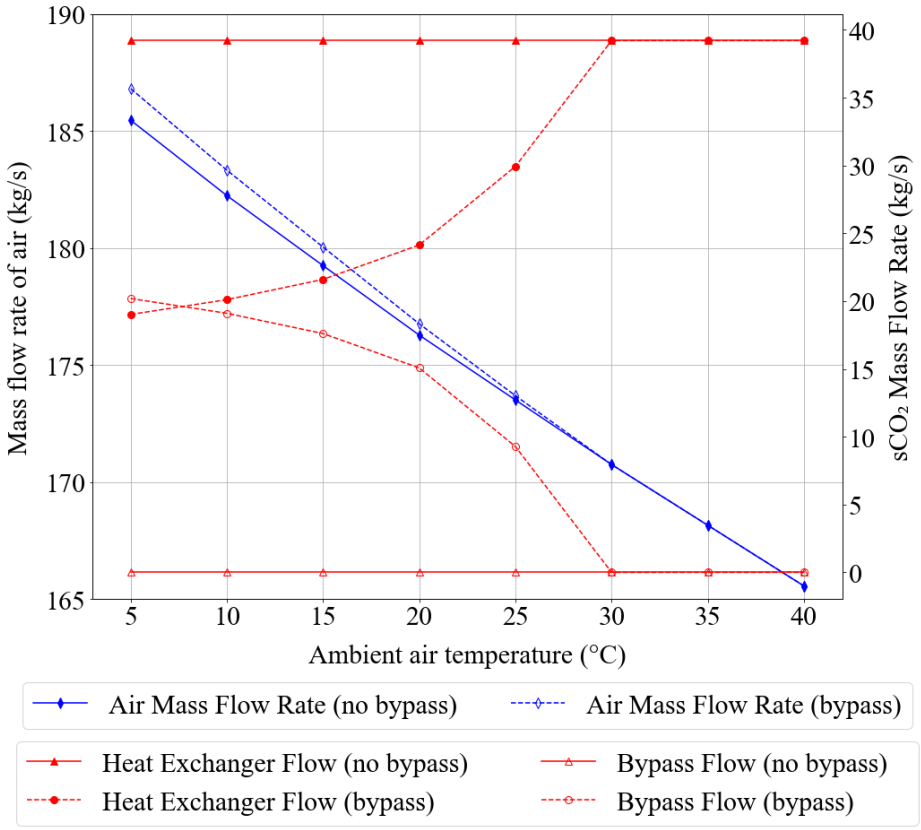

Figure 7-14: IC single cell air and sCO_2 mass flow rates with and without bypassing

The trends in Figure 7-14 also show that there is a very good agreement between the mass flow rates of the two fluids and their corresponding cycle performance variables seen below. As the mass flow rate of sCO_2 through the heat exchanger decreases, the PR increases and the frictional pressure drop decreases. All these variables follow a non-linear change as T_{amb} is adjusted. As previously noted, these non-linear trends present in the IC could be attributed to the different fluctuations in sCO_2 properties which take place at the average operating pressure of 10.5 MPa.

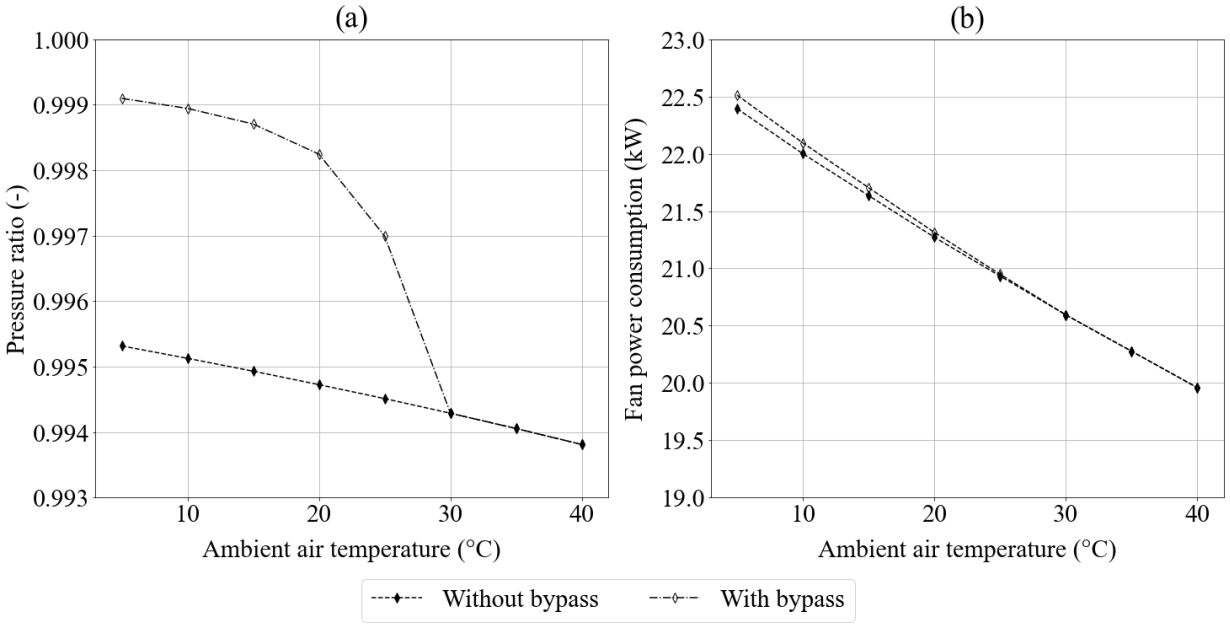

Figure 7-15: IC single cell (a) sCO2-side pressure ratio and (b) fan power consumption with and without bypassing

Appendix E-1 can be referred to for the density, Reynolds number, and Prandtl number plots. On the air-side, the trends in auxilliary fan power consumption shown in Figure 7-15 (b) and mass flow rate of air are the same because the fan power is a direct function of the mass and volume flow rate of air in the cell.

From a cycle performance perspective, the inclusion of bypassing has the advantage of increasing the PR of the IC, while having little to no effect on the air-side and fan power consumption. The sCO_2-side effect is shown in Figure 7-15 (a) where the PR is between 0.998 and 0.999 with bypassing and between 0.994 and 0.995 without bypassing. These differences may seem small but considering that the inlet sCO_2 pressure is10.515 MPa in the IC, it corresponds to about a 42 kPa lower pressure drop across the system. This comes with the previously discussed risks and non-linear trends but is a definite advantage of utilising a bypass mechanism. The cause of this increased PR is the lower mass flow rate of sCO_2 in the heat exchanger, shown in Figure 7-14, which directly affects the frictional pressure drop across the sCO_2-side of the system. As can be observed in Figure 7-16, the frictional pressure drop is almost the sole contributor to the sCO_2-side pressure drop. In theory, this would raise the frictional pressure drop across the heat exchanger. This does not occur because the main driver of the frictional pressure drop is the fluid's velocity.

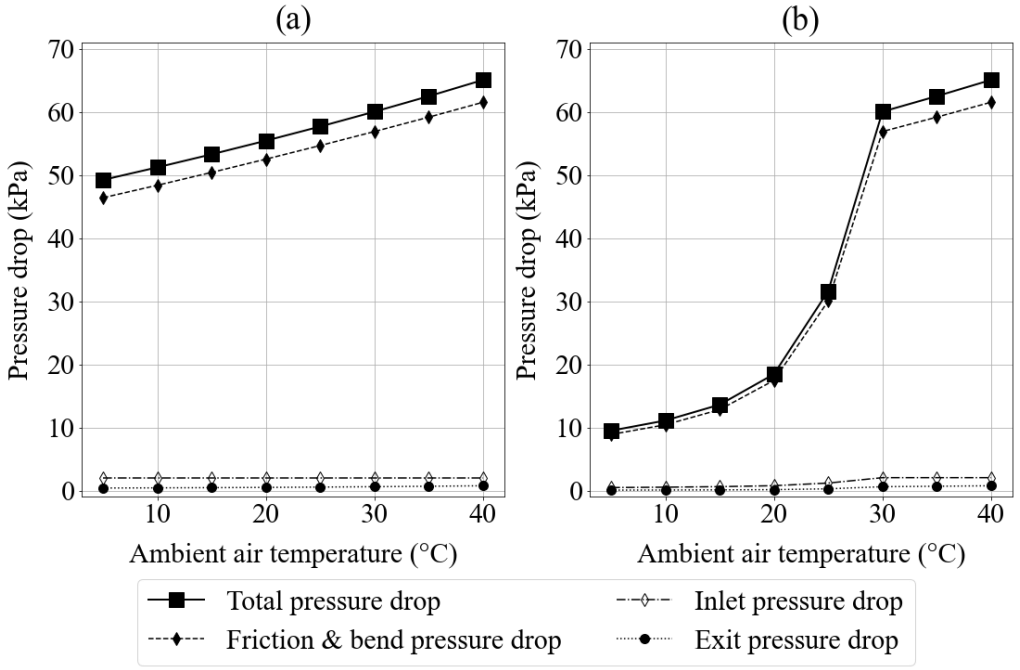

Figure 7-16: IC single sCO2-side pressure drops (a) without bypassing and (b) with bypassing

In summary, the IC heat transfer decreases linearly in the absence of control from 7.65 MW to 3.21 MW as the ambient air temperature rises. Ambient air temperature was also found to affect the outlet temperatures of both fluid streams with the exit air temperature ranging from 46.1 ℃ when it is cold to 59.1 ℃ when it is hot. The outlet sCO_2 temperature also varied, operating away from design conditions the majority of the time. These effects were shown to be controlled using a bypass method which stabilised the heat transfer at 4.63 MW when the ambient air temperature is below the design conditions. Bypassing also allowed for the control of the outlet sCO_2 temperature while also reducing the outlet air temperature, this has positive implications for heat exchanger longevity and the ability of the system to function as designed. From a cycle performance perspective, bypassing was also shown to have a positive effect on the pressure ratio of the heat rejection system, increasing it from 0.995 to 0.999 in the coldest conditions. In general, bypassing

provided a better performance as a result of reduced mass flow and frictional pressure losses in the heat exchanger. Fan performance and power consumption is largely unaffected by the control method used because bypassing does not significantly influence the air-side of the system. Furthermore, it was noted that controlling the mass flow rates of the two fluids is vital when focusing on improving the systems' performance from a cycle perspective. The benefits associated with controlling the system using bypassing are not without risks. Bypassing sCO_2 around the heat exchanger causes increased over-cooling within the heat exchanger. In turn, the fluid passes near to the critical point along the relevant pressure line, as shown in Figure 7-13. This presents a problem as the properties of the fluid which affect heat transfer and fluid mechanics fluctuate quite suddenly and significantly. Therefore, even though the output of the system is consistent, the performance within the heat exchanger can become unpredictable and may result in complications such as phase change if too much sCO_2 is bypassed. This indicates a potential need for an alternate control method when aiming to stabilise the performance of the entire heat rejection system and not just one cell.

7.3 Entire system ambient air temperature studies

Following the simulation of the single cell models and analysis of their sensitivity to ambient air temperature, the performance of the entire heat rejection systems was investigated. These systems were set up in Flownex SE ® as per Section 6.9 and the sensitivity of the entire Precooler and Intercooler were simulated at design conditions across a range of operating ambient air temperatures from 5.0 ℃ to 40.0 ℃ in 7.0 ℃ increments. This means that there are no crosswinds or recirculation and only the ambient air temperature changes. This time the sensitivity of the entire air-cooled systems to ambient temperature was investigated. As previously mentioned, air-cooled systems are noted to be sensitive to the ambient air temperature. This sensitivity needs to be controlled for in the systems to avoid off-design performance. The temperature range used comfortably covers the potential ambient air conditions which the heat rejection systems will have to operate at and is based on a typical year's weather data for Upington, South Africa. The reason for the larger increments in temperature, when compared to the single cell studies, was the scope of the analyses in this section. The systems were analysed in the absence of control, then with exclusively bypassing or only switching off fans, and finally with a combination of the two methods.

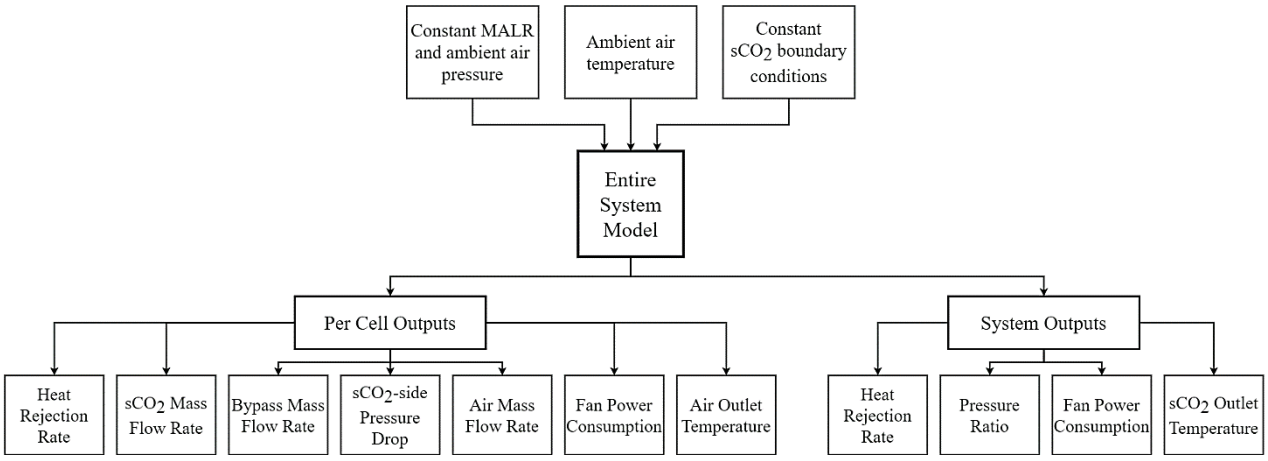

Figure 7-17: Entire heat rejection system ambient air temperature study inputs and outputs

The aim of these studies was to assess the sensitivity of several key performance variables to changing ambient air temperatures and determine how to best control for this on a system-level. These variables are shown in Figure 7-17, and can be divided into two major categories, per cell outputs and system outputs.

When controlling the system to reduce sensitivity to ambient air temperature, the focus was on stabilising the overall heat rejection rate of each system at a target value linked to the target outlet temperature for sCO_2 of 45 ℃. The effect of the control methods on other variables such as pressure ratio and fan power consumption were measured and not controlled. The trends extracted from the results then informed on the potential of each control method from a cycle performance perspective.

PRECOOLER

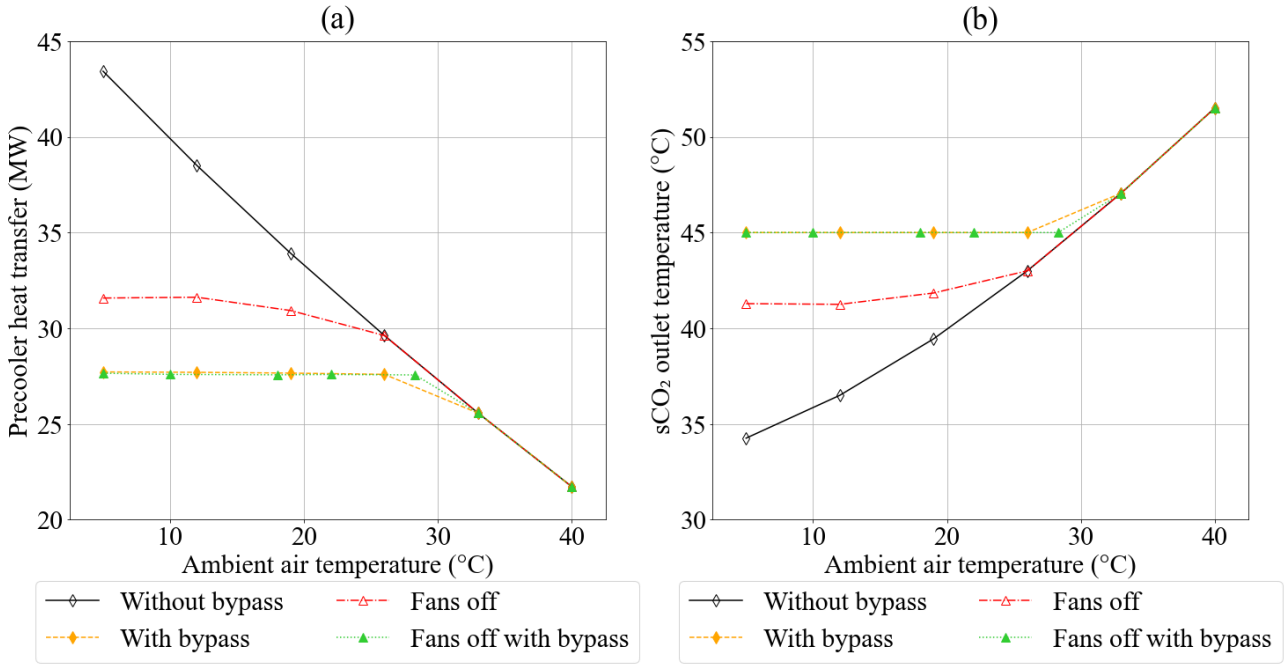

Figure 7-18: Precooler heat rejection rates and sCO_2 outlet temperatures for different control schemes

Figure 7-18 shows the heat rejection rates and outlet sCO_2 temperatures achieved using the different control methods. The uncontrolled behaviour of the system is very similar to the single cell results in Section 7.2. The outlet temperature increases less linearly but between almost the same amounts of 34 ℃ and 51 ℃, these results are slightly lower than those in the single cell study. The non-linear behaviour as the air changes temperature may be a result of the varied flow distribution between cells which occurs under steady-state conditions in the entire system model. Different flow rates can alter the heat transfer per cell and subsequently the sCO_2 inlet temperature and pressure because all cells have the same inlet air conditions a difference in sCO_2 outlet temperature and pressure becomes likely. This effect, coupled with the variation in sCO_2 properties which occurs when it is over-cooled, resulted in a non-linear trend in sCO_2 outlet temperature as the ambient air temperature increased. Notably, a linear trend was observed at higher ambient air temperatures where the sCO_2 did not experience over-cooling (or bypassing). Ambient air temperature was shown to increase the heat transfer in the system linearly across the range of temperatures examined and by almost 20 MW from the design value of 27.6 MW at its lowest value of 5 ℃. This could adversely affect the upstream and downstream components in the cycle, potentially leading to complications in the downstream compressor as a result of the sCO_2 properties being outside of the required operating

conditions. This was shown to be counteracted effectively by either bypassing both streets to reduce the sCO_2 mass flow rate through the heat exchangers or by switching off fans and bypassing both streets. In these cases, the heat rejection rate and sCO_2 outlet temperature stabilised at 27.6 MW and the design target of 45 °C respectively.

Exclusively turning fans off was not as effective as the above methods, this is because turning a cell's fan off results in an uncontrolled jump in heat rejection and sCO_2 outlet temperature. The specific number of fans switched off at each ambient temperature are shown in Figure 7-19 below, these were based on the number of fans one could turn off without under-cooling the sCO_2. In the model fans were switched off by setting their rotational speed to the lowest possible value of 2 rpm.

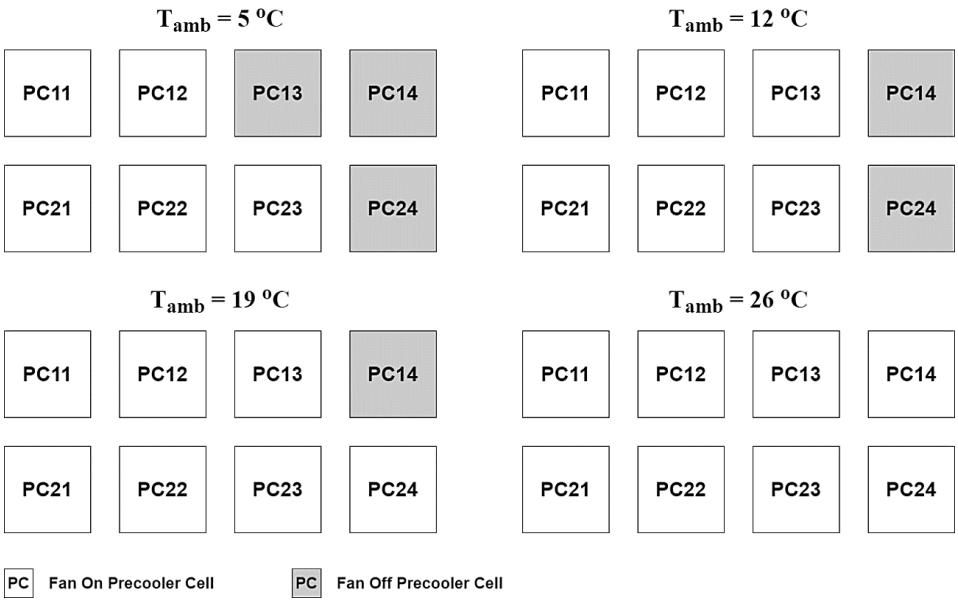

Figure 7-19: Precooler fans off strategy per increment

No fans were switched off for temperature increments above those shown in the diagram. It was noted that the temperature jumps were larger at higher ambient temperatures. This is because removing one cell's worth of heat rejection has less of an impact on overall heat rejection and sCO_2 outlet temperature when the air is colder as the maximum heat transfer possible is larger. Even if the mass flow rate through the other cells increases, which is shown in Figure 7-20 to be true, less heat is still extracted at higher ambient air temperatures and the bigger the jumps in sCO_2 outlet temperatures will be. The sCO_2 mass flow rates per cell and bypass fractions per street, shown in Figure 7-20 and Figure 7-21 respectively, indicate the flow distribution in the system for each control method. In the case where there are no control methods employed, there is an approximately equal flow distribution between cells, each having a sCO_2 mass flow rate of about 49.125 kg/s. This is shown graphically in Figure 7-20 and differs from the alternative operating conditions greatly. Exclusively bypassing specific streets in the heat rejection system is shown to have the greatest impact on flow rate. This was expected after the initial single cell studies showed that a large fraction of sCO_2 needed to be bypassed at the lowest ambient temperatures. In the case of the entire PC, the mass flow rate per cell varies from around 12 kg/s when the air is coldest to the baseline of 49.125 kg/s when it is hottest. This very low individual cell flow rate corresponds to a bypass fraction of approximately 0.75 (75%) flow around the heat exchangers, shown in Figure 7-21. Both the exclusively fans off and combined control

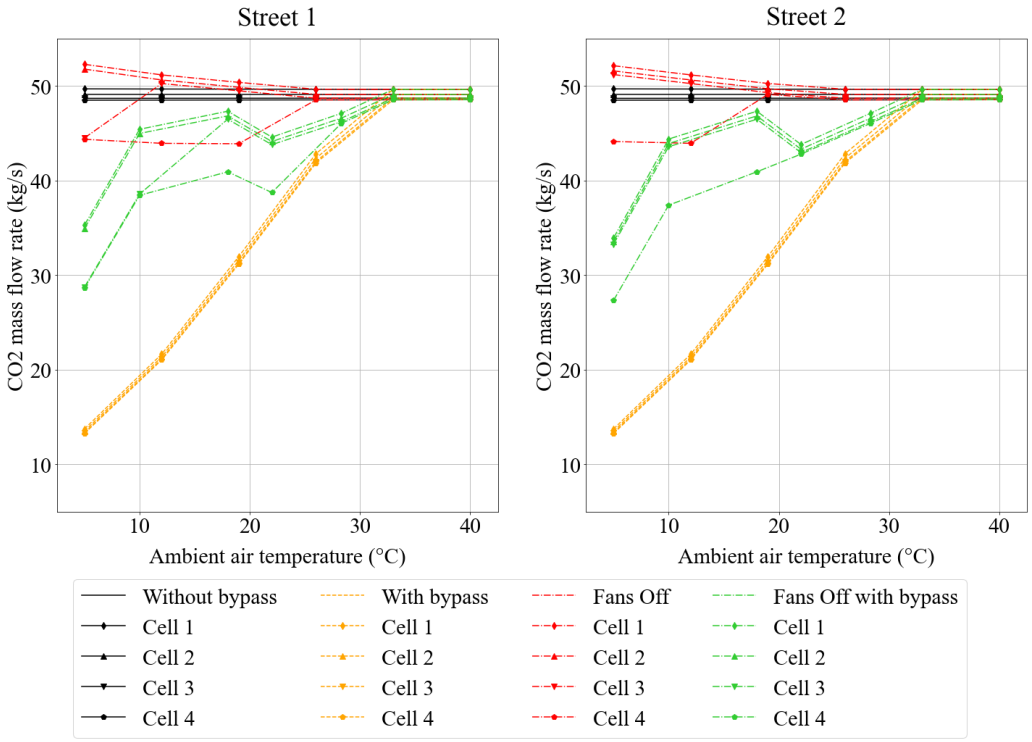

Figure 7-20: Precooler sCO_2 mass flow rates per cell for different control schemes

methods produced higher flow rates across all cells for the whole ambient temperature range. It was also observed, for these operating conditions, that turning fans off tends to cause the mass flow rate through the heat exchanger to drop by about 5 kg/s. This effect is exaggerated when coupled with bypassing as a control. It can be seen in Figure 7-20 that cells three and four in street 1 both have lower flow rates than the others, operating at about 29 kg/s for the combined method and 45 kg/s when only fans were switched off. Street 2 only ever has cell four's fan switched off, and the flow rate difference is just as obvious and approximately the same values as street 1's cells with their fans switched off.

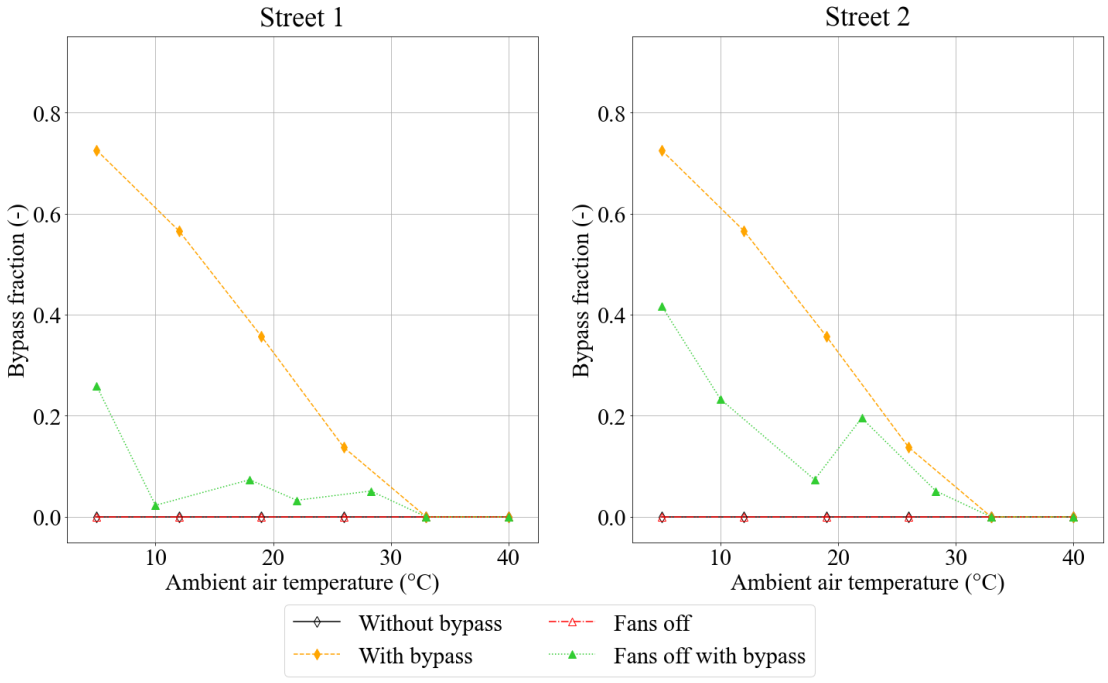

Figure 7-21: Precooler bypass fractions per street different control schemes

More importantly, in Section 7.2, mass flow rates through a single cell in the region of 10 kg/s to 20 kg/s were shown to drastically affect the fluid properties of sCO_2 through the cell and subsequently the heat transfer characteristics. This is the case for controlling using only bypass valves and the resulting irregular heat transfer and fluid properties have also been shown to influence the phase of the sCO_2. This is because the fluid passes close to the pseudocritical temperature along its pressure line from a temperature and entropy perspective. So, although bypassing the streets provides the desired system wide performance in terms of heat transfer and sCO_2 outlet temperature, it is undesirable because of the associated risks of over-cooling the sCO_2 too much and the required levels of monitoring to mitigate the risks. On the other hand, the combined control approach provides the same system wide performance with the added benefits of reduced fan power consumption, a competitive pressure ratio, and bypass fractions per street which don't result in low sCO_2 mass flow rates and unpredictable heat transfer performance per cell.

Figure 7-21 shows an interesting trend for the bypass fraction when there is an odd number of fans switched off in the PC. It was observed that the street with less fans off will require a higher bypass fraction. Despite this, the mass flow rates through the cells in the separate streets remained very similar, with street 2 (which had less fans off) having marginally lower flow rates per cell. Nonetheless, the sCO_2 mass flow rates through all cells in when using the combined method were acceptable, being in the region of 30 kg/s or above. Mass flow rates around these values were shown in the single cell study to produce predictable heat transfer trends with minimal variation in sCO_2 properties and low risk of phase change.

Throughout this section, the combination of switching fans off and bypassing has been shown to be just as effective as only bypassing in terms of controlling heat rejection and sCO_2 outlet temperature. This strategy was developed using the results of the study where only fans were switched off. The outlet sCO_2 temperatures at each increment helped decide on an ambient temperature range across which that specific number of fans should be off. The specific ranges can be seen in Table 7-3.

Table 7-3: Precooler combined control fan operation strategy

	$0℃ < T_{amb} \leq 10℃$		$10℃ < T_{amb} \leq 18℃$		$18℃ < T_{amb} \leq 22℃$		$22℃ < T_{amb}$	
	PC×1	PC×2	PC×1	PC×2	PC×1	PC×2	PC×1	PC×2
1	On	On	On	On	On	On	On	On
2	On	On	On	On	On	On	On	On
3	On	Off	On	On	On	On	On	On
4	Off	Off	Off	Off	Off	On	On	On

To aid in the development of a control strategy that deals with any ambient temperature, this combined control method was simulated by turning the appropriate number of fans off and iteratively solving for the bypass mass flow rate at the limits of each temperature range. This is why there are more data points for this control scheme shown in the plots. This combination of increasing outlet sCO_2 temperature in jumps by turning fans off and then bypassing to achieve the exact target also had a positive impact on the pressure ratio and fan power consumption of the precooler. This is evident in Figure 7-22 where it is shown that switching fans off and bypassing provides the best combined results across the temperature range. Figure 7-22 (a) shows that the pressure ratio was improved from the baseline level of around 0.997 across the ambient temperature range and Figure 7-22 (b) that the fan power consumed is decreased considerably

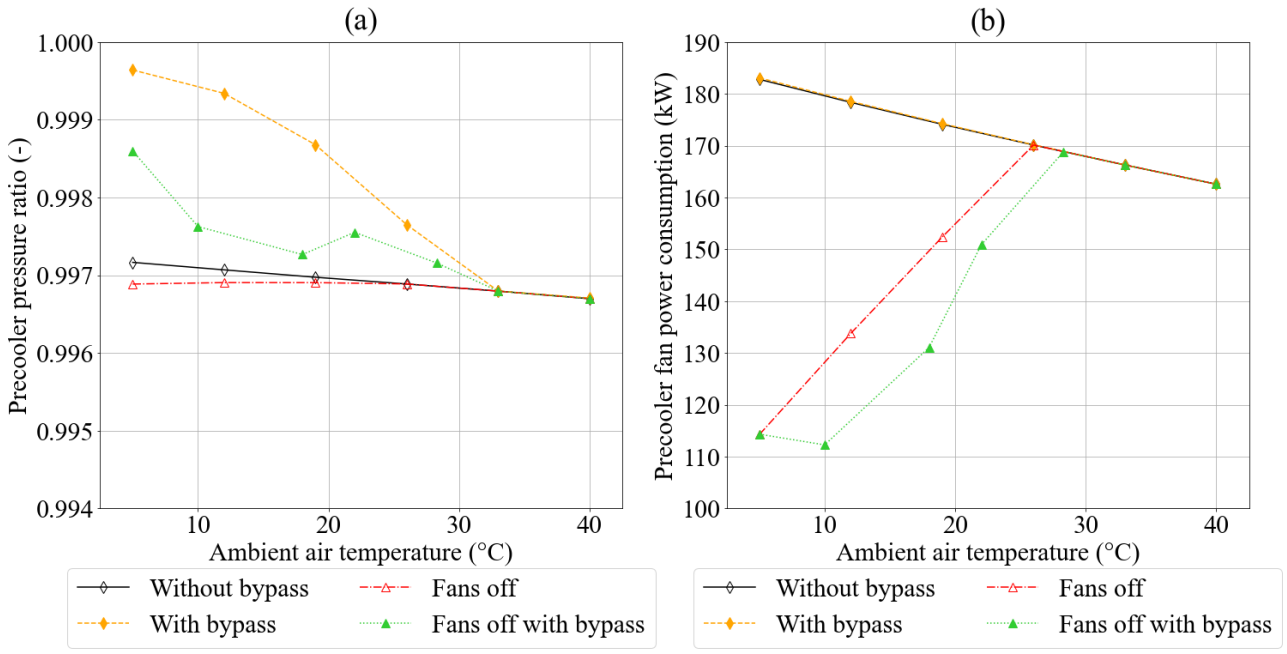

Figure 7-22: Precooler pressure ratios and fan power consumptions for different control schemes

compared to the case where no controls are used. In comparison with exclusively bypassing, the combined control's pressure ratio results are not as good, however, they reduce auxilliary power in the system which only bypassing does not. The pressure ratio results are also inflated by the fact that the bypass valve has not been sized and modelled accordingly in the system. The reality is that any valve and ducting used to bypass the street will have associated frictional and form pressure losses. This reduces the potential gains seen in the plots. Nonetheless, the baseline pressure ratio of 0.997 is high enough that any small changes will have little influence on the overall effect on the cycle performance. The reduced fan power consumption is an advantage to switching fans off in the system. This result also indicates that oversizing the heat rejection system by designing for a high ambient air temperature may be advantageous. Reductions in auxilliary power of up to 70 kW were observed, with the system consuming around 60% of what it would without any control measures in place.

INTERCOOLER

Figure 7-23 (a) shows the heat transfer trends and Figure 7-23 (b) shows the sCO_2 outlet temperature trends for the entire IC running using the various control schemes. In the absence of control, the heat rejection rate decreases linearly from 76.44 MW at 5 ℃ ambient air temperature to 32.08 MW at the highest ambient air temperature of 40 ℃. The sCO_2 outlet temperature rises across the same range of ambient temperatures, moving from 25.78 ℃ to 50.12 ℃ in a slightly non-linear manner. Again, this can be attributed to the differences in sCO_2 mass flow rate per cell as shown in Figure 7-26 as well as the fluid property behaviour of sCO_2 at temperatures near the pseudocritical value. The results observed were expected based on previous findings, over-cooling results in lower process fluid outlet temperatures and vice-versa for under-cooling.

The system also rejects more heat at colder ambient temperatures. Uncontrolled performance like this is not desirable as it can negatively impact the upstream and downstream components in the cycle. Fortunately, the control schemes implemented and analysed were found to control for these issues. They produced heat rejection rates either very near or exactly at the design point. This is evident in Figure 7-23 (a), where

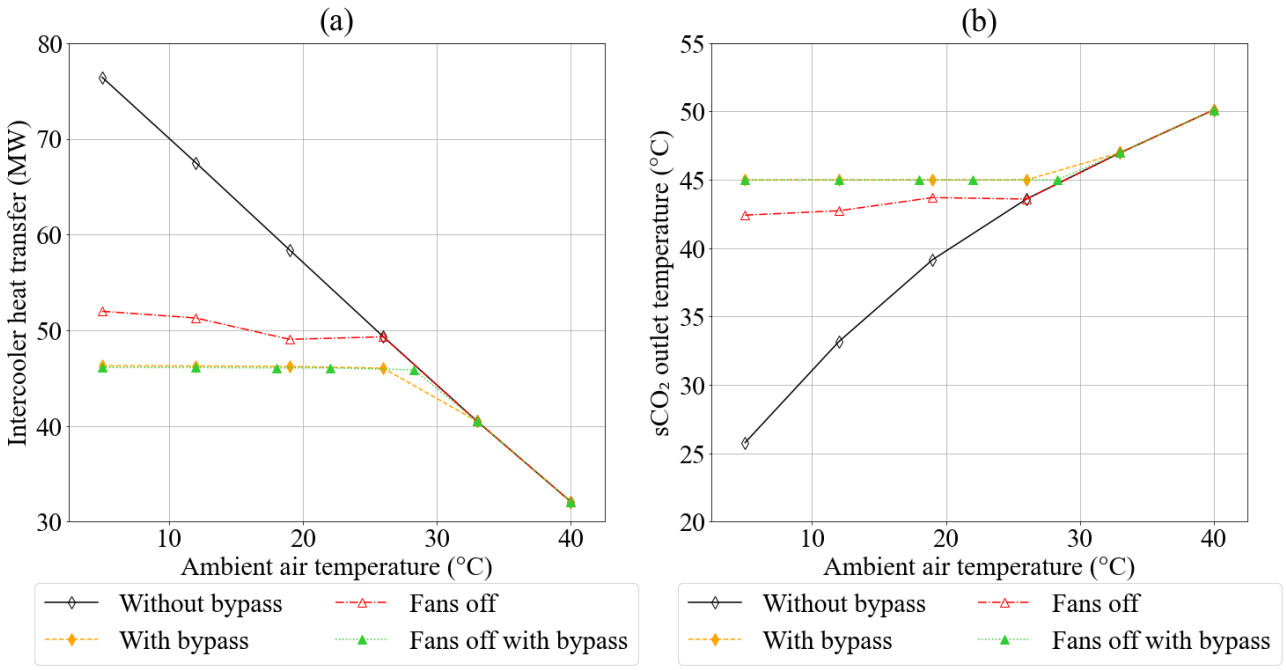

Figure 7-23: Intercooler heat rejection rates and sCO2 outlet temperatures for different control schemes

switching fans off produced heat rejection rates in the region of 52 MW and 49 MW. These values are much closer to the desired value of 46.2 MW than the uncontrolled case at the same air temperatures. This approximately stable performance is because, as previously mentioned, turning a cell's fan off results in an uncontrolled jump in heat rejection and sCO_2 outlet temperature. The specific number of fans switched off at each ambient temperature increment are shown in Figure 7-24 above, these were based on the number of fans one could turn off without under-cooling the sCO_2. None of the fans were switched off for temperature increments above those shown in Figure 7-24.

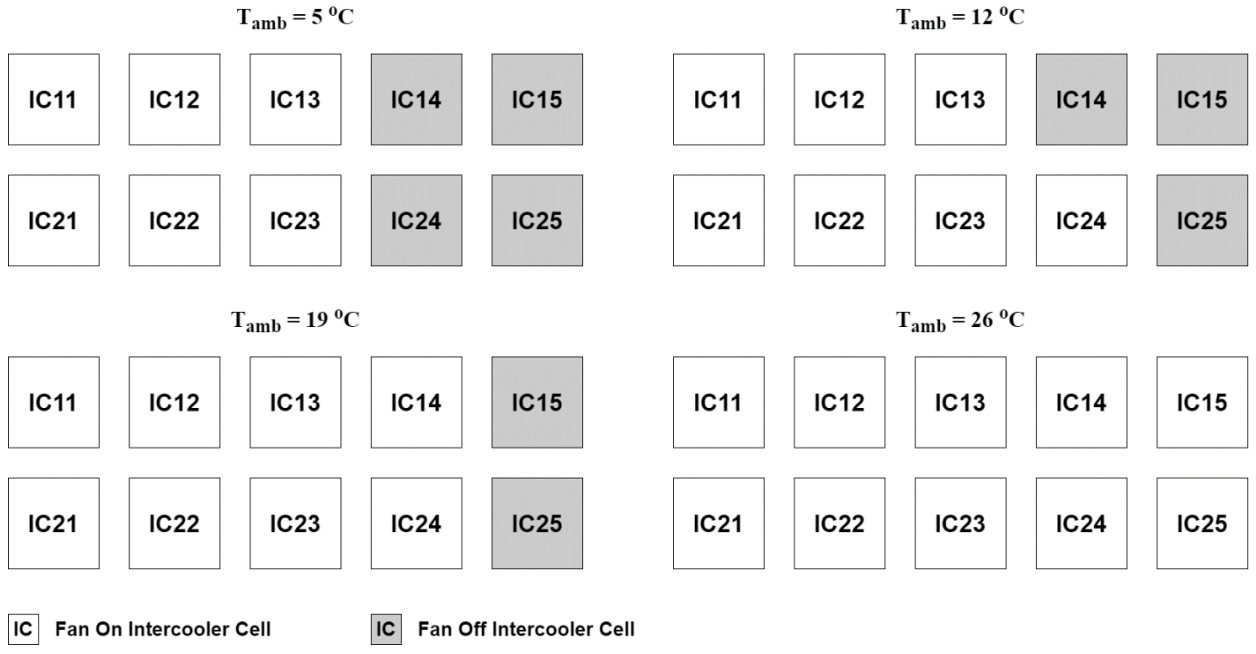

Figure 7-24: Intercooler fans off strategy per increment

The effect of the control methods on the important uncontrolled performance characteristics is shown in Figure 7-25. The pressure ratio increased in the case of the bypassing and combined methods, operating at values of almost 0.999 and around 0.9965 respectively. On the other hand, switching fans off decreased the pressure ratio. This was a result of the changes in the individual cells' mass flow rates, visible in Figure 7-26 further below. Switching fans off increases the sCO_2 mass flow rates in the cells with fans still on which directly increases the frictional pressure drop across those heat exchangers. Subsequently the pressure ratio gets lower as in Figure 7-25 (a). The fan power consumption is unchanged from the uncontrolled case when bypassing is implemented. Naturally, both schemes which involve switching fans off decreased the power consumed by fans in the Intercooler. At the coldest ambient temperature, both the combined and only fans off control methods decreased auxilliary power by almost 100 kW. This effect reduces linearly as the air temperature gets hotter, the slight deviation between 19 °C and 26 °C was attributed to the coarseness of the temperature increments which resulted in a jump from two fans off to no fans off.

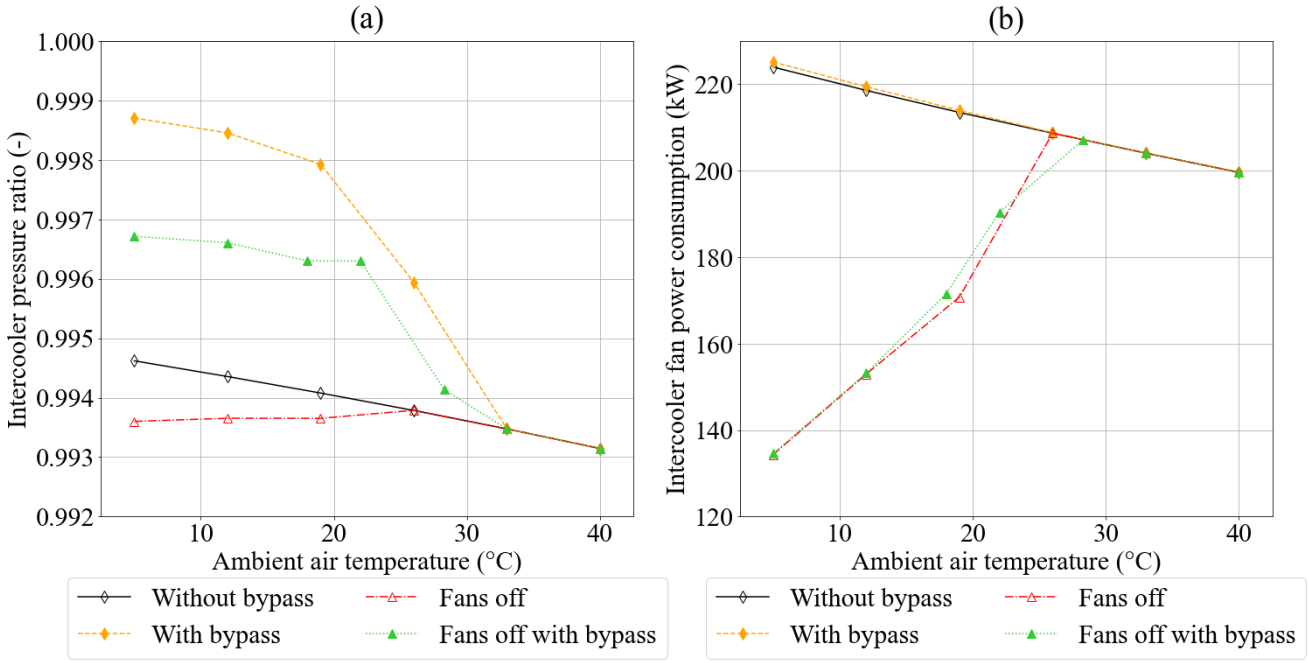

Figure 7-25: Intercooler pressure ratios and fan power consumptions for different control schemes across a range of ambient air temperatures

The combined approach follows a more linear trend because an additional point was added for the purpose of developing the automatic control method used in annual simulations. The specific fan operational strategy for the combined method can be seen in Table 7-4, note that temperatures greater than 22 °C incorporated only bypassing with no fans off. In summary, controlling using only bypassing improved pressure ratio performance and switching fans off improved the auxilliary power consumption of the system. The combined strategy improved both, the pressure ratio to a lesser extent, providing the best system performance from a cycle efficiency perspective. When assessing the impact on pressure ratio it is again important to note that the bypass valves were not properly sized and modelled in the system. In reality, any valve would have associated frictional and form pressure losses which would reduce the performance gains shown in Figure 7-25 (a). But, because each case was analysed with the same bypass modelling, the benefits of this type of control can be noted when compared relatively with the other types of control examined.

Table 7-4: Intercooler combined control fan operation strategy

	$0℃ < T_{amb} \leq 5℃$		$5℃ < T_{amb} \leq 12℃$		$12℃ < T_{amb} \leq 18℃$		$18℃ < T_{amb} \leq 22℃$	
	PC×1	PC×2	PC×1	PC×2	PC×1	PC×2	PC×1	PC×2
1	On	On	On	On	On	On	On	On
2	On	On	On	On	On	On	On	On
3	On	On	On	On	On	On	On	On
4	Off	Off	Off	On	On	On	On	On
5	Off	Off	Off	Off	Off	Off	Off	On

Figure 7-26 shows the sCO_2 mass flow rate distribution between the cells for each control scheme. It was found that across all schemes, flow rates decrease marginally from the inlet side of each street to the outlet. This was a result of the pressure losses experienced in the headers of the heat rejection system and is consistent with the PC results shown in Figure 7-20. The plots clearly show uncontrolled mass flow rates approximately equal to the original design point of 39.21 kg/s. The bypass results moving from low to high per cell flow rates as the ambient temperature increases, this process is gradual at lower temperatures (5 ℃ to 20 ℃) and sharper from 20 ℃ to the design point's ambient air temperature. This trend results from the over-cooling of sCO_2 in the heat exchanger when flow is bypassed. At temperatures of 12 ℃ and 19 ℃ the over-cooling is more extreme due to rapidly changing sCO_2 properties. This leads to a higher bypass mass flow rate than expected at these temperatures being required, and therefore the bypass fraction and per cell mass flow rates tend to resemble the lower, 5 ℃ ambient temperature results. The over-cooling described

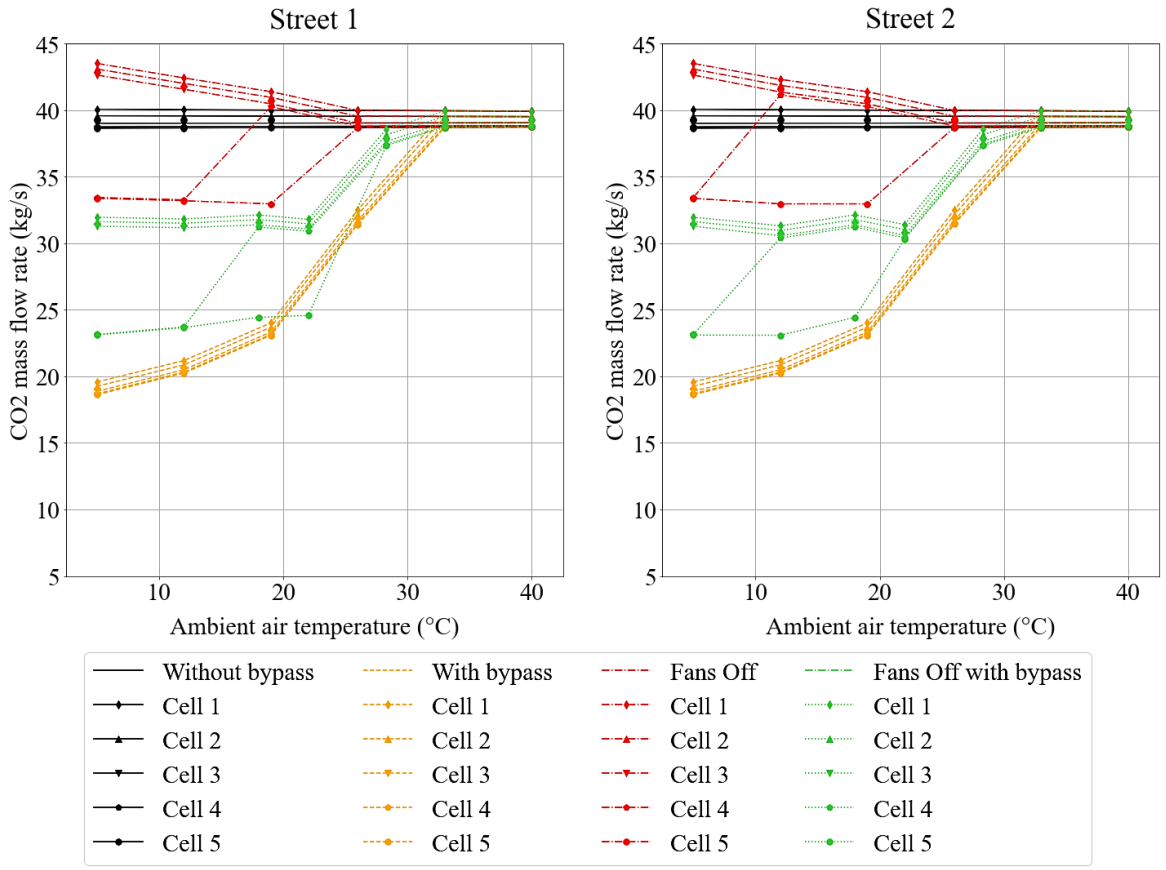

Figure 7-26: Intercooler sCO_2 mass flow rates per cell for different control schemes

above is also a potential risk of using this control method. When compared with the single cell results for the intercooler in Figure 7-14, it can be clearly seen that the entire system may experience adverse performance when exclusively bypassing to control the outlet temperature of the sCO_2. This is because each cell is receiving in the region of 20 kg/s to 25 kg/s while still experiencing forced draft heat rejection from the fans. This was shown previously to cause large, sudden changes in sCO_2 properties within the individual cells' heat exchangers. As a result, very strict monitoring of the system will be required to mitigate the possibility of phase change within the fluid. Figure 7-27 shows the per street bypass fractions which correspond to these per cell sCO_2 mass flow rate distributions. They were noted to be greater than 0.4 (40%) and up to around 0.51 (51%). These values are consistent with the required bypass fractions from the single cell analysis.

Figure 7-26 also demonstrates the way in which the sCO_2 distribution changes across the cells when fans are tuned off. The cells in street one and two with fans switched off experienced a sudden drop in sCO_2 mass flow rate. Subsequently, the other cells received more sCO_2 in accordance with governing equations of the system. Reduced, or negligible, air mass flow rate in a cell results in a lower sCO_2 mass flow rate being required in these particular cooling cells to balance the energy equation for that heat exchanger. The remaining cells, operating with their fans on, will reject far more heat, approximately four and a half times more heat. The density of sCO_2 increases as its temperature drops, and so the cells with active fans will experience a higher pressure loss, evident in Figure 7-25, which results in the increased mass flow rates seen in the plots. This sudden change in mass flow rate and pressure drop when switching fans off is something to be wary of when implementing the control method. As fans are switched off, the pressure of the sCO_2 will drop, which may lead to variations in fluid properties and heat transfer performance. However, it is important to note that the pressure change observed was minimal and will likely have no effect in the system as designed here. It is an effect which will need to be monitored when designing and controlling air-cooled heat rejection systems for sCO_2 power cycles.

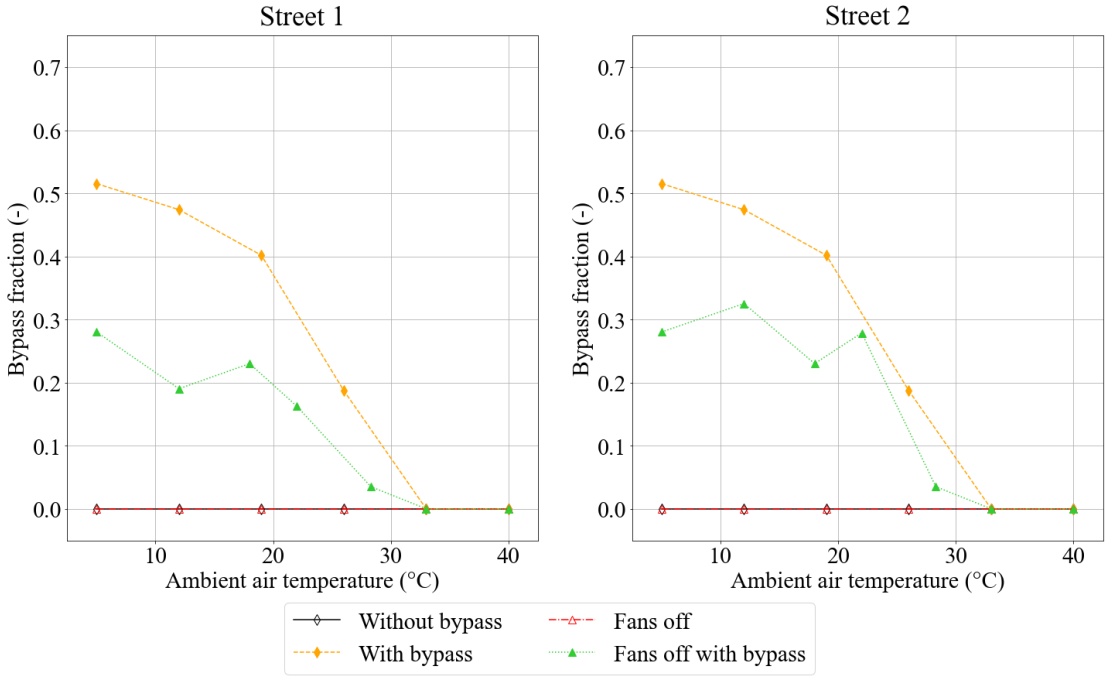

Figure 7-27: Intercooler bypass fractions per street different control schemes across a range of ambient air temperatures

It was expected that the combined control scheme would produce a flow distribution between only bypassing and exclusively switching off fans. This is shown in Figure 7-26 and Figure 7-27 where the per cell mass flow rates and per street bypass fractions lie between the results of the other two methods. It seems as though the results indicate that the individual cell's flow rates may be in the region of serious over-cooling. However, it is important to remember that these cells experience no bypassing and have their fans switched off. In the absence of serious heat rejection, the sCO_2 in these heat exchangers (cell four and five in both streets) is not at risk of changing phase or experiencing irregular heat transfer. Furthermore, the cells which were bypassed all experienced acceptable mass flow rates above 30 kg/s. An interesting trend noted for this control method was the inconsistent bypass fractions per street which can be seen in Figure 7-27. As with the precooler results, it was found that this is because the number of fans off in a single street changes the flow distribution to that entire street. Accordingly, the bypass fraction for that street needs to change too, and it was noted that it had to be higher in the street with less fans off. This trend means that the bypass valves need to have different controls setup which could potentially be avoided by having a single bypass for the entire intercooler.

The two best performing control methods were bypassing and a combination of bypassing with switching fans off. This is because they produced heat rejection rates of 46.2 MW as desired across the ambient air temperature range colder than the design point of 28.3 ℃. In summary, the combined control method provided the best performance from a cycle perspective while also stabilising the heat rejection rate of the intercooler and mitigating the risk of serious over-cooling the sCO_2. This is consistent with the findings for the PC. It was also noted that there was no way to control the system when the sCO_2 was under-cooled and the same is true for the PC. This presents a problem as the system is intended to be implemented in an area with generally high ambient air temperatures on an annual basis. This indicates that the system may need to be oversized so that control of the system and operation at the design point may be achieved regardless of ambient air temperature.

7.4 Load variation ambient air temperature studies

Observing the effect of varying cycle operational loads can assist in identifying the optimal operating conditions and improving the reliability of the heat rejection system designs. It is also valuable to observe the performance of the heat rejection systems at various loads. A cycle operational load refers to the amount of power generation required in the cycle. For the purposes of the studies carried out here, varying loads were simulated by changing the total inlet sCO_2 mass flow rate to the precooler and intercooler. The various loads examined are shown in Table 7-5 below along with the target heat rejection rates and sCO_2 outlet temperatures. Note that because of the number of load cases simulated and the number of control methods investigated, only ambient air temperatures representative of the average summer (31.53 ℃) and winter (18.15 ℃) months in Upington, South Africa were simulated for each load case.

Table 7-5: Cycle operational load and target values for heat rejection and sCO_2 outlet temperature

Load	Overall mass flow rate (kg/s)	Precooler heat rejection rate (MW)	Intercooler heat rejection rate (MW)	sCO_2 outlet temperature (℃)
100%	392.10	27.56	46.07	45.0
80%	313.68	22.10	36.90	45.0
60%	235.26	16.61	27.76	45.0
40%	156.84	11.09	18.53	45.0

The aim of these studies was to analyse the effect of changing ambient air temperatures on system performance at different cycle operational loads. Additionally, the efficiency and reliability of the control schemes previously implemented at full load conditions was investigated. The comparison tables and result maps shown below are coded by colour to indicate adherence to a target value (for heat rejection rate and sCO_2 outlet temperature) or improvement on the uncontrolled case (for pressure ratio and fan power consumption).

PRECOOLER

The precooler heat rejection rates and sCO_2 outlet temperatures, shown in Table 7-6 and Table 7-7 respectively, indicate that the most consistent form of control across all cycle loads is the combined control method. This is because it provided heat rejection rates and outlet sCO_2 temperatures very close to the PC targets in Table 7-5. It was also found that while bypassing achieves a good measure of control, it cannot be exclusively used at low loads. This was because the mass flow rates dropped too significantly within the heat exchanger without achieving the target heat rejection rate and outlet temperature. In general, it was observed that the required heat rejection in the precooler drops by about 5 MW for every 20% reduction in cycle load.

Furthermore, reducing the load to 80% resulted in over-cooling of the sCO_2 for summer conditions, which are at a higher ambient air temperature than the original design point of 28.3 ℃.

Table 7-6: Precooler heat rejection rates (MW) for various loads and ambient air temperatures

Load	Ambient air temperature (℃)	Uncontrolled	Bypass control	Fans off control	Combined control
100%	31.53	26.4015	26.4015	26.4015	26.4015
	18.15	34.4608	27.2538	28.3332	27.5670
80%	31.53	23.5377	22.1115	23.5377	22.1115
	18.15	31.2175	22.1688	25.8924	22.1426
60%	31.53	19.9160	16.4384	16.8399	16.6032
	18.15	27.2753	15.6572	18.2494	16.6174
40%	31.53	15.2403	*	13.2119	11.0894
	18.15	22.5519	*	11.7448	11.0871

*Bypassing at this load and these temperatures caused the model to fail

Poor adherence to target/reduced performance

Adequate adherence to target/no performance loss or gain

Very good adherence to target/performance gains

This is advantageous because when the sCO_2 is over-cooled, the control system can force the system to reject the desired amount of heat and output sCO_2 at the design temperature of 45.0 ℃. For example, the precooler rejects 23.5377 MW at 80% load and an ambient temperature of 31.53 ℃, when the required amount is 22.10 MW. Therefore, using a bypass approach or a combined approach, the heat rejection rate can be reduced to the target value. This is shown in the Table 7-6 above and Table 7-7 below where the target values are achieved for all cycle loads below 100%. This indicates that the heat rejection systems will perform well in the situation where the cycle has to be run at a partial load.

Table 7-7: Precooler sCO_2 outlet temperatures (℃) for various loads and ambient air temperatures

Load	Ambient air temperature (℃)	Uncontrolled	Bypass control	Fans off control	Combined control
100%	31.53	46.17	46.17	46.17	46.17
	18.15	39.06	45.00	44.22	45.00
80%	31.53	43.26	45.00	43.26	45.00
	18.15	36.29	45.00	40.71	45.00
60%	31.53	40.12	45.00	44.61	45.00
	18.15	33.70	45.00	42.41	45.00
40%	31.53	36.88	*	40.28	45.00
	18.15	31.96	*	43.41	45.00

*Bypassing at this load and these temperatures caused the model to fail

As is shown in Table 7-7, in the absence of control, the sCO_2 outlet temperature drops steadily as the load decreases by approximately 3.0 °C for every 20% reduction in load. This resulted in sCO_2 outlet temperatures near to the pseudocritical point at the heat exchanger exit for low cycle loads. This was noted to have potentially contributed to the simulation failure when trying to exclusively control the system using bypassing at 40% load. Despite the potential risks introduced at lower loads. A positive finding was that more fans could be switched off as the uncontrolled sCO_2 exit temperatures decreased. This led to large reductions in fan power consumption, as shown in Table 7-8. This will improve the cycle efficiency at lower loads. At colder temperatures, the fan power consumption values were 50% and 75% lower than the design case at 60% and 40% loads respectively. The corresponding consumption values were 87.4 kW at 60% load and 43.8 kW and at 40% load. This indicates that despite a lower power production in the cases where full load is not required or achieved, the cycle will be operating more efficiently. Being able to switch more of the fans off may also lead to increased lifespans in the fans and the associated subcomponents. Fans that are not running will not experience fatigue on components such as their shafts, bearings, and fasteners. This, in turn, may decrease the required number and frequency of fan maintenance activities. This is also a potential benefit when turning fans off at full load. It is important to note that fans should not be frequently started and stopped as this also impacts their lifespans, a well-developed control strategy will be required to avoid this.

Table 7-8: Precooler fan power consumptions (kW) for various loads and ambient air temperatures

Load	Ambient air temperature (°C)	Uncontrolled	Bypass control	Fans off control	Combined control
100%	31.53	167.1	167.1	167.1	167.1
	18.15	174.6	174.8	131.0	131.0
80%	31.53	167.1	167.2	167.1	167.2
	18.15	174.7	174.9	131.0	131.1
60%	31.53	167.2	167.3	125.4	125.4
	18.15	174.8	174.9	87.4	87.4
40%	31.53	167.3	*	125.5	125.5
	18.15	174.8	*	43.8	43.8

*Bypassing at this load and these temperatures caused the model to fail

Additionally, the combination of turning fans off and bypassing the heat exchangers in each street resulted in no failures, even at 40% load. The same can be said for exclusively switching off fans which indicates that at lower loads, switching fans off is a necessity for the precooler to operate as designed. This does have a negative effect on the pressure ratio of the system as seen in Table 7-9. Bypassing improves the pressure ratio, up to 0.9988 in some cases, while switching fans off always leads to pressure ratios lower than the uncontrolled case. The negative effect of turning fans off was noted to be marginal and not as significant as the alternative benefits seen when bypassing. That is why the combined method provides consistent improvements in precooler pressure ratio for all load cases. The improvements were not as large as the pure bypass control scheme, but the added benefit of reduced fan power consumption makes the combined control strategy more attractive. The trend for pressure ratio was observed to be a steady increase as the

cycle load decreased. This is a result of the lower sCO_2 mass flow rate into the system reducing the frictional and form pressure losses.

Table 7-9: Precooler pressure ratios (-) for various loads and ambient air temperatures

Load	Ambient air temperature (℃)	Uncontrolled	Bypass control	Fans off control	Combined control
100%	31.53	0.9968	0.9968	0.9968	0.9968
	18.15	0.9970	0.9988	0.9968	0.9972
80%	31.53	0.9980	0.9984	0.9980	0.9984
	18.15	0.9981	0.9995	0.9980	0.9990
60%	31.53	0.9989	0.9993	0.9988	0.9989
	18.15	0.9990	0.9998	0.9988	0.9992
40%	31.53	0.9995	*	0.9995	0.9997
	18.15	0.9996	*	0.9994	0.9996

*Bypassing at this load and these temperatures caused the model to fail

In summary, it was found that the precooler can operate as desired for a range of reduced loads up to 40% of full load. Bypassing was shown to be ineffective as a control at 40% load and it was noted that it is necessary to switch fans off at lower loads for the system to function as designed. Furthermore, at lower loads, an increased number of fans can be turned off. This improves both cycle efficiency and performance while potentially extending the lifespans of the fans and reducing fan maintenance frequency. Finally, the combined control method was observed to be best suited for the control of the precooler across all cycle loads, not just full load as previously noted in Section 7.3.

INTERCOOLER

The IC results for heat rejection rate and sCO_2 outlet temperature are shown in Table 7-10 and Table 7-11 respectively. It was found that the bypassing and a combined control approaches were best suited to stabilising the heat rejection rate and sCO_2 outlet temperature of the system across all cycle loads. The only instance where the targets shown in Table 7-5 were not achieved was the full load case where the sCO_2 was under-cooled. This is consistent with previously observed results in the PC. It was found that the combined

Table 7-10: Intercooler heat rejection rates (MW) for various loads and ambient air temperatures

Load	Ambient air temperature (°C)	Uncontrolled	Bypass control	Fans off control	Combined control
100%	31.53	42.3116	42.3116	42.3116	42.3116
	18.15	59.5011	46.2301	49.9913	46.0664
80%	31.53	39.1998	36.9135	39.1998	36.9135
	18.15	54.9494	37.0472	37.8157	36.8634
60%	31.53	34.6394	27.7891	29.6395	27.7511
	18.15	46.9978	27.8135	33.7729	27.7794
40%	31.53	26.7040	18.5493	19.9756	18.5339
	18.15	33.4417	18.5545	21.2509	18.5375

control method produced results slightly closer to the targets than the bypass control method from a heat rejection rate perspective. This was because switching fans off provided a drop in heat rejection rate, bringing the system close to the target before the bypass mass flow rates were iteratively solved for. This narrowed the solution space for these mass flow rates and increased the degree of accuracy and convergence to the targeted values for heat rejection and sCO_2 outlet temperature.

Table 7-11: Intercooler sCO_2 outlet temperatures (°C) for various loads and ambient air temperatures

Load	Ambient air temperature (°C)	Uncontrolled	Bypass control	Fans off control	Combined control
100%	31.53	46.32	46.32	46.32	46.32
	18.15	38.52	45.00	43.31	45.00
80%	31.53	43.80	45.00	43.80	45.00
	18.15	32.30	45.00	44.51	45.00
60%	31.53	39.62	45.00	43.69	45.00
	18.15	24.07	45.00	40.40	45.00
40%	31.53	33.79	45.00	43.50	45.00
	18.15	18.95	45.00	42.03	45.00

It was previously noted in Section 7.2 and Section 7.3 that the IC is more sensitive to changes in ambient air temperature than the precooler. This was also shown to be true when varying the cycle load. The system

over-cools the sCO_2 at both summer and winter ambient temperatures for every load besides 100%. Again, there was found to be an advantage to this trend from a control perspective. Because over-cooling of the sCO_2 means that the system can be controlled to perform as designed, the range of operating conditions expands as the cycle load decreases. The same is true for the PC. This is shown in the heat rejection rate of 39.1998 MW at 80% load and 31.53 ℃ ambient air temperature from Table 7-11 which is already well above the target for 80% load of 36.90 MW. Furthermore, the IC sCO_2 outlet temperature drops by much larger

increments than the precooler in the absence of control. The lowest PC sCO_2 outlet temperature was 31.96 ℃ at 40% load and 18.15 ℃ ambient temperature while the intercooler experienced a lowest sCO_2 outlet temperature of 18.95 ℃ under the same load and ambient conditions. These incremental drops in sCO_2 outlet temperature were also less consistent than in the precooler. Irregular heat transfer and sCO_2 outlet behaviour aside, the lower observed temperatures and higher observed heat rejection rates indicate that at lower cycle loads, a higher number of fans can be switched off in the IC than in the PC.

Table 7-12 below clearly shows the benefit of the excess heat rejection achieved in the system at low loads and temperatures. At winter temperatures (18.15 ℃) there are consistent reductions in fan power consumption. At 80% load this results in approximately 43 kW of auxilliary power being saved and at 40% load more than half of the intercooler's auxilliary power consumption is negated, with the fans only drawing around 86 kW instead of 215.0 kW. At summer temperatures (31.53 ℃) the reductions in auxilliary power were not as significant as they were for winter temperatures. However, consistent reductions in fan power consumption of 20% and 40% were achieved at the lowest two load cases. This indicates that the operating ambient temperature range expanded significantly for the system at loads of 60% and 40%. An additional benefit, as with the PC, of turning off so many fans is the potential to extend the lifespan of the fans and their subcomponents.

Table 7-12: Intercooler fan power consumptions (kW) for various loads and ambient air temperatures

Load	Ambient air temperature (℃)	Uncontrolled	Bypass control	Fans off control	Combined control
100%	31.53	205.0	205.0	205.0	205.0
	18.15	214.1	214.6	171.2	171.4
80%	31.53	205.1	205.2	205.1	205.2
	18.15	214.2	214.9	128.5	128.6
60%	31.53	205.2	205.5	164.2	164.2
	18.15	214.6	215.2	128.7	128.9
40%	31.53	205.5	205.7	123.3	123.3
	18.15	215.0	215.4	86.0	86.1

The pressure ratio results in the IC have similar trends to the PC results. Table 7-13 shows that the control method which improves pressure ratio the most is bypassing, while the combined control scheme provides decent improvement. Switching fans off caused a reduction in pressure ratio as a result of increased sCO_2 mass flow rate in the cells with fans on. This effect produced the smaller gains observed when the combined

control scheme was used. The general trend was also an increase in pressure ratio as the cycle load decreased which was also a result of reduced sCO_2 mass flow rate and subsequently pressure drops in the system. It was noted that the higher the pressure ratio in the uncontrolled case the harder it was to improve on the value when implementing either the bypass or combined control methods. However, the pressure ratios of 0.9996 and 0.9997, observed when bypassing at 40% load, result in an almost negligible pressure drop across the system. While this is beneficial from a cycle performance perspective, bypassing provides no advantages from a fan power consumption perspective. So, it is as in the precooler, the combined control method provides the best joint benefits across all cycle loads by improving pressure ratio and reducing the auxilliary load of the intercooler.

Table 7-13: Intercooler pressure ratios (-) for various loads and ambient air temperatures

Load	Ambient air temperature (℃)	Uncontrolled	Bypass control	Fans off control	Combined control
100%	31.53	0.9935	0.9935	0.9935	0.9935
	18.15	0.9941	0.9980	0.9937	0.9962
80%	31.53	0.9960	0.9970	0.9960	0.9970
	18.15	0.9964	0.9989	0.9958	0.9964
60%	31.53	0.9978	0.9989	0.9977	0.9982
	18.15	0.9981	0.9994	0.9977	0.9988
40%	31.53	0.9991	0.9996	0.9989	0.9991
	18.15	0.9992	0.9997	0.9989	0.9993

7.5 Annual control study

Based on the findings of the previous studies, the combined control strategy was selected for further analysis using data representative of a typical year's ambient air temperatures. A dataset representative of a typical year's mean ambient air temperature with a 95% confidence interval was used to perform an analysis of the heat rejection systems' steady-state performance. Also note that the scope of the analysis was limited to varying the ambient air temperatures and not the cycle load. To achieve this would require a more refined implementation of the combined control scheme. As it was, the combined control was used in the precooler, and intercooler models as described below for full cycle load. The aim of this study was to show the efficacy of the control scheme across an extended period with hourly changing ambient air temperatures. The generation of the data for this period, as well as the specific daily operational hours is also described further below. The results of the study were used to identify potential areas of improvement in the design of the air-cooled heat rejection systems and in the implementation of the control scheme. The study also provides insight into how the system will respond and perform on an annual basis.

COMBINED CONTROL STRATEGY IMPLEMENTATION

To control the systems automatically when running annual simulations, an Excel spreadsheet was implemented in the models. The spreadsheet takes the ambient air temperature as an input and conditionally

solves for which fans should be off and what the bypass mass flow rates should be for each street. It then outputs these values to the specific fans and bypass valves in the system models. Recall that a fan speed of 2 rpm indicates a fan which is off. This is because, in reality, the fans will stay spinning at a very low rate due to the natural draft pressure difference between the cells inlets and outlets. The fan control strategy was set up in the system according to the values from Table 7-3 and Table 7-4 for the precooler and intercooler respectively. The per street bypass mass flow rates were calculated using stepwise linear equations, see Appendix E-2, fitted to the combined control scheme results. Table 7-14 and Table 7-15 below provide the per street bypass mass flow rate polynomials used in the precooler and the intercooler respectively.

Table 7-14: Precooler per street bypass mass flow rate (kg/s) control strategy

Air temperature range (℃)	**Street 1**	**Street 2**
$0℃ < T_{amb} \leq 10℃$	$\dot{m} = -8.1304T_{amb} + 85.236$	$\dot{m} = -8.0782T_{amb} + 132.19$
$10℃ < T_{amb} \leq 18℃$	$\dot{m} = -7.3639T_{amb} + 146.98$	$\dot{m} = -7.3639T_{amb} + 146.98$
$18℃ < T_{amb} \leq 22℃$	$\dot{m} = -6.9811T_{amb} + 159.40$	$\dot{m} = -6.7807T_{amb} + 191.26$
$22℃ < T_{amb} \leq 28.3℃$	$\dot{m} = -6.7683T_{amb} + 201.58$	$\dot{m} = -6.7683T_{amb} + 201.58$

This method of automated control is not as elegant as a well-developed proportional-integral-derivative (PID) controller, which can be found in Flownex ® SE. However, PID controllers, by definition, require transient models to be implemented. This would have driven the simulation runtimes up significantly. Furthermore, this work was primarily focused on the development of steady-state models which were run in Section 7.5.

Table 7-15: Intercooler per street bypass mass flow rate (kg/s) control strategy

Air temperature range (℃)	**Street 1**	**Street 2**
$0℃ < T_{amb} \leq 5℃$	$\dot{m} = -3.1884T_{amb} + 70.872$	$\dot{m} = -3.1884T_{amb} + 70.872$
$5℃ < T_{amb} \leq 12℃$	$\dot{m} = -3.7105T_{amb} + 77.885$	$\dot{m} = -3.2807T_{amb} + 109.91$
$12℃ < T_{amb} \leq 18℃$	$\dot{m} = -4.1839T_{amb} + 131.77$	$\dot{m} = -4.1839T_{amb} + 131.77$
$18℃ < T_{amb} \leq 22℃$	$\dot{m} = -6.3308T_{amb} + 168.41$	$\dot{m} = -5.9717T_{amb} + 190.78$
$22℃ < T_{amb} \leq 28.3℃$	$\dot{m} = -9.6147T_{amb} + 278.97$	$\dot{m} = -9.6147T_{amb} + 278.97$

WEATHER DATA AND AMBIENT AIR TEMPERATURE DATASET

This study made use of real-world hourly weather data obtained from SolarGIS for Upington from the start of 1994 to the end of 2021 (SolarGIS, 2023). This weather dataset included hourly data for DNI, ambient air temperature, wind speed, and relative humidity. Each hourly datapoint was defined by a year ranging from

1994 to 2021, a month ranging from 1 to 12, a day ranging from 1 to 30, 31, or 28 depending on the month, and an hour ranging from 0 to 23. Unfortunately, the data cannot be shared here. Within each year, the data were trimmed to only include hours of the day between 2 pm (14:00) and 9 pm (21:00) for all days of each year. This time range is representative of a CSP plant which will operate at full capacity during peak demand hours. Using a normal distribution, the mean and standard deviation were extracted for each relevant hour of each day of the year for the ambient air temperature data from 1994 to 2021. The standard deviation was then subtracted and added to each mean value to create a 95% confidence interval on the typical ambient air temperature data. The code listing for this process is not included in the present work but is available on request.

To assess the efficacy of the combined control method, both the heat rejection rate and sCO_2 outlet temperature were recorded and plotted for both the PC and IC using the combined control described above for a typical year. The systems' pressure ratios and fan power consumptions, the two key performance variables from a cycle perspective, were also recorded and plotted. Because the dataset generated was only for 8 hours in each day, the plots do not represent an hour-by-hour performance spanning a year. Instead, for the heat rejection rates and power consumptions, the cumulative values for one day were calculated by summing the heat rejection rates recorded for each day as MWh and the fan power consumption recorded for each day as kWh. The pressure ratios, ambient air temperatures, and sCO_2 outlet temperatures were all calculated as averages so that they could be represented over the course of a year.

PRECOOLER

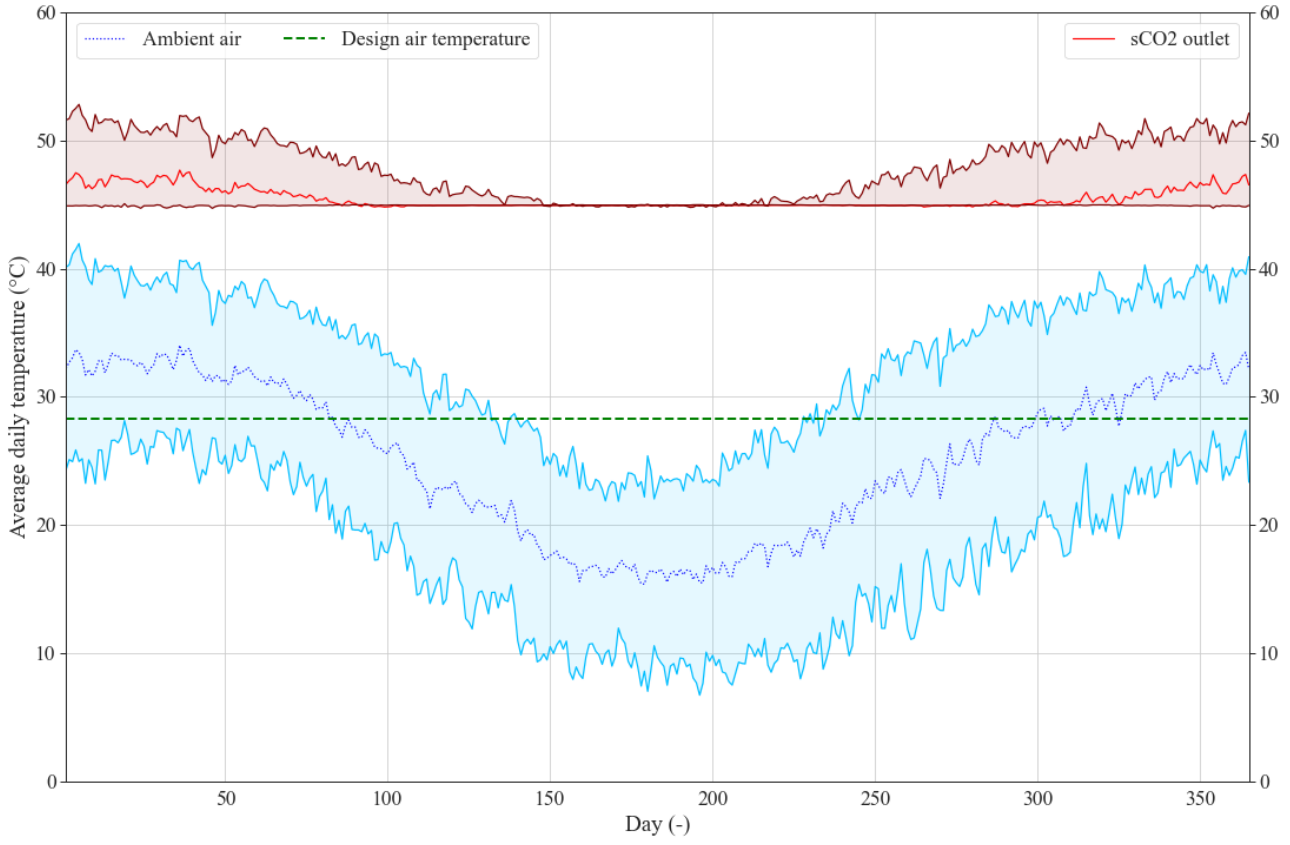

Figure 7-28: Precooler average daily sCO_2 outlet and ambient air temperature ranges for a typical year

The average daily sCO_2 outlet temperature for a typical year is shown in Figure 7-28. The plot also shows the average daily ambient air temperature and a line indicating the ambient air temperature that the heat rejection system was designed to operate at. It was found that for all temperatures below this design point, the sCO_2 outlet temperature converged to values near 45.0 ℃. As expected, this control is not as smooth as it could have been, there were small deviations above and below 45.0 ℃ which could be negated by implementing a more refined control system in the model. Furthermore, the system is only fully controlled at all three ambient temperature values (the mean, upper and lower 95% confidence interval values) for around 70 days of the whole year. This is only 20% of the time, approximately. The rest of the time, there is the potential that the sCO_2 outlet temperature could vary between 45 ℃ and 50 ℃. Ideally, the temperature can be controlled all year but that was not found to be the case. Fully controlling the sCO_2 outlet temperature using a lower plant and cycle load is impractical because for 80% of the year the plant will be operating below its capacity and designed power generation. Additionally, the power generation reduction may extend to 40% during the summer months, as shown in Section 7.3, which span at minimum 25% of the year. These findings indicate that to have a system which operates as required by the cycle design, the air-cooled heat rejection system will need to be oversized. For this reason, as well, the control method implementation was not refined to provide a smoother output. If the system needs to be resized, which is a relatively lengthy process, there is no benefit in refining the control implementation at this point.

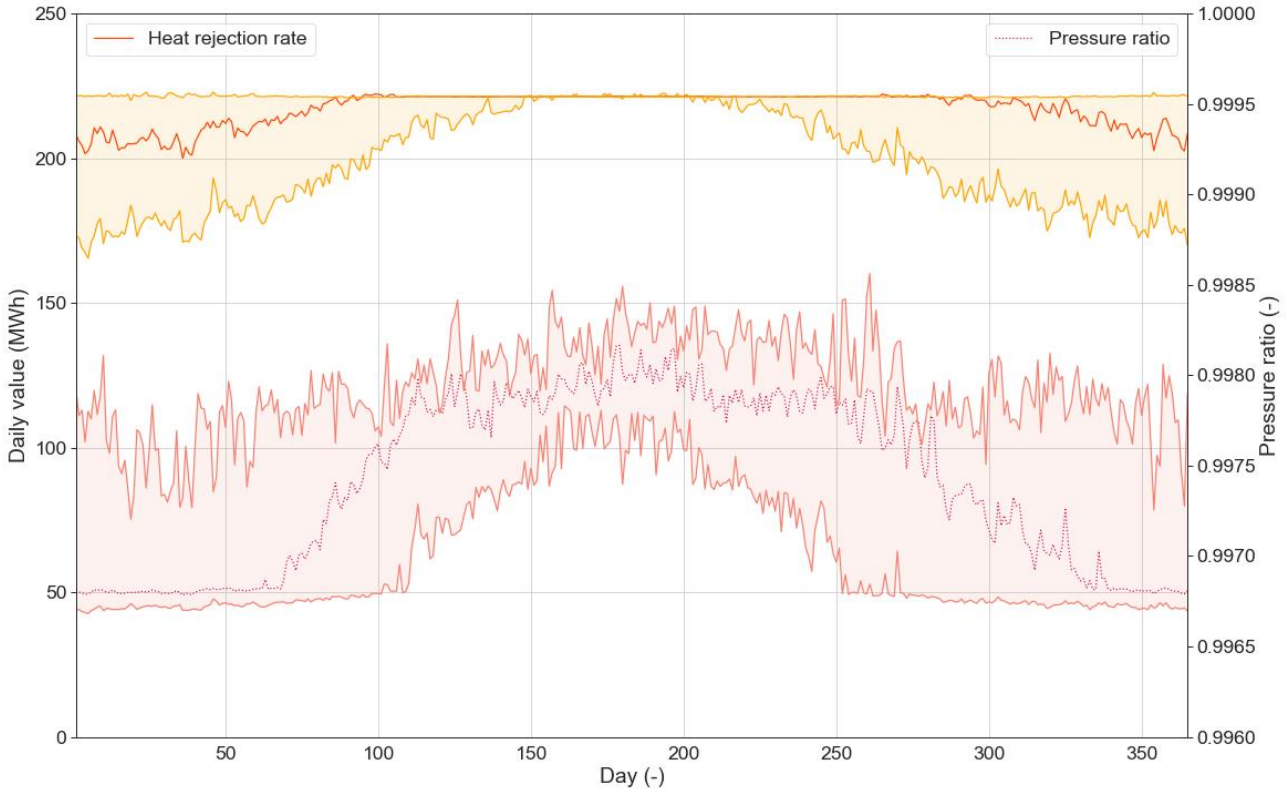

Figure 7-29: Precooler daily cumulative heat rejection and average pressure ratio for a typical year

The trend for heat rejection rate in Figure 7-29 was very similar to the sCO_2 outlet temperature trend. It is more accentuated, with cumulative heat rejection ranging between 220 MWh and 170 MWh in the summer months, because these were not average values. During the winter months when the control method was effective, the system rejected 220 MWh consistently. This compares nicely to the target value of 220.8 MWh which is the designed heat rejection rate of 27.6 MW from Section 7.3 multiplied by the 8 hours over which

the system will operate in a day. Because the trend is the same as before, the strategy to control the system for the whole year is the same. The system needs to be oversized or the cycle operated at a lower load as per the discussion in Section 7.3. Figure 7-29 also shows the trend for the precooler pressure ratio over the course of a typical year. These results show the benefits of the control strategy from a cycle performance perspective but also expose some of the shortcomings in the design of the system. Because it is too small and only the lower limit of ambient air temperatures was consistently below the control limit of 28.3 ℃, there is a wide range on the pressure ratios achieved over a typical year. However, it was noted that these pressure ratios ranged between 0.9967 and 0.9985. This is a relatively narrow range for pressure ratio and will make little difference from a cycle perspective. Fortunately, these are already high values for pressure ratio which indicates that the system was designed well from a pressure loss point of view. On an annual basis, the system will reduce the amount of work required by the upstream compressor consistently with a period of increased benefit during the winter months.

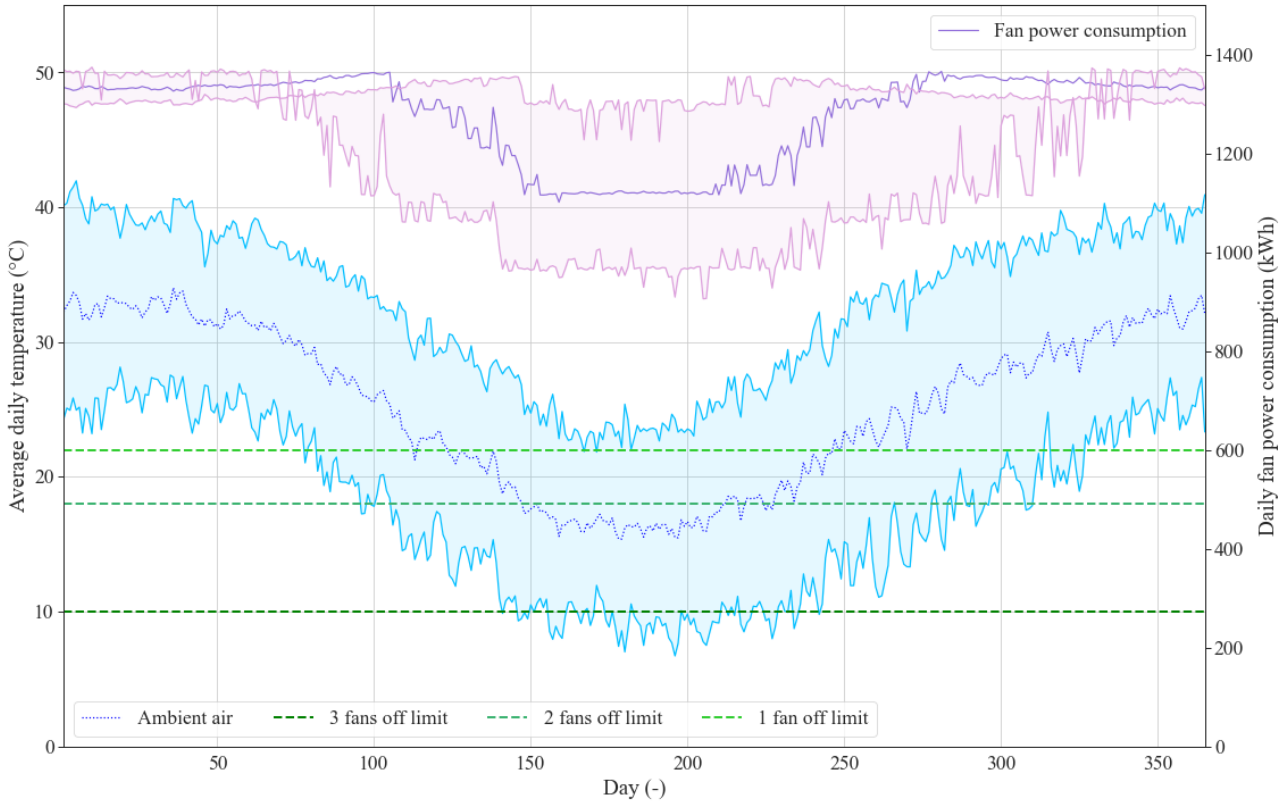

Figure 7-30: Precooler daily cumulative fan power consumption and average ambient air temperature for a typical year

Figure 7-30 shows the daily cumulative fan power consumption for the precooler over a typical year. This performance result was also plotted alongside the ambient temperature to observe the effect that switching fans off had on the likely performance of the system. To assist in this analysis, the plots include temperature lines which indicate the maximum temperature at which the specified number of fans were switched off. It is also important to remember that at lower ambient air temperatures, in the absence of control, fan power consumption is much lower than at higher ambient temperatures. Figure 7-22 (b) shows this clearly. In Figure 7-30 it was found that the fan power consumption never exceeds 1400 kWh daily, which corresponds to 175 kW for the entire system in one hour of the day assuming uniform hourly performance. This is advantageous from an auxilliary power perspective because the PC was designed to consume approximately

170 kW. An average maximum hourly fan power consumption of 175 kW therefore means that the system is not drawing excess power all year round. The trend in fan power consumption also shows some irregularities around days 100 and 300 of the year with the mean value falling outside the confidence interval bands. This is because the number of fans switched off is a discrete value dependent on the ambient air temperature. It is also due to the fact that less fan power is consumed at higher ambient air temperatures (see Figure 7-22 and Figure 7-20). This means that the upper line of the band for fan power in Figure 7-30 represents the performance at the maximum ambient air temperature. For example, on day 100, the mean air temperature results in no fans being switched off, so does the maximum temperature, and it results in a lower fan power consumption than the mean value. The minimum temperature meanwhile requires that 2 fans be turned off.

In cases like the abovementioned, the mean value will fall outside of the confidence interval band on the plot. In summary, the trends from Figure 7-30 indicate that fans will seldom be turned off during the year and the system will draw regular amounts of auxilliary power. The data also indicates that there may be none of the benefits from a fan maintenance and longevity perspective mentioned in Section 7.3. Once again, of the two potential solutions to this problem, oversizing the heat rejection system is the more attractive. It would not be beneficial to reduce the cycle load just to turn off fans and improve cycle efficiency as the plant would already be producing less power.

INTERCOOLER

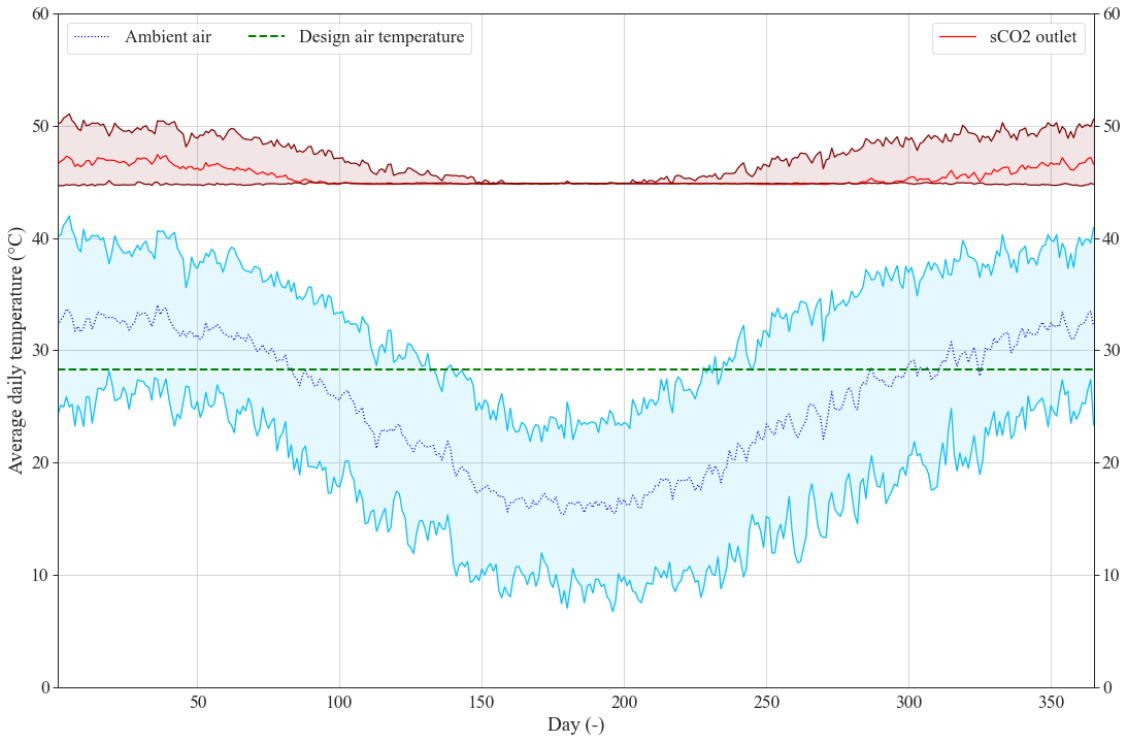

Figure 7-31: Intercooler average daily sCO_2 outlet and ambient air temperature ranges for a typical year

Figure 7-31 shows the average daily sCO_2 outlet temperatures for the intercooler over the course of a typical year. It was observed that the trends were very similar to those seen in the precooler study. The control scheme implementation in the model produces rough results and is only able to fully control the system during the coldest months. An additional observation not made before is that the upper confidence interval ambient temperature is not converged during some periods where it lies below the design point of the

system. This observation increased the evidence that the control scheme implementation was not accurate. Another cause of this effect is the fact that the control scheme implemented is based on bypass mass flow rate data generated at very specific limit points which was assumed to change linearly between those points. In reality, this will not occur, especially considering that sCO_2 properties are very sensitive to temperature changes. Small deviations above and below the target sCO_2 outlet temperature were therefore expected across the course of a year. Additionally, the sudden jumps in heat rejection and sCO_2 outlet temperature which occurred as fans were switched on or off will have affected the required bypassing more dynamically than could be captured using the control implemented in the models. A more refined control scheme implementation would be beneficial, however, considering that the systems under-cool the sCO_2 most of the year, revision of the control within the model was not carried out.

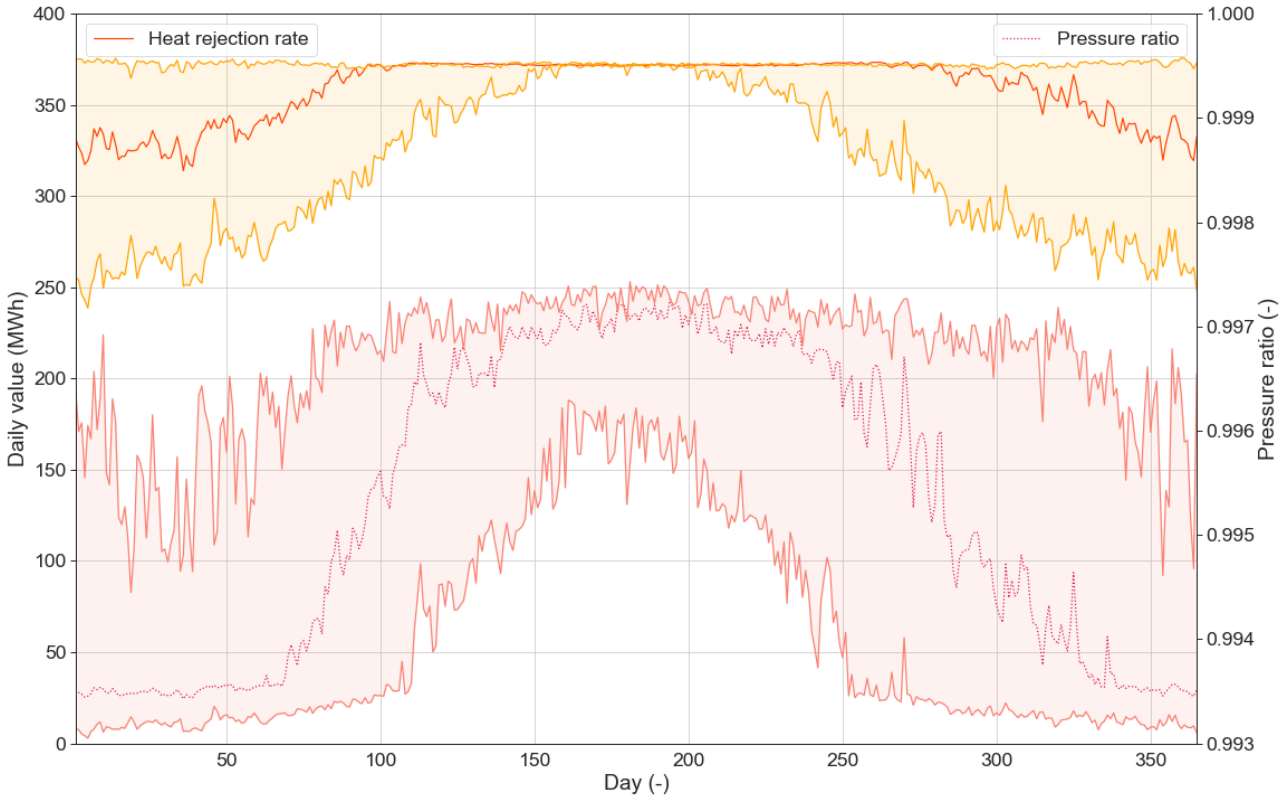

Figure 7-32: Intercooler daily cumulative heat rejection and pressure ratio ranges for a typical year

Figure 7-32 displays the cumulative heat rejection rate and average daily pressure ratio results for a typical year. The performance of the IC is also not ideal, especially during the summer months. Cumulative heat rejection ranged between 370 MWh and 250 MWh in these months. However, during the winter months when the control method was effective, the system rejected 370 MWh consistently. This compares nicely to the target value of 369.6 MWh which is the designed heat rejection rate of 46.2 MW from Section 7.3 multiplied by the 8 hours over which the system will operate in a day.

Overall, a key takeaway from both heat rejection systems' results is that the sCO_2 was not heavily over-cooled at any point throughout the year. However, under-cooling is very likely for most of the year, as seen in both Figure 7-31 and Figure 7-32, and it will affect the performance of upstream and downstream cycle components. Higher inlet temperatures to the compressors has been shown to negatively impact cycle efficiency (Sathish et al., 2021). Additionally, fluctuating temperatures at the compressors' inlets may result

in them operating at off-design conditions, this can have a negative impact on their longevity and maintenance requirements. Fortunately, the fluid properties of sCO_2 are fairly consistent at these higher temperatures which makes dramatic changes in the properties which affect heat transfer and fluid flow very unlikely. So, abnormal fluid properties will not impact on compressor performance. Nonetheless, it is essential for both the precooler and intercooler to perform as designed in the cycle and this means resizing them to over-cool the sCO_2 across the possible range of ambient air temperatures.

The pressure ratio varied in a very similar manner to the precooler. Figure 7-32 shows the trend of low mean pressure ratios with spikes in the lower confidence interval values as they drop below the design point during the summer months. This changed during the winter months where generally high pressure ratio values were observed. The difference between the two systems' pressure ratio performances was that the intercooler had the potential to increase the pressure ratio by a not insignificant amount. In other words, during the winter months there would be noticeable gains from a cycle efficiency perspective as the pressure ratio increases from 0.993 to 0.997. This corresponds to pressure drop reduction of approximately 42 kPa across the intercooler. The intercooler tends to experience more tangible gains from a pressure ratio perspective when its performance is controlled. This has been a consistent trend in Chapter 0 when comparing the PC and the IC in terms of pressure drop characteristics. It is a result of the increased number of cells present in the intercooler. Increased division of sCO_2 mass flow rate provides pressure ratio gains regardless of control scheme and, when coupled with a form of control which includes bypassing, it provides more tangible gains.

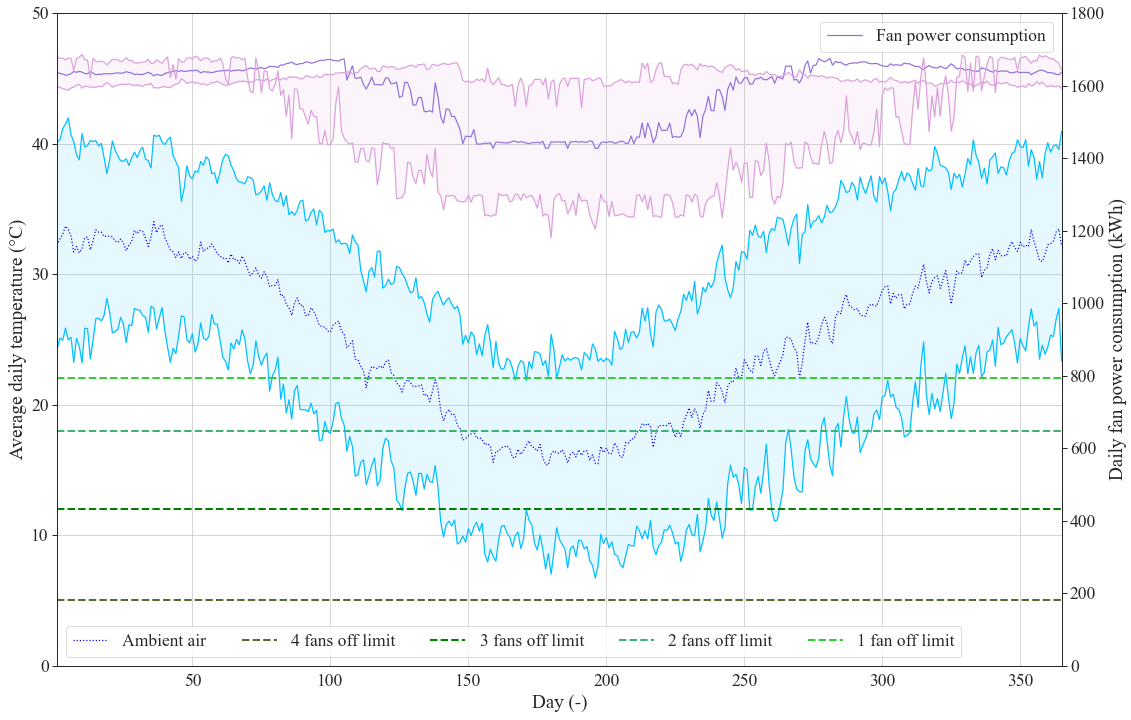

Figure 7-33: Intercooler daily cumulative fan power consumption and average ambient air temperature ranges for a typical year

Figure 7-33 shows the cumulative fan power consumption for the intercooler over the course of a typical year. The behaviour is observed is once again like that seen in the precooler's results. The difference is that the intercooler consumes more auxilliary power, up to approximately 1 700 kWh. This corresponds to 212.5 kW for the intercooler hourly, assuming uniform power consumption. This is around 40 kW higher than

the precooler's maximum fan power consumption which was expected considering the intercooler has two more cells than the precooler. It is, however, near the design IC fan power of approximately 205 kW from Figure 7-25. The same trend from the PC where the mean value is outside the bounds of upper and lower in terms of fan power consumption persists. Interestingly, it was noted that the point at which four fans could be switched off was never reached throughout the year. This is not beneficial and provides further evidence that the system should either be oversized, or the cycle should be run at a reduced load for portions of the year. As with the PC, he second option is not feasible as it does not make sense to reduce the generated power to try and save small amounts of auxilliary power in the cooling system. Additionally, the range of operating fan power consumption is wide throughout the year, this is also true for the PC. This means that the advantages of switching fans off previously identified in this work will not come into effect as often as they could. An alternative possibility is that, in the winter months, it is more likely that the system will operate at the mean temperature values or below. Unfortunately, the scope of this study is limited in this regard. A comprehensive Monte-Carlo analysis should provide better insight into the actual long-term performance and control of both air-cooled heat rejection systems.

It is important to consider that the ambient air temperatures observed are representative of the afternoon in Upington. It makes sense then that they are generally very high. However, implementation of the system may see the plant operate exclusively in the evenings to supply power during peak tariff hours and maximise the profitability of the proposed cycle. This operational period may also assist in the event of grid shortages during the evenings. To analyse the potential difference this could make, the hours of interest were altered when sampling the weather data to be from 17:00 (5 pm) to 21:00 (9 pm). This effectively cuts out the afternoon temperatures which are the hottest. Figure 7-34 shows the difference that this makes to the ambient air temperature dataset. The trends indicate an improvement from a control perspective.

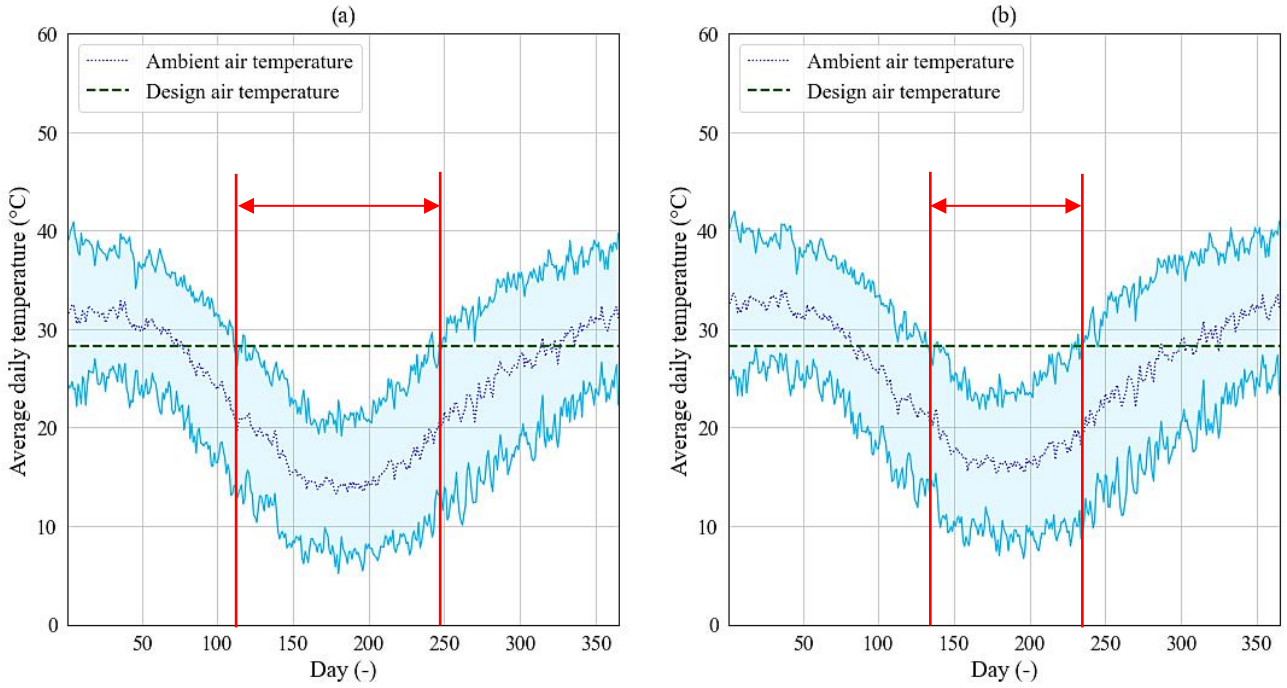

Figure 7-34: Ambient air temperature ranges for a typical year (a) from 5 pm to 9 pm and (b) from 2 pm to 9 pm

A comparison of the two plots shows that in the original case, Figure 7-34 (b), the mean ambient temperature is below the design ambient temperature 62.54% of the year while the upper confidence interval ambient

temperature is below the design ambient temperature 28.18% of the year. This corresponds to 103 days of the year where complete control of the system can be achieved with 95% certainty. On the other hand, if the plant were to operate in the evenings as in Figure 7-34 (a), the mean and upper confidence interval ambient temperatures are below the design ambient temperature 68.73% and 37.11% of the year respectively. This shows marginal improvement, with the plant being fully controlled for 135 days of the year instead of 103 days, this can be seen visually in Figure 7-34. However, this is far from the ideal case where the desired heat rejection rate is achieved at full load for 365 days of the year. Therefore, while the system developed functions as required, it would be necessary to increase its size, or reduce the plant load somewhat for design conditions to be met.

8. Conclusions and recommendations

This final chapter provides a summary of the main sections in this work and concludes them. A list of recommendations for future work has also been presented at the end of the section.

The present work focused on the development and performance analysis of steady-state 1D thermofluid models and a modelling methodology for air-cooled heat rejection systems in a proposed CSP plant operating using a sCO_2 Brayton cycle. With this objective in mind, relevant literature relating to the design and operation of air-cooled heat rejection systems applicable to sCO_2 CSP plants was reviewed. The project was then split into two major sections, firstly, development of thermofluid network models to size the PC and IC in the proposed cycle model, this includes the development of conceptual layouts for the systems. This section includes the use of the models to determine near-optimal process and geometrical designs as well as select key components. Secondly, the development of more advanced, discretised thermofluid networks in Flownex ® SE using the near-optimal process and geometrical designs and key components found previously. This portion of the work included use of the models to assess the sensitivity of the systems to off-design conditions such as varying ambient air temperatures and part-load operation. Additionally, several control schemes which counteract over-cooling within the systems were investigated in the second part of the project.

Initially, a 1-D thermofluid network modelling approach was taken using Python to model a potential utility-scale air-cooled heat rejection system at a proposed sCO_2 CSP plant in South Africa. Review of the relevant literature on air-cooled systems applicable to sCO_2 CSP plants revealed that previous modelling of these systems has typically neglected to consider one of the following: the mechanical integrity of the tubes under high sCO_2 pressures, appropriate sizing of distribution manifolds, or accurate air-side performance with the inclusion of fans used in industry and the relevant performance curves. The approach taken in the initial steady-state 1D thermofluid network model accounts for two of the above by including wall thickness calculations and using fan curves for a B2-fan from industry. The modelling methodology implemented was based on air-cooled heat exchanger design principles and correlations developed by Kröger (2004). Additional modelling techniques were taken from sources of well estabilished heat transfer and fluid mechanics design principles (*VDI Heat Atlas*, 2010). The model development process included the presentation of conceptual layout designs for the heat rejection systems used as the PC and IC in the cycle.

Before using the heat rejection system models to obtain near-optimal process and geometrical designs and select key components, they were verified for a converged steady-state solution using sample calculations as seen in Appendix F-4. The heat transfer calculated in the model had a relative error of 0.0015% when compared to the sample calculation. Furthermore, several other key steady-state results all had relative errors below 0.1%. It was therefore concluded that the models and methodology developed could be used further and in future work.

The steady-state models were then iteratively solved for a range of potential designs identified using a design of experiments approach where 3 000 potential design configurations were generated using a logarithmic hypercubic sampling method. This initiated the process by which near-optimal process and geometrical designs could be determined and key components selected. The size of the B2-fan was set at a 7.925 m diameter because larger fans (10.98 m in diameter) over-cooled the sCO_2 consistently. The 3 000 simulated designs for this fan size were then filtered before being coupled to a proposed cycle model using the pressure ratio and fan power consumption results as inputs. The best performing combination of PC and IC designs, in terms of cycle efficiency and apparent send-out-power, was then selected. To further improve the selected designs and move closer to near-optimal systems, a parametric study was performed using a MLR model which was developed to predict cycle efficiency using the air-cooled heat rejection system design inputs. The regression model predicted cycle efficiency with a maximum relative error 0.23% on cycle efficiency and a maximum absolute error of 0.08%. This level of accuracy was deemed acceptable for the purposes of near optimisation of the designs. For both the PC and IC, a sensitivity analysis of the MLR model showed that the tube longitudinal and transverse pitches, and fin pitch collectively influenced the systems' impact on cycle efficiency the most. Variation of these design inputs and prediction of cycle efficiency using the MLR model identified the trends used to improve the designs previously selected. For both systems, a collective increase in tube longitudinal pitch and decrease in tube transverse and fin pitches was shown to improve cycle efficiency. Aside from these trends, it was concluded that any improvement in either of the designs must be done together and with the cycle model because changing performance in one cycle component affects all upstream and downstream components. Nonetheless, the selected designs were perturbed in accordance with these trends to achieve an improved cycle efficiency of 39.41% (up from 39.39%). The highest theoretical cycle efficiency was shown to be 39.82% which indicates that there is room for further design improvement, however, this would require a formal optimisation. Even though the designs can be improved it was found that even just the inclusion of detailed cooler models within the cycle model improved the thermal efficiency from 44.15% to 44.59%. This demonstrated the value of adding detailed models in a cycle model and concluded the process of selecting key components and determining near-optimal process and geometrical designs.

The selected PC and IC designs were then modelled as 1D thermofluid networks in the Flownex® SE software using a similar modelling methodology and approach as described previously. The models developed needed to provide a platform for future dynamic simulation studies to be performed. With this in mind, the models were developed to account for sCO_2 distribution duct flow into streets of cells and included the associated momentum, frictional, and inlet losses. This also furthered the development of conceptual layout designs for the systems. Furthermore, a finer discretisation than the pass-by-pass method originally implemented in the initial Python models was included to increase the accuracy of the models. Single air control volume

connected to multiple sCO_2 control volumes were concluded to be easier to implement and slightly less computationally expensive. Four sCO_2 control volumes were set, this corresponds to an element length of 2.075 m. This level of discretisation was deemed acceptable due to the diminishing returns on accuracy when smaller control volumes were modelled. Prior to the addition of a finer discretisation scheme, the results of the Flownex® SE single cell models were verified using the results of the initial models (already verified by a sample calculation). The PC heat rejection rate was verified with a relative error of 2.941% to the initial model. The relatively large error when comparing the Flownex® SE and Python models was a result of discrepancies on the air-side where the mass flow rate had a relative error of 3.235%. The difference in air properties per pass contributed to this error. Recall that the air pressure was assumed constant between heat exchanger control volumes in the Python model. The same effect was observed in the IC, where the Flownex® SE model verified the heat rejection rate to within 3.009% of the Python model. Despite the difference in results and errors on the Python model results, it was concluded that the Flownex ® SE model was executing the thermofluid modelling methodology acceptably and most likely providing a more accurate solution. At this point in the project, the near-optimal heat rejections systems had been modelled in the Flownex ® SE software to provide a platform for future dynamic simulation studies.

Following the complete development of the Flownex® SE models for the PC and IC, four different off-design investigations were carried out for both systems, all of which included varying the ambient air temperature. In the present work, ambient air temperatures were varied across the reasonable operating range for the location of the proposed sCO_2 CSP plant in the region of Upington, South Africa using real-world weather data. The first study performed involved the observation of a single cell's performance as the ambient air temperature changes and controlling for undesirable operating conditions using a bypass valve. The second and third investigations conducted examined the sensitivity of the entire heat rejection systems to ambient air temperatures and a combination of air temperature and cycle load respectively. Several different control schemes were also implemented to try and regulate the systems' performance across a range of ambient temperatures. These were exclusively bypassing, exclusively switching off fans, and a combination of both. All of which were compared, and the best theoretical option selected for further analysis in the final investigation, the annual control study which used historical weather data for Upington, South Africa to simulate a typical year's ambient air temperatures.

Based on the findings of the single cell studies, it was concluded that the systems are very sensitive to ambient air temperature. The PC's heat rejection rate drops linearly by almost 50% from 5.4 MW at 5 ℃ to 2.75 MW at 40 ℃ and the IC's heat rejection rate drops by over 50% from 7.65 MW to 3.21 MW as the ambient air temperature rose. This established the need for control strategies to be recommended for use within the systems. Bypassing was shown to achieve the desired performance from a heat rejection and sCO_2 outlet temperature perspective. However, high levels of over-cooling resulted within the heat exchanger at the lowest. This indicated that exclusively bypassing presents risks and could cause complications if the sCO_2 were to change phase. This could, in turn, affect downstream cycle components. Alternative control methods therefore had to be considered on a system level. Notably, it was found that bypassing increased the pressure ratio in both systems, this is beneficial because it raises the cycle thermal efficiency. Additionally, the other variable impacting cycle efficiency, the fan power consumption, was found to be unaffected by bypassing and tended to increase as the ambient air temperature decreased.

The second study varied the ambient air temperature for the entire multiple cell PC and IC heat rejection systems from 5 ℃ to 40 ℃ in increments of 7 ℃. The heat transfer was found to drop by 20 MW in the PC and 34.3 MW in the IC as the air temperature increased. This further demonstrated the susceptibility of the systems to changes in ambient conditions and the necessity of a control strategy which could provide design operation in both systems. The pressure ratio was observed to drop linearly as the temperature increased while the fan power consumption decreased linearly as the air temperature rose. The pressure ratio varied negligibly around 0.997 in the PC and the fan power consumption had limits of 182 kW and 162 kW at the minimum and maximum air temperatures respectively. The IC was shown to have limits for pressure ratio of 0.9945 and 0.993 at the lowest and highest air temperatures respectively while the fan power consumption varied between 222 kW and 200 kW for the same temperatures. To summarise the trends, higher ambient air temperature resulted in larger pressure drops and lower fan power consumption. The opposite was true for lower ambient air temperatures. These trends only held for the uncontrolled performance of the systems. Bypassing was shown to be an effective control strategy in both the PC and IC, it also improved the pressure ratios in both systems. Maximum values of 0.9995 and 0.9988 were reached in the PC and IC respectively. Switching fans off, on the other hand, demonstrated that at lower ambient air temperatures, up to 70 kW of fan power could be saved in the PC while the IC fan power consumption could be reduced by up to 85 kW. The corresponding number of fans switched off in these cases is three in the precooler and four in the intercooler. The difference between these two methods is that bypassing achieved the desired operating conditions in terms of heat rejection whereas switching fans off provided jumps in performance which could not accurately control the system. Finally, a combined approach, switching off fans and bypassing, showed some measure of pressure ratio improvement while maintaining the same level of reduction in fan power consumption. It also provided system operation at the desired conditions. Using this approach, the PC achieved a maximum value of 0.9986 for pressure ratio and a minimum value of 115 kW for fan power consumption. The IC experienced a maximum value of 0.9968 for pressure ratio and a minimum value of 135 kW for fan power consumption. In both cases, significant gains were observed in performance results which directly impact cycle performance in terms of thermal efficiency. An added benefit of this control scheme is that the risks associated with bypassing sCO_2 were mitigated. Furthermore, switching off fans was concluded to potentially have a positive impact on their operational lifespan and maintenance requirements. The one concern for both designs is that under-cooling, which occurs at ambient air temperature greater than 28.3 ℃, cannot be controlled for. This was noted to be a large concern considering the systems are intended to operate in Upington which is a very hot region. Moreover, the biggest benefits to cycle performance provided by the heat rejection systems occurred at very low ambient air temperatures.

The effect of varying cycle loads by varying the mass flow rate of sCO_2 into the systems between 40% and 100% in 20% increments was then investigated for air temperatures typical of summer and winter months in Upington. The same control strategies were also investigated with the aim of recommending one for implementation during the annual control study. It was noted that the required amount of heat rejection dropped by between 6 MW and 5 MW per 20% load reduction in the PC and by between 10 MW and 9 MW in the IC. The combined control method proved the most beneficial across the entire range of cycle loads investigated for both heat rejection systems. Both a reduction in fan power consumption and an increased pressure ratio were achieved, whereas the alternative control methods provided only one of these aspects. In fact, at the lowest load of 40%, the PC model was not able to arrive at a steady-state solution when

exclusively bypassing sCO_2 to counteract over-cooling. This demonstrated the potential risk involved with a bypass only approach in the control of the PC in particular. It was also found that decreasing the inlet mass flow rate to both systems in combination with an effective control method expanded their operating limits. This meant that if part-load conditions are required in the cycle, both heat rejection systems will be able to perform as designed across a wider range of ambient air temperatures. The exact ambient air temperature limit in each load case was not determined though. It was also found that for decreased cycle loads a higher number of fans could be turned off. This indicated that, at part-loads, less auxilliary power will be drawn by the fans. Based on this investigation and the studies prior to it, the combined control method was recommended for further implementation.

The annual study performed tested the effectiveness of the combined control method across a range of ambient air temperatures for a typical year in Upington. It was found that the control strategy works well to counteract over-cooling, providing design operation for all ambient temperatures equal to and below 28.9 ℃. Furthermore, it resulted in decreased fan power consumption and increased pressure ratio throughout the colder months of the year. However, it was also found that this can only be achieved for 28.18% of the year, or 103 days. Even if the system were to run only in the evening, this number only rose slightly to 37.11%, or 135 days. To resolve this, the heat rejection systems either need to be resized or the cycle run at a lower load. Running the cycle at a lower load is not feasible and the study performed to assess part-load performance of the systems did not aim to present this as a strategy. It can therefore be concluded that full load should be maintained with larger heat rejection systems operating using a combined control using bypass valves and switching fans off. There are several approaches to resizing the heat exchangers and heat rejection systems. Over-sizing of the systems can be done by utilising the larger fans (10.98 m diameters); however, this will increase the fan power consumption which is not ideal. Alternatively, the modelling process can be redone starting with the design of experiments. Increasing the size of several geometric variables in the heat exchangers will be beneficial. The designs in the present work are limited in terms of fin diameters investigated, larger fins will increase the heat transfer area and subsequently the heat rejected in the systems. Furthermore, it has been concluded that increasing longitudinal tube pitches and decreasing fin pitches in the heat exchangers will also increase the heat rejected. An additional approach could be to examine designs with different discrete variables such as the number of rows and passes in the heat exchanger or the number of cells in the systems. However, the problem with changing the geometry of the heat exchangers (especially to make them larger) is that the mass of the systems will be adversely affected, increased mass results in increased cost. It is concluded that any resizing of the systems should involve investigating larger fan sizes and varying the heat exchanger geometry while also considering the effect on the mass of the systems and the thermal efficiency of the cycle.

The key conclusions based on the studies and results presented in this work are included below:

1. Based on current literature, air-cooled system models for sCO_2 CSP plant applications tend to neglect the mechanical integrity of the tubes under high sCO_2 pressures, appropriate sizing of distribution manifolds, or accurate air-side performance with the inclusion of fans used in industry and the relevant performance curves. The present work has incorporated all of these in the final Flownex ® SE models allowing for commentary on and analysis of the designs using comprehensive models.

2. The design methodology presents conceptual layouts for the heat rejection systems of the PC and IC in a proposed sCO_2 CSP plant. The model developed has been verified can be used to size heat rejection systems for use in sCO_2 Brayton cycles. It also includes an approach for achieving near-optimal process and geometrical designs by using the models together and with a cycle model.
3. The implementation of detailed heat rejection system models which have been improved using the methodology developed can lead to increased cycle performance from an entropy generation and auxilliary power consumption perspective.
4. Air-cooled heat rejection systems for sCO_2 power cycles were shown to be very sensitive to ambient conditions such as the air temperature.
5. Exclusively bypassing sCO_2 to control the operating point of the systems was concluded to be a risky control strategy. This was because the approach results in high levels of over-cooling within the heat exchangers.
6. The combined control strategy which utilises bypassing while switching off fans in specific cells was found to provide design operation for the PC and IC at all ambient air temperatures below the design value. This approach was concluded to be the most recommendable.
7. The heat rejection systems were concluded to operate well under part-load conditions using a combined control strategy. At lower loads, the range of design operation ambient air temperatures increased, and it was found that a higher number of fans can be turned off.
8. It was concluded that the system designed and implemented in the models should be increased in size because of under-cooling, which cannot be counteracted, and which was observed for large portions of a typical year's ambient conditions.
9. It is recommended that air-cooled heat rejection systems be over-designed for the region they are intended to operate in provided an effective control strategy can be implemented.
10. Over-design of the air-cooled systems can be achieved by investigating the use of larger fans and or increasing the finned tube geometry but must consider the effect on system mass and cycle efficiency.

Recommendations are presented here as well; these avenues should be considered when furthering the research carried out in the present work:

1. Improvement of the 1D thermofluid model used to size the system by including distribution header flow and the associated pressure losses along with air-side pressure drops per pass and increased discretisation of the sCO_2 control volumes. This would allow for more accurate designs to be developed outside of a complex modelling software.
2. An alternative solver methodology in the 1D thermofluid model used to size the system is also recommendable and can increase the number of designs for further investigation. Changing the fan speed in integer steps and increasing the tolerance for the outlet sCO_2 temperature will result in a higher number of steady-state solutions.
3. The investigation of alternative heat transfer correlations would further the research performed in this work by showing the difference in achieved heat rejection rates. This line of enquiry can also be later linked to any experimental results generated for air-cooled heat exchangers such as those in

this work and validated against the data. This would allow for the best modelling methods to be employed in the future design and practical implementation of these systems.

4. Applying a formal optimisation procedure to the design selection process which incorporates both cycle performance and heat rejection system mass. This would result in the development and implementation of the most beneficial designs from a cycle performance and cost perspective.
5. Exploration of alternative objective functions when deciding on the best performing designs would also be advantageous. For example, minimising or limiting the volume or mass of the system while meeting the heat transfer and pressure drop requirements allows for the cost of the systems to be used as a selection criterion.
6. Investigation and sizing of an indirect heat rejection method using an intermediate water loop and pump to transfer heat from the sCO_2 to water and then air. This alternative method of rejecting heat in the cycle may present a viable option in sCO_2 Brayton cycles and is worth investigating further.
7. Increased discretisation within the single cell models and subsequent system models would allow for a more detailed analysis of the effects observed during bypassing of the sCO_2. Investigation into these trends would further understanding of sCO_2 experiencing cooling which takes it near its pseudocritical temperature and pressure.
8. Appropriate design and modelling of the bypass valves which considers the mechanical integrity of the valves and the pressure drop characteristics through them. This would increase the accuracy of the observed benefits when implementing bypass control and provide more certainty in these trends.
9. Development of a model which assesses the effects of crosswinds on the systems using a co-simulation approach by linking the Flownex ® SE models to a CFD control volume which allows for better mapping between wind speeds and air volume flow rate reductions. This, in combination with the weather data available, would best inform the viability of the systems for practical usage and allow for mitigating strategies to be developed based on existing air-cooled heat exchanger research.
10. Study of the effects of recirculation on the systems using well-estabilished heat exchanger design methodologies would also provide increased insight into the performance of these potential heat rejection systems. Recirculation also affects air volume flow rate reduction in these systems and an investigation into the effects would allow for windwalls to be appropriately sized.
11. Perform a Monte-Carlo analysis using the raw weather data used in this work to predict the performance of the heat rejection systems more accurately over the course of a typical year.
12. The extension of the annual control studies to incorporate load variations as and when required. This would better inform the operating philosophy required in the proposed plant.
13. Investigation into the use of variable speed drives to increase fan rotational speed during the period when the cooling systems' duty is not being met. Maintaining a low sCO_2 temperature at the outlet of the cooling systems will reduce the work done by the compressors at the cost of fan power. It will be important to determine whether this is beneficial to the SOP of the cycle.
14. The development of over-sized heat rejection systems for the PC and IC and integration of these systems in an overall cycle model using a combined control method would demonstrate the advantages inherent in designing the heat rejection systems to operate at a much higher ambient air temperature than is usually required. The design point should be specified well above the average and annual temperature at a value which is exceeded for a total of 1% of the total hours in

a year. This will ensure that the systems operate as designed. The methodology described in this work could be applied to achieve this with the inclusion of system mass as part of the objective function.

9. List of references

Ahn, Y., Jun Bae, S., Kim, M., Kuk Cho, S., Baik, S., Ik Lee, J. & Eun Cha, J. 2015. Review of supercritical CO2 power cycle technology and current status of research and development.pdf. *Nuclear Engineering and Technology*. 47:647–661.

Al-Waked, R., Behnia, M., Consulting Engineers, B., Sydney, N. & Masud Behnia, A. 2007. The Effect of Windbreak Walls on the Thermal Performance of Natural Draft Dry Cooling Towers. *Heat Transfer Engineering*. 26(8):50–62. DOI: 10.1080/01457630591003763.

Augustyn, O.P.H. 2013. Experimental and numerical analysis of axial flow fans. University of Stellenbosch.

Augustyn, O.P.H. 2017. Medupi Power Station ACC Performance During Windy Conditions. In *Air-Cooled Condensers Users Group*. Las Vegas. 25.

Bell, I.H., Wronski, J., Quoilin, S. & Lemort, V. 2014. Pure and pseudo-pure fluid thermophysical property evaluation and the open-source thermophysical property library coolprop. *Industrial and Engineering Chemistry Research*. 53(6):2498–2508. DOI: 10.1021/ie4033999.

Bergelin, O., Colburn, A. & Hull, H. 1950. Heat transfer and pressure drop during viscous flow across unbaffled tube banks. *Bulletin No. 2*.

Binotti, M., Astolfi, M., Campanari, S., Manzolini, G. & Silva, P. 2017. Preliminary assessment of sCO2 cycles for power generation in CSP solar tower plants. *Applied Energy*. 204:1007–1017. DOI: 10.1016/j.apenergy.2017.05.121.

Bredell, J.R., Kröger, D.G. & Thiart, G.D. 2006. Numerical investigation of fan performance in a forced draft air-cooled steam condenser. *Applied Thermal Engineering*. 26(8–9):846–852. DOI: 10.1016/j.applthermaleng.2005.09.020.

Briggs, D.E. & Young, E.H. 1963. Convection Heat Transfer and Pressure Drop of Air Flowing across Triangular Pitch Banks of Finned Tubes. *Chemical Engineering Progress Symposium Series*. 59(41):1–10.

Brun, K., Friedman, P. & Dennis, R. 2017. *Fundamentals and Applications of Supercritical Carbon Dioxide (sCO2) Based Power Cycles*. 1st ed. K. Brun, P. Friedman, & R. Dennis, Eds. Woodhead Publishing Limited.

Bruneau, P.R.P. 1994. The design of a single rotor axial flow fan for a cooling tower application. University of Stellenbosch.

Bustamante, J.G., Rattner, A.S. & Garimella, S. 2016. Achieving near-water-cooled power plant performance with air-cooled condensers. *Applied Thermal Engineering*. 105:362–371. DOI: 10.1016/j.applthermaleng.2015.05.065.

Carvalho, C.B., Ravagnani, M.A.S.S., Bagajewicz, M.J. & Costa, A.L.H. 2019. Globally optimal design of air coolers considering fan performance. *Applied Thermal Engineering*. 161(February):114188. DOI: 10.1016/j.applthermaleng.2019.114188.

Cengel, Y. a. 2006. *Heat and Mass Transfer: A Practical Approach*.

Cengel, Y.A. & Boles, M.A. 2015a. The Brayton Cycle with Regeneration. In *Thermodynamics An Engineering Approach*. 8th ed. New York: McGraw-Hill Education. 513–515.

Cengel, Y.A. & Boles, M.A. 2015b. The Brayton Cycle with Intercooling, Reheating, and Regeneration. In *Thermodynamics An Engineering Approach*. 8th ed. New York: McGraw-Hill Education. 516–520.

Deshmukh, A. & Kapat, J. 2020. Pinch point analysis of air cooler in supercritical carbon dioxide brayton cycle operating over ambient temperature range. *Journal of Energy Resources Technology, Transactions of the ASME*. 142(5). DOI: 10.1115/1.4046083.

Doodman, A.R., Fesanghary, M. & Hosseini, R. 2009. A robust stochastic approach for design optimization of air cooled heat exchangers. *Applied Energy*. 86(7–8):1240–1245. DOI: 10.1016/j.apenergy.2008.08.021.

Dostal, V., Hejzlar, P. & Driscoll, M.J. 2006. High-performance supercritical carbon dioxide cycle for next-generation nuclear reactors. *Nuclear Technology*. 154(3):265–282. DOI: 10.13182/NT154-265.

Duniam, S., Jahn, I., Hooman, K., Lu, Y. & Veeraragavan, A. 2018. Comparison of direct and indirect natural draft dry cooling tower cooling of the sCO2 Brayton cycle for concentrated solar power plants. *Applied Thermal Engineering*. 130:1070–1080. DOI: 10.1016/j.applthermaleng.2017.10.169.

Engelbrecht, R.A. 2018. Numerical Investigation of Fan Performance in a Forced Draft Air-cooled Condenser. (December). Available: https://scholar.sun.ac.za/handle/10019.1/105082.

Engelbrecht, R., Laubscher, R. & van der Spuy, J. 2020. A co-simulation approach to modeling air-cooled condensers in windy conditions. *Proceedings of the ASME Turbo Expo*. 1:1–10. DOI: 10.1115/GT2020-16047.

Flownex. 2020a. Two-Phase Flow. In *Flownex Theory Manual*. Flownex. 23–40.

Flownex. 2020b. Piping. In *Flownex Library Manual*. 520–522.

Flownex. 2020c. Solution procedure. In *Flownex Theory Manual*. 20–21.

Gaddis, E. & Gnielinski, V. 1983. Druckverlust in querdurchstromten Rohrbundeln. *Verfahrenstechnik*. 17(7):410–418.

Gavic, D.J. 2012. Investigation of Water, Air and Hybrid Cooling for Supercritical Carbon Dioxide Brayton Cycles.

Gnielinski, V. 1976. New equations for heat and mass transfer in turbulent pipe and channel flow. *International Chemical Engineering*. 16(2):359–368.

Gu, X., Chen, W., Fang, Y., Song, S., Wang, C. & Wang, Y. 2020. Analysis of flow dead zone in shell side of a heat exchanger with torsional flow in shell side. *Applied Thermal Engineering*. 180(August):115792. DOI: 10.1016/j.applthermaleng.2020.115792.

Guo, J., Xiang, M., Zhang, H., Huai, X., Cheng, K. & Cui, X. 2019. Thermal-hydraulic characteristics of supercritical pressure CO2 in vertical tubes under cooling and heating conditions. *Energy*. 170:1067–1081. DOI: 10.1016/j.energy.2018.12.177.

He, Y., Huang, T. & Tan, M. 2017. Analysis on optimization and model selection of the heat transmission performance of heat exchanger. *Chemical Engineering Transactions*. 62:355–360. DOI: 10.3303/CET1762060.

Hearn, E.J. 1997. Thick Cylinders. In *Mechanics of Materials 1*. Third Edit ed. E.J. Hearn, Ed. Butterworth-Heinemann. 215–253. DOI: https://doi.org/10.1016/B978-075063265-2/50011-6.

Held, T.J., Miller, J. & Buckmaster, D.J. 2016. A Comparative Study of Heat Rejection Systems for sCO2 Power Cycles. *The 5th International Symposium-Supercritical CO2 Power Cycles*.

Holger, M. 2018. *Heat Exchangers*. New York: Hemisphere Publishing Corporation.

Howden. 2021. *High efficiency, low noise cooling fans*. Available: https://www.howden.com/en-gb/products/fans/cooling-fan/d-series-cooling-fans [2021, October 21].

IRENA. 2019. *Renewable power generation costs in 2018*. Abu Dhabi: International Renewable Energy Agency.

Konakov, P.K. 1946. A new correlation for the friction coefficient in smooth tubes. *Berichte der Akademie der Wissenschaften der UdSSR*. 51:503–506.

Kong, Y., Wang, W., Huang, X., Yang, L., Du, X. & Yang, Y. 2017. Circularly arranged air-cooled condensers to restrain adverse wind effects. *Applied Thermal Engineering*. 124:202–223. DOI: 10.1016/j.applthermaleng.2017.06.001.

Kong, Y., Wang, W., Zuo, Z., Yang, L., Du, X. & Yang, Y. 2019. Combined air-cooled condenser layout with in line configured finned tube bundles to improve cooling performance. *Applied Thermal Engineering*. 154(December 2018):505–518. DOI: 10.1016/j.applthermaleng.2019.03.099.

Kröger, G.D. 2004. Air-Cooled Heat Exchangers and Cooling Towers. In *Air-cooled heat exchangers and cooling towers: thermal flow performance evaluation and design*. Tulsa: PennWell Corporation. 1–49.

Kruizenga, A., Anderson, M., Fatima, R., Corradini, M., Towne, A. & Ranjan, D. 2011. Heat transfer of supercritical carbon dioxide in printed circuit heat exchanger geometries. *Journal of Thermal Science and Engineering Applications*. 3(3):1–8. DOI: 10.1115/1.4004252.

de la Calle, A., Bayon, A. & Soo Too, Y.C. 2018. Impact of ambient temperature on supercritical CO2 recompression Brayton cycle in arid locations: Finding the optimal design conditions. *Energy*. 153:1016–1027. DOI: 10.1016/j.energy.2018.04.019.

Lin, J., Mahvi, A.J., Kunke, T.S. & Garimella, S. 2020. Improving air-side heat transfer performance in air-cooled power plant condensers. *Applied Thermal Engineering*. 170(December 2019):114913. DOI: 10.1016/j.applthermaleng.2020.114913.

Liu, Z., Luo, W., Zhao, Q., Zhao, W. & Xu, J. 2018. Preliminary design and model assessment of a supercritical CO2 compressor. *Applied Sciences (Switzerland)*. 8(4):1–20. DOI: 10.3390/app8040595.

Louw, F.G., Von Backström, T.W. & Van Der Spuy, S.J. 2015. Lift and drag characteristics of an air-cooled heat exchanger axial flow fan. *Journal of Fluids Engineering, Transactions of the ASME*. 137(8):1–9. DOI: 10.1115/1.4030165.

Manzano-Agugliaro, F., Alcayde, A., Montoya, F.G., Zapata-Sierra, A. & Gil, C. 2013. Scientific production of renewable energies worldwide: An overview. *Renewable and Sustainable Energy Reviews*. 18:134–143. DOI: 10.1016/j.rser.2012.10.020.

McEligot, D.M. & Jackson, J.D. 2004. “Deterioration” criteria for convective heat transfer in gas flow through non-circular ducts. *Nuclear Engineering and Design*. 232(3):327–333. DOI: 10.1016/j.nucengdes.2004.05.004.

Mehos, M., Price, H., Cable, R., Kearney, D., Kelly, B., Kolb, G., Morse, F., Mehos, M., et al. 2020. Concentrating Solar Power Best Practices Study. (June).

Meyer, C.J. 2005. Numerical investigation of the effect of inlet flow distortions on forced draught air-cooled heat exchanger performance. *Applied Thermal Engineering*. 25(11–12):1634–1649. DOI: 10.1016/j.applthermaleng.2004.11.012.

Miller, D.S. 1978. *Internal flow systems.* V. 5. Cranfield, U.K.: BHRA The Fluid Engineering Centre.

Moisseytsev, A. & Sienicki, J.J. 2016. Transient load following and control analysis of advanced S-CO2 power conversion with dry air cooling. *International Congress on Advances in Nuclear Power Plants, ICAPP 2016*. 2:1314–1323.

Moisseytsev, A., Jian, L. & Sienicki, J.J. 2016. *Dry Air Cooler Modeling for Supercritical Carbon Dioxide Brayton Cycle Analysis*. Available: https://doi.org/10.1016/j.rser.2020.110055.

Monjurul Ehsan, M., Duniam, S., Li, J., Guan, Z., Gurgenci, H. & Klimenko, A. 2020. A comprehensive thermal assessment of dry cooled supercritical CO2 power cycles. *Applied Thermal Engineering*. 166(November 2019):114645. DOI: 10.1016/j.applthermaleng.2019.114645.

National Institute of Standards and Technology. 2013. *REFPROP*. Available: https://www.nist.gov/srd/refprop [2023, October 23].

Neises, T. & Turchi, C. 2019. Supercritical carbon dioxide power cycle design and configuration optimization to minimize levelized cost of energy of molten salt power towers operating at 650 °C. *Solar Energy*.

181(January):27–36. DOI: 10.1016/j.solener.2019.01.078.

Oh, H.K. & Son, C.H. 2010. New correlation to predict the heat transfer coefficient in-tube cooling of supercritical CO2 in horizontal macro-tubes. *Experimental Thermal and Fluid Science*. 34(8):1230–1241. DOI: 10.1016/j.expthermflusci.2010.05.002.

Pitla, S.S., Groll, E.A. & Ramadhyani, S. 2002. New correlation to predict the heat transfer coefficient during in-tube cooling of turbulent supercritical CO 2 ´ lation pour pre ´ voir le coefficient de transfert Nouvelle corre ´ gime thermique pendant le refroidissement du gaz CO 2 en re turbulent sup. 25:887–895.

Process Pipe. 2016. Available: https://www.processpipe.co.za/steel-tubes/.

Reza, M. & Zabihollah, S. 2011. Thermodynamic analysis and optimization of air-cooled heat exchangers. *Heat and Mass Transfer*. 35–44. DOI: 10.1007/s00231-010-0672-9.

Rohwer, J.N. 2019. Blade surface pressure measurements of an axial flow fan. University of Stellenbosch.

Salta, C.A. & Kröger, D.G. 1995. Effect of inlet flow distortions on fan performance in forced draught air-cooled heat exchangers. *Heat Recovery Systems and CHP*. 15(6):555–561. DOI: 10.1016/0890-4332(95)90065-9.

du Sart, C.F., Rousseau, P.G. & Laubscher, R. 2021. Cycle selection and system-level optimisation of a 50 MWe sCO2 CSP plant. *Proceedings of the 15th international conference on heat transfer, fluid mechanics and thermodynamics*. (July):560–565. Available: https://www.researchgate.net/publication/353572355_Cycle_selection_and_system-level_optimisation_of_a_50_MWe_sCO2_CSP_plant.

Sathish, S., Kumar, P. & Nassar, A. 2021. Analysis of a 10 MW recompression supercritical carbon dioxide cycle for tropical climatic conditions. *Applied Thermal Engineering*. 186(August 2020):116499. DOI: 10.1016/j.applthermaleng.2020.116499.

Sayed Ahmed, S.A.E., Mesalhy, O.M. & Abdelatief, M.A. 2015. Flow and heat transfer enhancement in tube heat exchangers. *Heat and Mass Transfer*. 51(11):1607–1630. DOI: 10.1007/s00231-015-1669-1.

Shabanian, S.R., Rahimi, M., Shahhosseini, M. & Alsairafi, A.A. 2011. CFD and experimental studies on heat transfer enhancement in an air cooler equipped with different tube inserts. *International Communications in Heat and Mass Transfer*. 38(3):383–390. DOI: 10.1016/j.icheatmasstransfer.2010.12.015.

Siegel, A.F. 2016. *Practical Business Statistics: Seventh Edition*. 7th ed. G. Nisbet & S. Ikeda, Eds. London: Elsevier Inc.

Solargis. 2017. *Solar resource maps of South Africa*. Available: https://solargis.com/maps-and-gis-data/download/south-africa [2022, February 02].

SolarGIS. 2023. *Solar resource maps and GIS data for 200+ countries*. Available: https://solargis.com/maps-and-gis-data/overview [2022, December 05].

Van Der Spuy, S.J. 2011. Perimeter Fan Performance in Forced Draught Air-cooled Steam Condensers. (December).

Van Der Spuy, S.J., Von Backström, T.W. & Kröger, D.G. 2009. Performance of low noise fans in power plant air cooled steam condensers. *Noise Control Engineering Journal*. 57(4):341–347. DOI: 10.3397/1.3151851.

SteelNumber. 2022. *P235GH (1.0345)*. Available: http://www.steelnumber.com/en/steel_composition_eu.php?name_id=437 [2022, November 10].

Swamee, Prabhata & Jain, A. 1976. Explicit eqations for pipe-flow problems. *ASCE Journal of the Hydraul ics Division*. (102):657–664.

Vallourec. 2022. Steam Tubes & Pipes Catalouge. 4–9.

VDI Heat Atlas. 2010. 2nd ed. Berlin: Springer. DOI: https://doi.org/10.1007/978-3-540-77877-6.

Wahl, A., Mertz, R., Laurien, E. & Starflinger, J. 2021. Heat transfer correlation for sCO2 cooling in a 2 mm

tube. *Journal of Supercritical Fluids*. 173(February):105221. DOI: 10.1016/j.supflu.2021.105221.

Wang, K., He, Y.L. & Zhu, H.H. 2017. Integration between supercritical CO2 Brayton cycles and molten salt solar power towers: A review and a comprehensive comparison of different cycle layouts. *Applied Energy*. 195:819–836. DOI: 10.1016/j.apenergy.2017.03.099.

Wang, X., Li, X., Li, Q., Liu, L. & Liu, C. 2020. Performance of a solar thermal power plant with direct air-cooled supercritical carbon dioxide Brayton cycle under off-design conditions. *Applied Energy*. 261(October 2019):114359. DOI: 10.1016/j.apenergy.2019.114359.

Weather Spark. 2021. *Average Weather in Upington South Africa*. Available: https://weatherspark.com/y/86569/Average-Weather-in-Upington-South-Africa-Year-Round [2021, May 07].

Weinstein, L.A., Loomis, J., Bhatia, B., Bierman, D.M., Wang, E.N. & Chen, G. 2015. Concentrating Solar Power. *Chemical Reviews*. 115(23):12797–12838. DOI: 10.1021/acs.chemrev.5b00397.

van der Westhuizen, R. 2020. Optimisation of a Supercritical Carbon Dioxide Solar Thermal Power System. University of Stellenbosch.

World Bank. 2021. Concentrating Solar Power.

Yang, L.J., Wang, M.H., Du, X.Z. & Yang, Y.P. 2012. Trapezoidal array of air-cooled condensers to restrain the adverse impacts of ambient winds in a power plant. *Applied Energy*. 99:402–413. DOI: 10.1016/j.apenergy.2012.06.006.

Yoon, S.H., Kim, J.H., Hwang, Y.W., Kim, M.S., Min, K. & Kim, Y. 2003. Heat transfer and pressure drop characteristics during the in-tube cooling process of carbon dioxide in the supercritical region. *International Journal of Refrigeration*. 26(8):857–864. DOI: 10.1016/S0140-7007(03)00096-3.

Zhang, H., Guo, J., Huai, X. & Cui, X. 2019. Thermodynamic performance analysis of supercritical pressure CO2 in tubes. *International Journal of Thermal Sciences*. 146(September):106102. DOI: 10.1016/j.ijthermalsci.2019.106102.

Appendix A Flownex ® SE grid independence studies

The details of the grid independence studies performed on the PC and IC to determine the appropriate discretisation scheme and sCO_2 control volume length are included below.

PRECOOLER

The heat rejection rate plots and trendlines can be seen in Figure A-1 while the steady-state solution times are shown in Figure A-2. Figure A-1 shows that the single air control volume approach results in higher heat rejection rates than the matching control volume approach. The trends also indicate that for the PC, increasing the fineness of the discretisation scheme drives the heat rejection rate upwards for matching control volumes and downwards for the single air control volumes. The 'zero spacing' heat transfer for matching control volumes is 3.511 MW while the corresponding value for the single air control volume is3.530 MW. The absolute difference between these values is 0.018 MW or 0.513% of the matching control volumes value, which is theoretically more accurate. This is a minimal difference and indicates that consistent results will be achieved regardless of the discretisation approach used. A detailed analysis and comparison for each level of discretisation is shown in Table A-1.

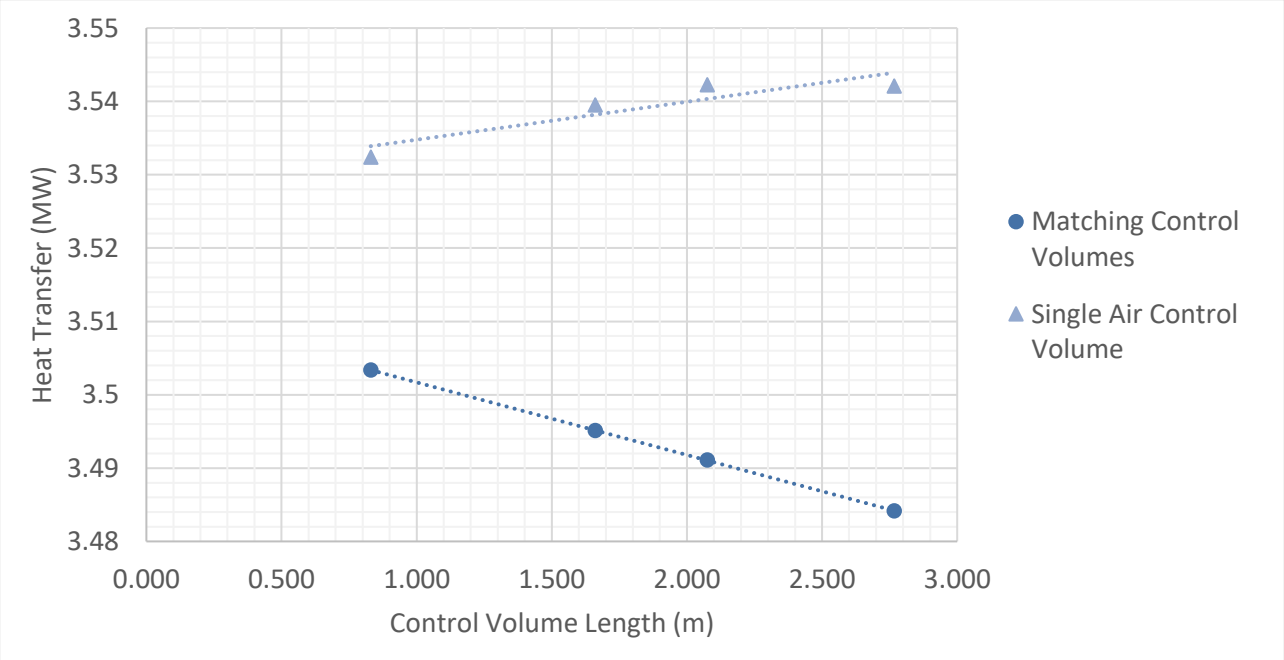

Figure A-1: Precooler heat rejection rate grid independence plot

Table A-1: Comparison of discretisation approaches and scheme fineness for the PC

Scheme	Control volume length (m)	Number of increments (-)	Matching Control Volumes compared to 'zero spacing'		Single air control volume compared to 'zero spacing'	
			Absolute difference (MW)	Error (%)	Absolute difference (MW)	Error (%)
Coarse	2.767	3	0.0274	0.781	0.0125	0.354
Medium-Coarse	2.075	4	0.0205	0.584	0.0127	0.359
Medium	1.660	5	0.0165	0.469	0.0099	0.281
Fine	0.830	10	0.0082	0.234	0.0028	0.080

Additionally, Figure A-2 shows that the single air control volume approach achieves quicker steady-state solutions across the range of discretisation increments tested. However, it is recognised that the differences in solution time are marginal and not a likely reason to select this approach above the matching control volumes approach.

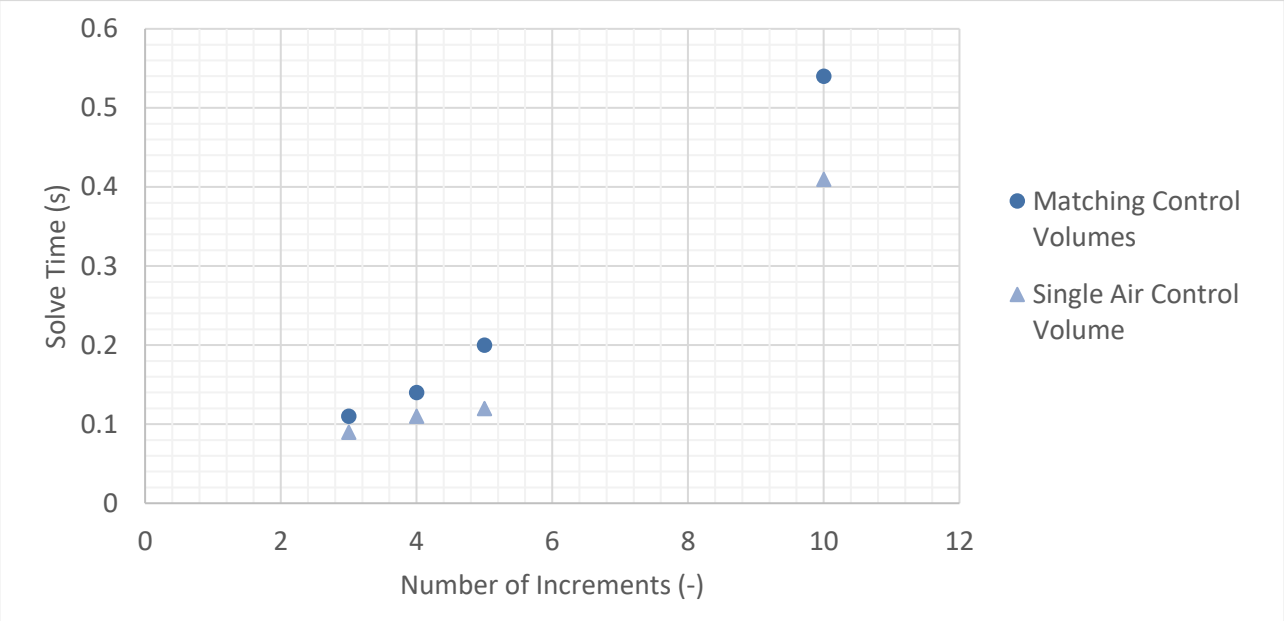

Figure A-2: Precooler steady-state solution time for a range of different discretisation increments

INTERCOOLER

Figure A-3 and Figure A-4 show the heat rejection rate trendlines plots and steady-state solution times respectively. The trend of higher heat rejection rates for the single air control volume method persists in the intercooler. However, for the IC, increasing the level of discretisation results in a decreasing trend for heat rejection rates for both approaches. It may not be the clear trend for the matching control volumes method, but the general linear trend is decreasing heat rejection with increased discretisation. The only way to check the consistency of this trend would be to build even finer models and this was deemed unnecessary because

the differences in heat transfer were not significant. The 'zero spacing' heat rejection rates were 4.665 MW and 4.714 MW for the matching control volumes and single air control volume approach respectively. The corresponding absolute difference between these values is 0.049 MW or 1.046% on the matching control volumes value. As with the PC, this is a minimal difference and shows that regardless of the discretisation approach, consistent results will be achieved. A detailed analysis and comparison of the various discretisation levels is shown in Table A-2. Another consistent trend between the PC and the IC models is the similar steady-state solution time similarities between the two discretisation approaches. This is shown in Figure A-4.

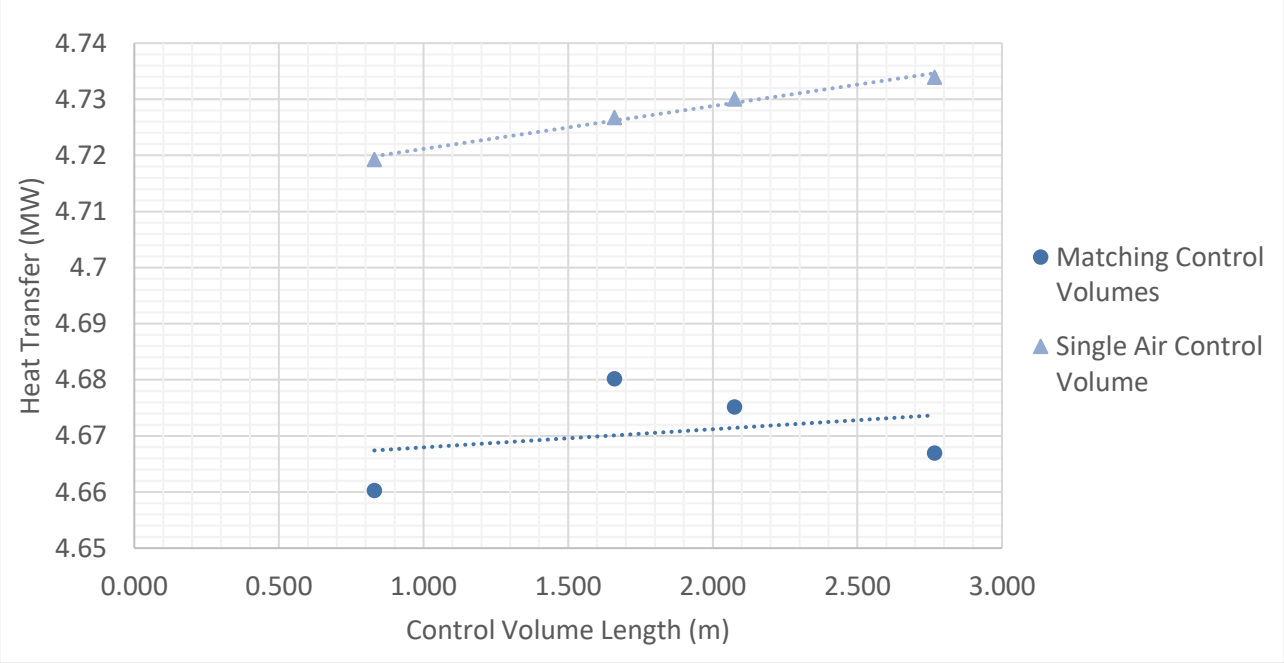

Figure A-3: Intercooler heat rejection rate grid independence plot

Table A-2: Comparison of discretisation approaches and scheme fineness for the IC

Scheme	**Control volume length (m)**	**Number of increments (-)**	**Matching Control Volumes compared to 'zero spacing'**		**Single air control volume compared to 'zero spacing'**	
			Absolute difference (MW)	Error (%)	Absolute difference (MW)	Error (%)
Coarse	2.767	3	0.0022	0.047	0.0204	0.434
Medium-Coarse	2.075	4	0.0104	0.224	0.0165	0.351
Medium	1.660	5	0.0155	0.332	0.0132	0.281
Fine	0.830	10	0.0044	0.095	0.0058	0.123

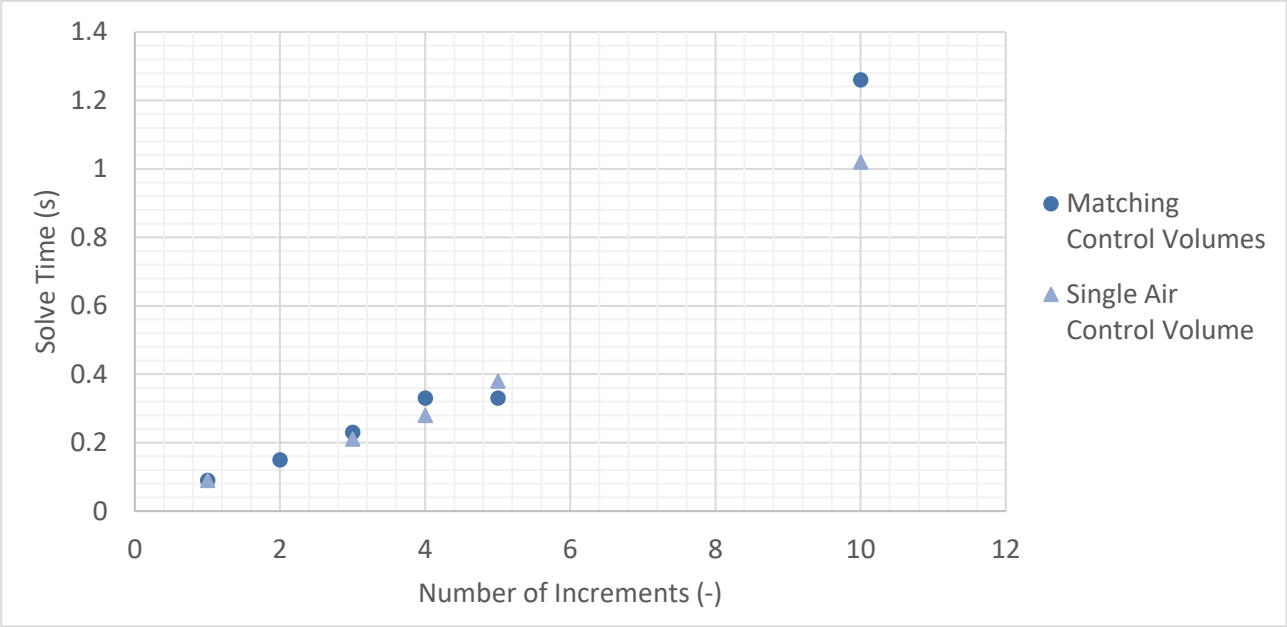

Figure A-4: Intercooler steady-state solution time for a range of different discretisation increments

Appendix B Additional commentary on steady state design results

To further analyse the effect of heat exchanger design has on cycle performance, several valid designs from the DoE with different discrete values (N_L, N_{passes}, N_{cells}) to those of the best performing designs were examined for the same key results. Additionally, a basic mass per cell calculation, done using Eq. (B-1) – Eq. (B-3), was included in this step for the sake of observing whether designs with a positive impact on cycle efficiency are also feasible from a size and mass perspective. This process also indicated whether it is worth sacrificing cycle performance from an efficiency perspective to make the heat rejection systems more feasible from a cost and mass point of view.

$$V_f = \frac{\pi}{4}\left({d_f}^2 - {d_o}^2\right)t_f \frac{L_{pass}N_{passes}}{S_f} N_{tubes} \quad (B\text{-}1)$$

$$V_{tbs} = \frac{\pi}{4}\left({d_o}^2 - {d_i}^2\right)L_{pass}N_{passes}N_{tubes} \quad (B\text{-}2)$$

$$m_{he} = \rho_{tbs}\left(V_f + V_{tbs}\right) \quad (B\text{-}3)$$

Table B-1 and Table B-2 show a comparison of several different designs taken from the entire DoE dataset with the best performing designs shaded and indicated in green. The results of this comparison are discussed below by comparing the systems according to their size in terms of the number of cells and then according to their detailed geometry.

PRECOOLER

The results for the PC in Table B-1 show that the larger PC systems with 12 cells have relatively high $\dot{W}_{aux}$ values of 345 kW and 291 kW, both at least 100 kW higher than the best performing designs. This is because the designs with 12 cells worked best with a four-pass single flow path configuration. The reason that this configuration works best is because the increased number of cells drops the heat rejection required in each cell and the mass flow rate of sCO_2 through each cell. Therefore, the flow does not need to be split to increase the heat transfer area or decrease the sCO_2-side velocity. This means that even if the longitudinal tube pitch was high, the heat exchanger height would still be low because there is a low number of passes which is equal to the number of longitudinal rows. This results in a lower Δp_{amb} across the heat exchanger and subsequently the fan needs to recover more of the pressure lost as air flows past the heat exchanger tube banks which raises the mass flow rate of air and auxiliary power drawn. Furthermore, $T_{a,ex}$ is the lowest of all the designs in the 12 cell PC systems. This result is a product of the reduced heat rejection per cell ($\dot{Q}_{cell}$) and means that the UA for these systems is lower than the others. Another trend that can be observed for these systems is that even when the finned tube bundles are tightly packed in the transverse direction as with the design having $S_T = 53.9$ mm, the performance does not increase drastically. In this design, it is because the fin

Table B-1: Comparison of various PC designs, sorted by number of cells, with the best performing case

S_L (mm)	S_T (mm)	S_f (mm)	t_f (mm)	d_f (mm)	N_L/n_{passes} (-)	N_{cells} (-)	H_F (m)	m_a (kg/s)	v_{tbs} (m/s)	$\dot{Q}_{cell}$ (MW)	$\dot{W}_{aux}$ (kW)	$T_{a,ex}$ (℃)	PR (-)	e_{he} (-)	UA (W/K)	m_{he} (tonnes)	m_{total} (tonnes)
51.6	53.9	3.8	0.5	35.6	4 / 4	12	31	205.189	5.039	2.2855	345.558	39.943	0.9949	0.297	80378	10.984	131.8078
68.3	71.9	2.2	0.8	35.6	4 / 4	12	24	195.480	6.675	2.2667	291.089	40.414	0.9912	0.297	80233	11.705	140.4595
74.9	54.0	3.1	1.5	36.9	4 / 4	10	26	201.570	6.046	2.7291	303.363	42.359	0.9927	0.302	99140	19.279	192.7859
80.0	70.1	4.8	0.8	38.8	4 / 4	10	30	274.830	7.810	2.7015	674.534	38.742	0.9882	0.292	93810	9.996	99.95513
59.4	65.6	4.0	1.2	44.1	8 / 4	10	30	200.948	3.661	2.7570	287.838	42.514	0.9972	0.304	100297	34.076	340.7642
60.5	77.8	3.9	1.0	44.0	8 / 4	10	39	230.788	4.339	2.7505	425.795	40.722	0.9962	0.300	97714	26.181	261.8085
77.3	53.1	4.7	1.1	45.6	8 / 4	8	39	221.141	3.707	3.4457	322.732	44.358	0.9971	0.309	128537	38.600	308.804
77.0	52.0	2.8	1.3	42.6	8 / 4	8	21	181.912	3.638	3.4463	184.495	47.728	0.9972	0.318	135090	52.826	422.6067
60.7	77.1	2.0	1.3	39.7	8 / 4	8	26	253.014	5.374	3.4228	453.025	42.413	0.9942	0.303	124641	38.499	307.9925
67.0	64.8	1.2	1.3	45.2	4 / 4	8	44	226.224	9.011	3.3462	307.103	43.540	0.9842	0.300	123313	46.846	374.766
53.5	55.7	3.1	0.7	48.2	6 / 6	8	35	190.517	7.758	3.3367	189.610	46.243	0.9829	0.221	127740	29.648	237.1831
62.6	57.3	5.0	1.0	36.2	6 / 6	8	24	194.128	8.024	3.3281	204.558	45.931	0.9818	0.220	127022	17.785	142.2768
65.4	50.9	1.5	0.5	40.4	8 / 4	6	26	251.084	4.733	4.5766	352.138	47.089	0.9954	0.316	178040	39.865	239.1923
75.2	71.8	1.2	1.4	45.0	8 / 4	6	23	255.611	6.675	4.5324	359.382	46.611	0.9912	0.312	175152	88.836	533.0141
64.9	68.9	2.0	1.1	49.9	8 / 4	6	24	339.219	6.401	4.5399	804.053	42.432	0.9919	0.303	166068	63.286	379.7131
70.2	57.3	2.9	1.3	46.2	8 / 4	6	40	324.165	5.349	4.5643	714.042	43.028	0.9942	0.305	167883	55.255	331.529

diameter and thickness are low, and the fin pitch is too high. This emphasises the importance that fin thickness and pitch have on the design performance, even for designs with differing numbers of passes, rows, and cells. The PR for these systems is relatively high which is a result of the reduced sCO_2 mass flow rate per cell, however, they do not perform as well as the best designs because there is only one flow path. This also explains the high sCO_2-side velocities which occur even when the transverse pitch is low. Splitting the sCO_2 flow per pass decreases the tube velocity of the fluid, this means that designs with only a single flow path have lower PR values than designs with two or more flow paths per pass. The masses of the systems having 12 cells are amongst the lowest seen in Table B-1. This is a result of the reduced number of tubes present in each bundle. It is important to note that the design with more transverse tubes is lighter than the design with less, this is because the design with fewer transverse tubes has a lower fin pitch and higher fin thickness. Once again, the importance of these variables is shown and the trend of increased performance from a fan power consumption perspective at the cost of increased heat exchanger mass is observed. However, the difference in mass is relatively slight for these designs and not as drastic as the cases where multiple flow paths are used.

Table B-1 also displays the results for PC systems with 10 cells. A wider range of performances is observed, and this is likely because more valid designs were found for this system configuration. These designs also introduce and show the difference between single and multiple flow path designs. In terms of their $\dot{W}_{aux}$, these designs all perform worse than the best performing PC by at least 100 kW. However, there are some designs which are much worse than others, as seen for the case where $\dot{W}_{aux} = 674.5$ kW. This design is poor because it is a 4-pass, 4 row heat exchanger with very high tube transverse and fin pitches, the heat transfer area is significantly reduced, and the fan is required to increase the airflow past the finned tubes by a significant amount to achieve the required heat rejection. But having a 4-pass, 4 row configuration does not prevent it from performing well. This is observed in the design just above it where the tubes are tightly packed ($S_T = 54.0$ mm), the fin pitch is lower, and the fin thickness is very high. Comparison of this design to one with two flow paths but worse values for tube longitudinal and transverse pitch, and fin pitch and thickness reveals that it performs much better from a $\dot{W}_{aux}$ perspective. But it is outperformed when a design having two sCO_2 flow paths utilises lower values for tube transverse pitch, seen for the design where $S_T = 65.6$ mm and $\dot{W}_{aux} = 287.8$ kW. Although the rest of the geometric inputs are not aiding the performance (the fin pitch is high and the longitudinal tube pitch is low), a better fan power consumption is achieved because having two flow paths doubles the heat transfer area and effect of reducing S_T. It can also be seen that once again $T_{a,ex}$ is a good indicator of system performance because it means increased heat transfer and conductance in the cell. The effect of splitting the flow is also more noticeable for these designs, two flow path designs result in a higher PR than the single flow path designs even when the transverse tube pitch is significantly higher and the number of transverse tubes lower. In general, the PR values for these designs are high, with the exception being the single flow path design with a high transverse tube pitch. This is a result of the sCO_2 mass flow rate being divided amongst 10 cells, which reduces the tube-side velocity. Furthermore, the effect of splitting the flow on PR is emphasised by the significantly lower sCO_2 tube

velocities present in these designs. The masses of the 10 cell PC designs also vary quite significantly, with the major trend demonstrating that increased mass is linked to the number of flow paths, the geometric input parameters: S_T, S_f, t_f, and results in a better performance from a $\dot{W}_{aux}$ and PR perspective. However, as discussed, relatively good performance can be achieved for a single flow path design provided the heat exchanger geometry is carefully selected. These systems have a lower mass as observed in the 4-pass, 4 row design with $m_{he} = 19.279$ tonnes.

The PC designs with 8 cells include the best performing design, additionally these designs also provide insight into what drives better performance in a design with the same sCO_2 mass flow through each cell. These designs were found to have the lowest $\dot{W}_{aux}$ values, all being within 100 kW of the best performing design's 184.5 kW fan power consumption. This is because designs with 8 cells tended to produce valid designs with heat exchangers configured with two flow paths or an increased number of equal tube passes and rows (six). Both configurations have increased heat transfer areas, requiring lower mass flow rates from the fan to reject the required amount of heat. The exception, seen in Table B-1, is the 4-pass, 4 row design with $\dot{W}_{aux} = 226.2$ kW. However, the reason this design achieves such a low $\dot{W}_{aux}$ is the extremely low fin pitch (1.2 mm) and extremely high fin thickness (1.3 mm), these values actually result in invalid geometry for the heat exchanger as interference will occur between fins. This should have been considered during the filtering of designs. In any case this design can be excluded from further analysis and comparison, further invalid designs have been shaded red in Table B-1 and Table B-2. Comparing the 6-pass, 6 row heat exchangers to the 4-pass, 8 row heat exchangers shows that aside from the best performing design, which has been improved using the parametric plots in Section 5.5, they produce much lower values for $\dot{W}_{aux}$. This comes at the cost of much lower PR values, for the reasons discussed previously, and the positive of significantly lower m_{he} and m_{total}. This is because both 6-pass, 6 row designs have low transverse tube pitches. It is important to note that the remainder of their geometric inputs could probably be improved, they have low longitudinal pitches and fin pitches that could be decreased. This indicates that PC designs with this heat exchanger configuration warrant further investigation in spite of their reduced PR, not only because they are able to perform well in terms of $\dot{W}_{aux}$ but also because they are lighter than the best performing design by at least half. Analysis of the 4-pass, 8 row designs show that they perform worse than the best performing design because they either have high a high fin or transverse tube pitch. Fortunately, these designs could be improved as shown in the previous section.

Finally, Table B-1 also shows results for PC designs having 6 cells. These designs tended to exclusively be valid for a 4-pass, 8 row heat exchanger configuration. This is a result of the increased sCO_2 mass flow rate per cell that occurs as the number of cells in the system decreases and the pressure drop filtering performed to select valid designs. To achieve a low enough pressure drop on the sCO_2-side, the flow had to be split in each pass to reduce the tube-side velocity and subsequently the pressure drop due to friction which is the primary contributor. In terms of their $\dot{W}_{aux}$ values, the designs perform relatively well, however, it must be noted that one of the better performing designs is constructed with invalid finned tube geometry. The decent performance for the remaining designs is attributable to their low transverse tube and fin pitches, and

relatively high fin thicknesses as well as the heat exchanger configuration. All these designs also have larger fin diameters above 40.0 mm which demonstrates the influence it can have on heat rejection system performance. The PR values for these designs are also relatively high because the sCO_2 is split in each pass, however, the masses of these systems are very high relative to the other designs. Per cell, they have the highest m_{he} values, exceeding the best performing design which is very densely packed from a tube and fin perspective. Additionally, they do not perform as well in terms of $\dot{W}_{aux}$ and PR.

In summary, the comparison of PC designs with different discrete values and heat exchanger configurations with the best performing design showed several key results. Firstly, the trends from the parametric study are consistent across configurations. Reducing transverse tube and fin pitches and increasing longitudinal tube pitch and fin thickness improves design performance from a $\dot{W}_{aux}$ and PR perspective. However, the extent to which the designs can be improved will differ depending on the number of cells, passes, and longitudinal rows, separate parametric studies and statistical analyses will therefore be necessary for each case. Furthermore, it was found that $T_{a,ex}$ is a good indicator of the system's performance, the higher the air outlet temperature, the lower the auxilliary power as the mass flow rate of air through the fan decreases. The number of cells was also found to influence the PR of a design along with the number of flow paths per pass and the tube transverse pitch. Finally, the mass of the heat exchangers in the cells was found to be very high for systems using multiple flow paths. An alternative design with 6 passes, 6 rows, and 8 cells was found to be significantly lighter while performing at a similar level to the best performing design in terms of $\dot{W}_{aux}$. However, these designs tend to have much lower PR values. Further investigation into these designs is likely warranted with the primary design consideration being whether the reduction in mass is worth the reduced system and cycle performance as a result of a low PR.

INTERCOOLER

The results for various IC system designs in Table B-2 show that the valid designs with the most cells (12) tend to only have 8-pass, 8 row heat exchangers. This is likely due to the number of cells driving the required heat rejection per cell down by almost 1 MW. In turn, this decreases the required finned tube area and therefore the number of passes required to extract the heat from the sCO_2. Additionally, this system configuration produces designs that perform much worse than the best performing case in terms of their $\dot{W}_{aux}$. Furthermore, the design with 12 cells and the lowest $\dot{W}_{aux}$ has a low transverse tube pitch ($S_T = 58.4$ mm), relatively low fin pitch ($S_f = 2.5$ mm) and consumes 378.3 kW of power. The PR values for these designs and the entire IC, with the exception of 6 cell system configurations, are all good. This is a result of the higher densities at which the IC operates, this can be seen by comparing Figure 6-3 to Figure 6-4; higher densities result in lower sCO_2-side velocities and pressure drops. This is also why it is not as important to split the flow to improve the PR in the design of the IC. The masses of the 12 cell IC systems range from low to high relative to the other designs and depend to a great extent on the transverse tube and fin pitches and the fin thickness. For example, the worst performing 12 cell system design has the lowest mass by almost

Table B-2: Comparison of various IC designs, sorted by number of cells, with the best performing case

S_L (mm)	S_T (mm)	S_f (mm)	t_f (mm)	d_f (mm)	N_L/n_{passes} (-)	N_{cells} (-)	H_F (m)	m_a (kg/s)	v_{tbs} (m/s)	$\dot{Q}_{cell}$ (MW)	$\dot{W}_{aux}$ (kW)	$T_{a,ex}$ (℃)	PR (-)	e_{he} (-)	UA (W/K)	m_{he} (tonnes)	m_{total} (tonnes)
51.6	54.7	3.5	1.1	45.7	8 / 8	12	37.0	230.662	2.813	3.8433	528.625	45.448	0.9966	0.146	177079	44.672	536.064
70.0	58.4	2.5	0.5	45.7	8 / 8	12	43.0	206.045	2.989	3.8401	378.297	47.348	0.9961	0.155	183394	32.444	389.328
74.8	79.6	3.3	0.6	47.4	8 / 8	12	28.0	276.384	4.060	3.8172	872.915	42.721	0.9932	0.139	167719	23.991	287.892
51.9	72.8	1.8	1.4	41.0	8 / 8	12	33.0	225.886	3.710	3.8250	489.767	45.725	0.9942	0.146	177223	50.374	604.488
64.5	51.8	1.6	1.0	38.3	10 / 10	10	21.0	181.300	3.188	4.5928	230.773	54.069	0.9945	0.174	256513	64.033	640.33
52.9	50.0	1.7	1.1	36.2	8 / 8	10	35.0	238.601	3.092	4.6055	499.529	48.094	0.9959	0.160	223909	47.198	471.98
79.7	55.0	1.8	0.8	40.1	8 / 8	10	29.0	219.677	3.398	4.5979	399.378	49.713	0.9950	0.172	231454	42.803	428.03
55.9	76.2	1.3	1.2	45.9	8 / 8	10	43.0	258.285	4.695	4.5584	602.174	46.438	0.9909	0.150	214194	71.934	719.34
59.9	53.3	1.2	1.0	43.7	6 / 6	10	24.0	275.954	3.289	4.6111	752.110	45.625	0.9965	0.189	213969	62.942	629.42
76.8	58.6	1.2	1.0	43.5	6 / 6	10	41.0	269.851	3.611	4.6047	697.270	45.889	0.9958	0.189	214237	56.699	566.99
79.5	52.0	2.7	1.2	40.7	10 / 10	8	27.0	251.303	4.010	5.7063	476.600	51.535	0.9916	0.154	299941	58.424	467.392
77.7	61.7	3.4	1.5	44.8	10 / 10	8	38.0	291.529	4.747	5.6684	713.075	48.308	0.9884	0.133	277398	59.751	478.008
64.8	70.2	1.2	0.6	46.3	10 / 10	8	32.0	255.765	5.380	5.6275	488.347	50.815	0.9852	0.148	290706	61.720	493.76
54.1	56.6	1.3	1.4	44.3	8 / 8	8	40.0	297.408	4.362	5.7121	742.595	48.069	0.9920	0.160	278114	100.938	807.504
76.9	50.2	1.8	0.9	44.8	10 / 10	6	41.0	332.055	5.154	7.5225	797.627	51.566	0.9863	0.154	396685	80.129	480.774
54.6	50.7	1.4	0.9	40.8	10 / 10	6	34.0	350.717	5.217	7.5178	940.318	50.429	0.9861	0.146	386968	77.039	462.234

10 tonnes ($m_{he} = 23.99$ tonnes) because it has sacrificed performance from a $\dot{W}_{aux}$ perspective by having a high transverse tube and a relatively high fin pitch ($S_T = 79.6$ mm and $S_f = 3.3$ mm).

The 10 cell systems in Table B-2, which include the best performing design are generally observed to perform the best from a $\dot{W}_{aux}$ and PR point of view. Note that one invalid design has been included here and that there are two more with unfeasible geometry. This means that although there is no interference between the fins, the space required between them by the design is not realistic. These have been shaded in orange in the table and would require slight adjustments to their fin pitch or thickness to make them feasible which would alter their performance. Once again, it was noted that interference and the feasibility of fin spacing, and thickness should have been considered when setting up the DoE. In any case, raising the fin pitch or decreasing the fin thickness in these designs would negatively impact their performance, leaving them further from the best performing design. Furthermore, both the unfeasible designs have a 6-pass, 6 row heat exchanger configuration and low transverse tube pitches and still consume more auxilliary power than the best design. This a trend across the range of 10 cell system designs, as the number of passes drops, so does the performance of the system in terms of $\dot{W}_{aux}$. Additionally, the designs with larger longitudinal tube pitches tend to perform better regardless of the number of passes. The reason for this is the lower Δp_{amb} that occurs when the heat exchanger reduces in height which results in the fan being required to recover more pressure to maintain momentum balance on the air-side. The other important geometric parameters (S_T, S_f, and t_f) while not irrelevant, can only influence performance for a set number of passes. When the number of passes increases or decreases, the longitudinal tube pitch becomes the driving factor behind performance increase or decrease. This is evident in the best performing design which has 10 passes and 10 rows. The longitudinal pitch is only 64.5 mm and is limited because any further increase would require the fan to recover a static pressure below the range of its operating envelope. The PR values for the 10 cell designs are all high, once again as a result of the high densities in the IC but also because the sCO_2 mass flow rate is being distributed between many cells relative to the other designs. The best performing design does not have the highest PR despite having a very low transverse tube pitch. This result is linked to the sensitivity of sCO_2 density to temperature in the IC, designs which achieve larger temperature drops per pass will see a more significant increase in sCO_2 density per pass as per Figure 6-4. Subsequently, the velocity and pressure drop per pass will be lower. Furthermore, designs with fewer passes will experience lower pressure drops due to friction as the length decreases in Eq. (C-5). In terms of mass, these systems tend to be of medium to high weights, however, for the designs that are not feasible, the increased mass is because the fins are very densely packed. It must be noted that the best performing design constitutes the heaviest valid design for the IC as a result of its 10 passes and tight packing in terms of transverse tubes, fins per tube, and fin size.

The IC system designs with 8 cells were analysed next and can be seen near the bottom of Table B-2, there is only one invalid design for this system configuration. While they tended to have a high number of passes per cell (10 for all valid designs), even the two best designs of this system configuration are outperformed by the best performing IC design by at least 200 kW, having $\dot{W}_{aux} = 476.6$ kW and $\dot{W}_{aux} = 488.3$ kW respectively. Both these designs either have a low transverse tube pitch, low fin pitch, high fin thickness or some combination of these. The reasons for their reduced performance are the reduced number of cells,

which increased the required heat transfer per cell, and low sCO_2 thermal conductivities across the range of operating temperatures. These led to poor performance from both a $\dot{W}_{aux}$ and a PR perspective. These designs also have the lowest values for e_{he} across the IC designs this is likely a result of the increased required heat rejection per cell and the increased C_{min} due to higher sCO_2 mass flow rates per cell. Both factors will drive the maximum heat extraction value up, and while the heat rejection is also increased, this is to a lesser extent. The low PR values and high sCO_2-side velocities seen for the 8 cell IC designs are also a result of the increased sCO_2 mass flow rate per cell. Most of the designs have $PR < 0.99$ which is uncommon for the IC designs seen in Table B-2, the designs are also not aided by their relatively high transverse tube pitches and longer flow paths. In terms of the heat exchanger and total system masses, these designs perform adequately, while the heat exchangers are on the heavier end of the IC mass spectrum, the total mass of each system is at an acceptable level relative to the other designs. This is because there are fewer cells and the reason behind the higher m_{he} values are the geometry of the finned tube bundles.

Finally, two valid designs were found for IC systems with 6 cells. They can be seen at the bottom of Table B-2 and perform the worst of all the designs when it comes to $\dot{W}_{aux}$ and the PR. They have $\dot{W}_{aux} = 797.6$ kW and $\dot{W}_{aux} = 940.3$ kW respectively and both have a $PR = 0.986$. The reason that their PR are so low compared to the other IC system configurations and designs is primarily the significantly higher sCO_2 mass flow rate per cell (65.35 kg/s). Another contributing factor is the extended flow path present in both designs, they need 10-pass, 10 row heat exchangers to reject the increased required amount of heat per cell. This, in turn, increases the frictional pressure drop across the heat exchanger. It can also be observed that even with very low transverse tube pitches ($S_T < 51.0$ mm) these designs still consume large amounts of fan power and experience high sCO_2-side pressure drops. Furthermore, their fin pitches and thicknesses are within the region of good performance that is consistent across the other IC designs. The only way to potentially make these designs more advantageous from a cycle efficiency perspective would be to increase the number of passes and potentially have thicker fins that are as tightly packed as possible. Both changes would increase the mass of the heat exchangers, which is currently at an acceptable level relative to the other designs. They would also do nothing to improve the PR, and would actually decrease it further due to the increased flow path length. Another option would be to use larger fans and overhaul the geometry because larger fans result in longer pass lengths and a higher heat exchanger width which would allow more tubes. Potential geometric changes would include increasing the transverse tube pitch and longitudinal pitch to allow larger fin diameters while simultaneously increasing the fin thickness as well as the fin pitch.

In summary, the comparison of the various IC system designs with different discrete geometric inputs (n_{passes}, N_L, N_{cells}) yielded several key results. Firstly, the IC designs operate best with a single flow path and increased numbers of passes because the sCO_2 density is high across the IC and each cell is extracting more heat than the PC. They also tend to have higher PR values than the PC designs because of the increased densities at their operating pressure and temperatures. As in the PC, it was also found that the best performing designs contained tube longitudinal and transverse pitches, fin pitches, and fin thicknesses in the regions of best performance indicated by the parametric study in Section 5.5. The results also indicate that IC designs should have higher numbers of cells to improve the PR and that for a 10-cell system configuration,

a 10-pass, 10 row heat exchanger is the best performing because it results in increased heat transfer area and ambient pressure rise. This requires less static pressure recovery across the fan and reduces $\dot{W}_{aux}$. Unfortunately, it was found that the best performing IC design is also the heaviest, however, no competitive alternate designs from a cycle efficiency perspective were found for the other configurations. Perhaps, the design could be changed to reduce its mass and sacrifice some measure of its performance. It was also found that the 6-cell IC designs are not feasible for this fan size, a large fan and altered geometry or extensive changes to the design limits from the DoE would be required to make them a realistic option.

Appendix C Thermohydraulic fundamentals

C-1. Fluid flow in ducts

Fluid flow in pipes and tubes can be categorized into one of three flow regimes, laminar, transitioning, or turbulent flow. The flow may also be hydrodynamically and thermally developing or fully developed. The point at which the flow is fully developed from a hydrodynamic perspective is not necessarily the same as the point at which it will be thermally fully developed.

From a hydrodynamic point of view, the flow regime may be categorized by the Reynolds number, given below.

$$Re = \frac{\rho v d_e}{\mu} s \qquad \textit{(C-4)}$$

Where ρ is the fluid density measured in kg/m^3, v is the fluid's free stream velocity in m/s, d_e is the hydraulic diameter of the tube or duct in meters and μ is the dynamic viscosity of the fluid in kg/m·s. The type of flow can be determined from the Reynolds number. For pipes, transitional flow occurs in the range of $2000 \leq Re \leq 4000$. A Reynolds number below 2 000 indicates laminar flow and one above 4 000 indicates turbulent flow.

Flow through ducts encounters several losses. These include frictional pressure drops and pressure drops from changing duct geometry (bends, inlets, outlets, abrupt contractions, and expansions, etc.). These pressure drops can be determined for single-phase flow using the relationships given in Equations (C-5) and (C-6).

$$\Delta p_{fric} = f_D \left(\frac{L}{d_e}\right)\left(\frac{\rho v^2}{2}\right) \qquad \textit{(C-5)}$$

$$\Delta p_{form} = K \frac{\rho v^2}{2} \qquad \textit{(C-6)}$$

In these equations both Δp values are in Pa. L refers to the duct length in meters, while *v* is the mean velocity of the fluid in m/s. The two dimensionless loss coefficients are f_D and K. f_D is the Darcy-Weisbach friction factor. Various correlations exist for the selection of an appropriate factor based on fluid properties, flow

regime and duct geometry. The same can be said for the form loss factor (K) although it is usually more dependent on the geometry. In the case of the friction factor, it is sometimes necessary to correct f_D using a dimensionless correction factor based on the mean wall temperature or viscosity.

C-2. Heat transfer in ducts

The modes of heat transfer relevant to this work are primarily conduction and convection. The well-known equations for basic conduction and convection heat transfer in circular ducts are shown in (C-7) and (C-8) respectively.

$$Q = 2\pi Lk \frac{(T_i - T_o)}{\ln\left(\frac{r_o}{r_i}\right)} \qquad (C\text{-}7)$$

Where L is the length of pipe in meters over which heat transfer occurs, r is a radius value in meters, k is the thermal conductivity in W/m·K, the subscripts i and o refer to the inside and outside surfaces of the duct and the temperature T is measured in Kelvin.

Equation (C-7) is a specific form of Fourier's Law, within this correlation the natural log of the inner to outer radii ratio over the thermal conductivity can be considered like series resistances to heat transfer. This means that they can be summed when there are multiple layers of different materials across which heat is conducted.

$$Q = hA(T_w - T_m) \qquad (C\text{-}8)$$

In the above equation, h is the convection heat transfer coefficient measured in W/m^2·K, A is the surface area across which heat is transferred in m^2 and the subscripts m and w, attached to the temperatures T, refer respectively to the wall and bulk mean fluid temperatures.

There are two primary forms of convection, forced and free or natural convection. Natural convection takes place when a temperature difference results in a density difference. This will cause a mass movement of the fluid and subsequently heat transfer. Forced convection is when the fluid movement and heat transfer results from an external source (like a pump or a fan).

Another common method of evaluating heat transfer is through what is known as the overall heat transfer coefficient, UA. This value has the units W/K and it allows for the collection of heat transfer modes in conductive-convective problems. Between two separated fluids, the overall heat transferred can be found using Equation (C-9).

$$Q = UA\Delta T \qquad (C\text{-}9)$$

Where ΔT is the temperature difference between the hot and cold fluids. UA can be determined by treating the various heat transfer coefficients present as resistances and summing them accordingly as in Equation (C-11). Another important value used to find the convective heat transfer coefficient is the

dimensionless Nusselt number, Nu. It is the ratio of convective conductance to molecular thermal conductance. Equation (C-10) shows the basic expression for the Nusselt number in a duct.

$$Nu = \frac{hd_e}{k} \tag{C-10}$$

The Nusselt number varies drastically depending on the flow regime and convective heat transfer mode. Several other variables and factors become important when this is the case. A variety of different correlations for Nu in ducts have been suggested and experimentally determined. Those relevant to this work are shown in Section 4.

$$UA_i = \frac{1}{\sum \frac{1}{hA} + \sum \frac{L}{kA} + \sum \frac{1}{hA}} \tag{C-11}$$

The Prandtl number is another dimensionless value used extensively in heat transfer calculations. This number is a ratio of the momentum diffusivity in a fluid to the thermal diffusivity and an expression for it is shown below.

$$Pr = \frac{\mu C_p}{k} \tag{C-12}$$

This value finds extensive use in further heat transfer correlations, specifically determination of the Nusselt number and heat transfer coefficients. The value for k and μ are as seen in previous equations. C_p refers to the isobaric specific heat capacity of the fluid, measured in J/kg.K.

C-3. Extended surfaces

In heat exchangers, a prime surface is the duct, cylinder or tube, and an extended surface adds to the prime. Extended surfaces are referred to as fins. Heat transfer through fins can be described by Equation (C-13) and this correlation relies on several assumptions. These are (i) the heat transfer coefficient is uniform along the fin, (ii) substantial temperature gradients exist only outwards from the root of the fin towards the tip and (iii) the heat lost at the fin tip is negligible. These assumptions allow for a "reasonable approximation in practice" according to Kroger (2004).

$$Q = \left(2hk_f t_f\right)^{0.5} L_f (T_r - T_a) \tanh\left(bH_f\right) \tag{C-13}$$

Where h is the convection heat transfer coefficient in W/m^2·K. The variables t_f, L_f and H_f are the thickness, length, and height of the fin in meters while k_f represents the thermal conductivity of the fin and the two temperatures (both in Kelvin) T_r and T_a are the root temperature and surrounding fluid (air) temperature, respectively. An expression for the dimensionless factor b, can be found below.

$$b = \left(\frac{2h}{k_f t_f}\right)^{0.5} \quad \text{(C-14)}$$

Fins in heat exchangers also have an associated efficiency, η_f, and overall surface effectiveness, η_o. The surface effectiveness is provided in Equation (C-17). The fin efficiency for circular fins is usually found using Bessel functions and an extensive formula (Kröger, 2004). This work makes use of the simplified empirical Equations (C-15) and (C-16) taken from Kröger (2004).

$$\eta_f = \frac{\tanh\left(\frac{\phi b d_o}{2}\right)}{\frac{\phi b d_o}{2}} \quad \text{(C-15)}$$

$$\phi = \left(\frac{d_f}{d_o} - 1\right)\left(1 + 0.35\ln\left(\frac{d_f}{d_o}\right)\right) \quad \text{(C-16)}$$

$$\eta_o = 1 - \frac{A_f\left(1 - \eta_f\right)}{A_{total}} \quad \text{(C-17)}$$

In the overall surface effectiveness correlation, all the area values are in m^2, A_f is the area of the fin and A is the sum of this fin area and the exposed root area. For circular fins, the fin height adjustment factor, ϕ, must be found before determining η_f, the overall surface effectiveness is still found as in Eq. (C-17).

C-4. Heat transfer in air-cooled heat exchangers

EFFECTIVENESS-NTU METHOD

Heat transfer in these units occurs between air (a) and a process fluid (p). Across the entire unit the heat transferred to the air from the fluid in Eq. (C-18) needs to be balanced with the heat transfer determined using the Effectiveness-NTU method in Eq. (C-19). This method of calculating heat transfer is best used when sizing these systems.

$$\dot{Q} = m_a c_{pa}(T_{ao} - T_{ai}) = m_p c_{pp}\left(T_{pi} - T_{po}\right) \quad \text{(C-18)}$$

$$\dot{Q}_{max} = C_{min}\left(T_{pi} - T_{ai}\right) \quad \text{(C-19)}$$

$$e = \frac{\dot{Q}}{\dot{Q}_{max}} \quad \text{(C-20)}$$

In these equations, m and c_p represent the mass flow rates in kg/s and the specific heats in J/kg·K, the heat transfer rate in W is represented by $\dot{Q}$, and e is the effectiveness of the heat exchanger – some useful correlations for a single pass of a heat exchanger are shown in Table C-3. C_{min} is the smaller of $m_a C_{pa}$ and $m_p C_{pp}$ and all the temperatures are measured in K.

Two important variables need to be defined for determining the effectiveness of a heat exchanger. These are the number of transfer units (NTU) in Eq. (C-21) and the heat capacity ratio (C) in Eq. (C-22):

$$NTU = \frac{UA}{C_{min}} \tag{C-21}$$

$$C = \frac{C_{min}}{C_{max}} \tag{C-22}$$

where UA is the conductance in W/K, C_{max} is the larger of $m_a C_{pa}$ and $m_p C_{pp}$, and C_{min} is the smaller of the two.

Table C-3: Heat exchanger effectiveness correlations

Type of Flow	Equation	
Counterflow	$e = \frac{1 - e^{-NTU(1-C)}}{1 - Ce^{-NTU(1-C)}}$	*(C-23)*
Counterflow with *C* = 1	$e = \frac{NTU}{NTU + 1}$	*(C-24)*
Crossflow with both streams unmixed	$e = 1 - e^{\frac{\left(NTU^{0.22} \times \left(e^{-CNTU^{0.78}} - 1\right)\right)}{C}}$	*(C-25)*
All exchangers with *C* = 0	$e = 1 - e^{-NTU}$	*(C-26)*

These are the most relevant correlations for e in this work. When mixing occurs between passes in a multi-pass overall counterflow heat exchanger, the overall effectiveness is represented below:

$$e = \left[\left(\frac{1 - e_{pass}C}{1 - e_{pass}}\right)^{n_{passes}} - 1\right] \Big/ \left[\left(\frac{1 - e_{pass}C}{1 - e_{pass}}\right)^{n_{passes}} - C\right] \tag{C-27}$$

Where e_{pass} is the effectiveness of each identical pass, often found using the correlations from Table C-3 above, and n_{pass} is the number of identical passes.

LMTD METHOD

The logarithmic mean temperature difference (LMTD) method is best used when analysing air-cooled heat exchangers. Once the heat rejection system has been sized, this method can be employed to find the overall conductance of the system.

$$\Delta T_{lm} = \frac{\Delta T_2 - \Delta T_1}{\ln\left(\frac{\Delta T_2}{\Delta T_1}\right)} \tag{C-28}$$

$$\dot{Q} = F_T U A \Delta T_{lm} \quad \text{(C-29)}$$

This achieved by using Eq.(C-28) and Eq. (C-29), with the temperature differences taken at the physical 'sides' of the heat exchanger as seen in Figure C- and the LMTD correction factor, $F_T = 1$.

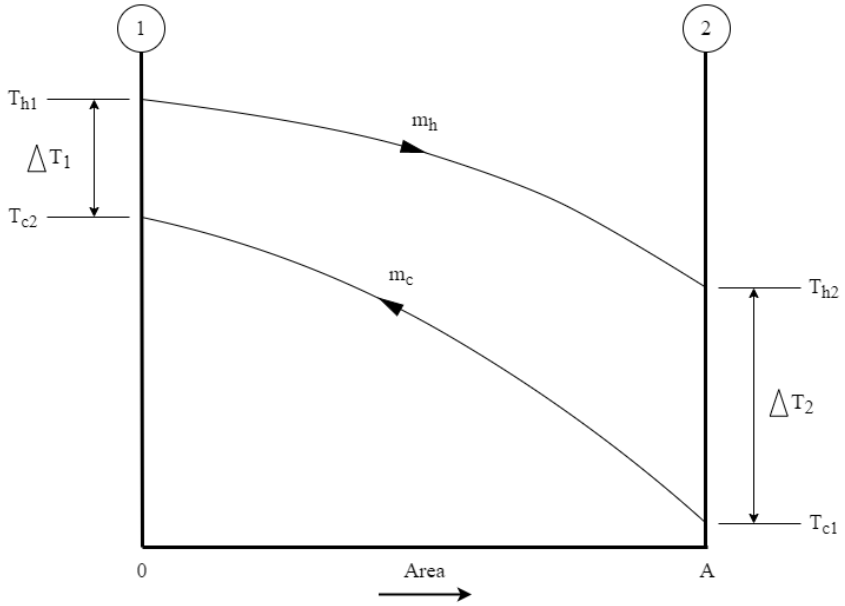

Figure C-5: LMTD method for a crossflow heat exchanger taken from Kröger (2004)

The LMTD method for crossflow heat exchangers must be adjusted by a value for F_T that is not 1.0 and depends on the heat exchanger arrangement. The process of finding F_T is complex and time-consuming, involving many empirical equations as seen in Kröger (2004). However, an approximate correlation has been presented for F_T in heat exchangers with four or more passes as seen below (*VDI Heat Atlas*, 2010). Eq. (C-39) is a function of the NTU and R for the hot stream, where R is a specific ratio of the two dimensionless temperature changes (Φ) for the hot (h) and cold (c) fluid streams:

$$\Phi_h = \frac{T_{h,in} - T_{h,ex}}{T_{c,ex} - T_{c,in}} \quad \text{(C-30)}$$

$$\Phi_h = \frac{T_{c,ex} - T_{c,in}}{T_{h,in} - T_{c,in}} \quad \text{(C-31)}$$

R_h is then defined as follows:

$$R_h = \frac{\Phi_c}{\Phi_h} \quad \text{(C-32)}$$

NTU_h can be found using Eq. (C-21), combining these values one can calculate the approximate value for the F_T of the heat exchanger:

$$F_T = \frac{n_{passes}}{NTU_h\sqrt{R_h}} \times \frac{3\sinh\left(\frac{NTU_h}{n_{passes}}\sqrt{R_h}\right)}{1 + 2\cosh\left(\frac{NTU_h}{n_{passes}}\sqrt{R_h}\right)} \quad \textit{(C-33)}$$

Eq. (C-29) can now be used again to find the actual UA value for the heat exchanger. The methodology above has been adopted when analysing the heat exchanger results in this work.

C-5. Fan systems

Fans form an essential part of any forced draft air-cooled heat exchanger. Fans introduce changes in pressure across the entire heat rejection unit while also drawing parasitic power.

FAN SCALING LAWS

Tests are performed on fans to determine their specifications. These tests are typically performed on smaller fans. When the application requires a fan with a much larger diameter, these specifications need to be scaled accordingly. These scaling laws are shown below in Equation (C-34) to (C-36). In these correlations, the subscript l refers to the specifications for the large fan.

$$\frac{V_l}{V} = \frac{N_l}{N}\left(\frac{d_{Fl}}{d_F}\right)^3 \quad \textit{(C-34)}$$

N is the rotational speed of the fan in rpm and d_F is the fan diameter in metres.

$$\frac{\Delta p_{Fsl}}{\Delta p_{Fs}} = \left(\frac{N_l}{N}\right)^2\left(\frac{d_{Fl}}{d_F}\right)^2\left(\frac{\rho_l}{\rho}\right) \quad \textit{(C-35)}$$

In the correlation above, Δp_{Fs} is the static pressure rise across the fan and ρ is the density of air at the fan.

$$\frac{P_{Fl}}{P_F} = \left(\frac{N_l}{N}\right)^3\left(\frac{d_{Fl}}{d_F}\right)^5\left(\frac{\rho_l}{\rho}\right) \quad \textit{(C-36)}$$

Equation (C-36) is for the power of the fan. These scaling laws apply to fans tested using a type A setup. When the fan is much larger the values may deviate slightly from those determined by the laws. This is because the scaling laws do not account for friction – there is no need to accord for the difference as it is negligible.

The fan static efficiency values, η_{Fs} remains the same for the larger fans. Static efficiency for the fans can be calculated from the test values (T subscripts) using the Equation below.

$$\eta_{FsT} = \frac{V_T \Delta p_{FsT}}{P_{FT}} \quad \textit{(C-37)}$$

If the test fan's Reynolds number, Re_F (based on diameter and tangential velocity) differs from the larger fan's Reynolds number then friction must be considered for the efficiency. This correlation is shown below.

$$\eta_{Fsl} = 1 - 0.5(1 - \eta_{Fs})\left[1 + \left(\frac{Re_F}{Re_{Fl}}\right)^{0.2}\right] \quad (C\text{-}38)$$

All the above scaling laws come from Kröger (2004).

FAN POWER AND STATIC PRESSURE

The power drawn by the fan (P_F) is a function of its test power value, P_{FT}, and the density of air during use and during testing. The electrical power utilised can be found after this using Equation (C-40). The correlation for fan power is shown below. In the case of fans which are much larger than their test models, the scaling laws from higher up in this section need to be used.

$$P_F = P_{FT}\left(\frac{\rho_a}{\rho_T}\right) \quad (C\text{-}39)$$

The value of P_{FT} is determined using an empirical relation that is commonly a function of the volumetric flow rate of air through the fan, V. The fan power curves, along with their third order polynomials are shown in Appendix F-2. The curves are a function of V and have been adjusted from their original test curves to represent the large fan's characteristics prior to the density adjustment.

$$P_{Fe} = \frac{P_F}{\eta_{Fs}} \quad (C\text{-}40)$$

The equation above gives the electrical power consumed by the fan, determined using a fan efficiency from equation (C-38). This is an important value from a cycle perspective as it constitutes a parasitic load which lowers the cycle efficiency.

$$K_{Fs} = \frac{2\Delta p_{Fs}\rho_a}{\left(\frac{m_a}{A_c}\right)^2} \quad (C\text{-}41)$$

In this Equation Δp_{Fs} is the static pressure gain across the fan which can be found by adjusting the test values of the fan by the density factor as in Equation (C-42).

$$\Delta p_{Fs} = \Delta p_{FsT}\left(\frac{\rho_a}{\rho_T}\right) \quad (C\text{-}42)$$

The subscript T refers to the test values for the fan. A common reference value for the density is 1.2 kg/m^3. The test value for the static pressure rise is found using an empirical curve and correlation. The curves relevant in this work are shown in Appendix F-2.

Appendix D Flownex ® SE header sizing

D-1. Header sizing

In the original Python model, it was assumed that the mass flow rate of sCO_2 was distributed equally between each cell. However, in reality, pressure drops across the headers will alter the mass flow rate into each cell, this is not desirable as it will result in potentially significant differences in performance between cells. These pressure drops are a function of the header surface roughness, diameter, and length. Considering that the headers are made from EN P235GH carbon steel and have set lengths for both the entry and distribution headers, the only design parameter that can be changed to try and equalise the flow distribution across all the cells are the header diameters. A study was performed using pipe sizes from industry are shown in Table D-1 as the potential options for the headers in both the PC and IC (Vallourec, 2022). These pipes have been designed in compliance with EN10216-2 standards.

Table D-1: EN10216-2 pipe sizes for EN P235GH carbon steel taken from Vallourec (2022)

Outer diameter (mm)	**Calculated wall thickness (mm)**	**Catalogue wall thickness (mm)**	**Weight (kg/m)**	**Inner diameter (mm)**	**Recalculated safety factor**
219.1	9.415	10	51.6	199.10	1.38
244.5	10.506	11	63.3	222.50	1.36
273.0	11.731	12.5	80.3	248.00	1.39
323.9	13.918	14.2	108	295.50**	1.33
355.6	15.280	16	134	323.60**	1.36
406.5	17.467	17.5	168	371.50**	1.30
457.0	19.637	20	216	417.00*	1.33
508.0	21.829	22.2	266	463.60*	1.32
559.0	24.020	25	329	509.00*	1.36
610.0	26.211	28	402	554.00*	1.39
660.0	28.360	28	436	604.00	1.28
711.0	30.551	32	504	647.00	1.36

*Pipe size used in the PC

**Pipe size used in the IC

In the table, the tube wall thicknesses were calculated based on the Vallourec (2022) catalogue's EN10216-2 pipe external diameters using Eq. (4-4), with a maximum allowable pressure of 16.2 Mpa and a safety factor of 1.3. This equates to an inferred design pressure of 21.1 Mpa. As with the finned tubes' wall thickness calculation, the maximum allowable pressure assumes that if the system shuts down with all its valves open, the sCO_2 pressure will equalise to the average of the cycle minimum and maximum pressures. The safety factor of 1.3 was selected to account for potential manufacturing defects and does not have to be as high as in the thin-walled heat exchanger tube case. The calculated wall thicknesses for each external diameter in the catalogue were then compared to the wall thicknesses available in the catalogue and an appropriate size was selected. The safety factors were also recalculated using Eq. (4-5) and the actual wall thickness values. Note that each potential header has a safety factor of at least 1.3 when recalculated. Table D-1 also shows the mass per metre for each potential header, this is important because the objective when sizing the headers in the studies that follow was to achieve good sCO_2 distribution between cells while maintaining realistic header sizes. This means that sCO_2 mass flow rates per cell were desired to have less than a 2% error on the equal distribution case and that the headers should be relatively light. The 2% tolerance was decided upon because it covers a range of approximately 1.5 kg/s with the equal distribution value at the centre. Mass flow rates differing by more than this across cells will have inconsistent heat rejection rates due to the high specific heat capacities of sCO_2 in both systems' operating pressure and temperature ranges. With regards to the header mass, note that the heaviest header in Table D-1 weighs 504.0 kg/m and the lightest weighs 51.6 kg/m. These correspond to total header masses of 53 626 kg and 5 490 kg for the PC and 61 992 kg and 6 347 kg for the IC assuming that all the headers are the same size.

The approach taken to size the headers for both the PC and IC involved setting the Inner diameters, shaded in Table D-1, to be equal initially then varying their equal sizes to observe the effect on sCO_2 mass flow rate per cell. If a suitable design case could not be found, headers of variable size were used, typically increasing, or decreasing from the inlet of each system to the outlet. In this way suitable header designs were found for both the PC and the IC and then set for the analyses that followed. Note that all the studies were done at design conditions, i.e., at an ambient temperature of 28.9 $^{\circ}C$ with no bypassing or recirculation.

PRECOOLER HEADERS

The equal distribution mass flow rate of sCO_2 per cell is 49.0125 kg/s for the PC, in the studies that follow, cell mass flow rate results within 2.0% of this value were shaded green, results between 2.0% and 5.0% were shaded orange, and any result outside a 5.0% tolerance on equal distribution was shaded red. These limits were set according to the reasons previously discussed. For each set of headers studied, the total header mass for the PC and the pressure ratio (PR) were recorded. Initially, headers of 222.5 mm were used across all headers in the PC, this size was selected as a good starting point based on a brief frictional pressure drop calculation. The results can be seen in Table D-2 below. Clearly, small, and equal header diameters provide poor distribution of the sCO_2 flow. This is because higher pressure drops are occurring in the initial headers as a result of a small flow area and high sCO_2 velocity. This is also the reason that the change in mass flow rate becomes less pronounced further into each street as the header pressure drop decreases. The PR has also dropped below the desired amount, likely because of the increased pressure drops in the headers and

Table D-2: Mass flow rate of sCO_2 per cell for a PC with all header diameters equal to 222.5 mm

	Mass flow rate per cell (kg/s)		Total Header Mass (kg)	Pressure Ratio (-)
	PC X 1	PC X 2		
1	70.5004	70.5004	6 735.1	0.9779
2	49.8323	49.8323		
3	39.3666	39.3666		
4	36.3507	36.3507		

because the first cells in each street are receiving sCO_2 at a much higher mass flow rate than the cells which receive less than the equally distributed amount. Interestingly, the second cells in each street receive very close to the desired mass flow rate of sCO_2 and in terms of mass the system is very light, for 8 headers and 2 entry headers it weighs 1791.4 kg which is approximately 3.5 m worth of the heaviest pipe in Table D-1. The next study aimed to observe whether increased inner diameters would

Table D-3: Mass flow rate of sCO2 per cell for a PC with all header diameters equal to 554.0 mm

	Mass flow rate per cell (kg/s)		Total Header Mass (kg)	Pressure Ratio (-)
	PC X 1	PC X 2		
1	49.3736	49.3736	42 772.8	0.9970
2	49.0176	49.0176		
3	48.8520	48.8520		
4	48.8069	48.8069		

help distribute the sCO_2 more evenly, the logic behind this decision involved increasing the flow area to reduce the pressure drop across each header. For this reason, headers with internal diameters of 554.0 mm were examined, the results are shown in Table D-3. As can be seen above, the results are good from a flow distribution and PR perspective. This is due to the significantly decreased pressure drops across both the entry and distribution headers. All the cells now have very similar inlet pressures which means that sCO_2

Table D-4: Mass flow rate of sCO2 per cell for a PC with all header diameters equal to 371.5 mm

	Mass flow rate per cell (kg/s)		Total Header Mass (kg)	Pressure Ratio (-)
	PC X 1	PC X 2		
1	51.5201	51.5201	17 875.2	0.9957
2	49.0519	49.0519		
3	47.8954	47.8954		
4	47.5826	47.5826		

splits relatively equally between all of them. However, this set of header designs is very heavy, weighing roughly 7.5 times more than the initial set of headers tested and close to the heaviest possible case. Subsequently these headers would be very expensive from both a production, maintenance, and transportation point of view.

Table D-5: Mass flow rate of sCO2 per cell for a PC with entry headers of 509 mm and decreasing header diameters across each street

	Mass flow rate per cell (kg/s)		Total Header Mass (kg)	Pressure Ratio (-)	Header diameter (mm)
	PC X 1	PC X 2			
1	50.7287	50.7287	18 621.4	0.9968	509.0
2	49.3201	49.3201			417.0
3	48.1578	48.1578			371.5
4	47.8435	47.8435			371.5

This was expected, and a solution somewhere between the two was considered in Table D-4, which shows the results for a PC using headers with 371.5 mm inner diameters and 406.5 mm outer diameters. The results show a decline in performance when it comes to distributing the sCO_2 but the PR is still high and the mass of the headers has been reduced by a factor of about 2.4 from the previous case. The most notable result is the sudden increase in the mass flow rate of the first cells in both streets, this shows that they are very sensitive to changes in diameter. On the other hand, the second cells always tend to be around the desired mass flow rate and the change in mass flow rate for the last two cells is minimal. It follows then that headers

with varying diameters may help. Larger initial diameters will keep the mass flow rate into the first cells acceptable and reducing diameters across each street should be acceptable. Therefore, the next set of headers studied was as follows from the entry to the fourth header in each street: 509 mm, 509 mm, 417.0 mm, 371.5 mm, 371.5 mm. The results for this case can be seen in Table D-5 above.

It is evident that the strategy mentioned previously has helped to a certain extent, both the flow distribution and PR are improved from the previous case where all the headers were of equal diameters. The headers are slightly heavier than before, but still less than half the weight of the heavier set seen in Table D-3 and approximately 3 times the weight of the lightest set in Table D-2, although this header configuration does not warrant consideration because of the very poor flow distribution it provides. At this stage it is important to note that the entry headers are the source of the highest pressure drops and masses, this makes it difficult to select them as larger diameters which reduce pressure drop and improve flow distribution come at the cost of significantly higher mass. The size of the entry headers was reduced to 463.3 mm and the study was concluded using the strategy outlined previously to find the PC headers seen in Table D-6. This set of headers

Table D-6: Final PC headers mass flow rate of sCO2 per cell

	Mass flow rate per cell (kg/s)		**Total Header Mass (kg)**	**Pressure Ratio (-)**	**Header diameter (mm)**
	PC X 1	PC X 2			
1	49.6586	49.6586	17313.2	0.9968	554.0
2	49.1212	49.1212			509.0
3	48.7253	48.7253			463.6
4	48.5449	48.5449			417.0

performs well from a flow distribution and a PR perspective while being on the middle to lower end of the header mass spectrum. These headers were also simulated for off-design ambient air temperatures representative of the coldest ($T_{amb} = 3.2$℃) and hottest ($T_{amb} = 40.2$℃) days for Upington. This was done to ensure that they would provide consistently good sCO_2 flow distribution across a range of ambient air temperatures. The results can be seen in Table D-7 where it was shown that the mass flow rate of sCO_2 per cell remains within 2.0% of the desired amount at both extremely hot and cold air temperatures. Furthermore, it can be noted that the PR increases under cold conditions.

Table D-7: Final PC headers sCO_2 flow distribution for the hottest and coldest ambient conditions

Conditions		Mass flow rate per cell (kg/s) PC X 1	PC X 2	Total Header Mass (kg)	Pressure Ratio (-)	Header diameter (mm)
Extremely Cold	1	49.7105	49.7105	17 313.2	0.9972	554.0
	2	49.1302	49.1302			509.0
	3	48.7022	48.7022			463.6
	4	48.5070	48.5070			417.0
Extremely Hot	1	49.6393	49.6393	17 313.2	0.9967	554.0
	2	49.1179	49.1179			509.0
	3	48.7339	48.7339			463.6
	4	48.5589	48.5589			417.0

INTERCOOLER HEADERS

Adopting the same approach as the PC, the headers in the IC were initially set with 199.10 mm inner diameters to assess whether small headers could be consistently used, these results are shown in Table D-8.

Table D-8: Mass flow rate of sCO2 per cell for an IC with all header diameters equal to 199.1 mm

	Mass flow rate per cell (kg/s) IC X 1	IC X 2	Total Header Mass (kg)	Pressure Ratio (-)
1	49.2578	49.2578	6 346.8	0.9796
2	41.5353	41.5353		
3	36.8050	36.8050		
4	34.5336	34.5336		
5	33.9182	33.9182		

They were then adjusted to have 509.0 mm inner diameters to examine the effect that increasing the header size has on flow distribution. Note that the mass flow rate of sCO_2 per cell for equal flow distribution in the IC is 39.21 kg/s. Analysis of Table D-8 and Table D-9 show that as in the PC, the smaller header sizes provide poor sCO_2 flow distribution and a significantly reduced PR across the sCO_2-side of the heat exchanger while being very light. On the other hand, the larger, heavier header sizes provide a very good flow distribution of sCO_2 between the cells and PR. This is a result of the pressure drops through the headers decreasing and the inlet pressures for each cell equalising to a certain extent. This effect was witnessed at a lower header inner diameter than in the PC because of the increased sCO_2 densities in the IC amplifying the reduction in pressure drop. Following the two limit cases examined above, an intermediate case was trialled with headers having 371.5 mm inner diameters as seen in Table D-10. The flow distribution of sCO_2 is still very good with these smaller diameters, and while the PR has decreased slightly, it is overshadowed by the reduction in header mass by a factor of approximately 2.0. It was also noted that the trend of less drastic change in sCO_2 mass flow rate between the cells furthest from the inlet is also present in the IC. Once again, this is due to the sCO_2 mass flow rate in the headers furthest into each street decreases as flow is split off into the preceding cells. This reduces the pressure drop across them and results in cell mass flow rates that are very close together. This indicated that a similar strategy to the PC could be employed, where the headers decrease in size from the beginning of each street. Before this strategy was implemented, the IC was simulated for headers with

Table D-9: Mass flow rate of sCO2 per cell for an IC with all header diameters equal to 509.0 mm

	Mass flow rate per cell (kg/s)		**Total Header Mass (kg)**	**Pressure Ratio (-)**
	IC X 1	IC X 2		
1	39.3279	39.3279		
2	39.2351	39.2351		
3	39.1813	39.1813	40 467.0	0.9942
4	39.1563	39.1563		
5	39.1495	39.1495		

323.3 mm inner diameters, these results, not shown here, showed that headers of that size had too large of a negative effect on the sCO_2 flow distribution to be utilised uniformly throughout the IC. Because the primary contributor towards the header cost in terms of mass is the entry headers, the size of these was maintained at this acceptable value. The remaining headers were sized to achieve a balance between a reduced mass and relatively equal flow distribution. The final header sizes for the IC, shown in Table D-11, were as follows from the first to the fifth cell in each street: 371.5 mm, 371.5 mm, 323.6 mm, 323.6 mm, and 295.5 mm. When designed like this, the headers achieved a good sCO_2 flow distribution and PR while also reducing the

mass by approximately 2 000 kg from the design case in Table D-10. It was decided that this reduction in mass was worth the slight decrease in the equality of the flow distribution and the cost involved from an

Table D-10: Mass flow rate of sCO2 per cell for an IC with all header diameters equal to 371.5 mm

	Mass flow rate per cell (kg/s)		Total Header Mass (kg)	Pressure Ratio (-)
	IC X 1	IC X 2		
1	39.7665	39.7665		
2	39.3280	39.3280		
3	39.0741	39.0741	20664	0.9937
4	38.9566	38.9566		
5	38.9248	38.9248		

operations and maintenance perspective. This cost is incurred because headers of different sizes must be stocked for replacements. Furthermore, it is unfortunate that there is no overlap between the header sizes used in the PC and those used in the IC as this would simplify the maintenance and repair of the systems. Having larger headers of equal sizes is something which should be considered when implementing heat rejection system designs into a real-life plants.

Table D-11: Final IC headers mass flow rate of sCO2 per cell

	Mass flow rate per cell (kg/s)		Total Header Mass (kg)	Pressure Ratio (-)	Header diameter (mm)
	IC X 1	IC X 2			
1	39.9704	39.9704			371.5
2	39.5355	39.5355			371.5
3	39.0349	39.0349	18539.2	0.9937	323.6
4	38.8033	38.8033			323.6
5	38.7058	38.7058			295.5

Lastly, the final IC header sizes were also simulated for the hottest and coldest ambient conditions to ensure consistent performance from a flow distribution perspective would be achieved. These results are shown in Table D-12 below and indicate that the system will distribute the sCO_2 adequately for hotter ambient air temperatures but may not perform as well when it is cold. However, it was noted that the increased mass flow rate in the first cell of each IC street was only slightly outside the 2.0% tolerance value and that this trend is common with the potential header sizes shown in Table D-9. The only way to prevent this would be to increase the entry header and first cell header sizes and potentially the size of the headers further into each street. This would raise the mass of the headers by a significant amount, therefore this slight deviation outside of the tolerance band was deemed acceptable. Additionally, the frequency of temperatures as low as 3.2 ℃ is low in the region of Upington. This means that the system will distribute sCO_2 nearly equally for most of its time in operation. Note that, as in the PC, the PR increases at lower ambient air temperatures because the sCO_2 temperature is falling considerably faster than at higher ambient air temperatures. This results in a larger increase in sCO_2 density across the passes of the heat exchanger which will reduce the tube-side velocities and subsequently the frictional pressure drops. The effect of higher sCO_2 densities is also the cause of the difference between the PC and IC header sizes. The IC can achieve nearly equal flow

Table D-12: Final IC headers sCO2 flow distribution for the hottest and coldest ambient conditions

Conditions		**Mass flow rate per cell (kg/s)**		**Total Header Mass (kg)**	**Pressure Ratio (-)**	**Header diameter (mm)**
		IC X 1	IC X 2			
Extremely Cold	1	40.0773	40.0773	18539.2	0.9947	371.5
	2	39.5820	39.5820			371.5
	3	39.0107	39.0107			323.6
	4	38.7458	38.7458			323.6
	5	38.6342	38.6342			295.5
Extremely Hot	1	39.9293	39.9293	18539.2	0.9931	371.5
	2	39.5176	39.5176			371.5
	3	39.0442	39.0442			323.6
	4	38.8254	38.8254			323.6
	5	38.7333	38.7333			295.5

distribution with much smaller headers because the sCO_2 density is higher at its inlet temperature and pressure than the PC. This means that the velocity of sCO_2 in the IC headers and pressure drop across them will be low, even with smaller flow areas.

In summary, the headers for both the PC and IC have been sized using real-world pipe dimensions to achieve a near equal distribution of sCO_2 per cell. Furthermore, these header designs have been shown to operate effectively at the extreme limits of potential ambient air temperatures. Additional analyses may now be conducted for the single cell models and entire system models following the verification of the single cell models with the Python models and sample calculations.

D-2. EN10216-2 pipe catalogue

The pipe catalogue shown below is for tubes and their respective wall thicknesses manufactured to the EN10216-2 standard (Vallourec, 2022):

Outside diameter D		Weight in kg/m																																				
		2	2.3	2.6	2.9	3.2	3.6	4	4.5	5	5.6	6.3	7.1	8	8.8	10	11	12.5	14.2	16	17.5	20	22.2	25	28	30	32	36	40	45	50	55	60	65	70	80	90	100
mm	in.	0.079	0.091	0.102	0.114	0.126	0.142	0.157	0.177	0.197	0.220	0.248	0.280	0.315	0.346	0.394	0.433	0.492	0.559	0.630	0.689	0.787	0.874	0.984	1.102	1.181	1.260	1.417	1.575	1.575	1.575	1.575	1.575	1.575	1.575	1.575	1.575	3,937
21.3	0.840	0.952	1.08	1.20	1.32	1.43	1.57	1.71	1.86	2.01																												
22	0.866	0.986	1.12	1.24	1.37	1.48	1.63	1.78	1.94	2.10																												
25	0.985	1.13	1.29	1.44	1.58	1.72	1.90	2.07	2.28	2.47	2.68	2.91																										
25.4	1.000	1.15	1.31	1.46	1.61	1.75	1.94	2.11	2.32	2.52	2.73	2.97																										
26.9	1.060	1.23	1.40	1.56	1.72	1.87	2.07	2.26	2.49	2.70	2.94	3.20	3.47	3.73																								
30	1.185		1.57	1.76	1.94	2.11	2.134	2.56	2.83	3.08	3.37	3.68	4.01	4.34																								
31.8	1.250		1.67	1.87	2.07	2.26	2.50	2.74	3.03	3.30	3.62	3.96	4.32	4.70																								
32	1.260		1.68	1.89	2.08	2.27	2.52	2.76	3.05	3.33	3.65	3.99	4.36	4.74																								
33.7	1.330		1.78	1.99	2.20	2.41	2.67	2.93	3.24	3.54	3.88	4.26	4.66	5.07	5.40																								
35	1.378			2.08	2.30	2.51	2.79	3.06	3.38	3.70	4.06	4.46	4.89	5.33	5.69																								
38	1.500			2.27	2.51	2.75	3.05	3.33	3.72	4.07	4.47	4.93	5.41	5.92	6.34	6.91																								
40	1.575			2.40	2.65	2.90	3.23	3.55	3.94	4.32	4.75	5.24	5.76	6.31	6.77	7.40																								
42.4	1.670			2.55	2.82	3.09	3.44	3.79	4.21	4.61	5.08	5.61	6.18	6.79	7.29	7.99																								
44.5	1.750			2.69	2.98	3.26	3.63	4.00	4.44	4.87	5.37	5.94	6.55	7.20	7.75	8.51	9.09	9.86																					
48.3	1.900			2.93	3.25	3.56	3.97	4.37	4.86	5.34	5.90	6.53	7.21	7.95	8.75	9.45	10.1	11.0																					
51	2.010			3.10	3.44	3.77	4.21	4.64	5.16	5.67	6.27	6.94	7.69	8.48	9.16	10.1	10.9	11.9																					
54	2.125			3.30	3.65	4.01	4.47	4.93	5.49	6.04	6.68	7.41	8.21	9.08	9.81	10.9	11.7	12.8	13.9																				
57	2.245				3.87	4.25	4.74	5.23	5.83	6.41	7.10	7.88	8.74	9.67	10.5	11.6	12.5	13.7	15.0																				
60.3	2.374				4.11	4.51	5.03	5.55	6.19	6.82	7.55	8.39	9.32	10.3	11.2	12.4	13.4	14.7	16.1	17.5																			
63.5	2.500				4.33	4.76	5.32	5.87	6.55	7.21	8.00	8.89	9.88	10.9	11.9	13.2	14.2	15.7	17.3	18.7																			
70	2.760				4.80	5.27	5.90	6.51	7.27	8.01	8.89	9.90	11.0	12.2	13.3	14.8	16.0	17.7	19.5	21.3	22.7																		
73	2.875				5.01	5.51	6.16	6.81	7.60	8.38	9.31	10.4	11.5	12.8	13.9	15.5	16.8	18.7	20.6	22.5	24.0																		
76.1	3.000				5.24	5.75	6.44	7.11	7.95	8.77	9.74	10.8	12.1	13.4	14.6	16.3	17.7	19.6	21.7	23.7	25.3	27.7																	
82.5	3.250					6.26	7.00	7.74	8.66	9.56	10.6	11.8	13.2	14.7	16.0	17.9	19.4	21.6	23.9	26.2	28.1	30.8	33.0																
88.9	3.500					6.76	7.57	8.38	9.37	10.3	11.5	12.8	14.3	16.0	17.4	19.5	21.1	23.6	26.2	28.8	30.8	34.4	36.5	39.4														
101.6	4-000						8.70	9.63	10.8	11.9	13.3	14.8	16.5	18.5	20.1	22.6	24.6	27.5	30.6	33.8	36.3	40.2	43.4	47.2	50.8													
108	4.250						9.27	10.3	11.5	12.7	14.1	15.8	17.7	19.7	21.5	24.2	26.3	29.4	32.8	36.3	39.1	43.4	47.0	51.2	55.2	57.5												
114.3	4.500						9.83	10.9	12.2	13.5	15.0	16.8	18.8	21.0	22.9	25.7	28.0	31.4	35.1	38.8	41.8	46.5	50.4	55.1	59.6	62.4	64.9											
127	5.000							12.1	13.6	15.0	16.8	18.8	21.0	23.5	25.7	28.9	31.5	35.3	39.5	42.8	47.3	52.8	57.4	62.9	68.4	71.8	75.0	80.8										
133	5.240							12.7	14.6	15.8	17.6	19.7	22.0	24.7	27.0	30.3	33.1	37.1	41.6	46.2	49.8	55.7	60.7	66.6	72.5	76.2	79.7	86.1	91.7									
139.7	5.500							13.4	15.0	16.6	18.5	20.7	23.2	26.0	28.4	32.0	34.9	39.2	43.9	48.8	52.7	59.0	64.3	70.7	77.3	81.2	85.0	92.1	98.4									
141.3	5.563								15.2	16.8	18.7	21.0	23.5	26.3	28.8	32.4	35.3	39.7	44.5	49.4	53.4	59.8	65.2	71.7	78.2	82.3	86.3	93.5	99.9									
152.4	6.000								16.4	18.2	20.3	22.7	25.4	28.5	31.2	35.1	38.4	43.1	48.4	53.8	58.2	65.3	71.3	78.5	85.9	90.6	95.0	103	111	119								
159	6.250								17.1	19.0	21.2	23.7	26.6	29.8	32.6	36.7	40.1	45.2	50.7	56.4	61.1	68.6	74.9	82.6	90.5	95.4	100	109	117	127								
168.3	6.625								18.2	20.1	22.5	25.2	28.2	31.6	34.6	39.1	42.7	48.0	54.0	60.1	65.1	73.1	80.0	88.3	96.9	102	108	117	127	137	146							
177.8	7.000									21.3	23.8	26.6	29.9	33.5	36.7	41.4	45.2	51.0	57.3	63.8	69.2	77.8	85.2	94.2	103	109	115	126	136	147	158	167						
193.7	7.625										26.0	29.1	32.7	36.6	40.1	45.3	49.6	55.9	62.9	70.1	76.0	85.7	93.9	104	114	121	128	140	152	165	177	188	198					
219.1	8.625											33.1	37.1	41.6	45.6	51.6	56.5	63.7	71.8	80.1	87.0	98.2	108	120	132	140	148	163	177	193	209	223	235	247	257			
244.5	9.625											37.0	41.6	46.7	51.2	57.8	63.3	71.5	80.8	90.2	98.0	111	122	135	149	159	168	185	202	221	240	257	273	288	301	325		
273	10.750											41.4	46.6	52.3	57.3	64.9	71.1	80.3	90.6	101	110	125	137	153	169	180	190	210	230	253	275	296	315	333	350	381		
323.9	12.750												55.5	62.3	68.4	77.4	84.9	96.0	108	121	132	150	165	184	204	217	230	256	280	310	338	365	390	415	438	481	519	552
355.6	14.000													68.6	75.3	85.2	93.5	106	120	134	146	166	183	204	226	241	255	284	311	345	377	408	437	466	493	544	590	630
406.5	16.000														86.3	97.8	107	121	137	154	168	191	210	235	261	278	295	329	361	401	439	477	513	547	581	644	702	756
457	18.000															110	121	137	155	174	190	216	238	266	296	316	335	374	411	457	502	545	587	628	668	744	815	880
508	20.000																135	153	173	194	212	241	266	298	331	354	376	419	462	514	565	614	663	710	756	844	928	1006
559	22.000																	168	191	214	234	266	294	329	367	391	416	464	512	570	628	684	738	792	844	945	1041	1132
610	24.000																	184	209	234	256	291	322	361	402	429	456	510	562	627	691	753	814	874	932	1046	1154	1258
660	26.000																					316	349	392	436	466	496	554	612	683	752	821	888	954	1019	1144	1265	1381
711	28.000																							423	472	504	536	599	662	739	815	890	963	1036	1107	1245	1378	1507

Tolerance range according to EN 10216-2

+/– 0.4 mm

+/– 12.5 %

+/– 20.0 %

+/– 15.0 %

+/– 10.0 %

Figure D-1: EN10216-2 pipe catalogue for tubes with an outside diameter up to 711 mm

Appendix E Additional off-design study plots

E-1. Single cell ambient air temperature plots

PRECOOLER

The plots for the Reynolds numbers, Prandtl numbers, and densities of SCO_2 are all included below.

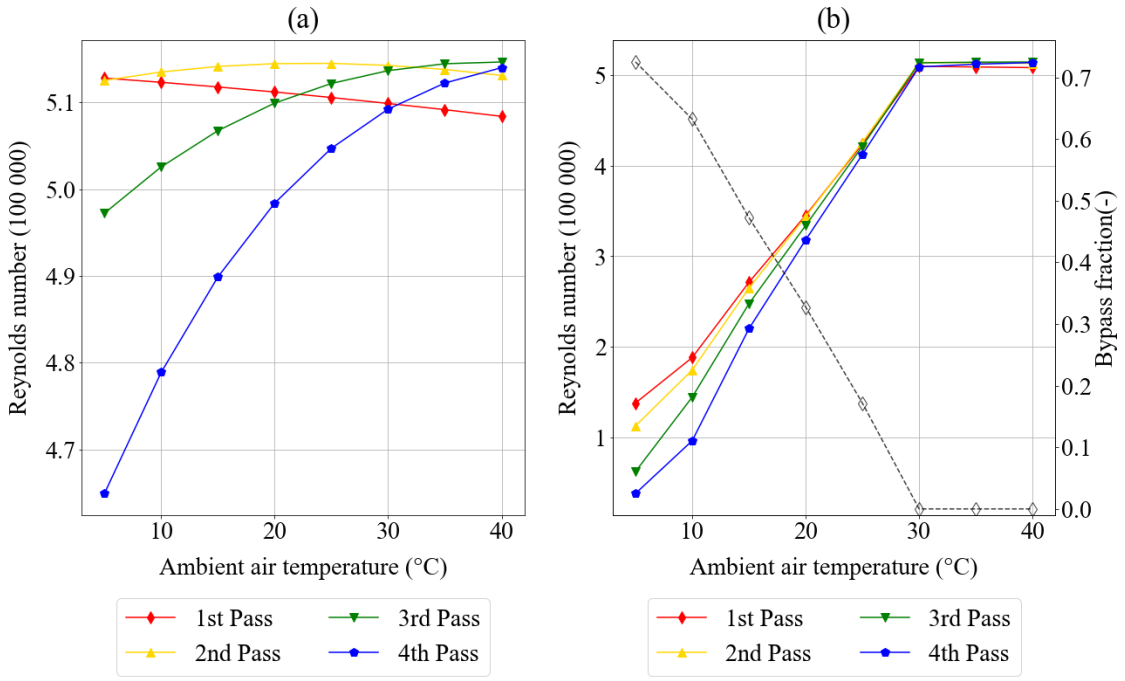

Figure E-1: PC single cell per pass Reynolds numbers (a) without bypassing and (b) with bypassing

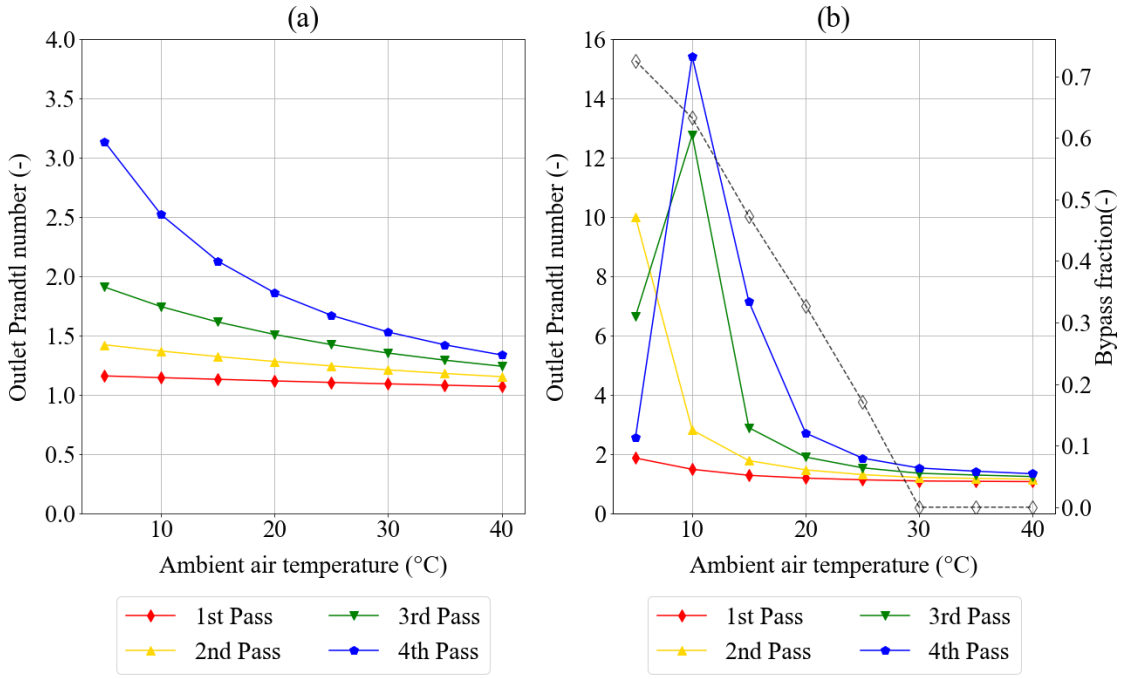

Figure E-2: PC single cell per pass Prandtl numbers (a) without bypassing and (b) with bypassing

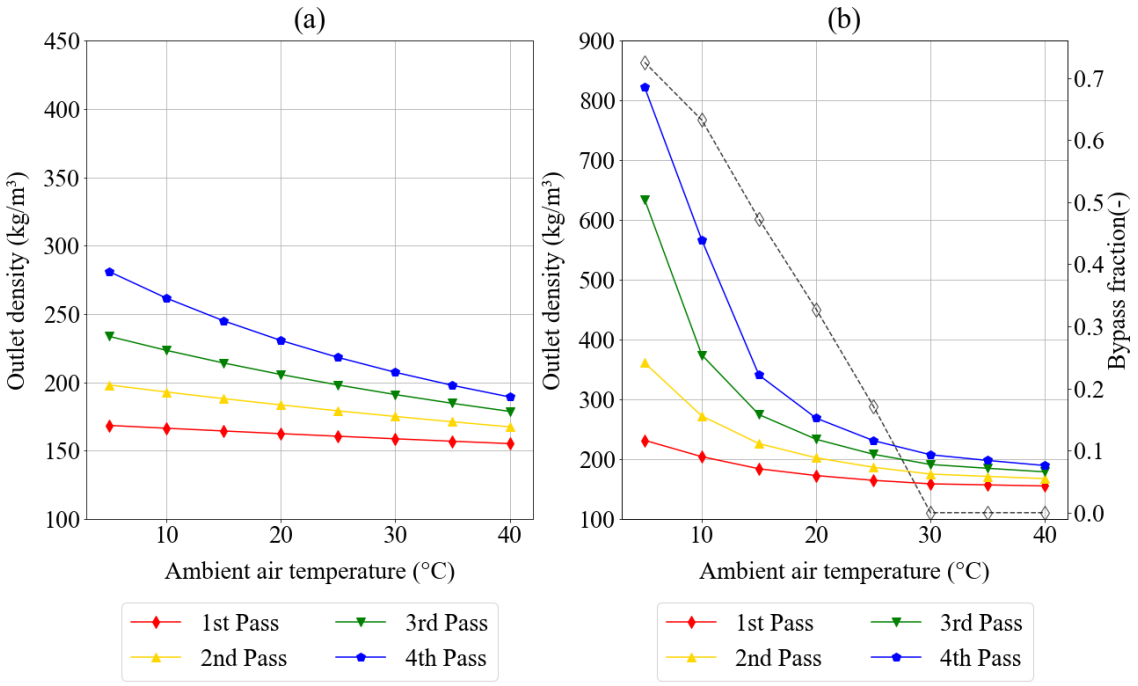

Figure E-3: PC single cell per pass densities (a) without bypassing and (b) with bypassing

INTERCOOLER

The plots for the Reynolds number, Prandtl number, and density of SCO_2 are all included below.

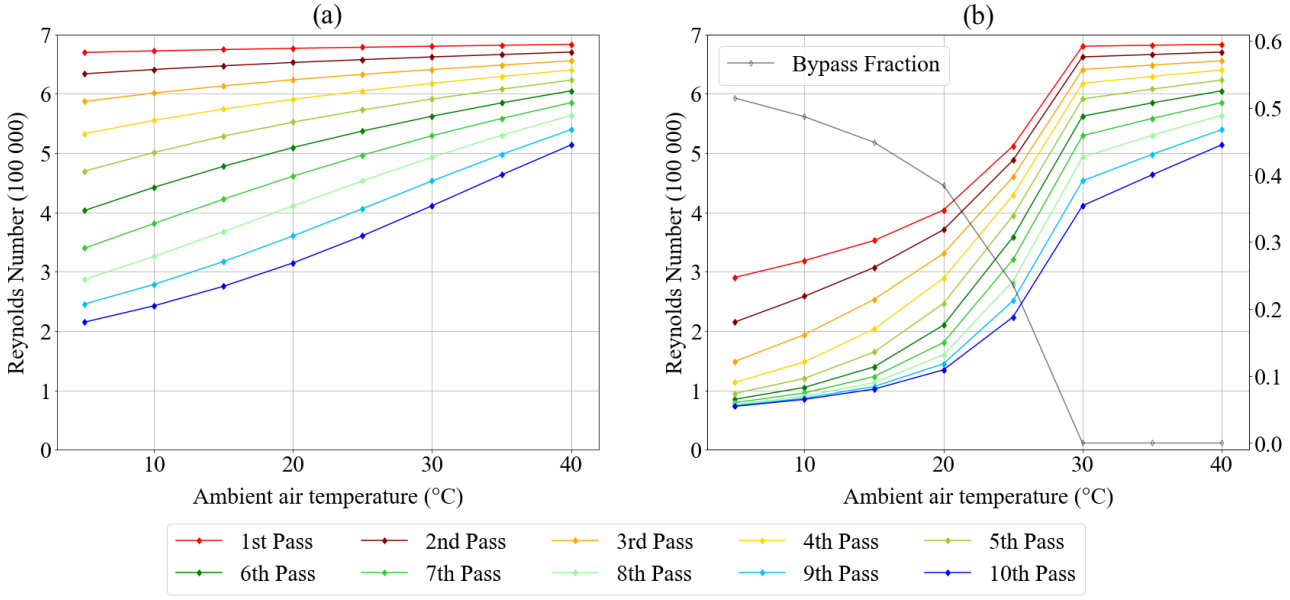

Figure E-4: IC single cell per pass Reynolds numbers (a) without bypassing and (b) with bypassing

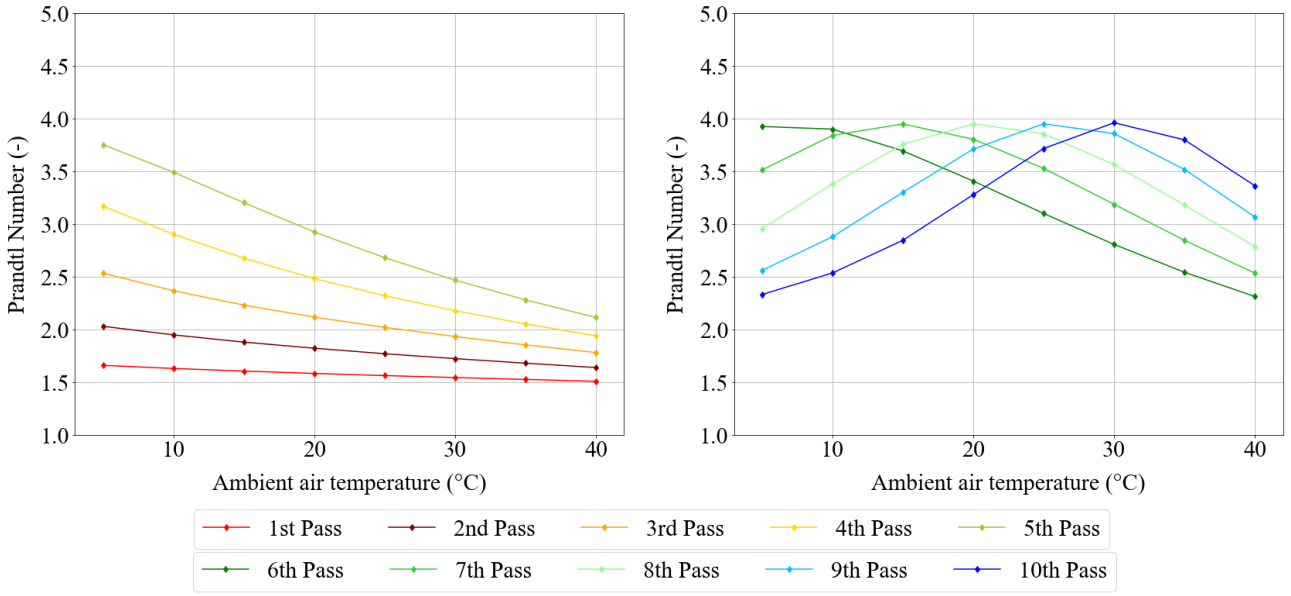

Figure E-5: IC single cell per pass Prandtl numbers without bypassing

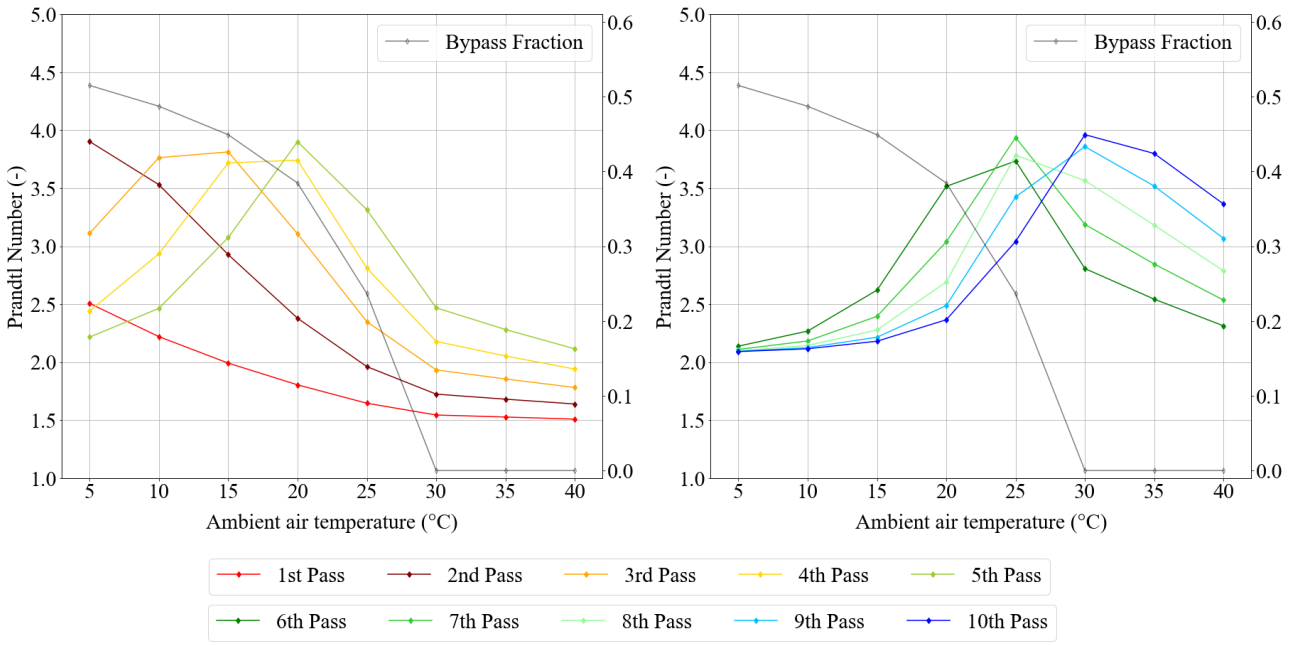

Figure E-6: IC single cell per pass Prandtl numbers with bypassing

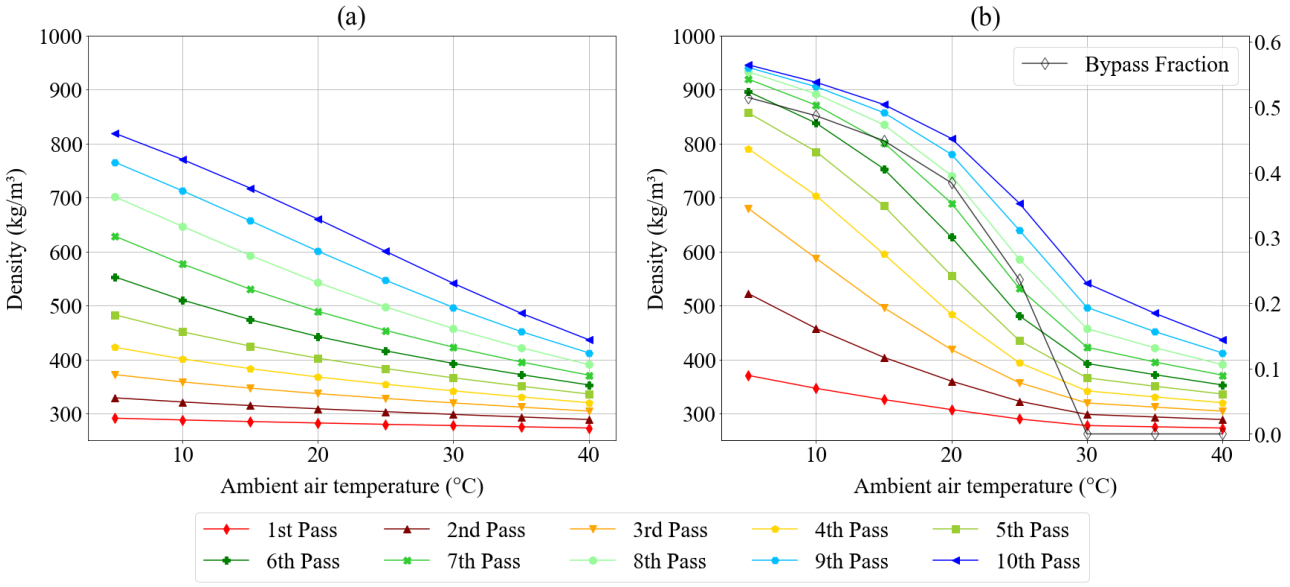

Figure E-7: IC single cell per pass densities (a) without bypassing and (b) with bypassing

E-2. Annual control study bypass mass flow rate plots

The plots used to develop the stepwise linear equations in Section 7.5 are included here.

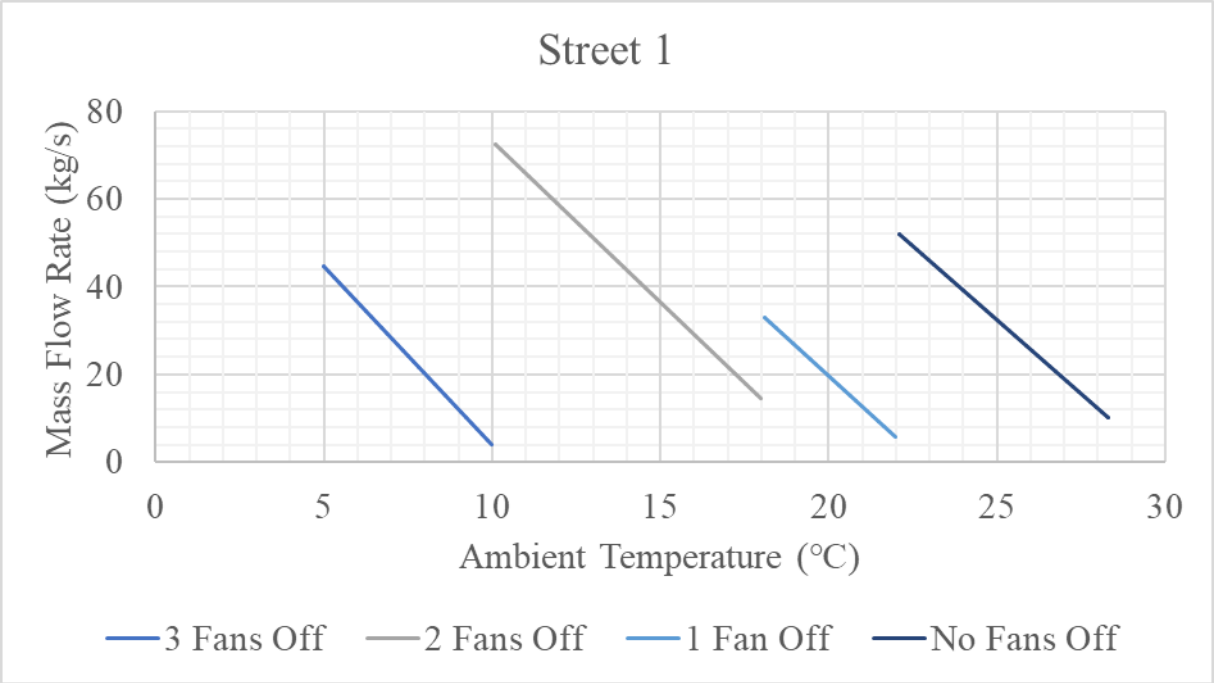

Figure E-8: Precooler Street 1 bypass sCO_2 mass flow rates for combined control strategy simulations

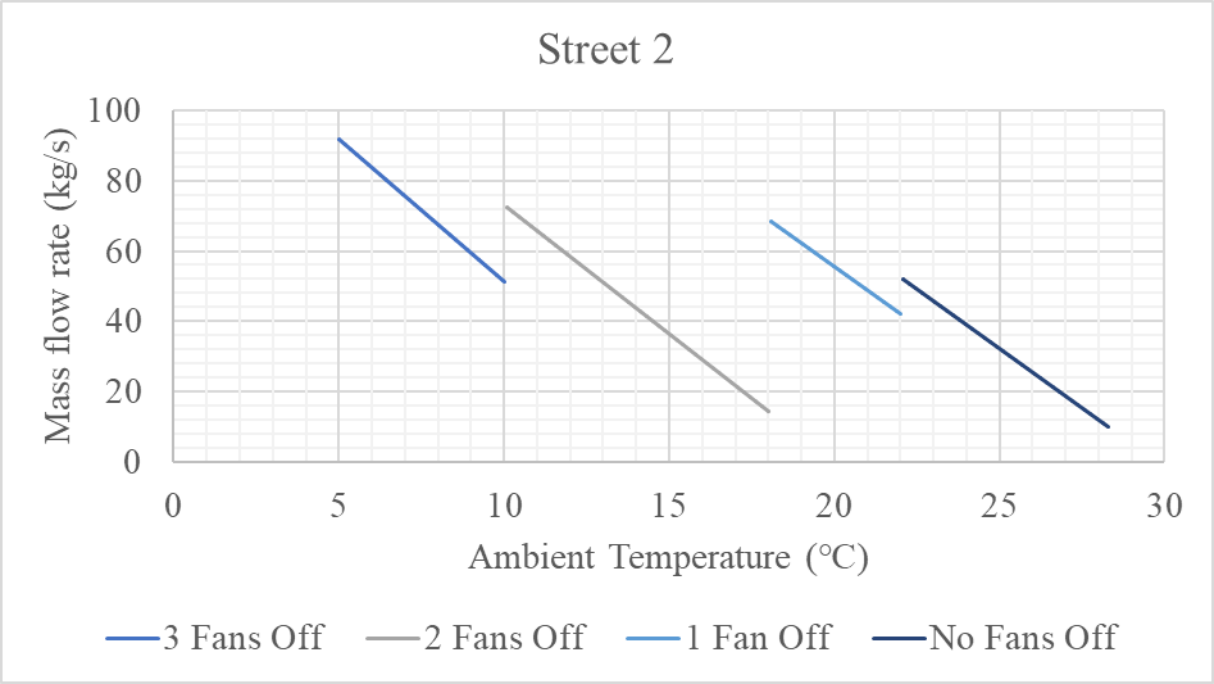

Figure E-9: Precooler Street 2 bypass sCO_2 mass flow rates for combined control strategy simulations

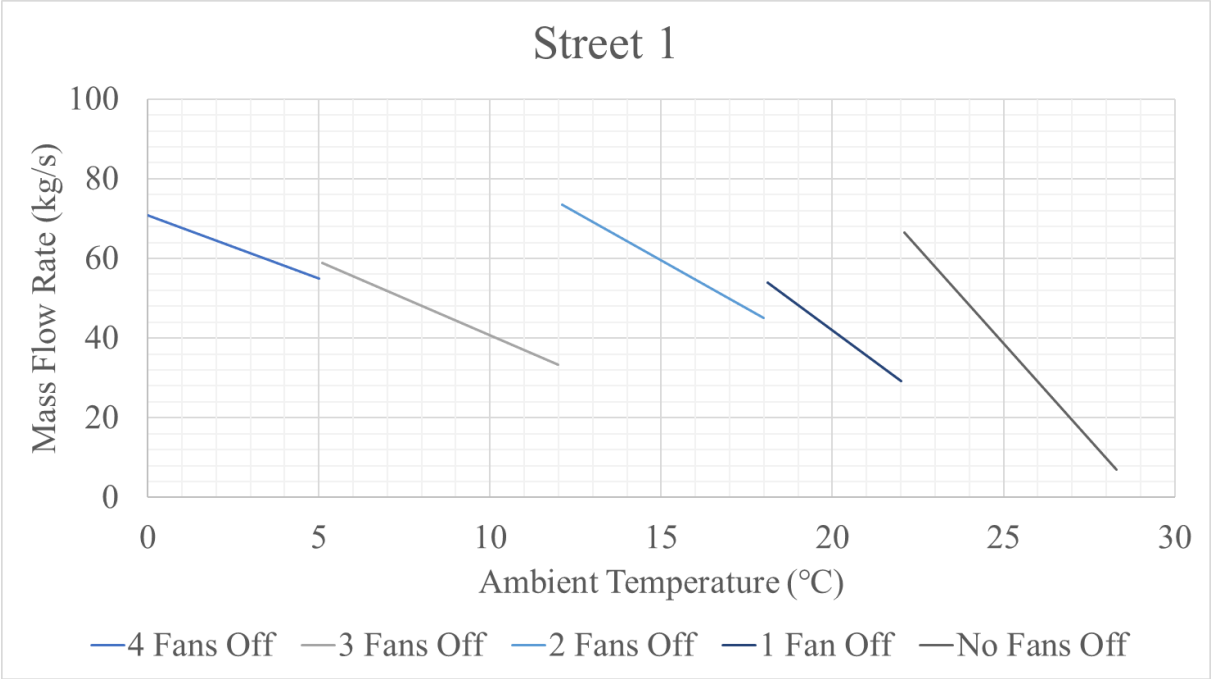

Figure E-10: Intercooler Street 1 bypass sCO_2 mass flow rates for combined control strategy simulations

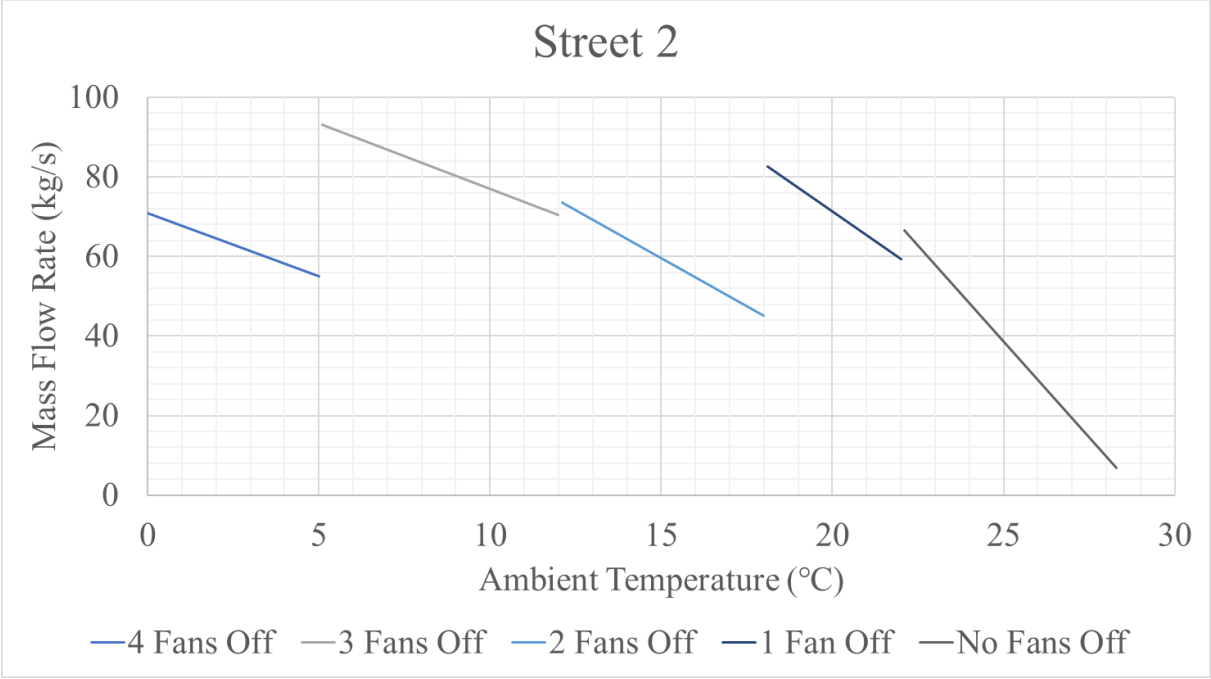

Figure E-11: Intercooler Street 2 bypass sCO_2 mass flow rates for combined control strategy simulations

Appendix F Mathematical derivation

All empirical polynomial curves and mathematical methods are included in this section. A detailed fundamental calculation for a single converged air-cooled system solution case is also provided. This is to demonstrate the capability of the model used to solve the system accurately.

F-1. Upstream and downstream loss coefficient curves

Pressure drops upstream and downstream of the fan will occur. These are included in the draft equation for a forced draft air-cooled system in Section 4.9. To determine the loss coefficients K_{do} and K_{up} it is necessary to know the projected area (A_{ob}) of the flow obstruction as well as the distance (x) from the fan. Using these values in conjunction with the fan casing diameter (d_c) and the casing area (A_c) it is possible to find the coefficients using the graphs in Figure F-1 and Figure F-2 taken from (2004).

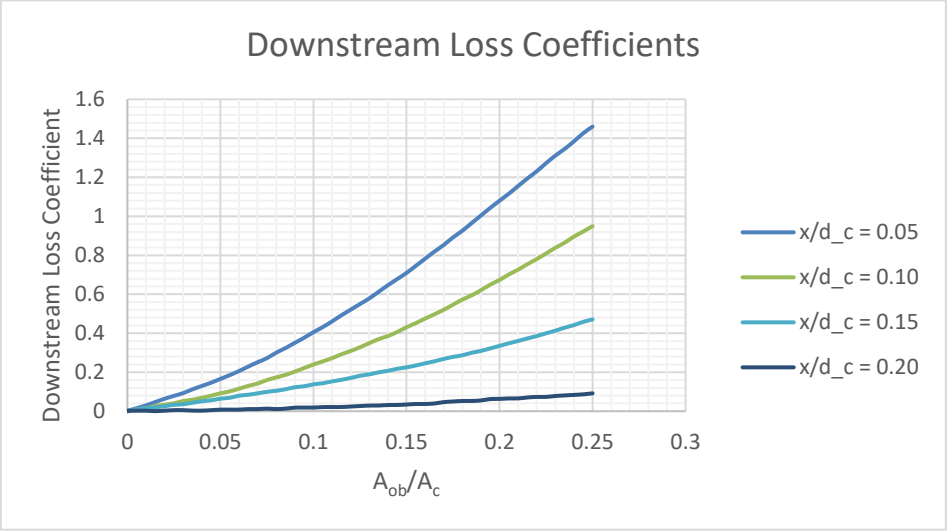

Figure F-1: Downstream loss coefficients for flow obstructions taken from Kröger (2004)

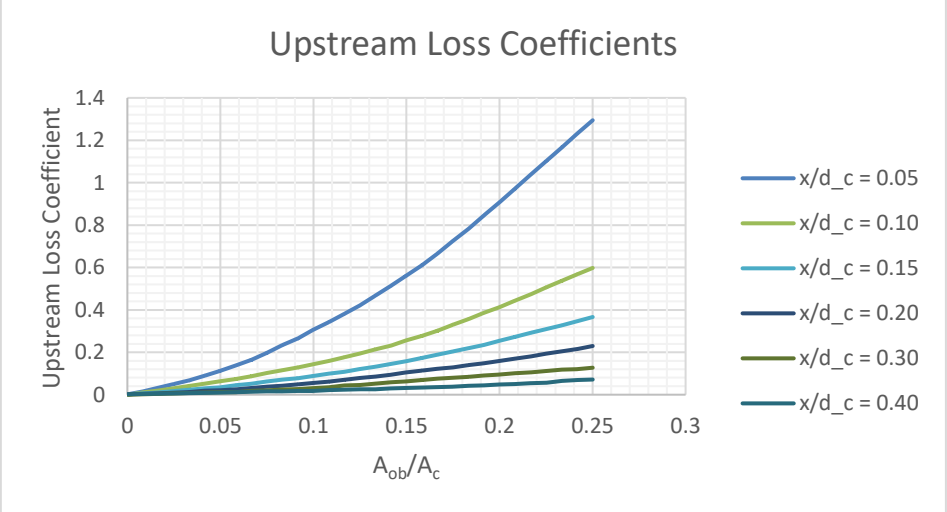

Figure F-2: Upstream loss coefficients for flow obstructions taken from Kröger (2004)

Correlations for the curves shown in the figures have been generated by fitting second order polynomials to digitised versions of the curves in Excel. These correlations are shown in Table F-1 and Table F-2. Downstream and upstream flow obstructions include things like support trusses and beams, inlet screens, and walkways for fan-motor access.

Table F-2 The value of A_1 in the correlations is simply equal to the ratio of A_{ob}/A_c.

Table F-1: Downstream loss coefficient correlations

x/d_c	Correlation
0.05	$K_{do} = 11.927A_1^2 + 2.9949A_1 - 0.0082$
0.10	$K_{do} = 9.5885A_1^2 + 1.4441A_1 - 0.002$
0.15	$K_{do} = 3.6857A_1^2 + 0.9167A_1 + 0.0069$
0.20	$K_{do} = 1.2922A_1^2 + 0.0361A_1 + 0.0018$

Downstream and upstream flow obstructions include things like support trusses and beams, inlet screens, and walkways for fan-motor access.

Table F-2: Upstream loss coefficient correlations

x/d_c	Correlation
0.05	$K_{up} = 14.641A_1^2 + 1.5815A_1 - 0.004$
0.10	$K_{up} = 6.9642A_1^2 + 0.6148A_1 + 0.011$
0.15	$K_{up} = 4.0985A_1^2 + 0.4274A_1 + 0.004$
0.20	$K_{up} = 2.3308A_1^2 + 0.3347A_1 - 0.0005$
0.30	$K_{up} = 1.0414A_1^2 + 0.2799A_1 - 0.004$
0.40	$K_{up} = 0.8096A_1^2 + 0.059A_1 + 0.0046$

These correlations are used in the development of the model in place of the physical graphs for calculation efficiency purposes. An interpolation scheme as described in Appendix F-3 was used to solve coefficients for any interstitial values of x/d_c.

F-2. B2-fan curves and specifications

The experimental testing of the B2-fan which produced the curves used in this work were conducted in a Type A (BS 848) test facility. The specifications and curves for this fan come from the work of Augustyn (2013) and are shown in Table F-3 and

Table F-4 respectively.

Table F-3: B2-fan test specifications (A type test)

Specification	Value
Fan diameter (m)	1.542
Hub-tip ratio	0.4
Number of blades (-)	8
Blade angle [chord line] (°)	59.0
Reference density (kg/m^3)	1.2
Rotational speed (rpm)	750.0

To capture the performance of the fan, the experimental results were used to develop curves for fan power and static pressure rise. These curves are for a fan of the same scale as the experiments. To use the curves for larger fans it is necessary to scale them using the laws shown in Appendix C-5. In this work, the fan power and static pressure curves were scaled to fit two larger versions of the fans. The specific fan diameters are 10.98 m (36 ft) and 7.9248 m (26 ft), the fans are referred to as the large and small fans respectively in this work. The scaled curves for these two fans at various set rotational speeds are shown in Figure F-3 – Figure F-6. Their third order polynomials, which were fitted in Excel using values generated by sweeping the volume flow rates of the larger fans, are shown in Table F-5 and Table F-6.

Table F-4: B2-fan test curves for power and static pressure

Rotational Speed (rpm)	Unit	Polynomial (power and static pressure)
750	W	$P = 0.8135V^3 - 63.171V^2 + 1192.5V - 39.467$
	Pa	$\Delta p = 0.091V^3 - 5.227V^2 + 69.508V + 60.622$

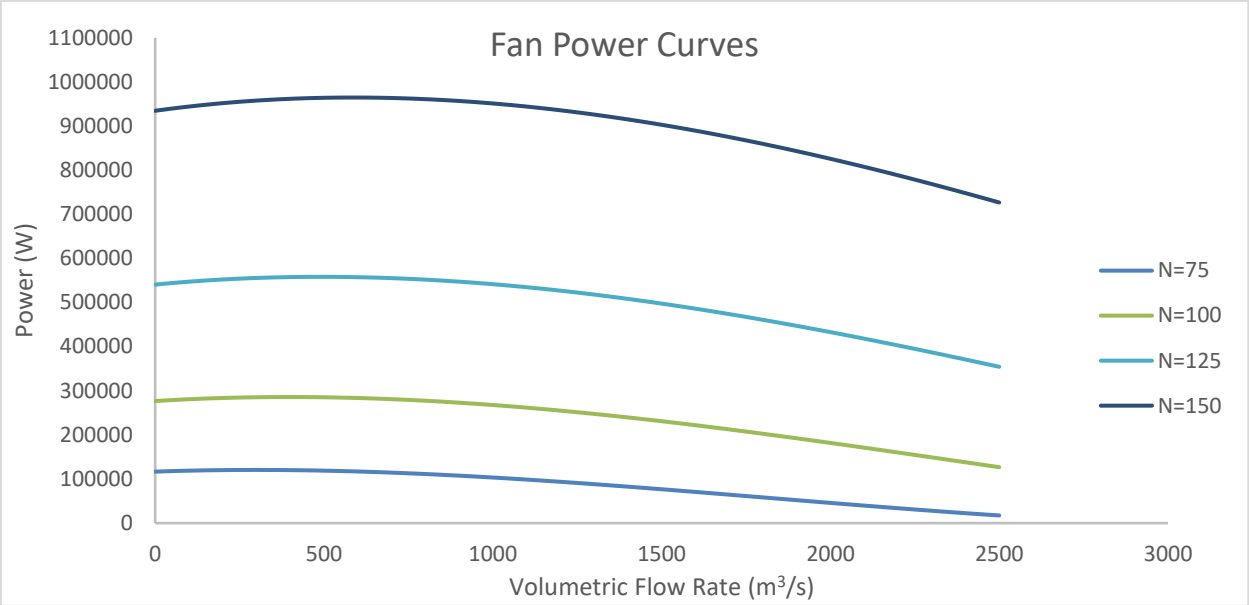

Figure F-3: Fan power curves for a 10.98 m (36 ft) B2-fan

These two curves, represent the power and static pressure for the large fan prior to the density adjustment. Air density was not considered during scaling and only included afterwards because it varies with the fan platform height. The power and static pressure values will still need to be scaled by a density factor as described in Appendix C-5.

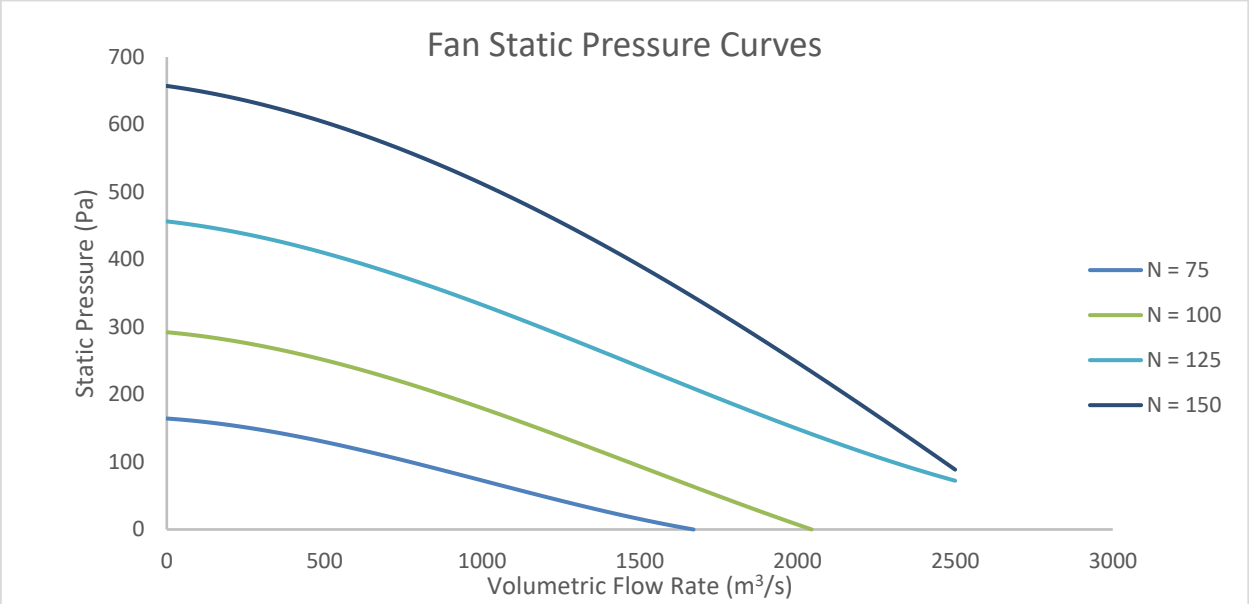

Figure F-4: Fan static pressure curves for a 10.98 m (36 ft) B2-fan

The curves for the small fan are shown below. They still need to be scaled using the same density factor described above.

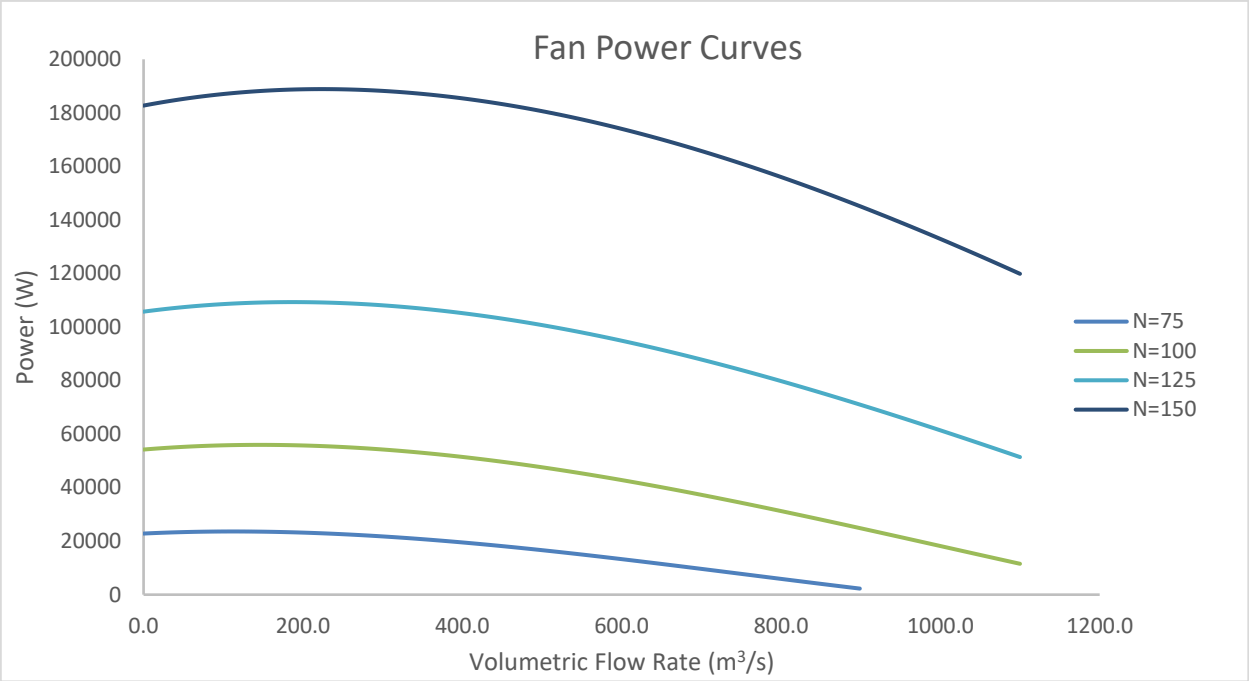

Figure F-5: Fan power curves for a 7.9248 m (26 ft) B2-fan

In terms of interpolation, it is important to note that the limits were set at 75 and 150 rpm for the rotational speed. Anything outside of these values was not considered.

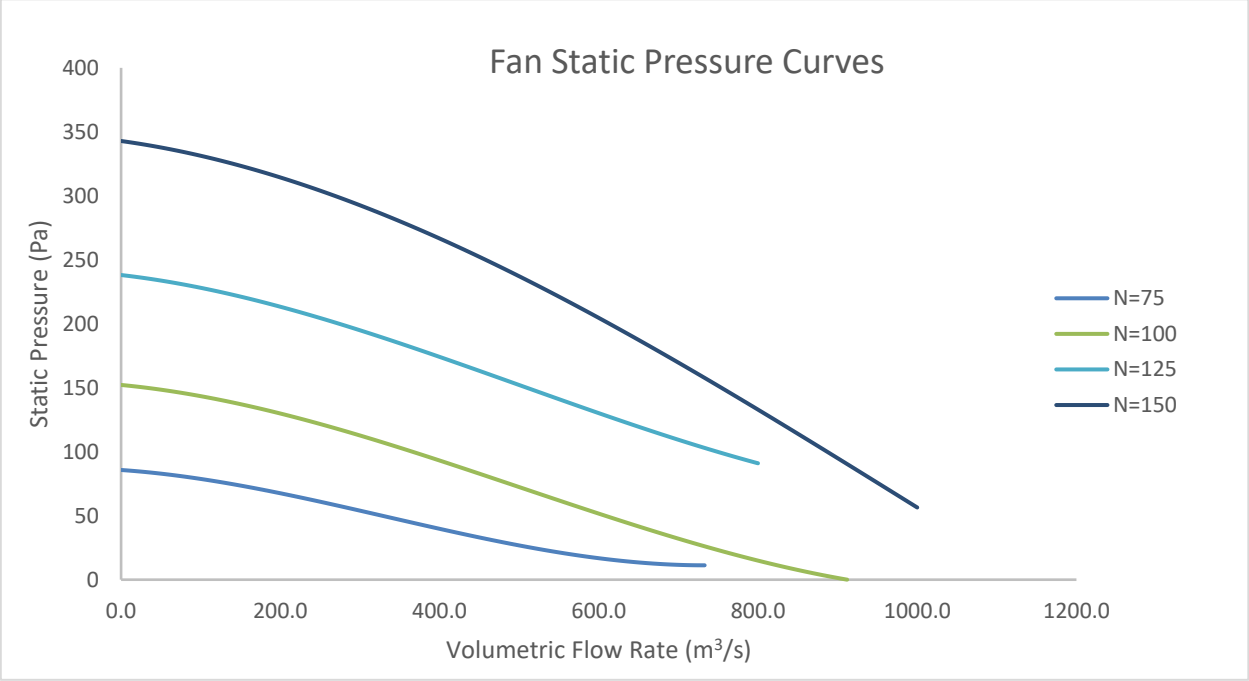

Figure F-6: Fan static pressure curves for a 7.9248 m (26 ft) B2-fan

The third order polynomials extracted from the curves for the large fan are shown below:

Table F-5: Third order polynomials for power and static pressure for a 10.98 m (36 ft) B2-fan

Rotational Speed (rpm)	Polynomial (power and static pressure)
75	$P = 9 \times 10^{-6}V^3 - 0.0491V^2 + 26.773V + 116708$
	$\Delta p = 3 \times 10^{-8}V^3 - 9 \times 10^{-5}V^2 - 0.0318V + 164.42$
100	$P = 9 \times 10^{-6}V^3 - 0.0655V^2 + 47.552V + 276657$
	$\Delta p = 2 \times 10^{-8}V^3 - 9 \times 10^{-5}V^2 - 0.0425V + 292.29$
125	$P = 9 \times 10^{-6}V^3 - 0.0818V^2 + 73.714V + 540612$
	$\Delta p = 2 \times 10^{-8}V^3 - 9 \times 10^{-5}V^2 - 0.0537V + 456.52$
150	$P = 9 \times 10^{-6}V^3 - 0.098V^2 + 105.59V + 934481$
	$\Delta p = 1 \times 10^{-8}V^3 - 9 \times 10^{-5}V^2 - 0.0649V + 657.20$

The third order polynomials extracted from the curves for the small fan are shown below:

Table F-6: Third order polynomials for power and static pressure for a 7.9248 m (26 ft) B2-fan

Rotational Speed (rpm)	Polynomial (power and static pressure)
75	$P = 3 \times 10^{-5}V^3 - 0.0682V^2 + 14.191V + 22832.0$
	$\Delta p = 3 \times 10^{-7}V^3 - 0.0003V^2 - 0.0429V + 85.729$
100	$P = 3 \times 10^{-5}V^3 - 0.0906V^2 + 24.562V + 54213.0$
	$\Delta p = 2 \times 10^{-7}V^3 - 0.0003V^2 - 0.0596V + 152.19$
125	$P = 3 \times 10^{-5}V^3 - 0.1136V^2 + 39.267V + 105732.0$
	$\Delta p = 2 \times 10^{-7}V^3 - 0.0003V^2 - 0.0719V + 238.09$
150	$P = 3 \times 10^{-5}V^3 - 0.1363V^2 + 56.49V + 182716.0$
	$\Delta p = 1 \times 10^{-7}V^3 - 0.0003V^2 - 0.0864V + 342.83$

F-3. Interpolation scheme

A bicubic interpolation scheme was used to interpolate between the polynomials shown in Appendix F-2. The method for interpolating this way is shown in detail here. The model used to perform bicubic interpolation takes on the basic form as seen in Equation (F-1).

$$f(x,y) = \sum_{i=0}^{n}\sum_{j=0}^{n} a_{ij}x^i y^j \qquad \textit{(F-1)}$$

Where $f(x,y)$ is the polynomial function which solves for interpolated values and n is the order of the polynomial that will predict interpolated results. n will also be one less than the number of curves that need to be interpolated between. For example, in the case of the fan power curves, there are four curves between which a bicubic interpolation scheme is needed to solve interstitial values. The curves are a function of volumetric flow rate (V) and fan rotational speed (N) and they will output a fan power (P). Equation (F-1) then takes on the form below:

$$P(V,N) = \sum_{i=0}^{3}\sum_{j=0}^{3} a_{ij}V^i N^j \qquad \textit{(F-2)}$$

The equation above expands to the form seen in Equation (F-3) below where the coefficient matrix can be solved using a set of 4 x 4 known data points.

$$P(N,V) = \begin{bmatrix} V^3 & V^2 & V & 1 \end{bmatrix} \begin{bmatrix} a_{33} & a_{32} & a_{31} & a_{30} \\ a_{23} & a_{22} & a_{21} & a_{20} \\ a_{13} & a_{12} & a_{11} & a_{10} \\ a_{03} & a_{02} & a_{01} & a_{00} \end{bmatrix} \begin{bmatrix} N^3 \\ N^2 \\ N \\ 1 \end{bmatrix} \qquad \textit{(F-3)}$$

In the case of the fan power curves, there are 4 known N-values and one associated known V-value that can be extracted with the relevant power outputs, this is demonstrated in Figure F-7. This allows for the coefficient matrix to be solved and used to calculate any N-values between the defined curves. The final form of the equation will simply be a cubic function of a known reference rotational speed (N_{ref}) and the interstitial rotational speed (N) for which the power is unknown. The known V- and N-values are accounted for in the coefficient matrix.

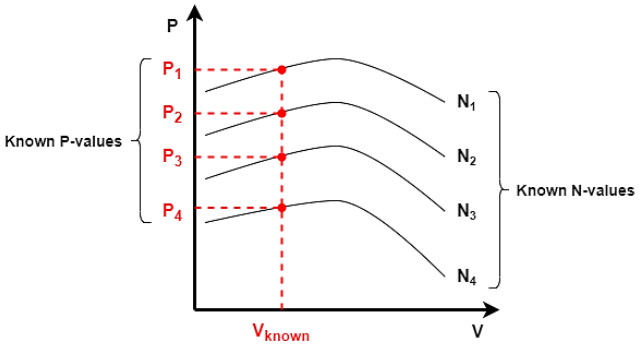

Figure F-7: Extracting known values from a fan power curve for interpolation purposes

This interpolation scheme can be applied to other cases with more curves, the process stays the same, but the order of the polynomial will change along with the size of the vectors and coefficient matrix. This occurred when interpolating between upstream loss coefficients as seen in Appendix F. A sample interpolation calculation for both fan speeds and loss coefficients can be seen in Appendix F-4.

F-4. Sample calculation

Sample calculations for a direct air-cooler in a sCO2 Brayton cycle:

Determining the heat rejected, the power consumed by the fan and the mass flow rate of air through the system.

This particular calculation is a verification of the steady-state solution for the PRECOOLER in a recompression Brayton cycle with intercooling and reheating.

The design is the best performing one (in tandem with the intercooler design) found from 3000 cases, with each design defined by 9 input parameters which affect the geometry and layout of the heat rejection system. These parameters have been highlighted in the calculation.

AMBIENT CONDITIONS:

Taken for an average warm day near Upington, in South Africa.

Air temperature (ground level): $T_a := 28.9\ °C = 302.05\ K$

Air temperature (sea-level): $T_{a\_sea} := 15\ °C = 288.15\ K$

Air pressure (sea-level): $p_{a\_sea} := 101.325\ kPa = 101325\ Pa$

Elevation: $H_{upington} := 808\ m$

Molar mass of dry air: $M_a := 0.02896968\ \frac{kg}{mol}$

Gas constants for dry air, universal, and water vapor:

$$R_d := 287.058\ \frac{J}{kg}$$

$$R_v := 461.5\ \frac{J}{kg}$$

$$R_0 := 8.3144626\ \frac{J}{K \cdot mol}$$

Calulate air pressure in Upington as a function of its elevation:

Air pressure: $p_a := p_{a\_sea} \cdot e^{\frac{-g \cdot M_a \cdot H_{upington}}{T_{a\_sea} \cdot R_0}} = 92067.362\ Pa$

Redefine the gravitational constant:

Gravity: $g := 9.81\ \frac{m}{s^2}$

Air properties at ground level, found using CoolProp library in python:

$$\rho_a := 1.06212 \ \frac{kg}{m^3}$$

$$\mu_a := 1.86347 \cdot 10^{-5} \ \frac{kg}{m \cdot s}$$

$$Cp_a := 1006.30624 \ \frac{J}{kg \cdot K}$$

Calculation of the moist adiabatic lapse rate (MALR), controls temperature change of air with height changes:

Vapor pressure of water at air temperature: $p_v := 3986.04856 \ Pa$

Latent heat of vaporization at air temperature: $\Delta H := 2432423.9116 \ \frac{J}{kg}$

Find the mixing ratio: $$r := \frac{\frac{R_d}{R_v} \cdot p_v}{p_a - p_v} = 0.028$$

Calculate the MALR: $$MALR := g \cdot \frac{\left(1 \cdot \frac{1}{K} + \frac{\Delta H \cdot r}{R_d \cdot T_a}\right)}{\left(1 \cdot \frac{J}{kg \cdot K^2} + \frac{\Delta H^2 \cdot r}{R_v \cdot T_a^{\ 2}}\right)} = 0.00443739 \ \frac{K}{m}$$

SCO2 CONDITIONS:

Taken from the larger cycle model.

CO2 inlet temperature: $T_{CO2i} := 85.77 \ °C = 358.92 \ K$

CO2 inlet pressure: $p_{CO2i} := 7503 \ kPa = 7503000 \ Pa$

Mass flow inlet: $m`_{CO2total} := 392.1 \ \frac{kg}{s}$

Cycle maximum pressure: $p_{max} := 25 \ MPa$

Properties at the inlet (density and viscosity), determined using CoolProp library in Python:

$$\rho_{CO2i} := 141.5405 \ \frac{kg}{m^3} \qquad \mu_{CO2i} := 1.98297 \cdot 10^{-5} \ \frac{kg}{m \cdot s}$$

Header/Collector specifications:

Loss coefficient: $K_{header} := 2.5$

Header diameter: $d_{header} := 1.25\ m$

Header cross-sectional area: $A_{header} := \frac{\pi}{4} \cdot d_{header}^{\ 2} = 1.227\ m^2$

Inlet contraction loss coefficient: $K_c := 0.6$

FAN SETUP AND HEAT EXCHANGER GEOMETRY:

The fan is a 26ft, B2-fan running at a set rotational speed that has been solved for iteratively in the model to acheive a 45 degrees celsius outlet temperature. The tip clearance is set at 1% for a conservative value.

Fan diameter: $d_{fan} := 26\ ft = 7.9248\ m$

Fan height: $H_{fan} := 21\ m$

Hub-tip ratio: $r_{hub} := 0.4$

Hub diameter: $d_{hub} := d_{fan} \cdot r_{hub} = 3.1699\ m$

Tip clearance: $s_{tip} := 0.01 \cdot d_{fan} = 0.0792\ m$

Fan casing diameter: $d_{casing} := d_{fan} + 2 \cdot s_{tip} = 8.0833\ m$

Fan rotational speed: $N_{fan} := 75.031471\ rpm$

Fan effective area: $A_e := \frac{\pi}{4} \cdot \left(d_{casing}^{\ 2} - d_{hub}^{\ 2}\right) = 43.426\ m^2$

Fan casing area: $A_{casing} := \frac{\pi}{4} \cdot d_{casing}^{\ 2} = 51.318\ m^2$

Fan to heat exchanger distance: $x_{fanHX} := 0.3 \cdot d_{casing} = 2.425\ m$

Geometry and parameters for a bellmouth inlet:

Bellmouth outlet diameter: $d_{so} := d_{casing} = 8.0833\ m$

Bellmouth inlet diameter: $d_{si} := 1.25 \cdot d_{casing} = 10.1041\ m$

Bellmouth height: $H_{si} := 0.19 \cdot d_{casing} = 1.536\ m$

Shroud loss factor: $K_{Fsi} := 0.0$

Test B2-fan parameters:

Test fan diameter: $d_{fanT} := 1.542\ m$

Test fan rotational speed: $N_{fanT} := 750\ rpm$

Test fan density: $\rho_T := 1.2\ \frac{kg}{m^3}$

Test fan viscosity: $\mu_T := 1.8254 \cdot 10^{-5}\ \frac{kg}{m \cdot s}$

Inlet conditions and air properties at the fan (found using CoolProp):

Air temperature at fan: $T_{aF} := T_a - MALR \cdot H_{fan} = 28.807\ °C$

Air density at fan: $\rho_{aF} := 1.06245\ \frac{kg}{m^3}$

Air dynamic viscosity at fan: $\mu_{aF} := 1.86302 \cdot 10^{-5}\ \frac{kg}{m \cdot s}$

Air specific heat at fan (isobaric): $Cp_{aF} := 1006.30260\ \frac{J}{kg \cdot K}$

FINNED TUBE BUNDLE SPECIFICATIONS:

The entire cooling unit consists of 4 heat exchangers, each with its own fan. The heat exchangers have 4 tube rows in the longitudinal direction, with 4 passes - this means that there is 1 flow path per tube element. The tubes are circular and so are the fins. Tube diameter is a standard size and so is the wall thickness, thickness is based on the maximum pressure of 25 MPa. Fins are treated as having one mean thickness value rather than a tip and a root value.

Number of cooling cells: $N_{cells} := 8$

Mass flow of CO2 into HX: $\dot{m}_{CO2HX} := \frac{\dot{m}_{CO2total}}{N_{cells}} = 49.013\ \frac{kg}{s}$

Tube specifications (EN P235 Structural Steel):

Tube outer diameter and radius: $d_{tbo} := 25.4\ mm$ $r_{tbo} := \frac{d_{tbo}}{2} = 12.7\ mm$

Tube yield strength: $\sigma_{yield} := 196\ MPa$

Safety factor for tube wall thickness: $SF := 2$

Tube density: $\rho_{tb} := 7750\ \frac{kg}{m^3}$

Tube surface roughness: $\varepsilon_{tb} := 0.0015\ mm$

Tube wall thickness (exact): $t_{wall} := r_{tbo} - \sqrt{\frac{r_{tbo}^{\,2}\left(\frac{\sigma_{yield}}{SF} - p_{max}\right)}{p_{max} + \frac{\sigma_{yield}}{SF}}} = 2.916\ mm$

Tube wall thickness (standardised): $t_w := \text{round}\left(t_{wall} \cdot \frac{1}{mm}, 0\right) \cdot mm = 3\ mm$

Tube inner diameter: $d_{tbi} := d_{tbo} - 2 \cdot t_w = 19.4\ mm$

Internal cross-sectional area: $A_{tbi} := \frac{\pi}{4} \cdot d_{tbi}^{\,2} = 295.592\ mm^2$

Tube thermal conductivity: $k_{tb} := 58\ \frac{W}{m \cdot K}$

Fin specifications:

Fin diameter & height: $d_{fin} := 42.6\ mm$ $h_{fin} := d_{fin} - d_{tbo} = 17.2\ mm$

Fin root diameter: $d_{root} := 27.6\ mm$

Fin thickness: $t_{fin} := 1.3\ mm$

Fin pitch: $P_{fin} := 2.8\ mm$

Fin thermal conductivity: $k_{fin} := 58\ \frac{W}{m \cdot K}$

Bundle specifications:

Transverse tube pitch: $S_T := 52\ mm$

Longitudinal tube pitch: $S_L := 77\ mm$

Number of longitudinal rows: $N_L := 8$

Number of passes: $n_{passes} := 4$

Number of flow paths: $n_{paths} := \frac{N_L}{n_{passes}} = 2$

Heat exchanger geometry and specifications:

Width and height based on fan casing and increased to ensure coverage. Height is based on the number of passes and longitudinal tube pitch. Distances have been rounded to 1 decimal place. All areas are calculated for one control volume (discretized step). The heat exchanger is discretized into its separate passes.

Heat exchanger overhang: $d_{overhang} := 0.2\ m = 0.2\ m$

Heat exchanger length: $L_{HX} := \text{round}\left(\left(d_{casing} + d_{overhang}\right) \cdot \frac{1}{m}, 1\right) \cdot m = 8.3\ m$

Heat exchanger width: $W_{HX} := L_{HX} = 8.3\ m$

Heat exchanger height: $H_{HX} := S_L \cdot N_L - 0.5 \cdot S_L = 0.578\ m$ [for staggered]

Plenum height: $H_{plenum} := H_{HX} + x_{fanHX} = 3.002\ m$

Windwall height: $H_{ww} := H_{HX} = 0.578\ m$ [at least same as HX height]

Heat exchanger exit height: $H_{HXexit} := H_{fan} + H_{plenum} = 24.002\ m$

Heat exchanger frontal area: $A_{fr} := L_{HX} \cdot W_{HX} = 68.89\ m^2$

Tube pass length: $L_{tbpass} := L_{HX} = 8.3\ m$

Total tube length: $L_{tbs} := L_{tbpass} \cdot n_{passes} = 33.2\ m$

Number of fins: $N_{fins} := \text{round}\left(\frac{L_{tbs}}{P_{fin}}, 0\right) = 11857$

Number of fins per pass $N_{finspass} := \frac{N_{fins}}{n_{passes}} = 2964.25$

Number of transverse tube rows: $N_{Trows} := \frac{W_{HX}}{S_T} + 1 = 160.615$

Number of transverse tubes: $N_T := \text{ceil}\left(N_{Trows}\right) = 161$

Number of tubes: $N_{tubes} := N_T \cdot n_{paths} = 322$

<u>Area and air porosity calculations:</u>

Free flow area of the air in one discretized control volume:

$$A_{ff} := \left(S_T - d_{root}\right) \cdot \left(P_{fin} - t_{fin}\right) \cdot \left(\frac{N_{fins}}{n_{passes}}\right) \cdot N_T = 17.467\ m^2$$

Air porosity: $\sigma_a := \frac{A_{ff}}{A_{fr}} = 0.254$

Fin root surface area: $A_{root} := \pi \cdot N_{tubes} \cdot L_{tbpass} \cdot d_{root} \cdot \left(\frac{P_{fin} - t_{fin}}{P_{fin}}\right) = 124.144\ m^2$

Finned surface area:

$$A_{finned} := N_{tubes} \cdot N_{finspass} \cdot \left(\pi \cdot \left(\frac{{d_{fin}}^2 - {d_{root}}^2}{2} + d_{fin} \cdot t_{fin}\right)\right) = 1744.834\ m^2$$

Total exposed area per control volume: $A_{total} := A_{root} + A_{finned} = 1868.978\ m^2$

Internal surface area: $A_{int} := \pi \cdot d_{tbi} \cdot L_{tbpass} \cdot N_{tubes} = 162.887\ m^2$

External surface area (base): $A_{ext} := \pi \cdot d_{tbo} \cdot L_{tbpass} \cdot N_{tubes} + A_{finned} = 1958.098\ m^2$

SOLUTION FOR THE CONVERGED CASE:

The solution for the model described by the inputs and specifications above has the following air mass flow rate and fan rotational speed which satisfy both the energy and draft equations:

Mass flow rate of air: $m`_{air} := 181.91180229\ \frac{kg}{s}$

Fan rotational speed: $N_{fan} = 75.03147\ rpm$

At this flow rate the temperature at the inlet to the first row of the heat exchanger is as follows, the CO2 temperature at the inlet is known. The enthalpy values are determined using the appropriate pressures at these points for CO2 and air.

Air temperature (inlet): $T_{ai} := 28.90944\ °C = 302.059\ K$

CO2 temperature (inlet): $T_{CO2i} = 85.77\ °C$

Air enthalpy (inlet): $h_{ai} := 428391.0996\ \frac{J}{kg}$

CO2 enthalpy (inlet): $h_{CO2i} := 504620.63518\ \frac{J}{kg}$

'The inlet and outlet temperatures, pressures, and enthalpies for the remaining control volumes follow below. 1, 2, 3, and 4 move from the top of the heat exchanger to the bottom, i.e. the temperature of air at 1 is the final outlet temperature while for CO2 this is the outlet temperature of the first pass and the inlet to the second. In the same way, the temperature of air at 4 is the outlet after its first pass and inlet to the second while the temperature of CO2 at 4 is the final outlet temperature.

Air temperatures:

$T_{a1} := 47.72798\ °C$

$T_{a2} := 41.31097\ °C$

$T_{a3} := 36.38991\ °C$

$T_{a4} := 32.37831\ °C$

CO2 temperatures:

$T_{CO21} := 69.37468\ °C$

$T_{CO22} := 58.37039\ °C$

$T_{CO23} := 50.64635\ °C$

$T_{CO24} := 45.00000\ °C$

The pressures at the inlet and outlet of each CV are shown below in the same format as the temperatures above. The air properties were all evaluated at the ambient pressure due to the very small changes in air pressure that occur across the entire system.

$p_{CO21} := 7496145.33580\ Pa$

$p_{CO22} := 7491283.42194\ Pa$

$p_{CO23} := 7486854.58329\ Pa$

$p_{CO24} := 7482164.93637\ Pa$

The actual inlet pressure of the CO2 flowing into the tubes is not the same as the pressure when it arrives at the cooler. Preliminary secondary losses occur due to the flow of CO2 from the header into the tubes and the contraction as the fluid enters the tubes. This actual inlet pressure is found below.

ACTUAL INLET PRESSURE DETERMINATION:

Find the velocity of fluid in the header and the tubes.

Header velocity: $v_{CO2header} := \frac{\dot{m}_{CO2HX}}{\rho_{CO2i} \cdot A_{header} \cdot N_{tubes}} = 0.00088\ \frac{m}{s}$

Tube velocity: $v_{CO2tb} := \frac{\dot{m}_{CO2HX}}{\rho_{CO2i} \cdot A_{tbi} \cdot N_{tubes}} = 3.638\ \frac{m}{s}$

Find the pressure drops at the inlet to the tubes and the headers to get the actual inlet pressure of the CO2:

Header pressure drop: $\Delta p_{header} := \frac{1}{2} \cdot K_{header} \cdot \rho_{CO2i} \cdot v_{CO2header}^{\ 2} = 0.00014\ Pa$

Inlet contraction pressure drop: $\Delta p_{in} := \left(1 - \sigma_a^{\ 2} + K_c\right) \cdot \frac{1}{2} \cdot \rho_{CO2i} \cdot v_{CO2tb}^{\ 2} = 1.439\ kPa$

Now the actual inlet pressure of the CO2 can be found:

$p_{CO2in} := p_{CO2i} - \Delta p_{header} - \Delta p_{in} = 7501561.485\ Pa$

ENTHALPIES AND MEAN VALUES FOR EACH PASS:

Air enthalpies:

$h_{a1} := 447336.12210\ \frac{J}{kg}$

$h_{a2} := 440874.09746\ \frac{J}{kg}$

$h_{a3} := 435919.89585\ \frac{J}{kg}$

CO2 enthalpies:

$h_{CO21} := 480636.57913\ \frac{J}{kg}$

$h_{CO22} := 462248.86691\ \frac{J}{kg}$

$h_{CO23} := 447262.38672\ \frac{J}{kg}$

$h_{a4} := 431882.08823 \ \frac{J}{kg}$ $h_{CO24} := 434305.44651 \ \frac{J}{kg}$

The mean pressures and enthalpies for each pass (1, 2, 3, 4) can now be calculated. These were used to determine the fluid properties for each pass.

Air pressures (mean):

$p_{am1} := p_a = 92067.362 \ Pa$

$p_{am2} := p_a = 92067.362 \ Pa$

$p_{am3} := p_a = 92067.362 \ Pa$

$p_{am4} := p_a = 92067.362 \ Pa$

CO2 pressures (mean):

$p_{CO2m1} := \frac{p_{CO2in} + p_{CO21}}{2} = 7498853.411 \ Pa$

$p_{CO2m2} := \frac{p_{CO21} + p_{CO22}}{2} = 7493714.379 \ Pa$

$p_{CO2m3} := \frac{p_{CO22} + p_{CO23}}{2} = 7489069.003 \ Pa$

$p_{CO2m4} := \frac{p_{CO23} + p_{CO24}}{2} = 7484509.76 \ Pa$

Air enthalpies (mean):

$h_{am1} := \frac{h_{a1} + h_{a2}}{2} = 444105.11 \ \frac{J}{kg}$

$h_{am2} := \frac{h_{a2} + h_{a3}}{2} = 438396.997 \ \frac{J}{kg}$

$h_{am3} := \frac{h_{a3} + h_{a4}}{2} = 433900.992 \ \frac{J}{kg}$

$h_{am4} := \frac{h_{a4} + h_{ai}}{2} = 430136.594 \ \frac{J}{kg}$

CO2 enthalpies (mean):

$h_{CO2m1} := \frac{h_{CO2i} + h_{CO21}}{2} = 492628.607 \ \frac{J}{kg}$

$h_{CO2m2} := \frac{h_{CO21} + h_{CO22}}{2} = 471442.723 \ \frac{J}{kg}$

$h_{CO2m3} := \frac{h_{CO22} + h_{CO23}}{2} = 454755.627 \ \frac{J}{kg}$

$h_{CO2m4} := \frac{h_{CO23} + h_{CO24}}{2} = 440783.917 \ \frac{J}{kg}$

Initial calculations prior to momentum and energy balances:

Volumetric flow rate of air: $V_{air} := \frac{\grave{m}_{air}}{\rho_{aF}} = 171.21917 \ \frac{m^3}{s}$

Free flow velocity through the heat exchanger: $v_{HX} := \frac{V_{air}}{A_{fr}} = 2.4854 \ \frac{m}{s}$

The fan power and static pressure rise were calculated using the scaled fan polynomials and a bicubic interpolation scheme.

The polynomials for the various fan rotational speeds found for the 7.9248m B2-fan are shown below:

$$\Delta p_{Fs75}(V) := 3 \cdot 10^{-7}\, V^3 - 0.0003\, V^2 - 0.0429\, V + 85.729$$

$$P_{F75}(V) := 3 \cdot 10^{-5}\, V^3 - 0.0682\, V^2 + 14.191\, V + 22832$$

$$\Delta p_{Fs100}(V) := 2 \cdot 10^{-7}\, V^3 - 0.0003\, V^2 - 0.0596\, V + 152.19$$

$$P_{F100}(V) := 3 \cdot 10^{-5}\, V^3 - 0.0906\, V^2 + 24.562\, V + 54213$$

$$\Delta p_{Fs125}(V) := 2 \cdot 10^{-7}\, V^3 - 0.0003\, V^2 - 0.0719\, V + 238.09$$

$$P_{F125}(V) := 3 \cdot 10^{-5}\, V^3 - 0.1136\, V^2 + 39.267\, V + 105732$$

$$\Delta p_{Fs150}(V) := 1 \cdot 10^{-7}\, V^3 - 0.0003\, V^2 - 0.0864\, V + 342.83$$

$$P_{F150}(V) := 3 \cdot 10^{-5}\, V^3 - 0.1363\, V^2 + 56.49\, V + 182716$$

Get the power values at each of the known rotational speeds and populate a vector with these, they are the known outputs:

Dimensionless volumetric flow rate of air: $V_a := V_{air} \cdot \frac{s}{m^3} = 171.219$

Dimensionless rotational speed of the fan: $N_{fan} := N_{fan} \cdot \frac{1}{rpm} = 75.031$

$$P\_output := \begin{bmatrix} P_{F75}(V_a) \\ P_{F100}(V_a) \\ P_{F125}(V_a) \\ P_{F150}(V_a) \end{bmatrix} = \begin{bmatrix} 23413.004 \\ 55913.039 \\ 109275.549 \\ 188542.983 \end{bmatrix}$$

Using 75 rpm as the reference for the other rotational speeds produces the following coefficient matrix:

$$P\_coefficient\_matrix := \begin{bmatrix} 1 & 75-75 & (75-75)^2 & (75-75)^3 \\ 1 & 100-75 & (100-75)^2 & (100-75)^3 \\ 1 & 125-75 & (125-75)^2 & (125-75)^3 \\ 1 & 150-75 & (150-75)^2 & (150-75)^3 \end{bmatrix} = \begin{bmatrix} 1 & 0 & 0 & 0 \\ 1 & 25 & 625 & 15625 \\ 1 & 50 & 2500 & 125000 \\ 1 & 75 & 5625 & 421875 \end{bmatrix}$$

Now we need to solve for the coefficients and set up the rotational speed array:

$$P\_coefficients := \mathrm{lsolve}(P\_coefficient\_matrix, P\_output)$$

$$P\_coefficients = \begin{bmatrix} 2.341 \cdot 10^4 \\ 949.985 \\ 12.656 \\ 0.054 \end{bmatrix} \qquad N_{terms} := \begin{bmatrix} 1 \\ (N_{fan} - 75) \\ (N_{fan} - 75)^2 \\ (N_{fan} - 75)^3 \end{bmatrix} = \begin{bmatrix} 1 \\ 0.031 \\ 9.904 \cdot 10^{-4} \\ 3.117 \cdot 10^{-5} \end{bmatrix}$$

The power before scaling by the density factor can now be found by taking the dot product of the coefficients and the fan terms:

$$P_{test} := P\_coefficients \cdot N_{terms} \cdot W = 23.443\ kW$$

$$P_{fan} := P_{test} \cdot \frac{\rho_{aF}}{\rho_T} = 20.756\ kW$$

The same process as above is repeated for the static pressure rise across the fan:

$$dP\_output := \begin{bmatrix} \Delta p_{Fs75}(V_a) \\ \Delta p_{Fs100}(V_a) \\ \Delta p_{Fs125}(V_a) \\ \Delta p_{Fs150}(V_a) \end{bmatrix} = \begin{bmatrix} 71.095 \\ 134.194 \\ 217.988 \\ 319.744 \end{bmatrix}$$

Using 75 rpm as the reference for the other rotational speeds produces the following coefficient matrix:

$$dP\_coefficient\_matrix := \begin{bmatrix} 1 & 75-75 & (75-75)^2 & (75-75)^3 \\ 1 & 100-75 & (100-75)^2 & (100-75)^3 \\ 1 & 125-75 & (125-75)^2 & (125-75)^3 \\ 1 & 150-75 & (150-75)^2 & (150-75)^3 \end{bmatrix} = \begin{bmatrix} 1 & 0 & 0 & 0 \\ 1 & 25 & 625 & 15625 \\ 1 & 50 & 2500 & 125000 \\ 1 & 75 & 5625 & 421875 \end{bmatrix}$$

Now we need to solve for the coefficients and set up the rotational speed array:

$$dP\_coefficients := \text{lsolve}(dP\_coefficient\_matrix, dP\_output)$$

$$dP\_coefficients = \begin{bmatrix} 71.095 \\ 2.074 \\ 0.019 \\ -2.915 \cdot 10^{-5} \end{bmatrix} \qquad N_{terms} = \begin{bmatrix} 1 \\ 0.031 \\ 9.904 \cdot 10^{-4} \\ 3.117 \cdot 10^{-5} \end{bmatrix}$$

The static pressure rise before scaling by the density factor can now be found by taking the dot product of the coefficients and the fan terms:

$\Delta p_{test} := dP\_coefficients \cdot N_{terms} \cdot Pa = 71.16\ Pa$ Matches value from Python

$\Delta p_{fan} := \Delta p_{test} \cdot \frac{\rho_{aF}}{\rho_T} = 63.0033\ Pa$ Matches value from Python

The fan electrical power for this unit and the entire Precooler (PC) can now be found:

Fan electrical efficiency: $\eta_{fan} := 0.9$

$P_{elec} := \frac{P_{fan}}{\eta_{fan}} = 23.062\ kW$ Matches value from Python

$P_{PCaux} := P_{elec} \cdot N_{cells} = 184.496\ kW$ Matches value from Python

At this stage it is also important to show how the heat exchanger inlet air temperature is found. This is done using the lapse rate and fan conditions.

Heat exchanger inlet height: $H_{inlet} := H_{fan} + x_{fanHX} = 23.425\ m$

Temperature at the heat exchanger inlet:

$$T_{ainlet} := T_a + \frac{P_{fan}}{m`_{air} \cdot Cp_{aF}} - MALR \cdot H_{inlet} = 302.059\ K$$

Comparing this to the previously stated inlet value shows that the error is 0% (approximately):

$$err_{Tai} := \frac{|T_{ai} - T_{ainlet}|}{T_{ai}} \cdot 100 = 0.00008\%$$

With the initial setup calculations complete, the momentum and energy balances for the sCO2-side can now be completed to find the heat transfer achieved.

ENERGY AND MOMENTUM BALANCES ACROSS THE HEAT EXCHANGER:

First CV (4th pass - CV1):

Determine the mean properties of the fluids in the CV, using the mean enthalpy and pressure of the control volume:

Air: $p_{am1} = 92067.362\ Pa$ $h_{am1} = 444105.11\ \frac{J}{kg}$

CO2: $p_{CO2m1} = 7498853.411\ Pa$ $h_{CO2m1} = 492628.607\ \frac{J}{kg}$

[CoolProp] Air properties: CO2 properties:

Prandtl number: $Pr_{a1} := 0.70491$ $Pr_{CO21} := 1.04601$

Specific heat: $Cp_{a1} := 1007.01349\ \frac{J}{kg \cdot K}$ $Cp_{CO21} := 1464.53846\ \frac{J}{kg \cdot K}$

Dynamic viscosity: $\mu_{a1} := 1.93771 \cdot 10^{-5}\ \frac{kg}{m \cdot s}$ $\mu_{CO21} := 1.96374 \cdot 10^{-5}\ \frac{kg}{m \cdot s}$

Conductivity: $k_{a1} := 0.02768\ \frac{W}{m \cdot K}$ $k_{CO21} := 0.02749\ \frac{W}{m \cdot K}$

Density: $\rho_{a1} := 1.00978\ \frac{kg}{m^3}$ $\rho_{CO21} := 149.60238\ \frac{kg}{m^3}$

MOMENTUM BALANCE (SCO2-SIDE):

Frictional pressure drops:

Find the Reynolds number in the tube to determine the flow regime and use the appropriate frictional pressure drop correlation:

Set the mass flow rate and velocity in the tube pass and determine the Reynolds number:

$$\grave{m}_{CO2tbs} := \frac{\grave{m}_{CO2HX}}{N_{tubes}} = 0.15221\ \frac{kg}{s}$$

$$v_{CO21} := \frac{\grave{m}_{CO2HX}}{\rho_{CO21} \cdot A_{tbi} \cdot N_{tubes}} = 3.4421\ \frac{m}{s}$$

$$Re_{tb1} := \frac{\grave{m}_{CO2tbs}}{A_{tbi}} \cdot \frac{d_{tbi}}{\mu_{CO21}} = 508715.987$$ [Flow is turbulent]

Now the friction factor can be found and used to find the pressure drop across this pass.

Darcy-Weisbach friction factor (Swamee & Jain):

$$f_D := \frac{0.25}{\left(\log\left(\frac{\varepsilon_{tb}}{3.7 \cdot d_{tbi}} + \frac{5.74}{Re_{tb1}^{0.9}}\right)\right)^2} = 0.01416$$

Frictional pressure drop: $\Delta p_{fric1} := f_D \cdot \left(\frac{L_{tbpass}}{d_{tbi}}\right) \cdot \frac{\rho_{CO21}}{2} \cdot v_{CO21}^2 = 5.37\ kPa$

Bend pressure drops:

$K_{bends} := 0.18$

Pressure drop across bends: $\Delta p_{bend1} := \frac{1}{2} \cdot K_{bends} \cdot \rho_{CO21} \cdot v_{CO21}^2 = 0.16\ kPa$

Exit pressure loss:

The loss coefficient is assumed unity, although there is no exit loss at this point.

Exit pressure loss: $\Delta p_{ex1} := \frac{1}{2} \cdot \rho_{CO21} \cdot v_{CO21}^2 \cdot 0 = 0\ kPa$

Total pressure loss across the tubes and actual outlet pressure:

Total pressure loss: $\Delta p_1 := \Delta p_{bend1} + \Delta p_{fric1} + \Delta p_{ex1} = 5.529\ kPa$

Actual outlet pressure: $p_{CO2o1} := p_{CO2in} - \Delta p_1 = 7496032.156\ Pa$

The calculated pressure can now be compared to the converged case pressure at the exit of the 1st pass (inlet of the 2nd pass):

$$err_{\Delta p1} := \frac{\left|p_{CO21} - p_{CO2o1}\right|}{p_{CO21}} = 0.00151\%$$

This level of error is deemed acceptable for the pressure drop across this pass, the energy balance can now be performed.

ENERGY BALANCE:

Find and compare the two 'C' values for air and CO2:

$$C_{a1} := m`_{air} \cdot Cp_{a1} = (1.832 \cdot 10^5)\ \frac{W}{K}$$

$$C_{CO21} := m`_{CO2HX} \cdot Cp_{CO21} = (7.178 \cdot 10^4)\ \frac{W}{K}$$

CO2 has the minimum 'C' value, it must be used as such in the e-NTU correlations.

$$C_{min1} := min(C_{a1}, C_{CO21}) = (7.178 \cdot 10^4)\ \frac{W}{K}$$

$$C_{max1} := \max(C_{a1}, C_{CO21}) = (1.832 \cdot 10^5)\ \frac{W}{K}$$

The 'C' ratio can now be found:

$$C_1 := \frac{C_{min1}}{C_{max1}} = 0.392$$

This value will be used in conjunction with the overall heat transfer coefficient - 'UA' - in the effectiveness calculation at a later point. The next step is to now determine this UA value by finding and summing the thermal resistances. Fouling and radiation have been neglected, so it is only the internal convection, thermal conduction through the tube wall, and external convection.

Thermal conduction resistance:

Tube wall properties

$$k_{tb} = 58\ \frac{W}{m \cdot K}$$

Calculate the conductivity resistance

$$R_{cond1} := \frac{\ln\left(\frac{d_{tbo}}{d_{tbi}}\right)}{\pi \cdot L_{tbpass} \cdot N_{tubes} \cdot k_{tb}} = 0.0000005534\ \frac{K}{W}$$

Internal convection resistance:

Calculate the Reynolds number to determine the flow regime

$$Re_{int1} := \left(\frac{m`_{CO2tbs}}{A_{tbi}}\right) \cdot \left(\frac{d_{tbi}}{\mu_{CO21}}\right) = 508715.987$$

Find the friction factor, this is specifically stated for use here, will be used in the Nusselt number correlation:

$$f_{D1} := \left(1.8 \log\left(Re_{int1}\right) - 1.5\right)^{-2} = 0.013$$

Find the Nusselt number and internal heat transfer coefficient (according to Gnielinski)

$$Nu_{int1} := \frac{\left(\frac{f_{D1}}{8}\right) \cdot Re_{int1} \cdot Pr_{CO21}}{1 + 12.7 \cdot \sqrt{\frac{f_{D1}}{8}} \left(Pr_{CO21}^{\frac{2}{3}} - 1\right)} \left(1 + \left(\frac{d_{tbi}}{L_{tbpass}}\right)^{\frac{2}{3}}\right) = 866.213$$

$$h_{int1} := Nu_{int1} \cdot \frac{k_{CO21}}{d_{tbi}} = 1227.433 \ \frac{W}{m^2 \cdot K}$$

Find the internal convective resistance:

$$R_{int1} := \frac{1}{h_{int1} \cdot A_{int}} = 0.0000050017 \ \frac{K}{W}$$

External convection resistance:

This calculation is split into two parts, the first involves finding the base heat transfer coefficient and the second involves the determination of the fin and overall surface efficiency.

1. Heat transfer coefficient calculation:

   Determination of the dimensionless values, void factor, and arrangement factors:

   Find the two dimensionless factors (a & b) associated with the tubes

   $$a := \frac{S_T}{d_{tbo}} = 2.047 \qquad b := \frac{S_L}{d_{tbo}} = 3.031$$

   b is greater than 1 therefore the void factor is found as follows

   Void factor: $$\psi := 1 - \frac{\pi}{4\ a} = 0.616$$

   The arrangement is staggered, therefore the arrangement factor is found as follows:

   Arrangement factor: $$f_{Astag} := 1 + \frac{2}{3\ b} = 1.22$$

   Characteristic length calculation:

$$l_{ext} := \frac{\pi}{2} \cdot \sqrt{d_{tbo}^{\ 2} + h_{fin}^{\ 2}} = 0.048 \ m$$

Determine the Reynolds number for the Nusselt correlations:

The hydraulic diameter for the air is required at this point and is calculated below. The Reynolds number also needs to be adjusted by the void factor.

Hydraulic diameter for air: $d_{air} := \frac{4\ A_{ff} \cdot S_L}{A_{finned}} = 3.083\ mm$

Reynolds number: $Re_{air1} := \left(\frac{m`_{air}}{A_{ff}}\right) \cdot \left(\frac{d_{air}}{\mu_{a1}}\right) = 1657.177$

Void Reynolds number: $Re_{void1} := \frac{Re_{air1}}{\psi} = 2.689 \cdot 10^3$

Now it is possible to find the laminar and turbulent Nusselt numbers (according to Gnielinski)

Laminar Nusselt number: $Nu_{lam1} := 0.664 \cdot \sqrt{Re_{void1}} \cdot \sqrt[3]{Pr_{a1}} = 30.642$

Turbulent Nusselt number: $Nu_{turb1} := \frac{0.037\ Re_{void1}^{0.8} \cdot Pr_{a1}}{1 + 2.443\ Re_{void1}^{-0.1} \cdot \left(Pr_{a1}^{\frac{2}{3}} - 1\right)} = 18.786$

The Nusselt number for one row and the entire bundle can now be found:

Row Nusselt number: $Nu_{row1} := 0.3 + \sqrt{Nu_{lam1}^{\ 2} + Nu_{turb1}^{\ 2}} = 36.242$

Bundle Nusselt number: $Nu_{bundle1} := \frac{1 + \left(n_{passes} - 1\right)\ f_{Astag}}{n_{passes}} \cdot Nu_{row1} = 42.219$

The external convective heat transfer coefficient can now be found:

$$h_{ext1} := Nu_{bundle1} \cdot \frac{k_{a1}}{l_{ext}} = 24.253\ \frac{W}{m^2\ K}$$

2. Fin efficiency and surface effectiveness calculations:

The 'b' adjustment factor must be found first:

$$b_1 := \sqrt{\frac{2 \cdot h_{ext1}}{k_{fin} \cdot t_{fin}}} = 25.364\ \frac{1}{m}$$

Now the height adjustment factor for circular tubes can be found:

$$\varphi_1 := \left(\frac{d_{fin}}{d_{tbo}} - 1\right) \cdot \left(1 + 0.35 \ln\left(\frac{d_{fin}}{d_{tbo}}\right)\right) = 0.8$$

Dimensionless factor 'X' $$X_1 := \frac{d_{tbo}}{2} \cdot \varphi_1 \cdot b_1 = 0.258$$

Calculate the fin efficiency for use in the surface effectiveness equation

$$\eta_{f1} := \frac{\tanh\left(X_1\right)}{X_1} = 0.978$$

Find the finned surface efficiency for the tubes

$$\eta_{surf1} := 1 - \left(1 - \eta_{f1}\right) \cdot \frac{A_{finned}}{A_{total}} = 0.97988$$

Now one can calculate the external convective resistance:

$$R_{ext1} := \frac{1}{\eta_{surf1} \cdot h_{ext1} \cdot A_{ext}} = 0.0000214896 \ \frac{K}{W}$$

Overall heat transfer coefficient and number of transfer units (NTU):

$$UA_1 := \left(R_{int1} + R_{cond1} + R_{ext1}\right)^{-1} = 36975.851 \ \frac{W}{K}$$

Number of Transfer Units: $$NTU_1 := \frac{UA_1}{C_{min1}} = 0.515$$

Effectiveness calculation for the heat exchanger:

The 'C' ratio is not insignificant (> 0.1) - the streams are assumed to both be unmixed. It is important to note that in the case where there is only a single flow path for each pass, the air stream may be considered mixed. However, in this work, the proximity and closing packing of the finned tubes was assumed to channel the air between the tubes, keeping it unmixed.

Using the ratio and the NTU, the effectiveness can be found for this row.

$$e_1 := 1 - \exp\left(NTU_1^{0.22} \cdot \frac{\exp\left(-C_1 \cdot NTU_1^{0.78}\right) - 1}{C_1}\right) = 0.368$$

Calculate the heat transfer for this longitudinal tube pass for the airside, CO2-side and based on the e-NTU method and compare:

$$Q_{a1} := m`_{air} \cdot \left(h_{a1} - h_{a2}\right) = 1.17552 \ MW$$

$$Q_{CO21} := m`_{CO2HX} \cdot \left(h_{CO2i} - h_{CO21}\right) = 1.17552 \ MW$$

$$Q_1 := e_1 \cdot C_{min1} \cdot \left(T_{CO2i} - T_{a2}\right) = 1.17545 \ MW$$

Python value for heat transfer: $Q_{py\_1} := 1.17551855 \ MW$

<u>Examining the error between these heat transfers will demonstrate that the energy equations balance:</u>

Error for the air heat transfer: $err_{Qa1} := \frac{\left|Q_{a1} - Q_1\right|}{Q_1} = 0.00568\%$

Error for the CO2 heat transfer $err_{QCO21} := \frac{\left|Q_{CO21} - Q_1\right|}{Q_1} = 0.00568\%$

<u>Examining the error between the heat transfer values in Python and calculated here will verify the Python model:</u>

Error for the air heat transfer: $err_{py\_a1} := \frac{\left|Q_{a1} - Q_{py\_1}\right|}{Q_{py\_1}} = 0.0000001\%$

Error for the CO2 heat transfer $err_{py\_CO21} := \frac{\left|Q_{CO21} - Q_{py\_1}\right|}{Q_{py\_1}} = 0.0000002\%$

Error for the e-NTU heat transfer $err_{py\_e1} := \frac{\left|Q_1 - Q_{py\_1}\right|}{Q_{py\_1}} = 0.00568\%$

With the errors for this row acceptably low, the calculation can now move forwards to the heat transfer for the next element (row). This level of error was deemed acceptable.

Second CV (3rd pass - CV2):

Determine the mean properties of the fluids in the CV, using the mean enthalpy and pressure of the control volume:

Air: $p_{am2} = 92067.362\ Pa$ $h_{am2} = 438396.997\ \frac{J}{kg}$

CO2: $p_{CO2m2} = 7493714.379\ Pa$ $h_{CO2m2} = 471442.723\ \frac{J}{kg}$

[CoolProp] Air properties: CO2 properties:

Prandtl number: $Pr_{a2} := 0.70554$ $Pr_{CO22} := 1.15259$

Specific heat: $Cp_{a2} := 1006.73423\ \frac{J}{kg \cdot K}$ $Cp_{CO22} := 1674.35878\ \frac{J}{kg \cdot K}$

Dynamic viscosity: $\mu_{a2} := 1.91095 \cdot 10^{-5}\ \frac{kg}{m \cdot s}$ $\mu_{CO22} := 1.94533 \cdot 10^{-5}\ \frac{kg}{m \cdot s}$

Conductivity: $k_{a2} := 0.02727\ \frac{W}{m \cdot K}$ $k_{CO22} := 0.02826\ \frac{W}{m \cdot K}$

Density: $\rho_{a2} := 1.02817\ \frac{kg}{m^3}$ $\rho_{CO22} := 166.62587\ \frac{kg}{m^3}$

MOMENTUM BALANCE (SCO2-SIDE):

Frictional pressure drops:

Find the Reynolds number in the tube to determine the flow regime and use the appropriate frictional pressure drop correlation:

Set the mass flow rate and velocity in the tube pass and determine the Reynolds number:

$$\dot{m}_{CO2tbs} := \frac{\dot{m}_{CO2HX}}{N_{tubes}} = 0.152\ \frac{kg}{s}$$

$$v_{CO22} := \frac{\dot{m}_{CO2HX}}{\rho_{CO22} \cdot A_{tbi} \cdot N_{tubes}} = 3.09\ \frac{m}{s}$$

$$Re_{tb2} := \frac{\dot{m}_{CO2tbs}}{A_{tbi}} \cdot \frac{d_{tbi}}{\mu_{CO22}} = 513530.317$$ [Flow is turbulent]

Now the friction factor can be found and used to find the pressure drop across this pass.

Darcy-Weisbach friction factor (Swamee & Jain):

$$f_D := \frac{0.25}{\left(\log\left(\frac{\varepsilon_{tb}}{3.7 \cdot d_{tbi}} + \frac{5.74}{Re_{tb2}^{0.9}}\right)\right)^2} = 0.01415$$

Frictional pressure drop: $\Delta p_{fric2} := f_D \cdot \left(\frac{L_{tbpass}}{d_{tbi}}\right) \cdot \frac{\rho_{CO22}}{2} \cdot v_{CO22}^2 = 4.816\ kPa$

Bend pressure drops:

$K_{bends} := 0.18$

Pressure drop across bends: $\Delta p_{bend2} := \frac{1}{2} \cdot K_{bends} \cdot \rho_{CO22} \cdot v_{CO22}^2 = 0.143\ kPa$

Exit pressure loss:

The loss coefficient is assumed unity, although there is no exit loss at this point.

Exit pressure loss: $\Delta p_{ex2} := \frac{1}{2} \cdot \rho_{CO21} \cdot v_{CO22}^2 \cdot 0 = 0\ kPa$

Total pressure loss across the tubes and actual outlet pressure:

Total pressure loss: $\Delta p_2 := \Delta p_{bend2} + \Delta p_{fric2} + \Delta p_{ex2} = 4.959\ kPa$

Actual outlet pressure: $p_{CO2o2} := p_{CO21} - \Delta p_2 = 7491186.544\ Pa$

The calculated pressure can now be compared to the converged case pressure at the exit of the 1st pass (inlet of the 2nd pass):

$$err_{\Delta p2} := \frac{\left|p_{CO22} - p_{CO2o2}\right|}{p_{CO22}} = 0.0013\%$$

This level of error is deemed acceptable for the pressure drop across this pass, the energy balance can now be performed.

ENERGY BALANCE:

Find and compare the two 'C' values for air and CO2:

$$C_{a2} := m`_{air} \cdot Cp_{a2} = \left(1.831 \cdot 10^5\right) \frac{W}{K}$$

$$C_{CO22} := m`_{CO2HX} \cdot Cp_{CO22} = \left(8.206 \cdot 10^4\right) \frac{W}{K}$$

CO2 has the minimum 'C' value, it must be used as such in the e-NTU correlations.

$$C_{min2} := min\left(C_{a2}, C_{CO22}\right) = \left(8.206 \cdot 10^4\right) \frac{W}{K}$$

$$C_{max2} := \max\left(C_{a2}, C_{CO22}\right) = \left(1.831 \cdot 10^5\right) \frac{W}{K}$$

'C' ratio can now be found:

$$C_2 := \frac{C_{min2}}{C_{max2}} = 0.448$$

This value will be used in conjunction with the overall heat transfer coefficient - 'UA' - in the effectiveness calculation at a later point. The next step is to now determine this UA value by finding and summing the thermal resistances. Fouling has been neglected, so it is only the internal convection, thermal conduction through the tube wall, and external convection

Thermal conduction resistance:

Tube wall properties

$$k_{tb} = 58 \frac{W}{m \cdot K}$$

Calculate the conductivity resistance

$$R_{cond2} := \frac{\ln\left(\frac{d_{tbo}}{d_{tbi}}\right)}{\pi \cdot L_{tbpass} \cdot N_{tubes} \cdot k_{tb}} = 0.0000005534 \frac{K}{W}$$

Internal convection resistance:

Calculate the Reynolds number to determine the flow regime

$$Re_{int2} := \left(\frac{m`_{CO2tbs}}{A_{tbi}}\right) \cdot \left(\frac{d_{tbi}}{\mu_{CO22}}\right) = 513530.317$$

Find the friction factor, this is specifically stated for use here, will be used in the Nusselt number correlation:

$$f_{D1} := \left(1.8 \log\left(Re_{int2}\right) - 1.5\right)^{-2} = 0.013$$

Find the Nusselt number and internal heat transfer coefficient (according to Gnielinski)

$$Nu_{int2} := \frac{\left(\frac{f_{D1}}{8}\right) \cdot Re_{int2} \cdot Pr_{CO22}}{1 + 12.7 \cdot \sqrt{\frac{f_{D1}}{8}} \left(Pr_{CO22}^{\frac{2}{3}} - 1\right)} \left(1 + \left(\frac{d_{tbi}}{L_{tbpass}}\right)^{\frac{2}{3}}\right) = 929.664$$

$$h_{int2} := Nu_{int2} \cdot \frac{k_{CO22}}{d_{tbi}} = 1354.242 \ \frac{W}{m^2 \cdot K}$$

Find the internal convective resistance:

$$R_{int2} := \frac{1}{h_{int2} \cdot A_{int}} = 0.0000045333 \ \frac{K}{W}$$

External convection resistance:

This calculation is split into two parts, the first involves finding the base heat transfer coefficient and the second involves the determination of the fin and overall surface efficiency.

1. Heat transfer coefficient calculation:

   Determination of the dimensionless values, void factor, and arrangement factors:

   Find the two dimensionless factors (a & b) associated with the tubes

   $$a := \frac{S_T}{d_{tbo}} = 2.047 \qquad b := \frac{S_L}{d_{tbo}} = 3.031$$

   b is greater than 1 therefore the void factor is found as follows

   Void factor: $$\psi := 1 - \frac{\pi}{4\ a} = 0.616$$

   The arrangement is staggered, therefore the arrangement factor is found as follows:

   Arrangement factor: $$f_{Astag} := 1 + \frac{2}{3\ b} = 1.22$$

   Characteristic length calculation:

   $$l_{ext} := \frac{\pi}{2} \cdot \sqrt{d_{tbo}^{\ 2} + h_{fin}^{\ 2}} = 0.048 \ m$$

Determine the Reynolds number for the Nusselt correlations:

The hydraulic diameter for the air is required at this point and is calculated below. The Reynolds number also needs to be adjusted by the void factor.

Hydraulic diameter for air: $d_{air} := \frac{4\ A_{ff} \cdot S_L}{A_{finned}} = 3.083\ mm$

Reynolds number: $Re_{air2} := \left(\frac{m`_{air}}{A_{ff}}\right) \cdot \left(\frac{d_{air}}{\mu_{a2}}\right) = 1680.383$

Void Reynolds number: $Re_{void2} := \frac{Re_{air2}}{\psi} = 2.726 \cdot 10^3$

Now it is possible to find the laminar and turbulent Nusselt numbers (according to Gnielinski)

Laminar Nusselt number: $Nu_{lam2} := 0.664 \cdot \sqrt{Re_{void2}} \cdot \sqrt[3]{Pr_{a2}} = 30.865$

Turbulent Nusselt number: $Nu_{turb2} := \frac{0.037\ Re_{void2}^{0.8} \cdot Pr_{a2}}{1 + 2.443\ Re_{void2}^{-0.1} \cdot \left(Pr_{a2}^{\frac{2}{3}} - 1\right)} = 18.992$

The Nusselt number for one row and the entire bundle can now be found:

Row Nusselt number: $Nu_{row2} := 0.3 + \sqrt{Nu_{lam2}^{\ 2} + Nu_{turb2}^{\ 2}} = 36.54$

Bundle Nusselt number: $Nu_{bundle2} := \frac{1 + \left(n_{passes} - 1\right)\ f_{Astag}}{n_{passes}} \cdot Nu_{row2} = 42.566$

The external convective heat transfer coefficient can now be found:

$h_{ext2} := Nu_{bundle2} \cdot \frac{k_{a2}}{l_{ext}} = 24.09\ \frac{W}{m^2\ K}$

2. Fin efficiency and surface effectiveness calculations:

The 'b' adjustment factor must be found first:

$b_2 := \sqrt{\frac{2 \cdot h_{ext2}}{k_{fin} \cdot t_{fin}}} = 25.278\ \frac{1}{m}$

Now the height adjustment factor for circular tubes can be found:

$$\varphi_2 := \left(\frac{d_{fin}}{d_{tbo}} - 1\right) \cdot \left(1 + 0.35 \ln\left(\frac{d_{fin}}{d_{tbo}}\right)\right) = 0.8$$

Dimensionless factor 'X' $$X_2 := \frac{d_{tbo}}{2} \cdot \varphi_2 \cdot b_2 = 0.257$$

Calculate the fin efficiency for use in the surface effectiveness equation

$$\eta_{f2} := \frac{\tanh\left(X_2\right)}{X_2} = 0.979$$

Find the finned surface efficiency for the tubes

$$\eta_{surf2} := 1 - \left(1 - \eta_{f2}\right) \cdot \frac{A_{finned}}{A_{total}} = 0.98$$

Now one can calculate the external convective resistance:

$$R_{ext2} := \frac{1}{\eta_{surf2} \cdot h_{ext2} \cdot A_{ext}} = 0.0000216319 \ \frac{K}{W}$$

Overall heat transfer coefficient and number of transfer units (NTU):

$$UA_2 := \left(R_{int2} + R_{cond2} + R_{ext2}\right)^{-1} = 37427.073 \ \frac{W}{K}$$

Number of Transfer Units: $$NTU_2 := \frac{UA_2}{C_{min2}} = 0.456$$

Effectiveness calculation for the heat exchanger:

The 'C' ratio is not insignificant (> 0.1) - the streams are assumed to both be unmixed. It is important to note that in the case where there is only a single flow path for each pass, the air stream may be considered mixed. However, in this work, the proximity and closing packing of the finned tubes was considered sufficient to channel the air between the tubes, keeping it unmixed.

Using the ratio and the NTU, the effectiveness can be found for this row.

$$e_2 := 1 - \exp\left(NTU_2^{0.22} \cdot \frac{\exp\left(-C_2 \cdot NTU_2^{0.78}\right) - 1}{C_2}\right) = 0.333$$

Calculate the heat transfer for this longitudinal tube pass for the airside, CO2-side and based on the e-NTU method and compare:

$$Q_{a2} := m`_{air} \cdot \left(h_{a2} - h_{a3}\right) = 0.9012 \ MW$$

$$Q_{CO22} := m`_{CO2HX} \cdot \left(h_{CO21} - h_{CO22}\right) = 0.9012\ \textit{MW}$$

$$Q_2 := e_2 \cdot C_{min2} \cdot \left(T_{CO21} - T_{a3}\right) = 0.9013\ \textit{MW}$$

Python value for heat transfer: $Q_{py\_2} := 0.9012277\ \textit{MW}$

Examining the error between these heat transfers will demonstrate that the energy equations balance:

Error for the air heat transfer: $err_{Qa2} := \frac{\left|Q_{a2} - Q_2\right|}{Q_2} = 0.00599\%$

Error for the CO2 heat transfer $err_{QCO22} := \frac{\left|Q_{CO22} - Q_2\right|}{Q_2} = 0.00599\%$

Examining the error between the heat transfer values in Python and calculated here will verify the Python model:

Error for the air heat transfer: $err_{py\_a2} := \frac{\left|Q_{a2} - Q_{py\_2}\right|}{Q_{py\_2}} = 0.0000049\%$

Error for the CO2 heat transfer $err_{py\_CO22} := \frac{\left|Q_{CO22} - Q_{py\_2}\right|}{Q_{py\_2}} = 0.000005\%$

Error for the e-NTU heat transfer $err_{py\_e2} := \frac{\left|Q_2 - Q_{py\_2}\right|}{Q_{py\_2}} = 0.006\%$

With the errors for this row acceptably low, the calculation can now move forwards to the heat transfer for the next element (row). This level of error was deemed acceptable because the exact values for fluid properties have not been used, values were determined in CoolProp and rounded to 5 decimal places.

Third CV (2nd pass - CV3):

Determine the mean properties of the fluids in the CV, using the mean enthalpy and pressure of the control volume:

Air: $p_{am3} = 92067.362\ Pa$ $h_{am3} = 433900.992\ \frac{J}{kg}$

CO2: $p_{CO2m3} = 7489069.003\ Pa$ $h_{CO2m3} = 454755.627\ \frac{J}{kg}$

[CoolProp] Air properties: CO2 properties:

Prandtl number: $Pr_{a3} := 0.70606$ $Pr_{CO23} := 1.28233$

Specific heat: $Cp_{a3} := 1006.53238\ \frac{J}{kg \cdot K}$ $Cp_{CO23} := 1947.30952\ \frac{J}{kg \cdot K}$

Dynamic viscosity: $\mu_{a3} := 1.88972 \cdot 10^{-5}\ \frac{kg}{m \cdot s}$ $\mu_{CO23} := 1.94946 \cdot 10^{-5}\ \frac{kg}{m \cdot s}$

Conductivity: $k_{a3} := 0.02694\ \frac{W}{m \cdot K}$ $k_{CO23} := 0.02960\ \frac{W}{m \cdot K}$

Density: $\rho_{a3} := 1.04313\ \frac{kg}{m^3}$ $\rho_{CO23} := 183.13983\ \frac{kg}{m^3}$

MOMENTUM BALANCE (SCO2-SIDE):

Frictional pressure drops:

Find the Reynolds number in the tube to determine the flow regime and use the appropriate frictional pressure drop correlation:

Set the mass flow rate and velocity in the tube pass and determine the Reynolds number:

$$\grave{m}_{CO2tbs} := \frac{\grave{m}_{CO2HX}}{N_{tubes}} = 0.152\ \frac{kg}{s}$$

$$v_{CO23} := \frac{\grave{m}_{CO2HX}}{\rho_{CO23} \cdot A_{tbi} \cdot N_{tubes}} = 2.812\ \frac{m}{s}$$

$$Re_{tb3} := \frac{\grave{m}_{CO2tbs}}{A_{tbi}} \cdot \frac{d_{tbi}}{\mu_{CO23}} = 512442.385$$ [Flow is turbulent]

Now the friction factor can be found and used to find the pressure drop across this pass.

Darcy-Weisbach friction factor (Swamee & Jain):

$$f_D := \frac{0.25}{\left(\log\left(\frac{\varepsilon_{tb}}{3.7 \cdot d_{tbi}} + \frac{5.74}{Re_{tb3}^{0.9}}\right)\right)^2} = 0.01415$$

Frictional pressure drop: $\Delta p_{fric3} := f_D \cdot \left(\frac{L_{tbpass}}{d_{tbi}}\right) \cdot \frac{\rho_{CO23}}{2} \cdot v_{CO23}^2 = 4.382\ kPa$

Bend pressure drops:

$K_{bends} := 0.18$

Pressure drop across bends: $\Delta p_{bend3} := \frac{1}{2} \cdot K_{bends} \cdot \rho_{CO23} \cdot v_{CO23}^2 = 0.13\ kPa$

Exit pressure loss:

The loss coefficient is assumed unity, although there is no exit loss at this point.

Exit pressure loss: $\Delta p_{ex3} := \frac{1}{2} \cdot \rho_{CO23} \cdot v_{CO23}^2 \cdot 0 = 0\ kPa$

Total pressure loss across the tubes and actual outlet pressure:

Total pressure loss: $\Delta p_3 := \Delta p_{bend3} + \Delta p_{fric3} + \Delta p_{ex3} = 4.513\ kPa$

Actual outlet pressure: $p_{CO2o3} := p_{CO22} - \Delta p_3 = 7486770.62\ Pa$

The calculated pressure can now be compared to the converged case pressure at the exit of the 1st pass (inlet of the 2nd pass):

$$err_{\Delta p3} := \frac{\left|p_{CO23} - p_{CO2o3}\right|}{p_{CO23}} = 0.0011\%$$

This level of error is deemed acceptable for the pressure drop across this pass, the energy balance can now be performed.

ENERGY BALANCE:

Find and compare the two 'C' values for air and CO2:

$$C_{a3} := m`_{air} \cdot Cp_{a3} = \left(1.831 \cdot 10^5\right) \frac{W}{K}$$

$$C_{CO23} := m`_{CO2HX} \cdot Cp_{CO23} = \left(9.544 \cdot 10^4\right) \frac{W}{K}$$

CO2 has the minimum 'C' value, it must be used as such in the e-NTU correlations.

$$C_{min3} := min\left(C_{a3}, C_{CO23}\right) = \left(9.544 \cdot 10^4\right) \frac{W}{K}$$

$$C_{max3} := \max\left(C_{a3}, C_{CO23}\right) = \left(1.831 \cdot 10^5\right) \frac{W}{K}$$

'C' ratio can now be found:

$$C_3 := \frac{C_{min3}}{C_{max3}} = 0.521$$

This value will be used in conjunction with the overall heat transfer coefficient - 'UA' - in the effectiveness calculation at a later point. The next step is to now determine this UA value by finding and summing the thermal resistances. Fouling has been neglected, so it is only the internal convection, thermal conduction through the tube wall, and external convection

Thermal conduction resistance:

Tube wall properties

$$k_{tb} = 58 \frac{W}{m \cdot K}$$

Calculate the conductivity resistance

$$R_{cond3} := \frac{\ln\left(\frac{d_{tbo}}{d_{tbi}}\right)}{\pi \cdot L_{tbpass} \cdot N_{tubes} \cdot k_{tb}} = 0.0000005534 \frac{K}{W}$$

Internal convection resistance:

Calculate the Reynolds number to determine the flow regime

$$Re_{int3} := \left(\frac{m`_{CO2tbs}}{A_{tbi}}\right) \cdot \left(\frac{d_{tbi}}{\mu_{CO23}}\right) = 512442.385$$

Find the friction factor, this is specifically stated for use here, will be used in the Nusselt number correlation:

$$f_{D1} := \left(1.8 \log\left(Re_{int3}\right) - 1.5\right)^{-2} = 0.013$$

Find the Nusselt number and internal heat transfer coefficient (according to Gnielinski)

$$Nu_{int3} := \frac{\left(\frac{f_{D1}}{8}\right) \cdot Re_{int3} \cdot Pr_{CO23}}{1 + 12.7 \cdot \sqrt{\frac{f_{D1}}{8}} \left(Pr_{CO23}^{\frac{2}{3}} - 1\right)} \left(1 + \left(\frac{d_{tbi}}{L_{tbpass}}\right)^{\frac{2}{3}}\right) = 993.321$$

$$h_{int3} := Nu_{int3} \cdot \frac{k_{CO23}}{d_{tbi}} = 1515.582 \ \frac{W}{m^2 \cdot K}$$

Find the internal convective resistance:

$$R_{int3} := \frac{1}{h_{int3} \cdot A_{int}} = 0.0000040507 \ \frac{K}{W}$$

External convection resistance:

This calculation is split into two parts, the first involves finding the base heat transfer coefficient and the second involves the determination of the fin and overall surface efficiency.

1. Heat transfer coefficient calculation:

   Determination of the dimensionless values, void factor, and arrangement factors:

   Find the two dimensionless factors (a & b) associated with the tubes

   $$a := \frac{S_T}{d_{tbo}} = 2.047 \qquad b := \frac{S_L}{d_{tbo}} = 3.031$$

   b is greater than 1 therefore the void factor is found as follows

   Void factor: $$\psi := 1 - \frac{\pi}{4\ a} = 0.616$$

   The arrangement is staggered, therefore the arrangement factor is found as follows:

   Arrangement factor: $$f_{Astag} := 1 + \frac{2}{3\ b} = 1.22$$

   Characteristic length calculation:

$$l_{ext} := \frac{\pi}{2} \cdot \sqrt{d_{tbo}^{\ 2} + h_{fin}^{\ 2}} = 0.048 \ m$$

Determine the Reynolds number for the Nusselt correlations:

The hydraulic diameter for the air is required at this point and is calculated below. The Reynolds number also needs to be adjusted by the void factor.

Hydraulic diameter for air: $d_{air} := \frac{4\ A_{ff} \cdot S_L}{A_{finned}} = 3.083\ mm$

Reynolds number: $Re_{air3} := \left(\frac{m`_{air}}{A_{ff}}\right) \cdot \left(\frac{d_{air}}{\mu_{a3}}\right) = 1699.261$

Void Reynolds number: $Re_{void3} := \frac{Re_{air3}}{\psi} = 2.757 \cdot 10^3$

Now it is possible to find the laminar and turbulent Nusselt numbers (according to Gnielinski)

Laminar Nusselt number: $Nu_{lam3} := 0.664 \cdot \sqrt{Re_{void3}} \cdot \sqrt[3]{Pr_{a3}} = 31.045$

Turbulent Nusselt number: $Nu_{turb3} := \frac{0.037\ Re_{void3}^{0.8} \cdot Pr_{a3}}{1 + 2.443\ Re_{void3}^{-0.1} \cdot \left(Pr_{a3}^{\frac{2}{3}} - 1\right)} = 19.159$

The Nusselt number for one row and the entire bundle can now be found:

Row Nusselt number: $Nu_{row3} := 0.3 + \sqrt{Nu_{lam3}^{\ 2} + Nu_{turb3}^{\ 2}} = 36.781$

Bundle Nusselt number: $Nu_{bundle3} := \frac{1 + \left(n_{passes} - 1\right)\ f_{Astag}}{n_{passes}} \cdot Nu_{row3} = 42.848$

The external convective heat transfer coefficient can now be found:

$$h_{ext3} := Nu_{bundle3} \cdot \frac{k_{a3}}{l_{ext}} = 23.956\ \frac{W}{m^2\ K}$$

2. Fin efficiency and surface effectiveness calculations:

The 'b' adjustment factor must be found first:

$$b_3 := \sqrt{\frac{2 \cdot h_{ext3}}{k_{fin} \cdot t_{fin}}} = 25.208\ \frac{1}{m}$$

Now the height adjustment factor for circular tubes can be found:

$$\varphi_3 := \left(\frac{d_{fin}}{d_{tbo}} - 1\right) \cdot \left(1 + 0.35 \ln\left(\frac{d_{fin}}{d_{tbo}}\right)\right) = 0.8$$

Dimensionless factor 'X' $$X_3 := \frac{d_{tbo}}{2} \cdot \varphi_3 \cdot b_3 = 0.256$$

Calculate the fin efficiency for use in the surface effectiveness equation

$$\eta_{f3} := \frac{\tanh\left(X_3\right)}{X_3} = 0.979$$

Find the finned surface efficiency for the tubes

$$\eta_{surf3} := 1 - \left(1 - \eta_{f3}\right) \cdot \frac{A_{finned}}{A_{total}} = 0.9801$$

Now one can calculate the external convective resistance:

$$R_{ext3} := \frac{1}{\eta_{surf3} \cdot h_{ext3} \cdot A_{ext}} = 0.0000217507 \ \frac{K}{W}$$

Overall heat transfer coefficient and number of transfer units (NTU):

$$UA_3 := \left(R_{int3} + R_{cond3} + R_{ext3}\right)^{-1} = 37943.757 \ \frac{W}{K}$$

Number of Transfer Units: $$NTU_3 := \frac{UA_3}{C_{min3}} = 0.398$$

Effectiveness calculation for the heat exchanger:

The 'C' ratio is not insignificant (> 0.1) - the streams are assumed to both be unmixed. It is important to note that in the case where there is only a single flow path for each pass, the air stream may be considered mixed. However, in this work, the proximity and closing packing of the finned tubes was considered sufficient to channel the air between the tubes, keeping it unmixed.

Using the ratio and the NTU, the effectiveness can be found for this row.

$$e_3 := 1 - \exp\left(NTU_3^{0.22} \cdot \frac{\exp\left(-C_3 \cdot NTU_3^{0.78}\right) - 1}{C_3}\right) = 0.296$$

Calculate the heat transfer for this longitudinal tube pass for the airside, CO2-side and based on the e-NTU method and compare:

$$Q_{a3} := m`_{air} \cdot \left(h_{a3} - h_{a4}\right) = 0.73452 \ MW$$

$$Q_{CO23} := m`_{CO2HX} \cdot \left(h_{CO22} - h_{CO23}\right) = 0.73452\ \textit{MW}$$

$$Q_3 := e_3 \cdot C_{min3} \cdot \left(T_{CO22} - T_{a4}\right) = 0.73453\ \textit{MW}$$

Python value for heat transfer: $Q_{py\_3} := 0.73452486\ \textit{MW}$

Examining the error between these heat transfers will demonstrate that the energy equations balance:

Error for the air heat transfer: $err_{Qa3} := \frac{\left|Q_{a3} - Q_3\right|}{Q_3} = 0.0007\%$

Error for the CO2 heat transfer $err_{QCO23} := \frac{\left|Q_{CO23} - Q_3\right|}{Q_3} = 0.0007\%$

Examining the error between the heat transfer values in Python and calculated here will verify the Python model:

Error for the air heat transfer: $err_{py\_a3} := \frac{\left|Q_{a3} - Q_{py\_3}\right|}{Q_{py\_3}} = 0.0000002\%$

Error for the CO2 heat transfer $err_{py\_CO23} := \frac{\left|Q_{CO23} - Q_{py\_3}\right|}{Q_{py\_3}} = 0.00000004\%$

Error for the e-NTU heat transfer $err_{py\_e3} := \frac{\left|Q_3 - Q_{py\_3}\right|}{Q_{py\_3}} = 0.00071\%$

With the errors for this row acceptably low, the calculation can now move forwards to the heat transfer for the next element (row). This level of error was deemed acceptable because the exact values for fluid properties have not been used, values were determined in CoolProp and rounded to 5 decimal places.

Fourth CV (1st pass - CV4):

Determine the mean properties of the fluids in the CV, using the mean enthalpy and pressure of the control volume:

Air: $p_{am4} = 92067.362\ Pa$ $h_{am4} = 430136.594\ \frac{J}{kg}$

CO2: $p_{CO2m4} = 7484509.76\ Pa$ $h_{CO2m4} = 440783.917\ \frac{J}{kg}$

[CoolProp]

	Air properties:	CO2 properties:
Prandtl number:	$Pr_{a4} := 0.70652$	$Pr_{CO24} := 1.44958$
Specific heat:	$Cp_{a4} := 1006.37557\ \frac{J}{kg \cdot K}$	$Cp_{CO24} := 2309.16387\ \frac{J}{kg \cdot K}$
Dynamic viscosity:	$\mu_{a4} := 1.87184 \cdot 10^{-5}\ \frac{kg}{m \cdot s}$	$\mu_{CO24} := 1.96993 \cdot 10^{-5}\ \frac{kg}{m \cdot s}$
Conductivity:	$k_{a4} := 0.02666\ \frac{W}{m \cdot K}$	$k_{CO24} := 0.03138\ \frac{W}{m \cdot K}$
Density:	$\rho_{a4} := 1.05601\ \frac{kg}{m^3}$	$\rho_{CO24} := 199.63818\ \frac{kg}{m^3}$

MOMENTUM BALANCE (SCO2-SIDE):

Frictional pressure drops:

Find the Reynolds number in the tube to determine the flow regime and use the appropriate frictional pressure drop correlation:

Set the mass flow rate and velocity in the tube pass and determine the Reynolds number:

$$\dot{m}_{CO2tbs} := \frac{\dot{m}_{CO2HX}}{N_{tubes}} = 0.152\ \frac{kg}{s}$$

$$v_{CO24} := \frac{\dot{m}_{CO2HX}}{\rho_{CO24} \cdot A_{tbi} \cdot N_{tubes}} = 2.579\ \frac{m}{s}$$

$$Re_{tb4} := \frac{\dot{m}_{CO2tbs}}{A_{tbi}} \cdot \frac{d_{tbi}}{\mu_{CO24}} = 507117.477$$ [Flow is turbulent]

Now the friction factor can be found and used to find the pressure drop across this pass.

Darcy-Weisbach friction factor (Swamee & Jain):

$$f_D := \frac{0.25}{\left(\log\left(\frac{\varepsilon_{tb}}{3.7 \cdot d_{tbi}} + \frac{5.74}{Re_{tb4}^{0.9}}\right)\right)^2} = 0.01417$$

Frictional pressure drop: $\Delta p_{fric4} := f_D \cdot \left(\frac{L_{tbpass}}{d_{tbi}}\right) \cdot \frac{\rho_{CO24}}{2} \cdot v_{CO24}^2 = 4.026\ kPa$

Bend pressure drops:

$K_{bends} := 0.18$

Pressure drop across bends: $\Delta p_{bend4} := \frac{1}{2} \cdot K_{bends} \cdot \rho_{CO24} \cdot v_{CO24}^2 = 0.12\ kPa$

Exit pressure loss:

The loss coefficient is assumed unity.

Exit pressure loss: $\Delta p_{ex4} := \frac{1}{2} \cdot \rho_{CO24} \cdot v_{CO24}^2 = 0.664\ kPa$

Total pressure loss across the tubes and actual outlet pressure:

Total pressure loss: $\Delta p_4 := \Delta p_{bend4} + \Delta p_{fric4} + \Delta p_{ex4} = 4.809\ kPa$

Actual outlet pressure: $p_{CO2o4} := p_{CO23} - \Delta p_4 = 7482045.396\ Pa$

The calculated pressure can now be compared to the converged case pressure at the exit of the 1st pass (inlet of the 2nd pass):

$$err_{\Delta p4} := \frac{\left|p_{CO24} - p_{CO2o4}\right|}{p_{CO24}} = 0.0016\%$$

This level of error is deemed acceptable for the pressure drop across this pass, the energy balance can now be performed.

ENERGY BALANCE:

Find and compare the two 'C' values for air and CO2:

$$C_{a4} := m`_{air} \cdot Cp_{a4} = \left(1.831 \cdot 10^5\right) \frac{W}{K}$$

$$C_{CO24} := m`_{CO2HX} \cdot Cp_{CO24} = \left(1.132 \cdot 10^5\right) \frac{W}{K}$$

CO2 has the minimum 'C' value, it must be used as such in the e-NTU correlations.

$$C_{min4} := min\left(C_{a4}, C_{CO24}\right) = \left(1.132 \cdot 10^5\right) \frac{W}{K}$$

$$C_{max4} := \max\left(C_{a4}, C_{CO24}\right) = \left(1.831 \cdot 10^5\right) \frac{W}{K}$$

'C' ratio can now be found:

$$C_4 := \frac{C_{min4}}{C_{max4}} = 0.618$$

This value will be used in conjunction with the overall heat transfer coefficient - 'UA' - in the effectiveness calculation at a later point. The next step is to now determine this UA value by finding and summing the thermal resistances. Fouling has been neglected, so it is only the internal convection, thermal conduction through the tube wall, and external convection

Thermal conduction resistance:

Tube wall properties

$$k_{tb} = 58 \frac{W}{m \cdot K}$$

Calculate the conductivity resistance

$$R_{cond4} := \frac{\ln\left(\frac{d_{tbo}}{d_{tbi}}\right)}{\pi \cdot L_{tbpass} \cdot N_{tubes} \cdot k_{tb}} = 0.0000005534 \frac{K}{W}$$

Internal convection resistance:

Calculate the Reynolds number to determine the flow regime

$$Re_{int4} := \left(\frac{m`_{CO2tbs}}{A_{tbi}}\right) \cdot \left(\frac{d_{tbi}}{\mu_{CO24}}\right) = 507117.477$$

Find the friction factor, this is specifically stated for use here, will be used in the Nusselt number correlation:

$$f_{D1} := \left(1.8 \log\left(Re_{int4}\right) - 1.5\right)^{-2} = 0.013$$

Find the Nusselt number and internal heat transfer coefficient (according to Gnielinski)

$$Nu_{int4} := \frac{\left(\frac{f_{D1}}{8}\right) \cdot Re_{int4} \cdot Pr_{CO24}}{1 + 12.7 \cdot \sqrt{\frac{f_{D1}}{8}} \left(Pr_{CO24}^{\frac{2}{3}} - 1\right)} \left(1 + \left(\frac{d_{tbi}}{L_{tbpass}}\right)^{\frac{2}{3}}\right) = 1063.099$$

$$h_{int4} := Nu_{int4} \cdot \frac{k_{CO24}}{d_{tbi}} = 1719.59 \ \frac{W}{m^2 \cdot K}$$

Find the internal convective resistance:

$$R_{int4} := \frac{1}{h_{int4} \cdot A_{int}} = 0.0000035702 \ \frac{K}{W}$$

External convection resistance:

This calculation is split into two parts, the first involves finding the base heat transfer coefficient and the second involves the determination of the fin and overall surface efficiency.

1. Heat transfer coefficient calculation:

   Determination of the dimensionless values, void factor, and arrangement factors:

   Find the two dimensionless factors (a & b) associated with the tubes

   $$a := \frac{S_T}{d_{tbo}} = 2.047 \qquad b := \frac{S_L}{d_{tbo}} = 3.031$$

   b is greater than 1 therefore the void factor is found as follows

   Void factor: $$\psi := 1 - \frac{\pi}{4\ a} = 0.616$$

   The arrangement is staggered, therefore the arrangement factor is found as follows:

   Arrangement factor: $$f_{Astag} := 1 + \frac{2}{3\ b} = 1.22$$

   Characteristic length calculation:

$$l_{ext} := \frac{\pi}{2} \cdot \sqrt{d_{tbo}^{\ 2} + h_{fin}^{\ 2}} = 0.048 \ m$$

Determine the Reynolds number for the Nusselt correlations:

The hydraulic diameter for the air is required at this point and is calculated below. The Reynolds number also needs to be adjusted by the void factor.

Hydraulic diameter for air: $d_{air} := \frac{4\ A_{ff} \cdot S_L}{A_{finned}} = 3.083\ mm$

Reynolds number: $Re_{air4} := \left(\frac{m`_{air}}{A_{ff}}\right) \cdot \left(\frac{d_{air}}{\mu_{a4}}\right) = 1715.493$

Void Reynolds number: $Re_{void4} := \frac{Re_{air4}}{\psi} = 2.783 \cdot 10^3$

Now it is possible to find the laminar and turbulent Nusselt numbers (according to Gnielinski)

Laminar Nusselt number: $Nu_{lam4} := 0.664 \cdot \sqrt{Re_{void4}} \cdot \sqrt[3]{Pr_{a4}} = 31.2$

Turbulent Nusselt number: $Nu_{turb4} := \frac{0.037\ Re_{void4}^{0.8} \cdot Pr_{a4}}{1 + 2.443\ Re_{void4}^{-0.1} \cdot \left(Pr_{a4}^{\frac{2}{3}} - 1\right)} = 19.303$

The Nusselt number for one row and the entire bundle can now be found:

Row Nusselt number: $Nu_{row4} := 0.3 + \sqrt{Nu_{lam4}^{\ 2} + Nu_{turb4}^{\ 2}} = 36.989$

Bundle Nusselt number: $Nu_{bundle4} := \frac{1 + \left(n_{passes} - 1\right)\ f_{Astag}}{n_{passes}} \cdot Nu_{row4} = 43.089$

The external convective heat transfer coefficient can now be found:

$h_{ext4} := Nu_{bundle4} \cdot \frac{k_{a4}}{l_{ext}} = 23.84\ \frac{W}{m^2\ K}$

2. Fin efficiency and surface effectiveness calculations:

The 'b' adjustment factor must be found first:

$b_4 := \sqrt{\frac{2 \cdot h_{ext4}}{k_{fin} \cdot t_{fin}}} = 25.147\ \frac{1}{m}$

Now the height adjustment factor for circular tubes can be found:

$$\varphi_4 := \left(\frac{d_{fin}}{d_{tbo}} - 1\right) \cdot \left(1 + 0.35 \ln\left(\frac{d_{fin}}{d_{tbo}}\right)\right) = 0.8$$

Dimensionless factor 'X' $$X_4 := \frac{d_{tbo}}{2} \cdot \varphi_4 \cdot b_4 = 0.255$$

Calculate the fin efficiency for use in the surface effectiveness equation

$$\eta_{f4} := \frac{\tanh\left(X_4\right)}{X_4} = 0.979$$

Find the finned surface efficiency for the tubes

$$\eta_{surf4} := 1 - \left(1 - \eta_{f4}\right) \cdot \frac{A_{finned}}{A_{total}} = 0.9802$$

Now one can calculate the external convective resistance:

$$R_{ext4} := \frac{1}{\eta_{surf4} \cdot h_{ext4} \cdot A_{ext}} = 0.0000218539 \ \frac{K}{W}$$

Overall heat transfer coefficient and number of transfer units (NTU):

$$UA_4 := \left(R_{int4} + R_{cond4} + R_{ext4}\right)^{-1} = 38494.926 \ \frac{W}{K}$$

Number of Transfer Units: $$NTU_4 := \frac{UA_4}{C_{min4}} = 0.34$$

Effectiveness calculation for the heat exchanger:

The 'C' ratio is not insignificant (> 0.1) - the streams are assumed to both be unmixed. It is important to note that in the case where there is only a single flow path for each pass, the air stream may be considered mixed. However, in this work, the proximity and closing packing of the finned tubes was considered sufficient to channel the air between the tubes, keeping it unmixed.

Using the ratio and the NTU, the effectiveness can be found for this row.

$$e_4 := 1 - \exp\left(NTU_4^{0.22} \cdot \frac{\exp\left(-C_4 \cdot NTU_4^{0.78}\right) - 1}{C_4}\right) = 0.258$$

Calculate the heat transfer for this longitudinal tube pass for the airside, CO2-side and based on the e-NTU method and compare:

$$Q_{a4} := m`_{air} \cdot \left(h_{a4} - h_{ai}\right) = 0.63505 \ MW$$

$$Q_{CO24} := m`_{CO2HX} \cdot \left(h_{CO23} - h_{CO24}\right) = 0.63505\ \boldsymbol{MW}$$

$$Q_4 := e_4 \cdot C_{min4} \cdot \left(T_{CO23} - T_{ai}\right) = 0.63501\ \boldsymbol{MW}$$

Python value for heat transfer: $Q_{py\_4} := 0.63505203\ \boldsymbol{MW}$

Examining the error between these heat transfers will demonstrate that the energy equations balance:

Error for the air heat transfer: $err_{Qa4} := \frac{\left|Q_{a4} - Q_4\right|}{Q_4} = 0.0069\%$

Error for the CO2 heat transfer $err_{QCO24} := \frac{\left|Q_{CO24} - Q_4\right|}{Q_4} = 0.0069\%$

Examining the error between the heat transfer values in Python and calculated here will verify the Python model:

Error for the air heat transfer: $err_{py\_a4} := \frac{\left|Q_{a4} - Q_{py\_4}\right|}{Q_{py\_4}} = 0.0000005\%$

Error for the CO2 heat transfer $err_{py\_CO24} := \frac{\left|Q_{CO24} - Q_{py\_4}\right|}{Q_{py\_4}} = 0.0000003\%$

Error for the e-NTU heat transfer $err_{py\_e4} := \frac{\left|Q_4 - Q_{py\_4}\right|}{Q_{py\_4}} = 0.00693\%$

With the errors for this row acceptably low, the calculation can now move forwards to the air-side momentum balance. This level of error was deemed acceptable because the exact values for fluid properties have not been used, values were determined in CoolProp and rounded to 5 decimal places.

All of the rows now have their energy balanced across them. The total heat extracted by the unit and then the whole PC setup can now be determined. Other important outputs are the outlet temperatures of air and CO2. All of these are compared to the Python model results as well. The draft equation (momentum balance across the entire cooling unit) will now be balanced.

SUMMARY & COMPARISON OF KEY RESULTS WITH PYTHON MODEL OUTUTS:

Heat extracted by one cell: $Q_{cell} := Q_1 + Q_2 + Q_3 + Q_4 = 3.44627\ MW$

Python model value: $Q`_{cell} := 3446582.60395\ W = 3.44658\ MW$

Absolute error: $err_{Q\_cell} := \frac{|Q`_{cell} - Q_{cell}|}{Q`_{cell}} = 0.009\%$

Heat extracted by PC: $Q_{PC} := Q_{cell} \cdot N_{cells} = 27.57017\ MW$

Python model value: $Q`_{PC} := 27.57266\ MW$

Absolute error: $err_{Q\_PC} := \frac{|Q`_{PC} - Q_{PC}|}{Q`_{PC}} = 0.009\%$

PC Pressure Ratio (CO2): $PR := \frac{p_{CO2o4}}{p_{CO2in}} = 0.9974$

DRAFT EQUATION BALANCE (MOMENTUM):

The pressure drops introduced by screens and walkways, the shroud inlet, and the heat exchanger need to be balanced by the natural pressure rise across the unit and the pressure rise introduced by the fan at its operating point. The plenum recovery is negligible because of the proximity of the heat exchanger to the fan and the fact that an A-frame configuration is not being used. A velocity distribution factor also contributes to this pressure term and is included accordingly.

Static pressure rise and fan coefficient:

Fan static pressure rise: $\Delta p_{fan} = 63.003\ Pa$

Fan coefficient: $K_{Fs} := 2 \cdot \Delta p_{fan} \cdot \rho_{aF} \cdot \left(\frac{A_{casing}}{m`_{air}} \right)^2 = 10.654$

Upstream and downstream losses:

These have been determined by polynomials generated from the relevant curves and based on the ratio of distance from the fan to casing diameter as well as the ratio of the projected obstruction area to the casing area.

There are 2 obstructions downstream (shroud inlet screen, support beams) and there are 2 obstructions upstream (walkway, support beams). These must all be included and combine to find the upstream and downstream secondary loss coefficients. A single interpolation is shown for the screen and then the loss factors are stated from the python model to save space and because the calculated values mathc perfectly.

1. Downstream losses:

Distance from fan: $x_{screen} := H_{si} = 1.536\ m$

Fan casing diameter: $d_{casing} = 8.083\ m$

Fan casing area: $A_{casing} = 51.318\ m^2$

Projected area: $A_{screen} := 53.0\ m^2$ [From Solidworks]

Now the area ratio and distance-to-casing ratio can be determined. These are the inputs to the polynomial curves.

Area ratio: $A_1 := \frac{A_{screen}}{A_{casing}} = 1.033$

Distance ratio: $DR := \frac{x_{screen}}{d_{casing}} = 0.19$

There are 4 second order polynomial curves used when detrmining the downstream loss coefficients, and the curve used is determined by the distance ratio (A):

$K_{do.05}(A) := 11.927\ A^2 + 2.9949\ A - 0.0082$

$K_{do.10}(A) := 9.5885\ A^2 + 1.4441\ A - 0.002$

$K_{do.15}(A) := 3.6857\ A^2 + 0.9167\ A + 0.0069$

$K_{do.20}(A) := 1.2922\ A^2 + 0.0361\ A + 0.0018$

Because the distance ratio is not on one of the exact curves (it is between 0.15 and 0.2), an interpolation is required to determine the coefficient:

Setup the results vector:

$$output := \begin{bmatrix} K_{do.05}(A_1) \\ K_{do.10}(A_1) \\ K_{do.15}(A_1) \\ K_{do.20}(A_1) \end{bmatrix} = \begin{bmatrix} 15.807 \\ 11.717 \\ 4.885 \\ 1.417 \end{bmatrix}$$

Estabilish the coefficient matrix, with 0.05 as the reference distance ratio:

$$coefficient\_matrix := \begin{bmatrix} 1 & 0 & 0 & 0 \\ 1 & 0.1-0.05 & (0.1-0.05)^2 & (0.1-0.05)^3 \\ 1 & 0.15-0.05 & (0.15-0.05)^2 & (0.15-0.05)^3 \\ 1 & 0.2-0.05 & (0.2-0.05)^2 & (0.2-0.05)^3 \end{bmatrix}$$

$$coefficient\_matrix = \begin{bmatrix} 1 & 0 & 0 & 0 \\ 1 & 0.05 & 0.0025 & 0.000125 \\ 1 & 0.1 & 0.01 & 0.001 \\ 1 & 0.15 & 0.0225 & 0.003375 \end{bmatrix}$$

$$coefficients := \text{lsolve}(coefficient\_matrix, output) = \begin{bmatrix} 15.807 \\ -13.663 \\ -1.77 \cdot 10^3 \\ 8.142 \cdot 10^3 \end{bmatrix}$$

$$DR_{terms} := \begin{bmatrix} 1 \\ DR-0.05 \\ (DR-0.05)^2 \\ (DR-0.05)^3 \end{bmatrix} = \begin{bmatrix} 1 \\ 0.14 \\ 0.0196 \\ 0.002744 \end{bmatrix}$$

The loss coefficient can now be found by taking the dot product of the coefficients and the distance ratio terms:

Screen coefficient: $K_{screen} := coefficients \cdot DR_{terms} = 1.54865$

Python screen coefficient: $K'_{screen} := 1.54865$

As can be seen, the values match exactly. The same process as above was performed for the remaining obstructions, with only the polynomials changing for the upstream coefficients, the results are summarised below:

Screen coefficient: $K_{screen} = 1.54865$

Downstream beam coefficient: $K_{beam\_do} := 0.13842$

Walkway coefficient: $K_{walkway} := 3.56068$

Upstream beam coefficient: $K_{beam\_up} := 0.05662$

Upstream loss coefficient: $K_{up} := K_{walkway} + K_{beam\_up} = 3.617$

Downstream loss coefficient: $K_{do} := K_{screen} + K_{beam\_do} = 1.687$

Tower support losses:

These are based on the cooling cell geometry and number of supports. The number of tower supports depends on the number of cooling cells. With a single tower support sufficient to hold 4 cells, that means that for the 8 cells present here, 2 tower supports are required. A drag coefficient of 2.01 is used for a long rectangular obstruction. An offset distance of 2.5m from the fan height to the tower supports is used to ensure the shroud fits beneath the platform.

Drag coefficient: $C_{Dts} := 2.01$

Number of supports: $n_{ts} := 2$

Diameter of supports: $d_{ts} := 4.5\ m$

Inlet area (free-flow): $A_{inlet} := H_{fan} \cdot W_{HX} = 174.3\ m^2$

Length of supports: $L_{ts} := H_{fan} - 2.5\ m = 18.5\ m$

The loss coefficient is now calculated as follows below for the cooling cells:

$$K_{ts} := \frac{C_{Dts} \cdot n_{ts} \cdot d_{ts} \cdot L_{ts}}{A_{inlet}} = 1.92$$

Heat exchanger losses:

The heat exchanger introduces pressure drops to the airstream as a result of contractions and expansions in the flow. The calculation depends on whether the tubes are arranged as staggered or inline as well as the fin shape. This calculation requires a lot of setup and dimensionless values. All of the properties used here are taken at the harmonic mean value for the heat exchanger based on the air inlet and outlet conditions.

Air inlet density: $\rho_{ai} := 1.06208464\ \frac{kg}{m^3}$

Air outlet density: $\rho_{ao} := 0.99966595\ \frac{kg}{m^3}$

Harmonic mean air density: $\rho_{am} := \frac{2}{\frac{1}{\rho_{ai}} + \frac{1}{\rho_{ao}}} = 1.02993\ \frac{kg}{m^3}$

Harmonic mean air viscosity: $\mu_{am} := 1.9070996 \cdot 10^{-5}\ \frac{kg}{m \cdot s}$ [Same method as density, taken from python]

Setup:

Free flow velocity of air: $v_{aFF} := \frac{V_{air}}{A_{fr}} = 2.4854 \ \frac{m}{s}$

Diagonal pitch: $S_D := \sqrt{\left(\frac{S_T}{2}\right)^2 + {S_L}^2} = 81.271 \ mm$

Dimensionless values based on geometry:

$a := \frac{S_T}{d_{tbo}} = 2.04724$ $b := \frac{S_L}{d_{tbo}} = 3.0315$

$c := \sqrt{\left(\frac{a}{2}\right)^2 + b^2} = 3.2$

$C := \frac{S_D}{d_{tbo}} \cdot c = 10.238$

Row correction factor is found as follows (for a bundle having less than 10 rows - anymore than 10 and the correction factor falls away):

Base correction factor: $f_0 := \left(\frac{2 \cdot (c-1)}{a \cdot (a-1)}\right)^2 = 4.21$

Row correction factor: $f_{nturb} := f_0 \cdot \left(\frac{1}{N_L} - \frac{1}{10}\right) = 0.1053$

It is now necessary to compare the 'b' value to an adjusted a value to determine which calculation method to use:

$a` := 0.5 \cdot \sqrt{2 \cdot a + 1} = 1.129$

'b' is greater than 'a prime'. Therefore, the following setup method is followed:

Number of main resistances: $n_{MR} := N_L = 8$

Effective velocity: $v_{eff} := v_{aFF} \cdot \frac{a}{a-1} = 4.85868 \ \frac{m}{s}$

Reynolds number: $Re_{HX} := \frac{v_{eff} \cdot d_{tbo} \cdot \rho_{am}}{\mu_{am}} = 6664.785$

Finding the contributing loss factors:

Adjusted laminar factor: $f`_{lam} := \frac{280 \ \pi \cdot \left(\left(b^{0.5} - 0.6\right)^2 + 0.75\right)}{\left(4 \cdot a \cdot b - \pi\right) \cdot a^{1.6}} = 26.45585$

Laminar factor: $f_{lam} := \frac{f`_{lam}}{Re_{HX}} = 0.00397$

Prime factor: $F := 1 - \exp\left(-\frac{Re_{HX} + 200}{1000}\right) = 0.99896$

Adjusted turbulent factor:

$$f`_{turb} := 2.5 + \frac{1.2}{(a - 0.85)^{1.08}} + 0.4 \cdot \left(\frac{b}{a} - 1\right)^3 - 0.01 \cdot \left(\frac{a}{b} - 1\right)^3 = 3.53276$$

Turbulent factor: $f_{turb} := \frac{f`_{turb}}{Re_{HX}^{0.25}} = 0.39099$

The heat exchanger loss coefficient is now ready to be determined. The first step is to find the drag coefficient for the tubes:

$$C_{Dtbs} := f_{lam} + \left(f_{turb} + f_{nturb}\right) \cdot F = 0.49971$$

The heat exchanger coefficient can be found by multiplying the drag coefficient by the number of resistances:

Heat exchanger loss coefficient: $K_{HX} := C_{Dtbs} \cdot n_{MR} = 3.99765$

Velocity distribution factor and recovery coefficient:

Recovery coefficient: $K_{rec} := 0.0$ [For horizontal bundles]

Velocity distribution factor: $\alpha_e := 1.6 - 0.48 \cdot \sigma_a - 0.012 \cdot K_{HX} = 1.43$

Draft equation left hand side:

The left hand side of the equation is the natural pressure rise that occurs across the system. It is dependent on the lapse rate, outlet and ambient temperatures.

Cooling cell exit height: $H_{exit} := H_{HXexit} + H_{ww} = 24.58\ m$

$$LHS := p_a \cdot \left(\left(1 - MALR \cdot \frac{H_{exit} - H_{HXexit}}{T_{a1}}\right)^{3.5} - \left(1 - MALR \cdot \frac{H_{exit} - H_{HXexit}}{T_a}\right)^{3.5}\right)$$

$LHS = 0.1604091\ Pa$

Draft equation right hand side:

This side of the equation is made up of all the losses and gains introduced by the components of the cooling cell.

Tower support pressure drop: $\Delta p_{ts} := \frac{K_{ts}}{2 \cdot \rho_a} \cdot \left(\frac{m`_{air}}{A_{inlet}} \right)^2 = 0.98455 \ Pa$

Shroud inlet pressure drop: $\Delta p_{si} := \frac{K_{Fsi}}{2 \cdot \rho_{aF}} \cdot \left(\frac{m`_{air}}{A_{casing}} \right)^2 = 0 \ Pa$

Obstacles pressure drop: $\Delta p_{obs} := \frac{K_{do} + K_{up}}{2 \cdot \rho_{aF}} \cdot \left(\frac{m`_{air}}{A_e} \right)^2 = 43.80499 \ Pa$

Fan-plenum pressure recovery: $\Delta p_{Fp} := \frac{K_{Fs} + K_{rec}}{2 \cdot \rho_{aF}} \cdot \left(\frac{m`_{air}}{A_{casing}} \right)^2 = 63.0033 \ Pa$

Heat exchanger pressure drop: $\Delta p_{hx} := \frac{K_{HX} + \alpha_e}{2 \cdot \rho_{am}} \cdot \left(\frac{m`_{air}}{A_{fr}} \right)^2 = 18.37422 \ Pa$

The RHS of the equation can now be determined and compared to the LHS:

$RHS := \Delta p_{ts} + \Delta p_{si} + \Delta p_{obs} - \Delta p_{Fp} + \Delta p_{hx} = 0.1604613 \ Pa$

Draft difference: $Draft_{diff} := LHS - RHS = -0.00005 \ Pa$

The draft equation is balanced because the two sides are approximately equal (within a tolerance value of 0.001). This indicates that the airside momentum balance has been satisfied and the mass flow of air is converged.

SUMMARY OF IMPORTANT RESULTS:

Mass flow rate of air: $m`_{air} = 181.9118 \ \frac{kg}{s}$

Total heat transfer: $Q_{PC} = 27.570173 \ MW$

Pressure Ratio (CO2): $PR = 0.9973984$

Total fan power consumed: $P_{PCaux} = 184.49573 \ kW$

Total heat transfer (Python): $Q_{PC\_py} := 27.5705854 \ MW$

Pressure Ratio CO2 (Python): $PR_{py} := 0.9972231$

Total fan power consumed (Python): $P_{PCaux\_py} := 184.4950829 \ kW$